(2)

Marine Physical Laboratory

AD-A239 183

MARINE PHYSICAL LABORATORY MULTI-DISCIPLINARY OCEAN SCIENCE AND TECHNOLOGY PROGRAM

Final Report
Prepared for the
Office of Naval Research
Contract N00014-87-K-0010
For the Period 10-01-86 - 10-01-90
Principal Investigator(s): Kenneth M. Watson, Director
Fred H. Fisher, Deputy Director

MPL-U-66/90
April 1991

Approved for public release; distribution unlimited.

University of California, San Diego
Scripps Institution of Oceanography

91-07225

91 8 07 073

SECURITY CLASSIFICATION OF THIS PAGE

REPORT DOCUMENTATION PAGE

1a. REPORT SECURITY CLASSIFICATION UNCLASSIFIED

1b RESTRICTIVE MARKINGS

2a. SECURITY CLASSIFICATION AUTHORITY

2b DECLASSIFICATION / DOWNGRADING SCHEDULE

3 DISTRIBUTION / AVAILABILITY OF REPORT Approved for public release; distribution unlimited.

4. PERFORMING ORGANIZATION REPORT NUMBER(S) MPL-U-66/90

5. MONITORING ORGANIZATION REPORT NUMBER(S)

6a. NAME OF PERFORMING ORGANIZATION Marine Physical Laboratory

6b. OFFICE SYMBOL *(If applicable)* MPL

7a. NAME OF MONITORING ORGANIZATION
Office of Naval Research
Department of the Navy

6c. ADDRESS *(City, State, and ZIP Code)*
University of California, San Diego
Scripps Institution of Oceanography
San Diego, CA 92152

7b. ADDRESS *(City, State, and ZIP Code)*
800 North Quincy Street
Arlington, VA 22217-5000

8a. NAME OF FUNDING / SPONSORING ORGANIZATION Office of Naval Research

8b. OFFICE SYMBOL *(If applicable)* ONR

9. PROCUREMENT INSTRUMENT IDENTIFICATION NUMBER N00014-87-K-0010

8c. ADDRESS *(City, State, and ZIP Code)*
Department of the Navy
800 North Quincy Street
Arlington, VA 22217-5000

10. SOURCE OF FUNDING NUMBERS

PROGRAM ELEMENT NO.	PROJECT NO.	TASK NO	WORK UNIT ACCESSION NO.

11. TITLE *(Include Security Classification)*
MARINE PHYSICAL LABORATORY MULTI-DISCIPLINARY OCEAN SCIENCE AND TECHNOLOGY PROGRAM

12. PERSONAL AUTHOR(S)
Kenneth M. Watson and Fred H. Fisher

13a. TYPE OF REPORT final report

13b TIME COVERED FROM ______ TO ______

14. DATE OF REPORT *(Year, Month, Day)* April 1991

15 PAGE COUNT 135

16. SUPPLEMENTARY NOTATION

17. COSATI CODES

FIELD	GROUP	SUB-GROUP

18. SUBJECT TERMS *(Continue on reverse if necessary and identify by block number)*
internal wave dynamics, ocean acoustics, ocean technology, undersea warfare

19 ABSTRACT

During the period of this contract, October 1, 1986 to October 1, 1990, scientists at the Marine Physical Laboratory of the Scripps Institution of Oceanography, UCSD, pursued investigations of problems in physical oceanography ranging in depth from acoustic noise fields at the surface, to studies of low frequency noise fields at the deep sea floor.

The spectrum of scientific topics included ocean measurements of the Newtonian Gravitational Constant, theoretical studies of internal wave dynamics and investigations of acoustic questions related to the performance of the SEABEAM bottom-mapping sonar. While the MPL program emphasized acoustic problems, interactions with geology and meteorology were also studied, as well as physical dynamics and oceanic gravimetry.

The diversity of scientific disciplines represented in the MPL scientific staff continues to produce innovative approaches to the investigation of problems important to the advancement of Navy capabilities in undersea warfare.

20 DISTRIBUTION / AVAILABILITY OF ABSTRACT
☐ UNCLASSIFIED/UNLIMITED ☒ SAME AS RPT. ☐ DTIC USERS

21. ABSTRACT SECURITY CLASSIFICATION UNCLASSIFIED

22a. NAME OF RESPONSIBLE INDIVIDUAL Kenneth M. Watson, Director, MPL

22b. TELEPHONE *(Include Area Code)* (619) 534-1803

22c. OFFICE SYMBOL MPL

DD FORM 1473, 84 MAR

83 APR edition may be used until exhausted.
All other editions are obsolete

SECURITY CLASSIFICATION OF THIS PAGE

☆ U.S. Government Printing Office: 1986—607-044

MARINE PHYSICAL LABORATORY MULTI-DISCIPLINARY OCEAN SCIENCE AND TECHNOLOGY PROGRAM

Final Report
Prepared for the
Office of Naval Research
Contract N00014-87-K-0010
For the Period 10-01-86 - 10-01-90
Principal Investigator(s): Kenneth M. Watson, Director
Fred H. Fisher, Deputy Director

DTIC COPY INSPECTED 6

MPL-U-66/90
April 1991

Accession For
NTIS GRA&I ☒
DTIC TAB ☐
Unannounced ☐
Justification
By
Distribution/
Availability Codes
Dist | Avail and/or Special
A-1

Table of Contents

I. Executive Summary 1

II. Project Reports

Surface Generated Noise Under Low Wind Speed at Kilohertz Frequencies
(E. C. Shang and V. C. Anderson) **5**

The Coupling of Surface and Internal Gravity Waves: Revisited
(Kenneth M. Watson) **15**

Richardson Number Criterion for the Nonlinear Stability of Three-Dimensional Stratified Flow
(Henry D. I. Abarbanel, Darryl D. Holm, Jerrold E. Marsden, and Tudor Ratiu) **33**

Vertical Directionality of Ambient Noise at 32 N as a Function of Longitude and Wind Speed
(W. S. Hodgkiss and F. H. Fisher) **39**

Coherence Lengths of Seafloor Noise: Effect of Ocean Bottom Structure
(Anthony E. Schreiner and LeRoy M. Dorman) **47**

Simultaneous Operation of the Sea Beam Multibeam Echo-Sounder and the SeaMARC II Bathymetric Sidescan Sonar System
(Christian de Moustier, Peter F. Lonsdale and Alexander N. Shor) **61**

A Seafloor and Sea Surface Gravity Survey of Axial Volcano
(John A. Hildebrand, J. Mark Stevenson, Philip T. C. Hammer, Mark A. Zumberge, and Robert L. Parker) **75**

Very Low Frequency Coherency Studies
(Spahr C. Webb) **79**

Open Ocean Surface Wave Measurement Using Doppler Sonar
(R. Pinkel and J. A. Smith) **82**

Long-Period Acoustic and Seismic Measurements and Ocean Floor Currents
(Spahr C. Webb) **91**

Evaluation and Verification of Bottom Acoustic Reverberation Statistics Predicted by the Point Scattering Model
(D. Alexandrou and C. de Moustier) **101**

On-Line Sea Beam Acoustic Imaging
(C. de Moustier and F. V. Pavlicek) **103**

Modulation of Short Wind Waves by Long Waves
(Jerome A. Smith) **111**

The Newtonian Gravitational Constant
(John A. Hildebrand, Alan D. Chave, Fred N. Spiess, Robert L. Parker, Mark E. Ander, and Mark A. Zumberge) **117**

The Performance of Two Classes of Active Sonar Detectors in a Shallow Water Environment
(D. Almagor and W. S. Hodgkiss) **125**

III. Bibliography 131

I. EXECUTIVE SUMMARY

During the period of this contract, October 1, 1986 to October 1, 1990, scientists at the Marine Physical Laboratory of the Scripps Institution of Oceanography, UCSD, pursued investigations of problems in physical oceanography ranging in depth from acoustic noise fields at the surface, to studies of low frequency noise fields at the deep sea floor.

The spectrum of scientific topics included ocean measurements of the Newtonian Gravitational Constant, theoretical studies of internal wave dynamics and investigations of acoustic questions related to the performance of the SEABEAM bottom-mapping sonar. While the MPL program emphasized acoustic problems, interactions with geology and meteorology were also studied, as well as physical dynamics and oceanic gravimetry.

The diversity of scientific disciplines represented in the MPL scientific staff continues to produce innovative approaches to the investigation of problems important to the advancement of Navy capabilities in undersea warfare.

II. PROJECT REPORTS

The following project reports are listed with their appropriate principal investigators. The pages where the project reports are annotated at the end.

1. Wind Generated Surface Noise (Victor C. Anderson)

Pages 5-14.

2. Internal Wave Mesoscale Interaction (Kennth M. Watson)

Pages 15-32.

3. Hydrodynamics of Stratified Fluids and Internal Wave Dynamics (Henry D. I. Abarbanel)

Pages 33-38.

4. Low Frequency Ambient Noise Observations with Multidimensional Arrays (William S. Hodgkiss and Victor C. Anderson

Pages 39-46.

5. (1) OBS Studies of the Interaction of Low-Frequency Ambient Noise With Sea-Floor Geology; (2) Low Frequency Ambient Noise Observations with Multidimensional Arrays (Leroy M. Dorman and John A. Hildebrand)

Pages 47-60.

6. Infererence of Seafloor Characteristics from Complex Sea Beam Acoustic Data (Christian de Moustier and Victor C. Anderson)

Pages 61-73.

7. Seafloor and Mid-Water Gravimetry (Fred N. Spiess and John A. Hildebrand)

Pages 75-77.

8. Very Low Frequency Coherency Studies (Spahr C. Webb)

Pages 79-80.

9. (1) Surface Waves, Ship Wakes, and Langmuir Cells: A Proposal Program for FY 1988; (2) Support for FLIP Towship;

(3) Upper Ocean Physics Program (Robert Pinkel)

Pages 81-89.

10. (1) Washington Coast Ultra-Low Frequency Ambient Noise Experiment; (2) ULF/VLF Instrumentation (Spahr C. Webb)

Pages 91-99.

11. Evaluation and Verification of Seafloor Acoustic Scattering Models (Christian de Moustier, Dimitri Alexandrou and Kenneth M. Watson)

Page 101.

12. Sea Beam Acoustic Measurements in the Deep Scattering Layer (Christian de Moustier, Kenneth L. Smith and Dimitri Alexandrou)

Pages 103-109.

13. A Theoretical Study of Modulation of Short Wind Waves and Surface Drift (Jerome A. Smith)

Pages 111-116.

14. Ocean Measurement of the Newtonian Gravitational Constant (Fred N. Spiess and John A. Hildebrand)

Pages 117-123.

15. Fluctuations of Ambient Noise (William S. Hodgkiss)

Pages 125-130.

Surface Generated Noise Under Low Wind Speed at Kilohertz Frequencies*

E. C. Shang and V. C. Anderson

---

*. Reprinted from the Journal of the Acoustical Society of America, Vol. 79 (4), pp. 964-971 (1986)

Surface-generated noise under low wind speed at kilohertz frequencies

E. C. Shang and V. C. Anderson
Marine Physical Laboratory, Scripps Institution of Oceanography, University of California, San Diego, California 92152

(Received 11 October 1984; accepted for publication 7 January 1986)

Some experimental observations of the ocean surface under low wind speed conditions, carried out with the high gain acoustic distribution array, ADA, indicate that bubbles may play an important role in the noise generating mechanism in this wind speed regime. One of the mechanisms discussed in the theory is that of bubble collapse in the surface turbulence layer as first proposed by Furduev [Atmos. Ocean. Phys. 2, 314 (1966)]. Under typical ocean conditions, low wind speeds, and the available bubble population data, the calculated noise level agrees well with experimental results, both in magnitude and in the shape of the spectrum. The spectrum has a peak in the frequency range of 100 to 1000 Hz and an ω^{-2} behavior at high frequencies. Several geophysical parameters could influence the noise generation. Local wind speed probably controls the population of bubbles, and swell-induced static pressure variations could play an important role in the critical turbulence pressure for bubble collapse. There seems to be further evidence that additional structure within the water, perhaps bubble density associated with different water masses, generates a patch type of distribution on the sea surface in the low wind speed situation.

PACS numbers: 43.30.Lz, 43.30.Nb, 92.10.Vz

INTRODUCTION

For almost half a century, since the time of Knudsen's experimental measurements, it has been recognized that the surface winds play a dominant role in the generation of ambient noise in the ocean in the kilohertz frequency region. In spite of the large amount of research that has gone on in the interim, the actual mechanisms of noise generation have not been clearly identified. That is not to say that there has not been any thought given to the question. Kerman (1984) provides an excellent review of the work that has gone on in attempting to identify these mechanisms. He emphasizes particularly the kilohertz region and wind speeds above the critical speed, that speed for which the friction velocity exceeds the minimum phase velocity in the wave spectrum that lies between the capillary and gravity wave regimes. The formation of whitecaps and the associated bubble excitation or the occurrence of spray are obvious mechanisms that occur in the higher wind speed region where waves are generated with sufficient amplitude to cause rupture and breaking of the crests. However, for wind speeds below this (approximately 5.5 m/s at a standard height of 10 m) there is no obvious noise-generating mechanism, and yet, experimental measurements of ambient noise indicate that noise does exist, and is wind speed dependent at these lower wind speeds.

One of the problems in data that has been taken in the low wind speed case is that in many instances the measurements are contaminated by noise sources other than the wind generated surface noise. Consequently, the indication of the dependence of noise level on wind speed in this region is quite uncertain. For example, Kerman (1984) in his Fig. 2, which is a composite of data from several sources, shows a third power dependence for low wind speed based on Evans and Watts (1981) but an indication of a lower power dependence for the other sources. By way of contrast, shallow water measurements reported by Wille and Geyer (1984) show essentially no dependence on wind speed for the minimum spectrum levels at kilohertz frequencies in the comparable wind speed region (wind speed below 6 kn).

The diversity of wind speed characteristics is illustrated in Fig. 1 where wind speed data from several authors have been combined. The data are normalized to a reference level

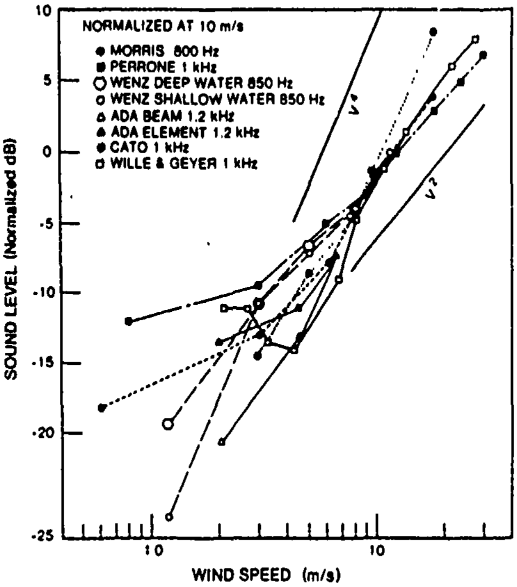

FIG. 1. Wind speed dependence of surface noise, various authors: Cato (1979), Morris (1978), Perrone (1969), Wenz (1962), Wille and Geyer (1984).

at 10 m/s. The slopes range from u^0 for Wille and Geyer to u^4 for shallow water data from Wenz (1962). The ADA data come from the same data set as that of Figs. 3 and 4. For this data set a significantly higher slope, approximately u^5, is observed for data from a beam directed toward the surface which preferentially receives the surface-generated noise, than for that from an individual element which has a broad cardioid response directed horizontally and is responsive to noise sources not located at the surface.

Without some degree of confidence in the power law dependence on wind speed or some visible manifestation of the mechanism, it is difficult to ascertain what the real sound generating process is.

In this paper we will present some of the clues of an indirect nature which relate to the low wind speed condition and also introduce conjectures as to the mechanism or mechanisms which could be generating the noise. The wind speed dependence of the noise intensity given by the theoretical analysis in the present paper is

$$I \sim u^{\alpha} \quad (\alpha = 3.0 \text{ to } 4.5).$$

I. EXPERIMENTAL OBSERVATIONS

The two data sets shown here were collected with the large Acoustic Distribution Array (ADA) illustrated in Fig. 2. This array is described in considerable detail in an earlier paper (Anderson, 1980). It is an array which has a planar aperture of roughly 20 by 5 m, filled with approximately 700 cardioid hydrophone units. Contained within the pressure case is a digital DIMUS beamformer which filters and hard limits the set of hydrophone signals and then transforms it into a set of directional beams. These beams cover one full hemisphere, formatted in subsets of constant elevation, with shoulder to shoulder beams in each elevation subset covering ± 90 deg in azimuth.

The first data set was taken in September 1979 at a very opportune time when the wind speed changed from an initial value of about 2 m/s in a quite linear manner up to 6.5 m/s as shown in Fig. 3. The hydrophone signals were filtered to a 200-Hz band centered at 1200 Hz. During this run the array was moored at a depth of about 300 m below the surface in 3600-m-deep water. In Fig. 4 the original beam data have been interpolated to reformat them into a display that maps uniform linear displacement on the ocean surface to a uniform linear displacement in the figure. Thus, a constant velocity track on the ocean surface will appear as a straight line with the appropriate slope. Two such tracks are identified in Fig. 4(a) with slope magnitudes of 1.0 and 4.4 m/s.

The top portion of the figure shows the start of the linear increase in wind speed. In interpreting the data, it should be

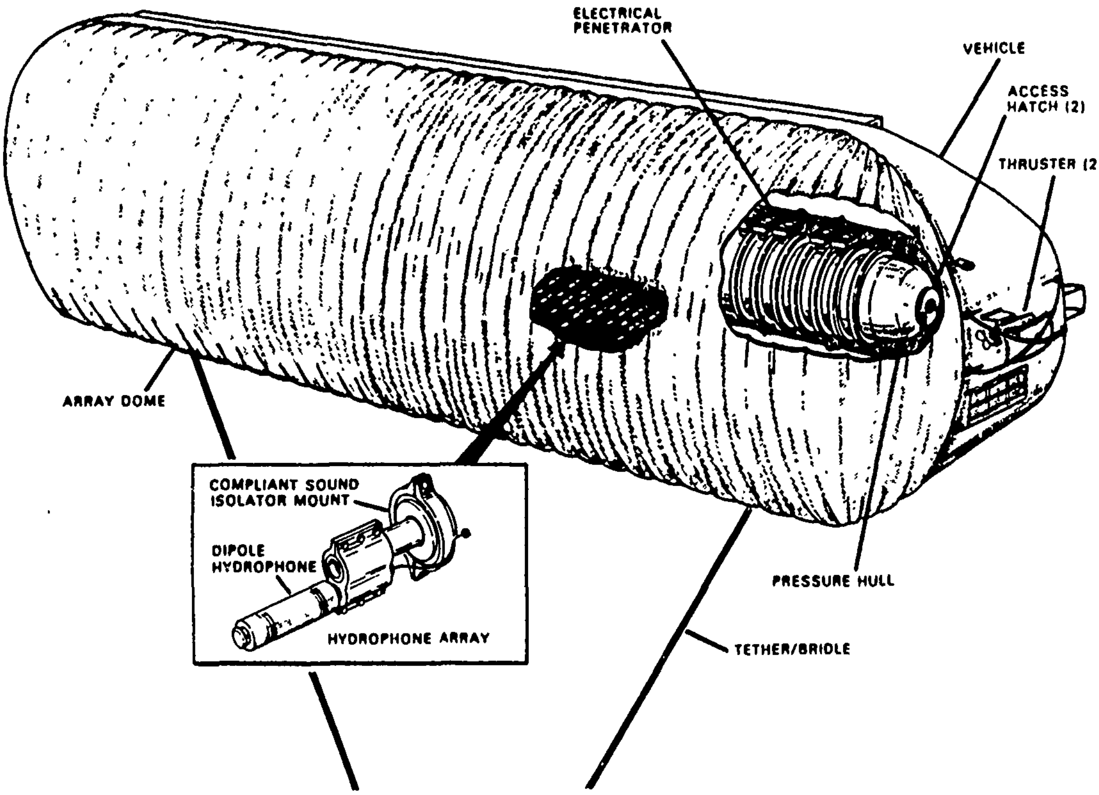

FIG. 2. Artist's rendering of ADA, acoustic distribution array

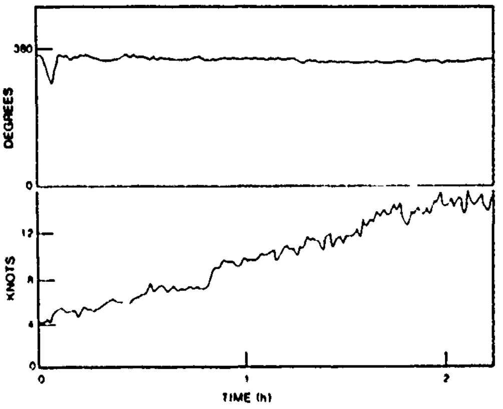

FIG. 3. Wind speed and direction versus time for data of Fig. 4.

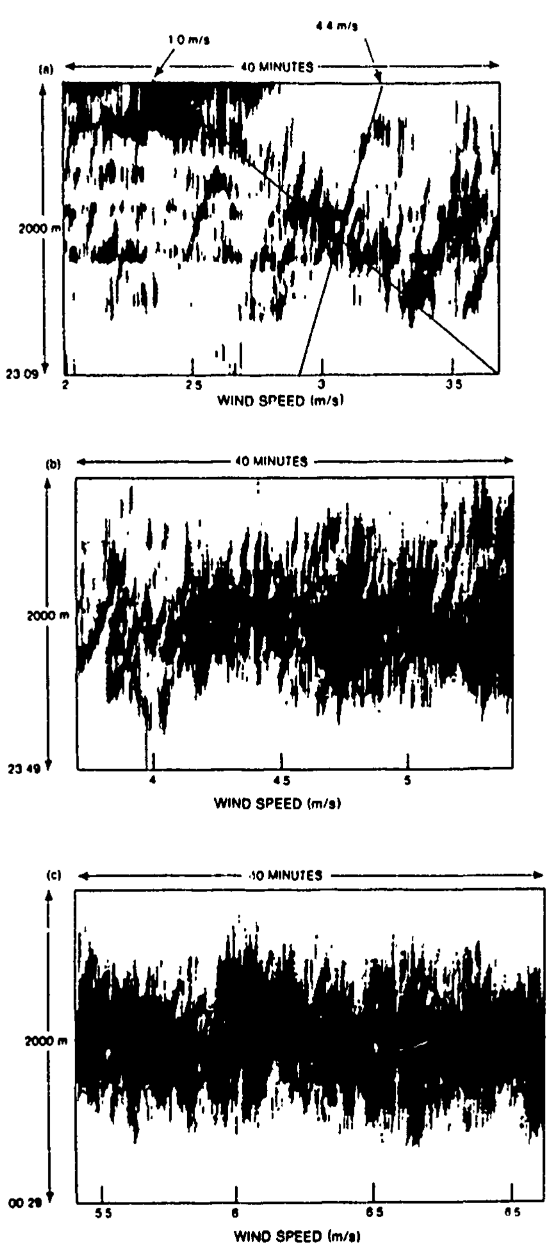

FIG. 4. Surface noise structure as observed from ADA for wind speeds increasing from 2–6.5 m/s.

pointed out that the array itself was located almost a kilometer away from the surface platform ORB (Ocean Research Buoy) on which the wind speed sensor was mounted. Thus, there could be a significant time lag between the wind speed effect evidenced on the acoustic record and that recorded at ORB. Further, it should also be noted that the display has been normalized to constant total power by the inherent normalization of the DIMUS beamformer and by the image enhancement algorithm used in generating the display from the raw beamformer data. In the early part of the record the ambient noise level is quite low corresponding to the very low wind speed. The sea at this time was glassy smooth. Three horizontal bands can be seen at the early part of the record. These are caused by distant shipping noise (beyond our 40-mi radar range) entering through the sidelobes of the beams. As the wind speed increases with time these bands are suppressed by the rising ambient wind generated noise level.

The features of interest are the diagonal tracks having a slope comparable to the 4.4-m/s slope drawn on the figure. This velocity corresponds to the group velocity of gravity waves with a 6-s period. One thing is clear, that, whatever the physical phenomenon, the manifestation as a source of acoustic radiation undergoes a definite translation over the ocean surface. This same slope is observed for the remainder of the record, independent of wind speed, from which we infer that the 6-s waves would be associated with swell originating outside of the region of local wind activity. The effect of wind speed is to increase the occurrence of the noise tracks until, at the 6-m/s wind speed, they are barely distinguishable from a continuum of noise. Another word of explanation for the display: The lack of resolvable wave structure at the extreme ranges, top and bottom of the display, is caused by a combination of the reduced sensitivity of the directivity pattern of the individual cardioid hydrophone elements for these directions and the larger beam "footprint" on the surface associated with the shallow grazing angle at these longer ranges.

We consider this record to be direct evidence that ambient noise generation in the low wind speed region is governed by both the magnitude of the local wind speed, and the roughness of the sea surface, particularly that associated with the swell which originates outside of the influence of the local wind stress. This corroborates the findings of other authors, Wille and Geyer (1984) and Cato (1979), who concluded that both surface roughness, particularly swell, and local wind stress influence the noise level in the low wind speed region. It also shows that a mechanism, or mechanisms, governed by these factors exist for the generation of surface noise at wind speeds below that at which whitecaps are formed.

Another data set obtained in December 1980 provides further insight into the noise generating mechanisms at low wind speed. In particular, isolated noise bursts were observed indicating that the noise generation consisted of discrete events resolvable in space and time. In this experiment, acoustic radiation from patches on the sea surface was measured with ADA suspended in a deep water moor at a depth of 50–90 m below the surface. In the experiment the beamformer was configured to focus the array for surface sources lying approximately normal to the plane of the array. Figure 5 is an illustration of the fine scale acoustic radiation patterns observed in the experiment. The individual traces of the two waterfall displays represent 50-ms averages of the rectified beam outputs. The beam data have been interpolated and enhanced for the display. The fine scale structure is seen predominately in the central region of the display where the nearfield focusing of the array is at its best. For the 1.8-m/s wind speed record the individual events are quite short in duration, mainly one, or at the most two, scan times. At 3.6 m/s with a lower display gain, the events are of higher intensity and of longer duration, several hundred milliseconds.

At 1.8 m/s the wind speed is below the minimum required to excite capillary waves. Also, the events are of very short duration. Hence, the more probable candidate mechanisms at this very low wind speed would be cavitation collapse of bubbles in saturated water below the surface or bursting bubbles at the surface.

The 3.6-m/s wind speed will generate capillary waves, and, particularly in light of the extended duration of the acoustic events, unstable capillary waves or Crapper waves which entrain bubbles could play an important role here.

Although we have managed to observe these discrete acoustic events as components of the low wind speed generated surface noise, additional experiments will be required in order to obtain synoptic measurements of the physical events accompanying the acoustic emission.

II. BUBBLE CAVITATION MODEL

In this section, the mechanism of bubble cavitation under the surface is treated with a detailed theoretical analysis. Undersurface cavitation as a source of noise in the ocean was first proposed by Furduev (1966). In the intervening 18 years little note has been made of his work until recently when authors such as Kerman (1984) mention it as a possible mechanism. One reason that it may have been ignored is that there is a lack of theoretical estimation of the absolute level and its relation to the parameters of wind speed and surface roughness on the one hand, and there is a lack of observed experimental evidence on the other hand. The theoretical model which is presented here incorporates:

(1) Sound pressure radiated by the collapse of a vapor/air bubble derived by Khoroshev (1964).

(2) Bubble distributions given by Novarini and Bruno (1982).

(3) Turbulence under the surface layer from Kitaigorodskii (1961).

(4) Surface roughness statistics given by Longuet-Higgins (1952).

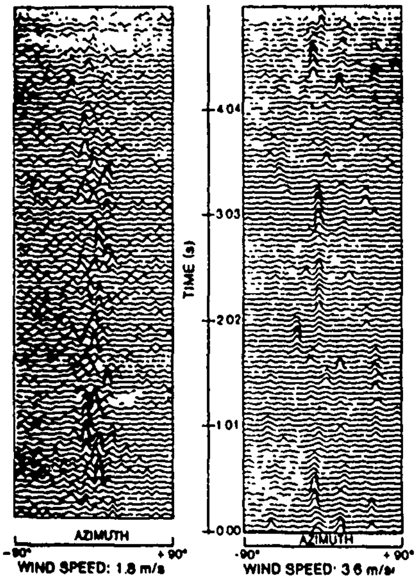

FIG. 5. Short-time averaged directional structure of surface noise observed from ADA.

The presence of bubbles in the ocean is essential to this model. There are many sources in nature to supply an ample population of subsurface bubbles. Here, only surface-induced, wind-dependent bubbles are considered. Small scale capillary waves, possibly in the form of unstable Crapper waves, lead to bubble entrainment. Bubble cloud entrainment has also been observed above a threshold of about 2.5-m/s wind speed [Thorp and Humphries (1980)]. Probability distributions have been measured *in situ* by means of acoustics and optics [Medwin (1977), Glotov (1962), Johnson, Cooke (1979)], and several authors have given distribution functions recently [Crowther (1979), Novarini and Bruno (1982), Kerman (1982)].

Briefly, the process of bubble cavitation in the surface turbulent layer is initiated when the turbulent pressure surrounding a vapor–air cavity of sufficient radius (greater than 10^{-4} cm) is reduced to the Hsieh–Plesset (1961) threshold whereupon the bubble would grow to larger radius by rectified diffusion. Some of the larger bubbles will be transformed into a transient cavity determined by the dynamic equation. According to Flynn (1964), whether or not a cavity becomes a transient cavity, i.e., one which undergoes a rapid collapse, depends on the competition in the dynamic equation between the inertial function F_1, which represents the portion of acceleration due to the spherical contraction of the liquid, and the quasistatic function F_2, which is the net pressure divided by the radius. The condition for this transformation is that the relative maximum radius on expansion be greater than a critical value during the pressure fluctuation period. A shock wave will be radiated as a result of collapse of the transient cavity. The absolute noise level corresponding to this phenomenon will be estimated later in the paper.

There are two geophysical parameters playing different roles in the model of surface noise generation. First, local wind speed mainly controls the bubble entrainment or equivalently the distribution function of the bubbles, and second, the swell-induced static pressure variations will mainly control the turbulent features in the surface layer, so these turbulent features will be most strongly influenced by the distance fetch, wind history and travel time, but not by the local wind speed.

A. Critical radius of the expanding bubble under rectified diffusion

The relation between the critical radius of the expanding bubble and the fluctuating pressure p' was given by Hsieh and Plesset (1961):

$$p' = \sqrt{\tfrac{2}{3}}P_0(1 + 2\alpha/R_c P_0 - \gamma)^{1/2}, \quad (1)$$

where P_0 is the static pressure, γ is the coefficient of saturation by dissolved air of the water surrounding the cavity, α is the coefficient of surface tension of the water ≈ 72 dyn/cm, and R_c is the critical radius for a bubble expanding by rectified diffusion.

Considering the saturation case for which $\gamma = 1$, one gets

$$R_c = \tfrac{4}{3}P_0[\alpha/(p')^2] \quad (2)$$

or, from Bernoulli's law,

$$R_c = \tfrac{4}{3}P_0[\alpha/(\rho V'^2)^2], \quad (3)$$

where V' is the particle motion velocity of the turbulence layer.

B. Sound pressure and spectrum from a single collapsing bubble

The sound pulse radiated by a collapsing bubble is a function of its radius R and air content of the bubble δ:

$$P(R,t) = P_A(R,\delta)S(t), \quad (4)$$

where the peak pressure P_A was given by Khoroshev (1964) for a vapor–air bubble collapsing:

$$\begin{aligned} P_A(R,\delta) &= P_0(R_m/r)F(\delta)\times 10^{-6} \\ &= P_0(K_E R/r)F(\delta)\times 10^{-6}, \end{aligned} \quad (5)$$

where P_0 is the hydrostatic pressure, R_m is the maximum bubble radius (μm) at the moment collapse begins, K_E as defined here is the coefficient of expansion ($K_E \doteq 3$–5, Furduev; $K_E \doteq 2$, Flynn); r is the measurement distance (m) from the bubble, and the function $F(\delta)$ is

$$F(\delta) = [(1 + 3\delta)(1 + 3\delta - \delta^{1.6})]^2/27\delta^2, \quad (6)$$

where δ is the parameter of the air content. In general it ranges from 0.002 to 0.1 under typical conditions.

The pulse form $S(t)$ is an exponential pulse for a vaporous bubble observed by Harrison (1952) experimentally. Owing to the fact that the bubble is beneath a free surface, and taking into account the reflection effect, $S(t)$ can be modeled by an approximate pulse shape (Furduev, 1966)

$$S(t) = Ae^{-t/\tau_0}\sinh(mt - \beta), \quad (7)$$

where the three parameters A, β, m are determined by the physical restriction

$$A = 1/\sinh(-m\tau_1), \quad \text{for } S(0) = 1, \quad (8)$$

$$\beta = m\tau_1, \quad \text{for } S(\tau_1) = 0, \quad (9)$$

$$m = \frac{1}{\tau_0}\tanh(\beta), \quad \text{for } \int_0^\infty S(t)dt = 0, \quad (10)$$

$$m < 1/\tau_0, \quad \text{for convergence.} \quad (11)$$

From Eq. (10) we get

$$\tau_0 = \tau_1[\tanh(m\tau_1)/m\tau_1] < \tau_1. \quad (12)$$

Thus, we must have $\tau_0 < \tau_1$; and if the parameter m in the model is chosen to keep the convergence rate not too much slower than $1/\tau_0$, we have $m\tau_0 \ll 1$; then from Eq. (10) and Eq. (12) we get

$$\tau_0 \approx \tau_1 \quad (13)$$

and τ_1 is given by

$$\tau_1 = 2D/c_0, \quad (14)$$

where D is the effective depth of the bubble population and c_0 is the sound speed in water.

Although τ_0 and τ_1 represent two physically different parameters—one being the decay rate of the cavitation impulse and the other representing the travel time delay between the direct and image paths, the times are comparable as pointed out by Furduev and they have been set equal for convenience here.

From Eq. (7), the frequency spectrum of the radiating pulse is

$$S(\omega) = \frac{\omega}{[(2\omega/\tau_0)^2 + (1/\tau_0^2 - m^2 - \omega^2)^2]^{1/2}}. \quad (15)$$

There is a peak at $\omega_{\max}$:

$$\omega_{\max} = 1/\tau_0 \cosh(m\tau_1) \approx 1/\tau_1. \quad (16)$$

The spectrum peak value is given by

$$\hat{S}(\omega_{\max}) = \omega_{\max}/(2\omega_{\max}/\tau_0) = \tfrac{1}{2}\tau_0 \approx \tfrac{1}{2}\tau_1. \quad (17)$$

C. Pressure pulsation, surface layer turbulence, and surface roughness

In spite of the large body of knowledge about turbulence in pipes, in boundary layers near solid walls, in jets, and in the atmosphere, unfortunately little is known about turbulence in the ocean (Monin, 1977). Apparently surface waves play a particularly important role for the upper ocean layer turbulence. The disturbed sea surface can be regarded as a moving random surface. The random surface waves induce in the upper ocean layer a random field of wave motions, which can be described by a model called "turbulence waves of large amplitude" by Kitaigordskii (1961). Such a "turbulence wave" motion was characterized by an average orbital velocity $\bar{u}_{\text{orb}}$ superimposed by random turbulent pulsation of different scales:

$$v' = \bar{u}_{\text{orb}} + v'' \quad (18)$$

and the average orbital velocity $\bar{u}_{\text{orb}}$ was given by Kitaigordskii (1961):

$$\bar{u}_{\text{orb}} \approx \bar{H}\bar{\omega}e^{-\bar{K}z}, \quad (19)$$

where $\bar{H}$ is the average wave height of the large amplitude surface waves, $\bar{\omega}$ is the average angular frequency, and $\bar{K}$ is the average wavenumber. The Reynolds number of the average motion is

$$R_{e\,\text{wave}} \approx \bar{u}_{\text{orb}} \bar{\lambda} / \nu, \tag{20}$$

where ν is the molecular viscosity coefficient of water $[\nu = 10^{-2} (\text{cm})^2/\text{s}]$. For a typical real condition the magnitude of $R_{e\,\text{wave}}$ is

$$R_{e\,\text{wave}} \approx 10^6\text{–}10^7. \tag{21}$$

So, the criterion for turbulence generation

$$R_{e\,\text{wave}} > R_{e\,\text{cr}} \sim 3000 \tag{22}$$

is satisfied by a large margin.

Measurements in shallow water (Bowden and White, 1966) indicated that the random component which is superimposed on the orbital component is approximately 20%. Thus, the pressure pulsation is mainly contributed by the periodic orbital motion, specified by the average wave height $\bar{H}$. Here, $\bar{H}$ can be regarded as one of the parameters of the surface roughness.

For a random sea surface, the statistical description was given by Longuet-Higgins (1980). If the sea surface is assumed to be the sum of many sine waves in random phase, and if the frequency spectrum is sufficiently narrow, then the wave amplitudes (a wave amplitude is here defined as one half of the height of a wave crest above the preceding trough) are distributed according to a Rayleigh distribution. That is, the probability P that the amplitude H of any given wave exceeds the value H_1 is given by

$$P(H_1) = \exp[-2(H_1/H_{1/3})^2] \tag{23}$$

or

$$P(H_1) = \exp(-H_1^2/\sigma^2), \tag{24}$$

where $H_{1/3}$ is the significant wave height, and σ is the rms wave height. In the derivation of this law it was implied that the sea surface slopes were sufficiently small that the component waves could be linearly superposed and hence that there was no correlation between the phases of the different Fourier components.

Obviously, under the low wind speed condition, the surface roughness influencing the orbital movement is mainly due to swell, not the wave height of "sea" induced by the local wind (because $H^2_{\text{swell}} \gg H^2_{\text{sea}}$). So, for the model of surface noise generation, under low wind speed, the parameter $\bar{H}$ will be considered approximately as

$$\bar{H} \approx \bar{H}_{\text{swell}} \tag{25}$$

and the orbital velocity at the upper layer in Eq. (19) is

$$\bar{u}_{\text{orb}} \approx \bar{H}_{\text{swell}} \cdot \bar{\omega}_{\text{swell}}. \tag{26}$$

In addition to this orbital velocity it should be noted that there will also be a drift flow at the surface produced by a direct action of the wind.

D. Estimation of noise level

For the estimation of the noise field produced by the bubbles distributed under the surface, the interaction between bubbles is neglected and energy summation is assumed. The resulting noise level spectrum can be written as

$$I(\omega,R_c) = \Omega(R_c) \int_v \int_{R_c}^{\infty} K_T \eta(R,z) \times [P_A S(\omega)]^2 D(\theta) dr\, dv, \tag{27}$$

where $\Omega(R_c)$ is the collapse formation frequency for bubbles having a radius greater than R_c, K_T is the percentage of the bubbles that can be transformed into a transient cavity, $\eta(R,z)$ is the bubble distribution function, P_A is the peak pressure radiated by a transient cavity, given by Eq. (5), $S(\omega)$ is the spectrum of the radiated pulse, given by Eq. (15), and $D(\theta)$ is the directivity function of the bubble radiation. Because of the proximity of the free surface, $D(\theta)$ is a dipole,

$$D(\theta) = \cos^2(\theta), \tag{28}$$

where θ and the element volume of integration dv are shown in Fig. 6, and dv is given by

$$dv = 2\pi l\, dl\, dz = 2\pi h^2 \sec^2(\theta) \tan(\theta) d\theta\, dz. \tag{29}$$

Substituting Eq. (29), Eq. (28), and Eq. (5) into Eq. (27), and completing the integral with respect to θ, we get

$$I(\omega,R_c) = \Omega(R_c)\pi \int_{R_c}^{\infty} \int_0^{\infty} (K_T K_E^{\frac{1}{2}}) \eta(R,z) [P_0 F(\delta)]^2 \times S^2(\omega) R^2 \times 10^{-12} dR\, dz, \tag{30}$$

where R is in μm. For simplicity, and because we have no knowledge of the dependence of K_T and K_E on r and u, $(K_T K_E^{\frac{1}{2}})$ is considered as constant. Then we get the peak of the spectrum,

$$\hat{I}(\omega,R_c) = \Omega(R_c)\pi (K_T K_E^{\frac{1}{2}}) [P_0 F(\delta)]^2 S^2(\omega) \times 10^{-12} \int_{R_c}^{\infty} \int_0^{\infty} \eta(R,z) R^2 dR\, dz. \tag{31}$$

A bubble distribution function given by Novarini and Bruno (1982) will be used:

$$\eta(R,u,z) = 8.6 \times 10^9 R^{-4\,3} (u/6)^2 \exp(-z/D), \tag{32}$$

where u is the wind speed in knots and D is the bubble-layer thickness in m that is wind speed dependent.

Since we are interested in larger bubbles and lower wind speeds, in view of reduced turbulent entrainment forces and larger bouyancy forces, the decay with bubble size may be more rapid. For simplicity, we take

$$\eta(R,u,z) = 8.6 \times 10^9 R^{-5} (u/6)^2 \exp(-z/D). \tag{33}$$

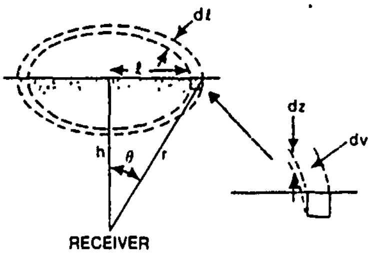

FIG. 6 Geometry for integration of surface noise

Substituting Eq. (17) and Eq. (33) into Eq. (31), and completing the integral with respect to R, and z, we get

$$I(\hat{\omega},R) = 3.3\times 10^{-3}(K_T K_E^2)\Omega(R_c)[P_0F(\delta)]^2 \times \tau_0^2\,(u/6)^2 D\, R_c^{-2}. \qquad (34)$$

As analyzed above, the critical radius R_c of the cavitating bubble is dependent on the geophysical condition of the turbulence in the upper surface layer due to swell. From Eqs. (3), (18), and (19), if the given swell is specified by wave height H and circular frequency ω_c, we get

$$R_c = \tfrac{1}{3}[P_0\alpha/\rho^2(H\omega_c)^4]. \qquad (35)$$

Taking account of Eq. (23), and the theory given by Rice (1945), the formation frequency Ω is given by

$$\Omega(H) = \exp\left[-2\left(\frac{H}{H_{1/3}}\right)^2\right]\left(\frac{\int_0^\infty f^2E(f)df}{\int_0^\infty E(f)df}\right)^{1/2}, \qquad (36)$$

where $E(f)$ is the power spectral density function of the surface wave process.

If H is considered as the average wave height $\overline{H}$, then

$$\Omega(\overline{H}) = \exp[-2(\overline{H}/H_{1/3})^2](\overline{\omega}/2\pi) = 0.46/T. \qquad (37)$$

Substituting Eq. (37) into Eq. (34):

$$\hat{I}(\hat{\omega},u,\overline{H}) = (1.52\times 10^{-3}/T)(K_T K_E^2)[P_0F(\delta)]^2 \times \tau_0^2\,(u/6)^2 D\,[R_c(\overline{H},\overline{\omega})]^{-2}. \qquad (38)$$

Now, we may make a quantitative estimation for the absolute level under typical oceanic conditions:

wind speed: $u = 6$ kn,

typical swell parameters:

$\overline{H} = 2.3$ m,

$T = 9.4$ s,

effective bubble layer: $D = 0.2$ m,

coefficient of expansion: $K_E = 2$,

coefficient of transient transformation $K_T = 0.2$,

parameter of air content: $\delta = 0.1$.

From Eqs. (14) and (13):

$$\tau_1 \approx \tau_0 = 2D/C_0 = 0.26\times 10^{-3}\ \text{s}. \qquad (39)$$

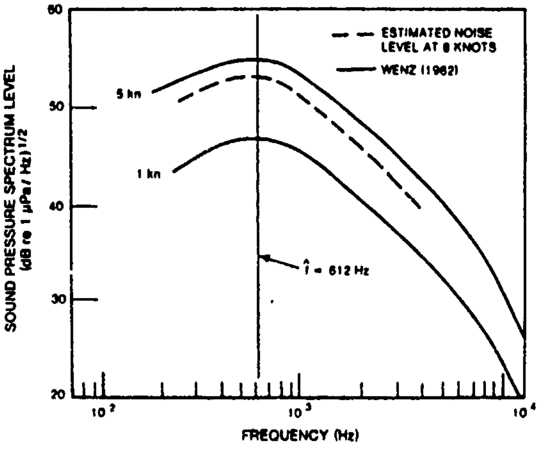

FIG. 7. Comparison of estimated noise spectrum with Wenz's data.

From Eq. (16):

$$\hat{\omega} \approx 1/\tau_1 = 3.8\times 10^3\,\text{rad/s},$$
$$f \approx 612\ \text{Hz}. \qquad (40)$$

From Eq. (6):

$$F(\delta) = 6.3,$$
$$[P_0F(\delta)]^2 = 3.9\times 10^{13}. \qquad (41)$$

From Eq. (37):

$$R_c(\overline{H},\overline{\omega}) = 1700\,\mu\text{m}. \qquad (42)$$

Substituting all the above quantities into Eq. (38), we get

$$\begin{aligned} I(\hat{\omega},u,H) &= [(1.52\times 10^{-3})/T](K_T K_E^2) \\ &\quad\times [P_0F(\delta)]^2\,\tau_0^2(u/6)^2DR_c^{-2} \\ &= (0.16\times 10^{-3})[0.8][3.9\times 10^{13}] \\ &\quad\times[0.26\times 10^{-3}][0.2](1700)^{-2} \\ &\simeq 0.07\ \text{W/m}^2/\text{Hz} \\ &\approx -47\ \text{dB}\ re\text{: 1 dyne/cm}^2/\sqrt{\text{Hz}}. \end{aligned} \qquad (43)$$

The result is demonstrated in Fig. 7. The absolute values computed above are near the 5-kn wind speed curve of Wenz and both the shape of the spectrum and the location of the maximum are in good agreement with his data.

The wind speed dependence of $\hat{I}$ given by Eq. (38) is up to $\sim(u)^2D(u)$. Unfortunately, it seems that there is not a very clear expression of the wind speed dependence available. Novarini and Bruno (1982) suggested

$$D(u)\sim U^{2.5}$$

and Crowther (1979) suggested

$$D(u)\sim U^{1.0}.$$

So, in the present paper, the power law of the wind speed dependence of $\hat{I}$ will be described as:

$$\hat{I}\sim U^{\alpha} \quad (\alpha = 3.0\text{–}4.5).$$

III. BURSTING BUBBLES AS SOUND SOURCES

Another possible mechanism for sound generation by bubbles is the rupture or bursting of bubbles on the ocean surface. The nature of the radiation from a bursting bubble is readily computed. We begin with the internal overpressure for a bubble on the surface which is given by

$$\Delta p = 2T\pi D/(\pi D^2/4) = 4T/R, \qquad (44)$$

where R is the radius of curvature of the double-surfaced upper bubble wall. This pressure is balanced by a combination of the differential hydrostatic head associated with the lower surface of the bubble and the upward force created by the surface tension T of the water at the lower boundary. When the upper wall ruptures, the dimple left at the water surface provides a decaying step function restoring force over the depressed area.

The basic sound source of the breaking bubble then is modeled as an initial pressure step function of magnitude Δp acting over a circular area approximately equal to πR^2 at the pressure release boundary of an infinite half-space. The boundary conditions match closely the solution of a vibrating sphere in free field. The free field model is appropriate because the plane of the surface, normal to the motion of the sphere, is a plane of zero acoustic pressure corresponding to the pressure release of the air/water interface.

From Morse (1948), the radiated intensity from a dipole sound source or vibrating sphere, assuming that the source is very small compared to a wavelength, is given by

$$\Upsilon \simeq \frac{1}{8} \frac{\omega^4 \rho a^6 U_0^2 \cos^2(\theta)}{c^3 r^2}. \qquad (45)$$

In order to determine a value for u_0, from the driving pressure p, we use the expression for one-half of the impedance of the sphere, also given by Morse for $ka \ll 1$:

$$Z_r = F/u_0 \simeq -i(u/2)(\tfrac{4}{3}\pi \rho_0 a^3). \qquad (46)$$

The force F is equal to $\Delta p \pi a^2$, thus

$$U_0 = -3\Delta p / i\omega \rho_0 a = i(3\Delta p / \rho_0 cka). \qquad (47)$$

Combining Eqs. (45) and (47), the radiated intensity is then

$$\Upsilon = \tfrac{9}{8}[(ka)^2 a^2 \Delta p^2 \cos^2(\theta)/\gamma^2 \rho_0 c]. \qquad (48)$$

Now, assuming the pressure impulse to be approximated by an exponential step function, $\Delta p(t) = \Delta p(0) e^{-t/\tau}$, Δp^2 would have a pressure spectrum proportional to $1/\omega^2$. Then the spectral shape of the radiated intensity will be

$$\Upsilon(\omega) \propto (1/\rho)[a^4 \cos^2(\theta)/c^3 r^2], \qquad (49)$$

which represents a flat spectrum with no frequency dependence.

It is apparent that this bursting bubble model does not match the conventional Knudsen spectrum shape for wind noise in the kilohertz region, but it is still a viable candidate for the extremely low wind speeds under 2.5 m/s where no capillary wave action is produced, and when swell conditions are low. Because of the scarcity of uncontaminated measurements of wind generated noise in this extremely low wind speed regime, there is a question as to whether or not the conventional ω^{-2} spectrum is valid for this regime. For example, the limited data from Wenz (1962) in his Figs. 2 and 3 for 2-kn wind speeds do not support an ω^{-2} slope in the 10^3- to 10^4-Hz region.

The analysis shows that the signatures of collapsing subsurface bubbles and surface bursting bubbles are distinctively different. If close range wideband acoustic measurements can be carried out it should be possible to identify the events from the distinctive character of their respective acoustic signatures.

ACKNOWLEDGMENT

This work was supported by the Office of Naval Research, Code 420, Contract N0014-79-C-0472 and by a private grant.

Anderson, V C (1980) "Nonstationary and Nonuniform Oceanic Background in a High-gain Acoustic Array," J Acoust. Soc. Am. 67, 1170–1179

Bowden, K. F, and White, R. A. (1966). "Measurements of the Orbital Velocity of Sea Waves and Use in Determining the Directional Spectrum," Geophys J R. Astron. Soc. 12, 33–54

Cato, D H (1979) "Wind Dependent Sea Noise," Ocean Sciences Review, RAN Research Lab, NSW 2010, Australia.

Crowther, P A (1979) "Acoustical Scattering from Near-Surface Bubble Layers," in *Cavitation and Inhomogeneities in Underwater Acoustics*, edited by W Lauterborn (Springer, New York).

Evans, D L, and Watts, D. R (1981). "Wind Speed and Stress at the Sea Surface from Ambient Noise Measurements," in *Proceedings of International Symposium on Acoustic Remote Sensing of the Atmosphere and Oceans*, Univ Calgary, Calgary, Canada (21–25 June 1981).

Flynn, H G (1964). "Physics of Acoustic Cavitation in Liquids," in *Physical Acoustics* (Academic, New York), Vol 1B

Furduev, A. V (1966). "Undersurface Cavitation As a Source of Noise in the Ocean," Atmos. Oceanic Phys 2, 314

Glotov, J P (1962). "Investigation of the Scattering of Sound by Bubbles Generated by an Artificial Wind in Seawater and the Statistical Distribution of Bubble Sizes," Sov. Phys. Acoust. 7, 341–345.

Harrison, M. (1952) "An Experimental Study of Single Bubble Cavitation Noise," J. Acoust Soc. Am. 24, 776.

Hsieh, D Y, and Plesset, M. S. (1961). "Theory of Rectified Diffusion of Mass into Gas Bubbles," J. Acoust. Soc. Am. 33, 206.

Johnson, B D., and Cooke, R. C (1979) "Bubble Population and Spectra in Coastal Waters: A Photographic Approach," J. Geophys. Res. 84, 3761–3766

Kerman, B. R. (1982). "Underwater Sound Generation at Low Wind Speeds" (unpublished).

Kerman, B. R (1984) "Sound Generation by Breaking Wind Waves," J. Acoust. Soc. Am. 75, 149–165.

Kitaigorodskii, G. A. (1961). "On Small Scale Turbulence in the Surface Layer of the Sea with Wind Swell," Trans. Inst. Ocean, Moscow 52, 87–96 (in Russian).

Khoroshev, G A. (1964) "Collapse of Vapor–Air Cavitation Bubble," Sov Phys Acoust 9(3), 275–279.

Longuet-Higgins, M. S (1952) "On the Statistical Distribution of Heights of Sea Waves," J. Marine Res 11, 245–266

Longuet-Higgins, M. S (1980). "On the Distribution of the Height of Seawaves Some Effects of Nonlinearity and Finite Bandwidth," J. Geophys Res 85, 1519–1523.

Medwin, H. (1977). "*In Situ* Acoustic Measurements of Microbubbles at Sea," J Geophys Res. 82, 971–975

Monin, A. S (1977). "On the Generation of Oceanic Turbulence," Atmos Ocean Phys 1, 789–803.

Morris, G. B (1978) "Depth Dependence of Ambient Noise in the North Eastern Pacific Ocean," J. Acoust. Soc Am. 64, 581–590.

Morse, P. M. (1948). *Vibration and Sound* (McGraw-Hill, New York), p 248.

Novarini, J. C, and Bruno, D. R (1982) "Effects of the Sub-Surface Bubble Layer on Sound Propagation," J. Acoust. Soc. Am. 72, 510–514.

Perrone, A. J. (1969). "Deep Ocean Ambient Noise Spectra in the North West Atlantic," J. Acoust. Soc. Am 46, 762–770.

Rice, S O (1945). Bell Syst. Tech. J. 23, 282.

Thorp, S A., and Humphries, P N (1980) "Bubbles and Breaking Waves," Nature 283, 463–465.

Wenz, G M. (1962). "Acoustic Ambient Noise in the Ocean: Spectra and Sources," J Acoust. Soc. Am. 34, 1936–1956.

Wille, P. C, and Geyer, D. (1984). "Measurements on the Origin of the Wind-Dependent Ambient Noise Variability in Shallow Water," J. Acoust. Soc. Am. 75, 173–185

The Coupling of Surface and Internal Gravity Waves: Revisited[*]

Kenneth M. Watson

---

[*]. Reprinted from the Journal of Physical Oceanography, Vol. 20, No. 9, pp. 1233-1248 (1990).

Reprinted from JOURNAL OF PHYSICAL OCEANOGRAPHY, Vol. 20, No. 9, September 1990
American Meteorological Society

The Coupling of Surface and Internal Gravity Waves: Revisited

KENNETH M. WATSON

Marine Physical Laboratory, Scripps Institution of Oceanography, University of California, San Diego, California

(Manuscript received 29 September 1988, in final form 13 September 1989)

ABSTRACT

A new investigation is made of internal wave generation by surface waves. Previous theories are put into a unified form that includes a model of surface wave damping. Calculations using the complete theory, which do not seem to have been made previously, indicate that for wind speeds between 7 and 20 m s^{-1} the internal wave field *loses* about 10^{-4} W m^{-2} to the surface wave field. This would lead to a decay time of about 10 days for the high frequency portion of the internal wave field if an energy source were not available to maintain it. Possible sources for this energy are discussed. In contrast to this result for wind waves, a strong, highly collimated ocean swell can lead to rapid growth of high frequency internal waves. The effects of nonlinear surface wave modulation and wave blocking are also discussed.

1. Introduction

According to the model of Garrett and Munk (1972a), the nominal energy in the internal wave field is about 3 kJ m^{-2}. Except for local variations this appears to be more-or-less steady, which has led to the view that generation and dissipation mechanisms balance each other. Garrett and Munk (1972b) estimated from turbulent fluxes that the dissipation rate for the internal wave (IW) field is in the range of 10^{-3} W m^{-2}. Dissipation rates for small scale turbulence (assumed to be fed by internal waves) observed, for example, by Garget et al. (1981) and by Osborn (1978) imply dissipation rates in the range of 10^{-3} to 10^{-4} W m^{-2}. Vertical fluxes of IW energy observed by Leaman and Sanford (1975) and by Leaman (1976) are also in this range. These rates suggest that the IW field would decay in 10 to 100 days if it were not maintained by external sources. Further observations by Lueck et al. (1983), by Gregg et al. (1986), and by Gregg (1987, 1989) lead to estimates of about 50 to 100 days for the IW decay time.

Theoretical calculations of turbulent fluxes within the IW field by McComas (1978), McComas and Muller (1981), and Pomphrey et al. (1980) predict dissipation rates in the range of 10^{-3} to 10^{-4} W m^{-2}. Careful predictions by Flattè et al. (1985) give values toward the lower end of this range, in agreement with Gregg (1989).

A number of plausible mechanisms have been proposed for the generation of internal waves. Bell (1975) has suggested that large scale flow over topography can be a significant source of IW energy. Bell (1978) has also concluded that inertial oscillations of the upper ocean can generate internal waves. Kanthu (1979) has investigated mixed layer turbulence as a generation mechanism. Mesoscale flow as a source of IW energy has been studied by Watson (1985). Each of these mechanisms appears able to account for much of the energy in the IW field.

Striking visual evidence of the interaction of internal waves with surface waves has been often noted (for example, see Hughes and Grant 1978; Phillips 1973; Hughes 1978; Apel et al. 1975; Curtin and Mooers 1975; Fu and Holt 1984). This interaction has led to a number of calculations of the rate of generation of the IW field by surface waves.

Theoretical models for a "wave triad" consisting of two surface waves and one internal wave have been developed by Ball (1964), Thorpe (1966), and Brekhovskikh et al. (1972). Energy transfer occurs when a frequency resonance condition is met.

Calculations of the transfer of energy from a surface wave (SW) spectrum to internal waves have been given by Kenyon (1968), Watson et al. (1976), Olbers and Herterich (1979), and Dysthe and Das (1981). Kenyon used a constant N (i.e., Väisälä frequency) profile. Olbers and Herterich chose N to be constant in a prescribed depth interval and to vanish outside this interval. Dysthe and Das (1981, hereafter DD) assumed N to vanish outside a thin thermocline region. Watson et al. (1976, hereafter WWC) chose N to vanish in a mixed layer, below which they used the Garrett–Munk (1972a) exponential scaling.

Olbers and Herterich (1979) made use of the spectral transfer equations of Hasselmann (1967). They con-

---

Corresponding author address. Dr. Kenneth M. Watson, University of California, San Diego, Marine Physical Laboratory, Scripps Institution of Oceanography, San Diego, CA 92152-6400.

sidered a mechanism of "spontaneous creation" by which pairs of surface waves generate internal waves. This mechanism does not require that internal waves be initially present. Dysthe and Das describe another mechanism by which a weak IW grows (or decays) exponentially through interaction with a pair of surface waves. They refer to this as "modulation interaction" or "modulational instability."

Olbers and Herterich (1979) concluded that the transfer rates for the *spontaneous creation* mechanism are relatively insensitive to the detailed form of the SW spectrum, but are sensitive to the wind speed. A large Väisälä frequency, a thin mixed layer, or strong winds were required to give significant IW growth rate, however.

Dysthe and Das performed calculations for only a narrow band SW system. They concluded that the energy rate for *modulation interaction* mechanism is very sensitive to the form of the SW spectrum and that a very narrow angular spread is required to give significant growth rates of the IW amplitudes.

The mode coupling equations of WWC were expressed in the form of Hamilton s equations. They obtained an analytic expression for the IW growth rate using a "locked phase assumption." This gave a significant energy transfer rate, but because of the locked phase approximation could be considered as only an upper limit on the IW growth rate. Watson et al. also performed a numerical integration of their equations. This was criticized by Olbers and Herterich (1979) as ignoring the detuning effects of SW dissipation processes. Because of computational limitations, WWC chose a narrow band SW spectrum similar to that shown by DD to give high energy transfer rates.

The conclusions from these calculations has been that SW–IW interactions cannot account for the energy needed to maintain the IW field. It appears however that, although the theory has been well developed, detailed calculations of the SW–IW energy exchange have not been made. Studies have not been made that include simultaneously both the spontaneous and modulation mechanisms, nor have comparisons of the relative importance of these been given.

The purpose of this paper is to provide such calculations that include both the modulation and the spontaneous mechanisms and to do these for environmental conditions of physical interest. In contrast to what has sometimes been expected, we find rather rapid energy transfer rates, but predominantly a transfer of energy from the IW field to the SW field.[1] This transfer of energy is significant, however, only for the long vertical wavelength IW modes having frequencies greater than about a tenth of the upper ocean Väisälä frequency. In this band and for wind speeds in the 7 to 20 m s^{-1} range the predicted time for IW decay is a few days. Expressed differently, for a Garrett–Munk spectrum the power delivered to the SW field at the expense of the IW field is about 10^{-4} W m^{-2}. This is not of course a significant energy source for the wind waves, but (as we shall discuss later) it does raise a question as to the source for the IW energy in this band.

For a wind increasing above 15 m s^{-1} there is a tendency in some spectral domains for transfer of energy to the IW field, although at even 20 m s^{-1} the net transfer is to the SW field.

The theories of WWC, DD, and Olbers and Herterich (1979) are described (without derivation)[2] in sections 2 and 3. An innovation in the present work is to take account of surface wave dissipation. This dissipation broadens the triad resonance condition of the previous theories. This broadening has some numerical impact, but does not significantly change our conclusions. The calculations described in the paragraph above are presented in Section 4. In Section 5 we show the implications of some calculations of IW generation by ocean swell, which can effectively stimulate IW growth. Finally, in Section 6 some implications of nonlinear SW modulation are described.

2. Notation and ocean model

In this section we shall review for later use certain properties of linear surface and internal waves (for a more detailed description of the linear wave fields see, for example, Phillips 1977). Where appropriate, we will follow the notation of WWC.

Capillary waves will be excluded from our model. Characteristic IW frequencies Ω are assumed to be small compared to frequencies ω of the interacting SW field, but much larger than the inertial frequency. Similarly, horizontal IW wavenumbers K are assumed to be small compared to wavenumbers k of the SW field:

$$\Omega \ll \omega$$
$$K \ll k. \qquad (2.1)$$

The undisturbed surface of the ocean is assumed to coincide locally with the plane $z = 0$ of a rectangular coordinate system. The ocean bottom is assumed to coincide with the plane $z = -B_b$. The Väisälä frequency $N(z)$ is assumed to vanish in a mixed layer of domain $-D < z < 0$. It will be supposed that D is large enough that surface wave currents can be neglected for $z < -D$. Specific models for $N(z)$ in the domain $-D > z > -B_b$ will be introduced when calculations are presented.

Following the notation of WWC, for *linear* internal waves we expand the vertical component of velocity in the form

---

[1] We emphasize that our present calculations do not disagree with other calculations of which we are aware. The pertinent calculations seem not to have been done before.

[2] A very simple derivation of the energy transfer resulting from the modulation mechanism is given Section 3, using arguments of energy conservation.

$$w_l(\mathbf{x}, z, t) = \sum_{j=l}^{\infty} \sum_{\mathbf{K}} e^{i\mathbf{K}\cdot\mathbf{x}} A_{j,\mathbf{K}}(t) W_{j,K}(z). \quad (2.2)$$

The sum on K represents a Fourier expansion in some conveniently chosen rectangular Area A_0. The symbol j labels vertical mode numbers. The vertical mode function $W_{j,K}(z)$ is obtained from the equations

$$W_{j,K}(z) = K\sinh(Kz), \quad -D < z \leqslant 0,$$

$$W''_{j,K}(z) + K^2(N^2/\Omega^2 - 1)W_{j,K} = 0, \qquad -B_b < z < -D \quad (2.3)$$

where $W'' = d^2W/dz^2$ and Ω is the angular frequency of the mode (j, K). At the ocean bottom we have the boundary condition

$$W_{j,K}(-B_b) = 0.$$

The rigid-lid approximation has been used to give the boundary condition at $z = 0$ in (2.3). Olbers and Herterich (1979) have discussed the validity of this and the Bousinesq approximation for the present application. We have used their analysis to explicitly verify the validity of these approximations for the parameter ranges used in our calculations. For linear waves we have the relation

$$\ddot{A}_{j,\mathbf{K}} = -\Omega^2(j, K)A_{j,\mathbf{K}} \quad (2.4)$$

where $\ddot{A} \equiv d^2A/dt^2$.

We shall encounter the integrals

$$\int_{-B_b}^{0} N^2 W_{j',K} W_{j,K} dz = \delta_{j,j'} V_{j,K} N_0^2/B. \quad (2.5)$$

Here N_0 and B are convenient scale parameters for N and for the vertical scale of stratification, respectively. The quantity $V_{j,K}$ above is dimensionless. It will be seen to represent a kind of IW inertial response to SW driving.

The horizontal component of the IW current is

$$\mathbf{u}(\mathbf{x}, z, t) = \sum_{j,\mathbf{K}} i\mathbf{K} A_{j\mathbf{K}} W'_{j,K} e^{i\mathbf{K}\cdot\mathbf{x}}/K^2. \quad (2.6)$$

It is convenient to write

$$iK^{-1}A_{j,\mathbf{K}} = \frac{1}{2}[\hat{U}(j, \mathbf{K})\exp(-i\Omega(j, K)t) - \hat{U}^*(j, -\mathbf{K})\exp(i\Omega(j, K)t)]. \quad (2.7)$$

Then at the surface $z = 0$ we may use (2.4) to express (2.6) in the form

$$\mathbf{U}(\mathbf{x}, t) = \sum_{j,\mathbf{K}} \hat{\mathbf{K}}[\hat{U}(j, \mathbf{K})\exp(i(\mathbf{K}\cdot\mathbf{x} - \Omega t)) + \text{c.c.}]/2. \quad (2.8)$$

The internal wave energy/unit area in the mode (j, K) is

$$\hat{E}_i(j, \mathbf{K}) = \frac{\rho_0 N_0^2 V_{j,K}}{2B\Omega^2 K^2}\left|\hat{U}(j, \mathbf{K})\right|^2, \quad (2.9)$$

where ρ_0 is the density of sea water (say, in the mixed layer). The spectrum of internal wave energy $E_i(j, \mathbf{K})$ is obtained from (2.9) as

$$\int E_i(j, \mathbf{K})d^2K = \sum_{\mathbf{K}} \hat{E}_i(j, \mathbf{K}). \quad (2.10)$$

The corresponding action/unit area is

$$F_i(j, \mathbf{K}) = E_i(j, \mathbf{K})/\Omega(j, K). \quad (2.11)$$

For the calculations to be given later we shall need a model for E_i, for which we take, unless specified otherwise, the venerable Garrett–Munk spectrum of Munk (1981). Since we are interested only in IW frequencies much larger than the inertial frequency, we write this as

$$E_i(j, K) = \frac{0.013\rho_0 N_0^2 \xi_0^2 j}{2\pi K^3(1 + j^2/9)} \quad (2.12)$$

valid for $KB \gg f_0\pi j/N_0$, where f_0 is the inertial frequency. We recognize that (2.13) does not always describe very well internal wave observations in the upper ocean (see Pinkel 1985). We do not think, however, that our conclusions are sensitive to details of the IW spectrum.

For linear surface waves we write the vertical displacement and velocity potential at $z = 0$ in the form

$$\zeta_s(\mathbf{x}, t) = -\sum_{\mathbf{k}} [B_{\mathbf{k}} e^{i\mathbf{k}\cdot\mathbf{X}} - \text{c.c.}]/(2i\sqrt{\rho_0 V_k}),$$

$$\phi_s(\mathbf{x}, t) = \sum_{\mathbf{k}} \sqrt{V_k/(2\rho_0)}[B_{\mathbf{k}} e^{i\mathbf{k}\cdot\mathbf{x}} + \text{c.c.}]. \quad (2.13)$$

Here $V_k = \sqrt{g/k}$ is the surface gravity wave phase speed. The surface wave spectrum of action/unit area is F_s. This may be obtained from (2.13) using the Wigner (1932) relation

$$\int d^2k F_s(\mathbf{x}, \mathbf{k}, t) = \sum_{\mathbf{k}} \sum_{\mathbf{l}} e^{i\mathbf{l}\cdot\mathbf{x}} \langle B_{\mathbf{k}+\mathbf{l}/2} B^*_{\mathbf{k}-\mathbf{l}/2} \rangle \quad (2.14)$$

where $\langle \;\; \rangle$ represents an ensemble average over many realizations of the SW field. The corresponding SW energy spectrum is

$$E_s(\mathbf{x}, \mathbf{k}, t) = \omega_k F_s(\mathbf{x}, \mathbf{k}, t) \quad (2.15)$$

where $\omega_k = \sqrt{gk}$ is the angular frequency corresponding to wavenumber k.

It is convenient to introduce an ambient SW field for which we can use one of the current equilibrium models. We shall denote the action density spectrum for this ambient field by $F_a(\mathbf{k})$. The ambient spectrum of vertical displacement Ψ_a is expressed in terms of the action density with the relation

$$F_a(\mathbf{k}) = \rho_0 V_k \Psi_a(\mathbf{k}). \qquad (2.16)$$

The ratio of the actual to the "ambient" spectrum represents the SW modulation M:

$$F_s(\mathbf{x}, \mathbf{k}, t) = M(\mathbf{x}, \mathbf{k}, t) F_a(\mathbf{k}). \qquad (2.17)$$

We shall see in the next section that for the modulation mechanism it is M that can be considered as the *driver* of the IW field.

For the calculations presented in this paper we shall use the wind wave spectral model of Donelan et al. (1985) and Phillips (1985):

$$\Psi_a(\mathbf{k}) = S(k) G(\theta - \theta_w). \qquad (2.18)$$

Here θ is the angle of the vector **k** with respect to the direction of **K** and θ_w is the corresponding direction of the wind vector. The function S is

$$S(k) = \frac{A}{k^{3.5}\sqrt{k_*}} e^{-\Gamma},$$

$$\Gamma = 0.6(k_*/k)^2 - 0.5 \exp[-1.2(1.2\sqrt{k/k_*} - 1)^2],$$

$$k_* = g/W^2, \quad A = 3 \times 10^{-3}. \qquad (2.19)$$

and W is the wind speed. The "spreading function" of Donelan et al. (1985) is

$$G(\theta - \theta_w) = \sigma \operatorname{sech}^2[\sigma(\theta - \theta_w)]/2. \qquad (2.20)$$

The Donelan model used for the parameter σ is

$$\sigma = \begin{cases} 2.9(k_*/k)^{0.67}, & \text{for} \quad k/k_* < 4 \\ 1.2, & \text{for} \quad k/k_* > 4. \end{cases} \qquad (2.21)$$

We shall also consider a "collimated" model for which

$$\sigma = 8. \qquad (2.22)$$

Our calculated results will be seen to be rather sensitive to the spreading function used, but do not seem very sensitive to modest changes in S. Omitting the "JONSWAP peak enhancement" in (2.19) or using a k^{-4} spectrum in the equilibrium range does not modify our results significantly.

3. The interaction between surface and internal waves

In this section we shall present the equations that describe the response of the IW field to SW forcing. The derivations given by DD and WWC lead to equivalent results for the modulation mechanism, which we now quote without derivation. (Since the form in which we express the modulation mechanism is somewhat different from that given by WWC and DD, we show in the Appendix how to obtain this specific form using expressions derived in WWC.) A very simple derivation is given at the end of this section, however, for the transfer of energy between the IW and SW fields, as implied by the modulation mechanism.

The equations of Olbers and Herterich (1979) describing the spontaneous model are also quoted in this section, re-expressed in the present notation.

The SW and IW fields are treated as linear, except for the coupling between them. This coupling is assumed to be weak in the sense that the linear wave frequency Ω is large compared to the evolution rate of the amplitudes $\hat{U}(j, \mathbf{K})$:

$$\Omega \gg |\dot{\hat{U}}/\hat{U}|. \qquad (3.1)$$

The nonlinear coupling is evaluated in lowest order as a triad wave interaction. A typical triad from a field of interacting waves would include two surface waves of wavenumbers **k** and **k**′ and an internal wave of mode $(j, \mathbf{K})$. Energy exchange among these waves occurs when a resonance condition is met:

$$\mathbf{k} - \mathbf{k}' = \mathbf{K},$$

$$\omega_k - \omega_{k'} = \Omega(j, K). \qquad (3.2)$$

Higher order resonances, involving harmonics of the linear wave frequencies, can also transfer energy. When condition (3.1) is satisfied, we do not expect significant transfer rates from these higher order interactions. We shall see that SW relaxation mechanisms can lead to more general conditions than (3.2) for energy exchange, however.

Because of the conditions (2.1) we may rewrite the second equation above as

$$\mathbf{c}_g(\mathbf{k}) \cdot \hat{\mathbf{K}} = c_I, \qquad (3.3)$$

where $c_I = \Omega/K$ is the IW phase velocity and c_g is the SW group velocity. This is the condition that the component of SW group velocity parallel to K match the IW phase velocity. An obvious generalization of (3.3) is the expression

$$[\mathbf{c}_g(\mathbf{k}) + \mathbf{U}] \cdot \hat{\mathbf{K}} = c_I. \qquad (3.4)$$

As will be discussed in more detail in Section 6, (3.4) is the condition that an overtaking SW will be turned back, or *blocked*, by the IW generated surface current U. In the case of sufficiently weak interactions (3.3) and (3.4) are equivalent (recall that $|U|$ must be significantly less than c_I if the IW field can be treated as linear). The relation (3.4) leads us to anticipate that SW blocking plays a role in the energy transfer between the two wavefields.

The derivations of the modulation mechanism given by WWC and DD lead to an expression for the rate of change of the IW current amplitude introduced in (2.9):

$$\dot{\hat{U}}(j,\mathbf{K}) = -i\left(\frac{\Omega^3 KB}{N_0{}^2\rho_0 V_{j,K}}\right)\mathbf{K}\cdot\int d^2k\mathbf{k}\int\frac{d^2x}{A_0}$$
$$\times\exp[-i(\mathbf{K}\cdot\mathbf{x}-\Omega t)]F_s(\mathbf{x},\mathbf{k},t). \quad (3.5)$$

Here A_0 is the rectangular area within which the Fourier expansion (2.4) was introduced. [As noted earlier, we show in the Appendix how Eq. (2.29) of WWC may be transformed into the form used here.] We may rewrite (3.5) using the modulation function M of (2.17).

$$\dot{\hat{U}}(j,\mathbf{K}) = i\left(\frac{\Omega^3 KB}{N_0{}^2\rho_0 V_{j,K}}\right)\mathbf{K}\cdot\int d^2k\mathbf{k}\int d^2x\Big/A_0$$
$$\times\exp[-i(\mathbf{K}\cdot\mathbf{x}-\Omega t)][M(\mathbf{x},\mathbf{k},t)-1]F_a(\mathbf{k}). \quad (3.6)$$

This shows explicitly how modulation of the SW spectrum is required to excite the IW field.

The rate of change of the IW energy is obtained from (2.9) and (3.5) as

$$\dot{E}_t(j,\mathbf{k}) = i\left(\frac{\hat{\mathbf{K}}}{2}\right)\cdot\int d^2k\mathbf{k}\int\frac{d^2x}{A_0}F_s(\mathbf{x},\mathbf{k},t)$$
$$\times\Omega[\hat{U}\exp[i(\mathbf{K}\cdot\mathbf{x}-\Omega t)]-\text{c.c.}]. \quad (3.7)$$

Using the condition (3.1) and (2.10) we can put this in the compact form

$$\dot{E}_t = \sum_{j,\mathbf{K}}\dot{E}_t(j,\mathbf{K})$$
$$\approx -\int d^2k\mathbf{k}\cdot\int\frac{d^2x}{A_0}\dot{\mathbf{U}}(\mathbf{x},t)F_s(\mathbf{x},\mathbf{k},t). \quad (3.8)$$

To continue, we need a model or a prescription for calculating F_s. There are several possibilities: 1) The IW field surface current can modulate the SW field. An equation from which to determine F_s from $\hat{U}$ will close the system, permitting $\hat{U}$ and F_s to be calculated simultaneously. This is the approach used by DD and by WWC (with their analytic calculation). 2) The SW modulation may be determined by external environmental factors. This might be due to wind variability (for example, see Gill 1984), spatial variation of swell, Langmuir circulation, etc. An example, assuming a modulated ocean swell, will be described in section 5. 3) Modulation can also result from random statistical fluctuations of the SW field.

To describe the first of these modulation possibilities we shall adopt a simple, often used model that takes account of the inequalities (2.1). In the ray path approximation we can write (for example, see Hasselmann 1968)

$$\left[\frac{\partial}{\partial t}+\dot{\mathbf{x}}\nabla_{\mathbf{x}}+\dot{\mathbf{k}}\cdot\nabla_{\mathbf{k}}\right]F_s(\mathbf{x},\mathbf{k},t) = S(\mathbf{x},\mathbf{k},t). \quad (3.9)$$

Here

$$\dot{\mathbf{x}} = \nabla_{\mathbf{k}}H,\quad \dot{\mathbf{k}} = -\nabla_{\mathbf{x}}H,$$
$$H = \omega_k + \mathbf{k}\cdot\mathbf{U}. \quad (3.10)$$

The source term S is often expressed as

$$S = S_{nl} + S_w + S_d, \quad (3.11)$$

where S_{nl} represents nonlinear SW–SW interactions (Hasselmann 1967 or 1968), S_w represents wave excitation by the wind, and S_d represents wave damping due to viscosity.

Equations (3.9) and (3.11) are overly complex for our current study [see, however, van Gastel (1987), who investigated SW modulation using this full set of equations for capillary waves], so we shall adopt a model for S introduced by Hughes (1978) and by Phillips (1984). We set

$$S = -\beta(k)(F_s - F_a), \quad (3.12)$$

which is the form of the Hughes and Phillips models when $|F_s - F_a| \ll F_a$. The non-negative constant β used in this paper is that deduced by Watson (1986). His calculations may be scaled in the approximate form

$$\beta(k) = \omega_k\exp(-G(p)),$$
$$p = W/V_k,$$
$$G = \frac{14.5C(p)}{0.4+p^{0.579}},$$
$$C(p) = \begin{cases} 1, & \text{if } p < 15, \\ \dfrac{5}{p-10}, & \text{if } p > 15. \end{cases} \quad (3.13)$$

When the action source term S in (3.9) is negligible, we expect the total energy of both wave fields to be constant. (The Hamiltonian formulation of WWC assures energy conservation when there is no SW damping.) To verify this, we write

$$\int\frac{d^2x}{A_0}\int d^2k\omega_k\left[\frac{\partial}{\partial t}+\dot{\mathbf{x}}\cdot\nabla_{\mathbf{x}}+\dot{\mathbf{k}}\cdot\nabla+\dot{k}\cdot\nabla_{\mathbf{k}}\right]F_s = 0,$$

or

$$\dot{E}_s + \int\frac{d^2x}{A_0}\int d^2k[(\dot{x}\cdot\nabla_x+\dot{k}\cdot\nabla_k)(\omega_k\times F_s)$$
$$- F_s(\nabla_{\mathbf{k}}\omega_k)\cdot\dot{\mathbf{k}}] = 0.$$

Then

$$\dot{E}_s = \int\frac{d^2x}{A_0}\int d^2k\dot{\mathbf{k}}\cdot\mathbf{c}_g(\mathbf{k})F_s. \quad (3.14)$$

Now

$$\dot{\mathbf{k}}\cdot\mathbf{c}_g = -\mathbf{c}_g\cdot\nabla_x(\mathbf{U}\cdot\mathbf{k}) \approx \mathbf{k}\cdot\dot{\mathbf{U}},$$

where we have made use of the condition (3.3). Thus (3.14) becomes

$$\dot{E}_s = \int d^2x/A_0 \int d^2k\mathbf{k}\cdot\dot{\mathbf{U}}F_s(\mathbf{x}, \mathbf{k}, t) = -\dot{E}_t. \tag{3.15}$$

The last form follows from energy conservation. In obtaining (3.15) we have made use of the condition (3.3).

We see that this provides an alternate derivation of (3.8). When SW damping is significant, (3.15) remains valid for the IW energy rate, but an additional term is added to the SW energy rate of change.

Equations (3.5) and (3.14) describe the response of the IW field to a modulated SW field. When this modulation is driven by the IW field, (3.9) may be used (this is the case explicitly considered by WWC and DD, who did not include SW relaxation, however) to close the set of equations.

Olbers and Herterich (1979) presented calculations using the "spontaneous creation" mechanism. (We use this term since internal wave energy does not have to be present for this process to work.) The rate at which the IW field receives energy from the SW field, as obtained by Olbers and Herterich (1979), is

$$\left.\frac{\partial E_t(j, K)}{\partial t}\right)_s = \frac{4\pi\alpha g\rho_0 N_0\Omega}{KB^2}\int d^2k(k_x{}^2/k)\Psi_a(\mathbf{k}) \times \Psi_a(\mathbf{k}')\delta(\omega_k - \omega_{k'} - \Omega). \tag{3.16}$$

Here the x-axis has been chosen as the direction of the vector $\mathbf{K}$ and $\mathbf{k}' = \mathbf{k} - \mathbf{K}$, $\Omega = \Omega(j, K)$. The dimensionless quantity α is

$$\alpha = \frac{(\Omega KB/N_0)^3}{2V_{j,K}}, \tag{3.17}$$

where $V_{j,K}$ is given by (2.7).

In the next section we shall present calculations of the energy exchange between SW and IW fields using (3.5) and (3.9) for the modulation mechanism and (3.16) for the spontaneous mechanism. In Section 5 we discuss IW generation by a naturally modulated ocean swell. Finally, in section 6 we investigate the case that the SW field is strongly modulated by a packet of internal waves.

4. The case of weak modulation

When the IW surface current is sufficiently weak we may linearize (3.9) in U. In this case there is no coupling among the modes and it suffices to consider only a single IW mode, say (j, K). We may take K parallel to the x-axis and write

$$\mathbf{U}(\xi, t) = \mathbf{i}[\hat{U}(t)e^{iK\xi} + \text{c.c.}]/2, \tag{4.1}$$

where $\mathbf{i}$ is a unit vector parallel to the x-axis and $\xi = x - c_lt$. We shall also omit writing the (j, K) label on U, etc., except where it is needed for clarity.

The distortion in F_a due to the IW current is

$$F'(\xi, \mathbf{k}, t) \equiv F_s - F_a, \tag{4.2}$$

and the linearized form of (3.9) is

$$\left[\frac{\partial}{\partial t} + (c_x - c_l)\frac{\partial}{\partial\xi}\right]F' = k_x\frac{\partial U}{\partial\xi}\frac{\partial F_a}{\partial k_x} - \beta F' \tag{4.3}$$

where c_x is the x-component of c_g. It is convenient to introduce positive and negative frequency parts of F' in (4.3)

$$F' = [H(\mathbf{k}, t)e^{iK\xi} + \text{c.c.}]/2,$$

so (4.3) becomes

$$\left[\frac{\partial}{\partial t} + \beta + iK(c_x - c_l)\right]H = iKk_x\frac{\partial F_a}{\partial k_x}\hat{U}. \tag{4.4}$$

Equation (3.9) for $\hat{U}$ can now be expressed as

$$\frac{\partial\hat{U}}{\partial t} = -[i\alpha N_0/(KB^2\rho_0)]\int d^2kk_xH, \tag{4.5}$$

where the dimensionless quantity α is given by (3.17).

We may suppose that $\hat{U}$ and H evolve from initial values $\hat{U}(0)$ and $H(k, 0)$ at time $t = 0$. An explicit solution to (4.4) and (4.6) is then readily obtained using a Laplace transform.

$$\bar{U} = \int_0^\infty e^{-pt}\hat{U}dt,$$

$$\bar{H} = \int_0^\infty e^{-pt}Hdt.$$

For the quantity $\bar{U}$ we find

$$[p - \alpha J]\bar{U} = \hat{U}(0) - i[\alpha N_0/(KB^2\rho_0)] \times \int d^2kk_xH(\mathbf{k}, 0)\Big/[p + \beta + iK(c_x - c_l)], \tag{4.7}$$

with

$$J = (N_0/B^2)\int\frac{d^2kk_x{}^2\dfrac{\partial}{\partial k_x}[V_k\Psi_a(\mathbf{k})]}{p + \beta + iK(c_x - c_l)}. \tag{4.8}$$

Here Ψ_a is the SW displacement spectrum (2.18).

The free response of the system is obtained from the equation

$$p = \alpha J. \tag{4.9}$$

It will be seen that $|p|$ is sufficiently small that the term p can be dropped in the denominator of (4.8). Also we need calculate only the real part of (4.9), which is then

$$\text{Re}(p) = (\alpha N_0\pi/B^2)\int d^2kk_x{}^2\left\{\frac{\partial}{\partial k_x}[V_k\Psi_a(\mathbf{k})]\right\} \times \Delta[K(c_x - c_l)] \tag{4.10}$$

where

$$\Delta = \frac{\beta/\pi}{\beta^2 + K^2(c_x - c_I)^2}. \qquad (4.11)$$

When β is much less than Ω,

$$\Delta[K(c_x - c_I)] = \delta[K(c_x - c_I)]. \qquad (4.12)$$

To be compatible with (3.16) we shall replace (4.10) by

$$\nu_m = 2\,\mathrm{Re}(p) \qquad (4.13)$$

describing the rate at which IW energy grows. Olbers and Herterich (1979) also obtained, but did not discuss, a result equivalent to (4.10) and (4.12).

The mean IW growth rate, averaged over all K-directions (equivalent to averaging over all directions θ_w), is

$$\bar{\nu}_m = \frac{1}{2\pi}\int_{-\pi}^{\pi} \nu_m d\theta_w. \qquad (4.14)$$

The rate at which energy is received in unit area of ocean, in mode j, and within the interval dK is

$$P_m(j, K)dK = 2\pi\bar{\nu}_m E_I(j, K)KdK. \qquad (4.15)$$

For E_I we use (2.12).

To obtain a growth rate for the spontaneous mechanism we use (3.16):

$$\nu_s = \frac{\partial E_I(j, K)}{\partial t}\Big/ E_I(j, K)$$

$$= \frac{4\pi\alpha g\rho_0 N_0\Omega}{KB^2E_I}\int d^2k(k_x{}^2/k)\Psi_a(\mathbf{k})\Psi_a(\mathbf{k}')$$

$$\times \Delta(K(c_x - c_I)). \qquad (4.16)$$

Here for consistency we have replaced the δ-function in (3.16) by the function (4.11), for which plausible arguments may be given. The mean rate for all K-directions is

$$\bar{\nu}_s = \frac{1}{2\pi}\int_{-\pi}^{\pi} \nu_s d\theta_w. \qquad (4.17)$$

The rate at which power is received per unit area by the IW field is then

$$P_s(j, K)dK = 2\pi\bar{\nu}_s E_I(j, K)KdK.$$

Net e-folding rates for the IW field are

$$\nu = \nu_m + \nu_s, \qquad (4.18)$$

$$\bar{\nu} = \bar{\nu}_m + \bar{\nu}_s. \qquad (4.19)$$

The total power received by the IW field per unit area is[3]

$$P(j, K) = P_m(j, K) + P_s(j, K). \qquad (4.20)$$

Olbers and Herterich (1979) presented calculations for the spontaneous model using (3.16). They used a "box" Väisälä profile. (We have repeated selected examples of their calculations to compare numerical results, but have not systematically pursued this somewhat unphysical Väisälä profile.) An expression equivalent to (4.10) and (4.12) was used by DD to discuss IW generation by the modulation mechanism for a thin thermocline and a narrow band ocean swell.

A systematic investigation of the implications of (4.10) and (4.16) does not seem to have been made, perhaps because of the very slow IW growth rates found. It is our present purpose to present calculations of the implications of the theory using somewhat realistic Väisälä profiles (emphasizing the upper ocean waters) and the SW relaxation model of Watson (1986). Unless otherwise specified, the GM Väisälä frequency model is chosen here for all of our calculations:

$$N(z) = \begin{cases} 0, & 0 > z > -D, \\ N_0 \exp[(z + D)/B], & -D > z > -B_h \end{cases}$$

$$B = 1200\text{ m}, \quad N_0 = 0.01\text{ sec}^{-1}. \qquad (4.21)$$

We shall, however, describe some calculations done with a "Patchex" model and also with a constant N model. The mode functions $W_{j,K}$ were evaluated numerically from (2.3) using both a WKB approximation (where valid) and numerical integration of the differential equation. The results from use of the relaxation model (3.13) were compared with those using the δ-function limit (4.12). Generally, the two sets of calculations were within a "factor of two" range of agreement, those done with the relaxation model tending to be somewhat larger. It should be noted in this context that when β is large Δ is small, and when β is small Δ can be replaced by the δ-function. The short waves for which β is large do not contribute strongly to the coupling. Thus, we do not expect dramatically different results from the two models. For consistency with the condition (2.1) we have limited the integration in (4.10) and (4.16) to the domain $k > K$. This constraint did not seem to affect our numerical results, however.

In Fig. 1 we show the e-folding rate $\nu(\theta_w)$ [defined in (4.18) and expressed in days^{-1}] for a mixed layer depth $D = 20$ m, a wind speed $W = 10$ m s^{-1}, and the first vertical mode corresponding to $j = 1$. The curves are labeled by the value of KB. The striking feature here is that the energy transfer is overwhelmingly from the IW field to the SW field. Although ν_s (4.16) is positive definite, the net rate is strongly dominated by the

---

[3] It might be noted that to evaluate the mean rates it is easiest to first do an analytic integration of (4.10) and (4.16) over θ_w before integrating over k. To verify our numerical evaluations, we have done this and also integrated over wind angles last, as implied by (4.14) and (4.17).

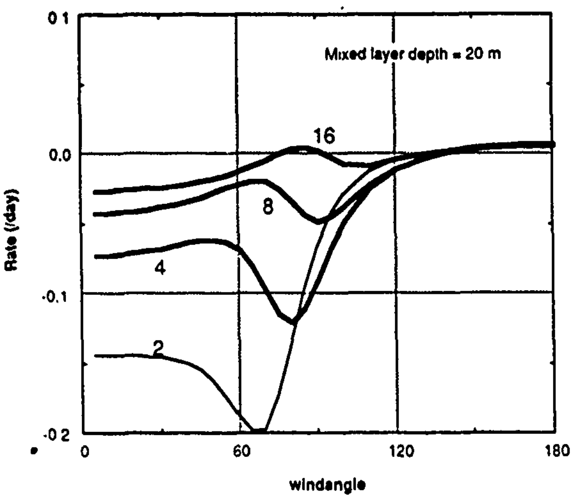

FIG. 1 The *e*-folding rate (day^{-1}) (4.18) is shown as a function of wind angle θ_w (with respect to the direction of horizontal propagation of the internal wave) for several values of KB and the mode $j = 1$. The surface wave spectrum is that given by (2.19), (2.20), and (2.21), and the wind speed is 10 m s^{-1}. Positive rates correspond to internal wave growth, negative rates to internal wave decay.

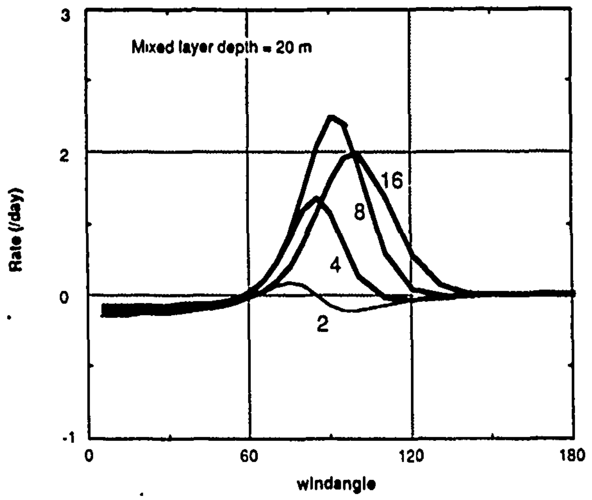

FIG. 3. As in Fig. 1, except that the wind speed is 20 m s^{-1}.

contribution from the modulation mechanism. The small positive value of ν at certain angles θ_w is sensitive to the SW spectral model, as was observed by DD. This is illustrated in Fig. 2, where the above calculation is repeated using the "collimated" SW model (2.22). The possibility of IW growth at certain angles is much more pronounced in this case.

In Fig. 3 we repeat the calculation of Fig. 1, but with a wind speed $W = 20$ m s^{-1}. Except for $KB = 2$, the pronounced effect is IW growth, or energy transfer from the SW field to the IW field. In Fig. 4 we repeat the calculation of Fig. 3 using the collimated SW model (2.22), but with $D = 60$ m. An even more pronounced growth of the IW field is seen.

There are two reasons for the significant difference between wind speeds of 10 and 20 m s^{-1}. First, at higher wind speeds $\nu_m(\theta_w)$ tends to have a greater range of positive values; second, ν_s grows rapidly with increasing wind strength.

In Fig. 5 we show the average growth rate (4.19) as a function of wind speed. Here, again, the mode corresponds to $j = 1$ and the curves are labeled by the IW horizontal wavelength expressed in meters. The same calculation is repeated in Fig. 6, but with a mixed layer depth $D = 60$ m. We see from these results that for $W < 15$ m s^{-1} or for longer wavelengths the predominant effect is to transfer energy from the IW field to the SW field. This contrasts with the view frequently expressed

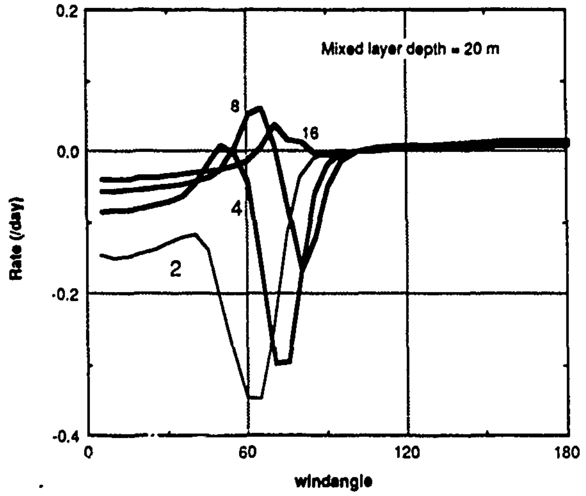

FIG. 2. The *e*-folding rate is shown for the same conditions as in Fig. (1), except that the collimated spreading function (2.22) is used.

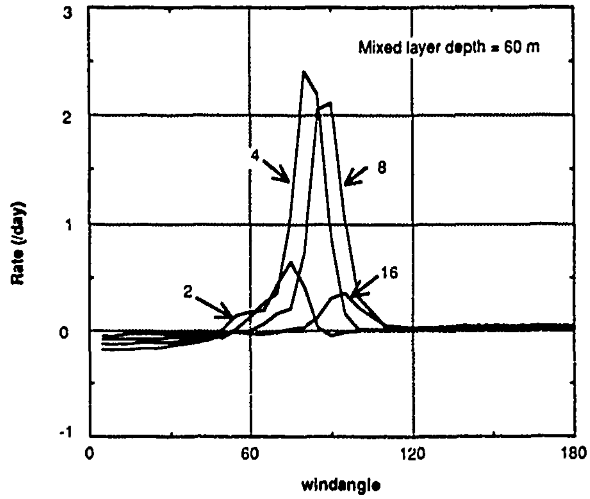

FIG. 4. As in Fig. 2, except that the wind speed is 20 m s^{-1} and the mixed layer depth has been changed as indicated.

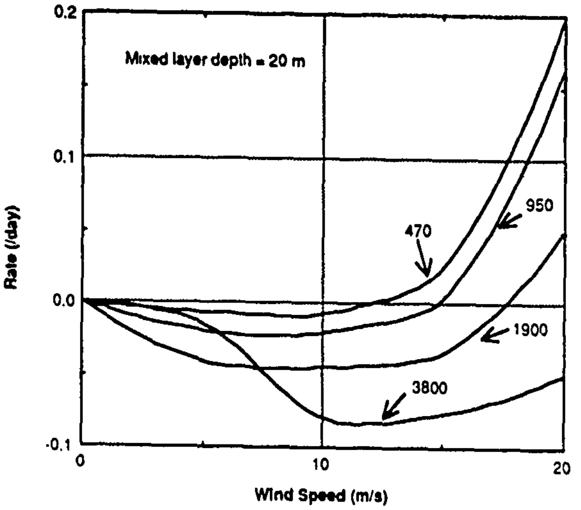

FIG. 5. The mean e-folding rate (day^{-1}) (4.19) is shown for several IW horizontal wavelengths (expressed in meters) and mode $j = 1$ as a function of wind speed. The SW spectrum is that of (2.21).

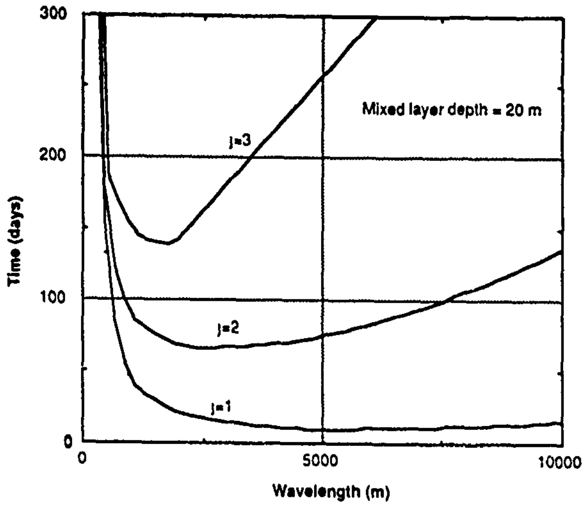

FIG. 7. The decay time [the negative of the inverse of the expression (4.19) expressed in days] for the internal wave field is shown as a function of IW horizontal wavelength and a wind speed of 10 m s^{-1}. Results are shown for the first three vertical modes and the surface wave spectrum is that of (2.21).

that wind waves tend to generate internal wave energy, however slowly.

In Figs. 7 and 8 we show the IW decay time (= $-\nu^{-1}$), expressed in days, as a function of the IW horizontal wavelength and for $j = 1, 2, 3$. The wind speed is 10 m s^{-1} and $D = 20$ and 60 m. Although not shown, the decay time for $j = 1$ increases with horizontal wave length for lengths greater than 15 km.

For the first mode, corresponding to $j = 1$, the time scales presented here tend to be significantly less than the 50 to 100 day decay times quoted in the Introduction. The decay times for the second mode tend to lie in this 50 to 100 day range. For the higher modes the energy exchange between the SW and IW fields does not appear to be very significant.

In Fig. 9 we show the ratio

$$\left|\frac{\nu_s}{\nu_m}\right|$$

as a function of wind speed for several IW horizontal wavelengths and $D = 60$ m. When $W < 15$ m s^{-1} the contribution of the spontaneous mechanism to the net energy exchange is seen to be negligible.

The power delivered to the SW field from the IW field,

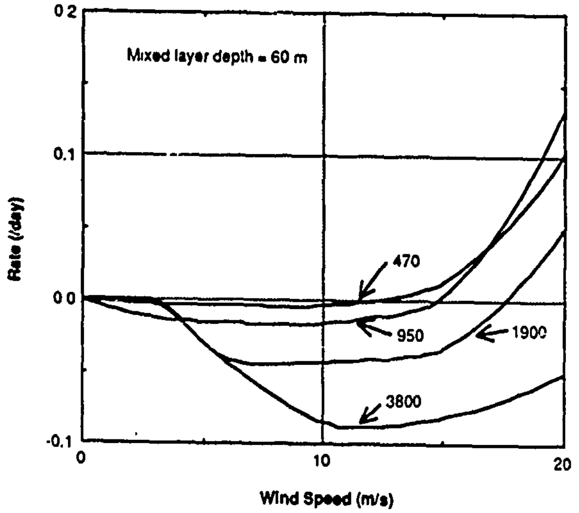

FIG. 6. As in Fig. 5, except for the indicated change in mixed layer thickness.

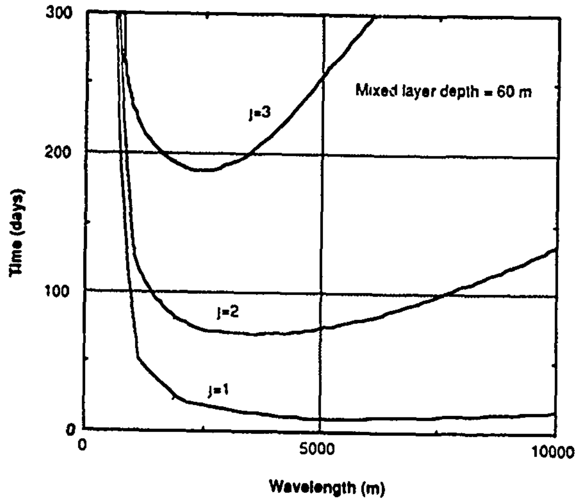

FIG. 8. As in Fig. 7, except that the mixed layer depth is changed as indicated.

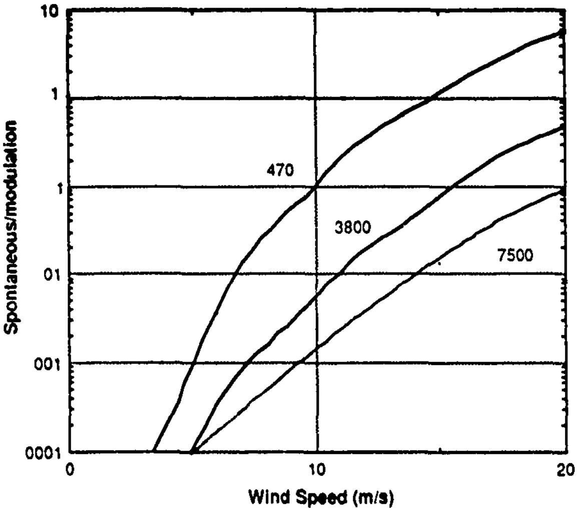

FIG. 9. For the data obtained for Fig. 6 we show the ratio of contributions from the spontaneous and modulation mechanisms as a function of wind speed for several IW horizontal wavelengths (expressed in meters).

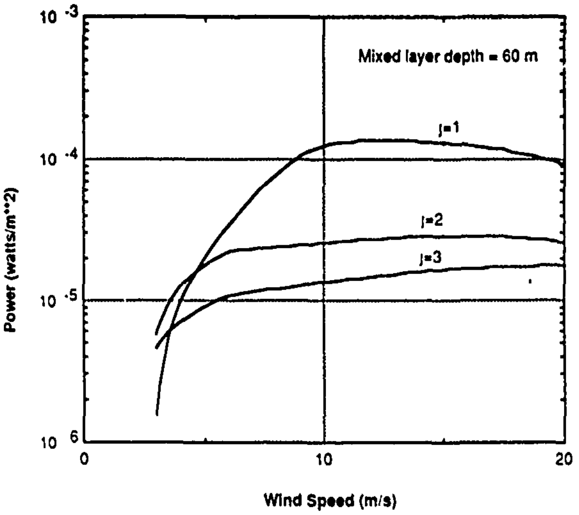

FIG. 10. The power per unit area (4.23) extracted from the IW field by the SW field shown as function of wind speed for the first three vertical modes. The SW spectrum is that specified by (2.21).

$$P(j) = -\int_{K_0}^{\gamma} P(j, K)dK, \qquad (4.23)$$

is shown as a function of wind speed in Fig. 10. The curves are labeled by the mode number j. The mixed layer depth is 60 m and we have taken $K_0 B = 0.5$. The total GM energy (2.12) for the first mode in this wavelength range is about 70 J m^{-2}, so a few days are required to deplete this mode when the wind speed is in the 10 m s^{-1} range.

The dependence of $\bar{\nu}$ on mixed layer depth D is shown in Fig. 11 for several selected IW horizontal wavelengths and $j = 1$. The wind speed here is 10 m s^{-1}. The variation of the rates ν with D is dominated by the exponential factor $\exp(KD)$ in (2.3).

We have examined several data sets for $N(z)$ taken by Pinkel[4] during the Patchex experiment. Representative of some of these is a strong thin thermocline at 50 m depth superimposed on a Väisälä profile similar to (4.21). We model this thermocline as a density discontinuity of strength

$$\int_{\text{thermocline}} N^2 dz = 0.035 \text{ m s}^{-2}.$$

The IW decay time for this "Patchex" profile is shown in Fig. 12 for a wind speed of 10 m s^{-1}. These results are seen to differ little from those of Fig. 8. The energy transfer rates are certainly sensitive to gross variations in the Väisälä profile, however.

To see the effects of a significant change in the Väisälä profile we consider the model

$$N(Z) = \begin{cases} 0, & 0 > Z > -50 \text{ m} \\ N_0 = 0.01, & -50 \text{ m} > Z > -1000 \text{ m}, \end{cases}$$

with the ocean bottom at 1000 m depth. The resulting IW decay times are shown in Fig. 13.

To illustrate the significance of our calculations, we refer to Table 1, where yearly means for wind speed and mixed layer thickness are quoted for three locations on the North Pacific Ocean. We recognize that the mixed layer is much more complex than accounted for in our model and can vary significantly in a day's time, as can the wind. Reference to Figs. 8 and 10 does,

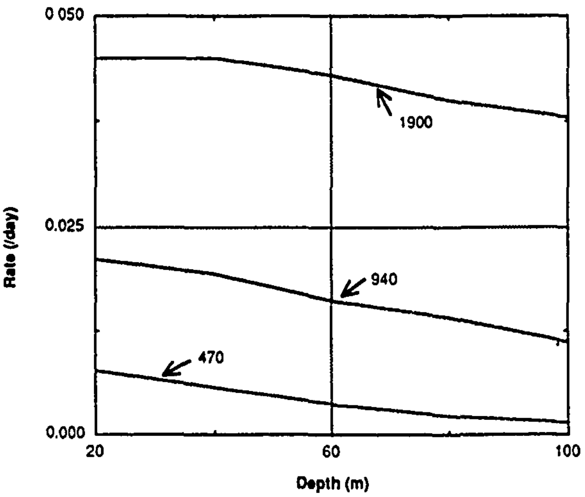

FIG. 11. The negative of the e-folding rate (4.19) shown as a function of mixed layer depth for $j = 1$, a wind speed of 10 m s^{-1}, and the SW spectrum (2.21). The curves are labeled by the IW horizontal wavelength.

---

[4] We are indebted to Dr. Pinkel for the use of this data.

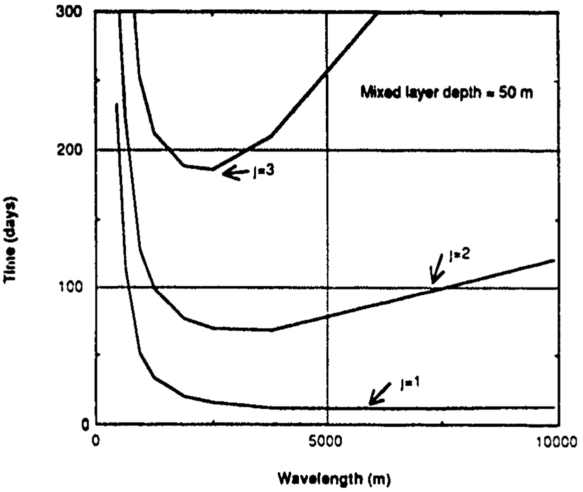

FIG. 12. The IW decay time is shown for the same conditions as those of Fig. 7, except that the "Patches" Vaisala profile is assumed.

TABLE 1. Yearly average wind speed and mixed layer thickness* for three areas of the North Pacific Ocean. Data taken from the 1989 U.S. Pilot Charts.

Location	Mean wind speed (m s^{-1})	Average mixed layer thickness (m)
50°N, 175°W	9 0	50
35°N, 165°W	7 5	45
25°N, 135°W	6.7	70

* Robinson, M., 1976. Atlas of the North Pacific Ocean Monthly Mean Temperatures and Mean Salinities of the Surface Layer. Naval Oceanographic Office.

Reid, J. (private communication) data from 1966 Boreas Expedition.

Reid, J., 1982. On the use of dissolved oxygen concentrations as an indicator of winter convection. Naval Research Reviews, No. 3.

however, suggest that for these areas the first mode internal wave should decay rapidly, if no source for maintaining this exists. To be more precise, we are led to expect IW decay within, perhaps, 10 to 20 days for internal waves in the wavenumber-frequency range:

horizontal wavelength: 1 to 20 km

vertical wavelength: >1 km

frequency/N_0: 0.15 to 0.7. (4.24)

Theories for the transport of internal wave energy imply that the long vertical wavelength (low mode number) waves act as a source of energy which flows to higher mode numbers, where shear instabilities lead to turbulent dissipation (for example, see Gregg 1989). McComas (1978) conjectured on the basis of the work of McComas and Bretherton (1977) that the high frequency-low mode number region of the IW spectrum is fed by an external energy source and that this energy flows to lower frequency and high mode numbers. The detailed studies of energy balance within the IW spectrum made by McComas and Bretherton (1977) and by Pomphrey et al. (1980) were not, however, extended into the high frequency domain where we find strong SW–IW interactions. The careful analysis of Flattè et al. (1985) also did not address this high frequency domain. The injection of energy from mesoscale current shears into the IW field occurs within the inertial frequency band, according the calculations of Watson (1985). Bell (1978) has given a calculation that suggests that energy can be injected into the internal wave field at high frequency and low mode numbers by mixed layer flow. Rates could not be given with confidence by Bell because of a lack of knowledge of the relevant environmental parameters.

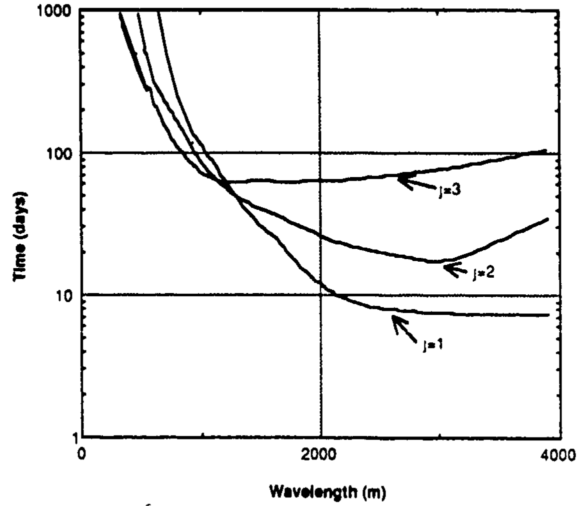

FIG. 13. As in Fig. 12, except a constant Vaisala profile is assumed.

We are left with an unclear picture of the energy source (of sources) required to maintain the internal wave spectrum in the domain (4.24), and in fact of the actual levels of internal wave energy in this domain.

5. Generation by ocean swell

Several observations have been reported (for example, see Apel et al. 1975; Briscoe 1983) which suggest that a strong ocean swell may generate internal waves. Generation by a sharply collimated swell was investigated by DD, who found IW growth for a sufficiently narrow SW spreading function and a sharp thermocline Väisälä model.

In this section we illustrate IW generation from a narrow band SW system by two mechanisms. The first is the modulation mechanism as described by (4.10). The second is generation from a swell wave field that has a prescribed modulation (not resulting from IW interactions). Equation (3.15) is used to calculate IW generation by this mechanism. We can use the exact resonance condition (4.12) for both of these because of the relatively long wavelength of ocean swell.

For the first mechanism described above, we replace (2.19) by

$$S(k) = \left[\frac{\langle\zeta^2\rangle}{\sqrt{2\pi}\,\Delta k}\right]\exp[-(k - k_p)^2/(2\Delta^2)], \quad (5.1)$$

where Δ and k_p are parameters. It is supposed that

$$\Delta \ll k_p.$$

Equation (2.20) is used for the spreading function and it is now assumed that

$$\sigma \gg 1.$$

We replace the angle θ_w in G by θ_s to indicate that this is the angle between the direction of swell propagation and that of K.

Conditions (5.2) and (5.3) permit an analytic evaluation of (4.10). If we choose θ_s to give maximum IW growth rate (that is, approximately 90°) we obtain

$$\text{Rate}\,(\text{day}^{-1}) = 1.7 \times 10^5\ \text{Re}(p)$$
$$= \frac{1.9 \times 10^4\langle\zeta^2\rangle k_p^2\alpha\sigma^2}{(KB)^2H}\left(\frac{\Omega^2}{Kg}\right), \quad (5.4)$$

where

$$H = 1 + \left(\frac{2\sigma\Delta\Omega}{K\sqrt{gk_p}}\right)^{1.5}.$$

Here α is defined by (3.17).

To illustrate (5.4) we choose a swell wavelength of 145 m, $H = 1$, $\sigma = 10$, $\langle\zeta^2\rangle k_p^2 = 0.04$, and the Väisälä profile (4.21). The growth times [that is, the reciprocal of (5.4)] for the first three modes are shown in Fig. 14. Reference to Fig. 4, which describes a similarly collimated spectrum, illustrates the sensitivity of the growth rate on the angle θ_s. It is seen that e-folding rates in the range of (1 day)$^{-1}$ may be expected.

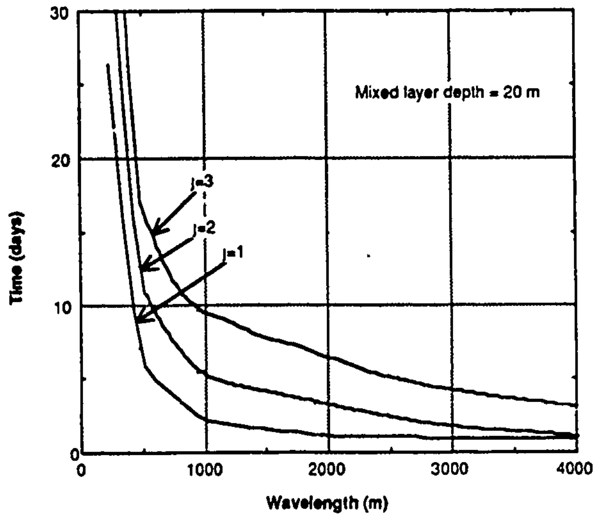

FIG. 14. The IW growth time [the reciprocal of (5.4), expressed in days] due to interaction with ocean swell is shown as a function of horizontal wavelength for the first three vertical modes.

To even a casual observer a swell wave train exhibits modulation in the direction of its propagation (as a time record taken at a fixed position would show). Because the resonance condition (3.3) requires that the swell angle θ_s be nearly 90°, we require modulation also along the wave crests. One might, for example, expect such modulation to be related to the width σ^{-1} of the spreading function. Snodgrass et al. (1966) have discussed a number of phenomena which may determine the swell spectrum, such as the dimensions of the region in which swell is produced, refraction by currents, and scattering from wind waves, islands, or shallow areas in the swell path.

We have not, however, found data from which to model F_s in (3.15), so are led to a very simplified model that illustrates the mechanism and permits analytic integration of (3.15). We consider the swell to be represented as a sequence of wave trains, each of length T and of the form:

$$F_s = \rho_0 V_\lambda \Psi(x, k, t),$$
$$\Psi = M(x, t)S(k)G(\theta - \theta_s),$$
$$M(x, t) = \sum_L P(L)\{1 + e^{-t/T}\cos[L\cdot(x - c_g)]\}, \quad (5.5)$$

where $t > 0$ and

$$\sum_L P(L) = 1.$$

Here c_g is the group velocity of the swell and we suppose that P describes modulation along the swell crests.

To continue, we assume that E_t in (3.15) represents the IW energy in a restricted band which matches the resonance condition (3.3). The current U is that due to this restricted IW band. For S in (5.5) we use (5.1).

Equation (3.15) may be integrated analytically for a narrow band collimated swell. We define the average power received by the IW field as

$$\text{power} = E_t/T, \quad (5.6)$$

which is appropriate if swell groups such as (5.5) arrive at intervals T. We find from (3.15) that

$$\text{power} = 0.25\rho_0(N_0B)^2B\alpha(\Omega/N_0)(T\omega_{k_p})^2$$
$$\times [\langle\zeta^2\rangle/B^2]^2(\bar{P}^2/(KBT)). \quad (5.7)$$

Here $\bar{P}$ is the weighted sum of $P(K)$ over the specified IW band.

To illustrate (5.6) we take $k_p = 2\pi/145\ \text{m}^{-1}$, $T = 100$ s and $\langle\zeta^2\rangle = 20\ \text{m}^2$. The quantity

$$\text{power}/\bar{P}^2$$

is shown in Fig. 15 for the first three modes. We see from these results that if the swell modulation well

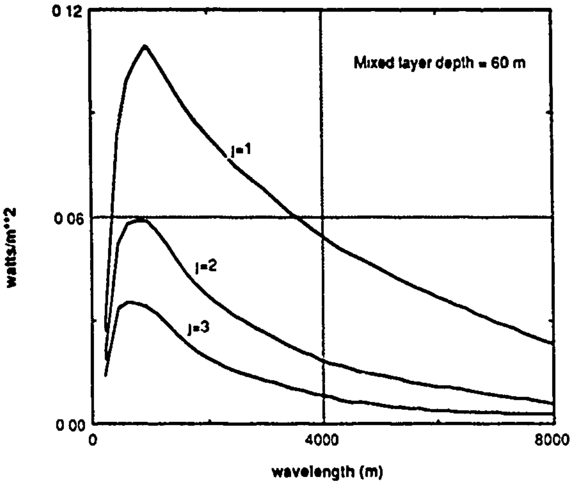

FIG. 15. The IW power per unit area received from a modulated ocean swell (5 7) is shown for the first three vertical modes as a function of horizontal wavelength.

matches the IW field that rather intense generation of internal waves can result.

6. Nonlinear modulation of surface waves

In this section we shall investigate the interaction of surface waves with an IW packet that has a finite extent in the x-direction, but is uniform in the y-direction. A finite packet of internal waves may arise from statistical fluctuations in the ambient field, from uneven topography, or a transient source. In the interest of numerical simplicity we shall set $S = 0$ in (3.9). Damping will be accounted for by ignoring those portions of the SW spectrum for which a significant SW–IW interaction time T_I is greater than the relaxation time, or

$$T_I > \beta^{-1}(k). \qquad (6.1)$$

We express the IW surface current U in the form

$$\mathbf{U} = \mathbf{i} U_0 V(\xi). \qquad (6.2)$$

It is supposed that

$$V \approx 0 \quad \text{for} \quad \xi < \xi_1 \quad \text{or} \quad \xi > \xi_2 \qquad (6.3)$$

and that within the range $\xi_1 < \xi < \xi_2$

$$V \approx \cos(K\xi). \qquad (6.4)$$

We may now write (3.9) in the form

$$\left[\dot{\xi}\frac{\partial}{\partial \xi} + \dot{k}_x \frac{\partial}{\partial k_x}\right] F_s = 0, \qquad (6.5)$$

where

$$\dot{\xi} = C_g(\mathbf{k})(k_x/k) - C_I + U_0 V(\xi),$$
$$\dot{y} = C_g(\mathbf{k})(k_y/k),$$
$$\dot{k}_x = -k_x U_0 \frac{\partial V}{\partial \xi},$$
$$\dot{k}_y = 0. \qquad (6.6)$$

We shall consider only surface waves which travel in the positive x-direction and overtake the packet. For those waves which have not yet reached the IW packet, say at time t_0 and position $\xi < \xi_1$, we have

$$F_s = F_a. \qquad (6.7)$$

Similarly, we have

$$\mathbf{k} = \mathbf{k}_0, \quad \text{a constant for} \quad t < t_0. \qquad (6.8)$$

Then having integrated the ray equations (6.6) to a point (k, ξ) within the packet we may set

$$F_s(\mathbf{k}, \xi) = F_a(\mathbf{k}_0). \qquad (6.9)$$

A simple technique for evaluating $F_s(k, \xi)$ is to choose a specific value of (k, ξ) and to integrate (6.6) backward in time to a location $\xi < \xi_1$. For $\xi < \xi_1$, we know that $k = k_0$. Then with the use of (6.9) we obtain immediately the numerical value of $F_s(k, \xi)$.

On integrating (6.6) we must distinguish four trajectory types:

1) those which pass through the packet from ξ_1 to ξ_2

2) those which have entered the packet at ξ_1, and are turned back at the point where $d\xi/dt = 0$ [equivalent to the resonance condition (3.4)], and then pass back out of the packet at $\xi = \xi_1$.

3) those which have been overtaken by the packet at $\xi = \xi_2$

4) those which are trapped within the packet.

We shall ignore the type 3 and type 4 trajectories. We must, however, calculate the type 1 and type 2 trajectories. The type 1 trajectories do not lead to an energy exchange between the two fields, since on emerging from the packet a SW has the same wavenumber as it had on entering.

The rate of energy exchange to the IW field is obtained from (3.8) and (6.9) as

$$\dot{E}_I(j, K) = -U_0 K \int_{\xi_1}^{\xi_2} d\xi \Big/ L_x \int d^2k c_x k_x$$
$$\times \sin(K\xi) F_s(\mathbf{k}, \xi). \qquad (6.10)$$

Here we have taken $L_x = \xi_2 - \xi_1$.

As a first example we set

$$V(\xi) = 1.46 \cos(K\xi)/\{[1 + \exp(-0.5K\xi)]$$
$$\times [1 + \exp(0.5K\xi - 6.28)]\} \qquad (6.11)$$

and take (here λ_I is the internal wave wavelength)

standard profile (4.21)

$D = 20$ m

$$\begin{aligned} U_0 &= 0.25 \text{ m s}^{-1} \\ c_I &= 0.56 \text{ m s}^{-1} \\ \lambda_I &= 470 \text{ m} \\ \theta_w &= 30^\circ. \end{aligned} \tag{6.12}$$

This is a strong internal wave, corresponding to a vertical displacement at the thermocline of 8 m.

The resulting modulation function $M(k, \xi)$ [see (2.17)] is shown as the solid curves in Fig. 16 for the location $K\xi = 3\pi$. The lines are labeled by the direction of k and shown as functions of k. The corresponding results obtained from linear perturbation theory (4.4) are represented by the dashed lines. The blocking of the SW field is seen at those values of k where M vanishes.

To study the energy transfer (6.10) we take

$$V(\xi) = \begin{cases} \cos(K\xi), & \pi/2 < K\xi < 5\pi/2 \\ 0, & \text{outside above range,} \end{cases} \tag{6.13}$$

and continue to use the parameters given in (6.12).

We have seen that waves having type (1) trajectories may be excluded from the integrand in (6.10). We also exclude those type (2) waves for which the time T_t to propagate from $\xi = \pi/(2K)$ to the turning point exceeds β^{-1} [condition (6.1)]. We see, then, that just as in the linear theory of the last Section, the triad resonance condition must be met in order that energy be exchanged between the two fields.

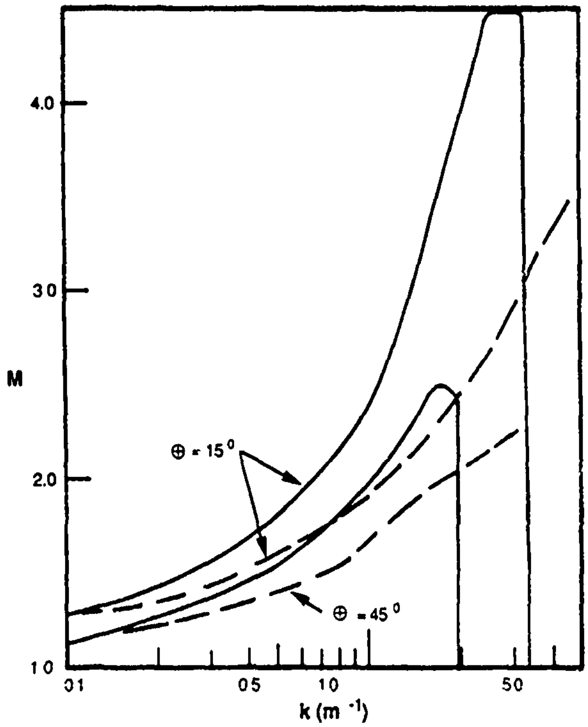

FIG. 16. The modulation function $M(K, \xi)$ is shown for the parameters (6.12) and a location corresponding to $K\xi = 3\pi$ The curves are labeled by the direction of k. The solid curves obtained using nonlinear theory, the dashed curves from the linearized equation (4.3).

Surface waves reaching the packet (6.13) encounter an IW current in the negative x-direction. This current tends to drive the surface waves back out of the packet. If there is a turning point, corresponding to $d\xi/dt = 0$, this will occur in the interval $\pi/2 < K\xi < \pi$. The adverse current does work on the SW field, so tends to increase the SW energy. This is seen mathematically in (6.10), since $M > 1$ and $\sin(K\xi)$ is positive in the interval $\pi/2 < K\xi < \pi$.

For the parameters given in (6.12) the expression (6.10) was evaluated. A characteristic time was obtained:

$$T_d = [\dot{E}_I(j, K)/E_I(j, K)]^{-1} = -24 \text{ days}. \tag{6.14}$$

For a mixed layer depth $D = 80$ m, we would have obtained $T_d = -70$ days. We note (see Fig. 16) that for this case waves near the spectral peak do not contribute to the energy exchange.

Because (6.9) is nonlinear, the coupling leads to spectral transfer within the IW field. For example, let us consider a second IW mode (j', K') for which

$$U' = U'_0 \cos(K'x - c'_I t + \alpha'). \tag{6.15}$$

The total IW current is the sum of (6.13) and (6.15). If, however, U'_0 is too small to significantly modulate F_s, then

$$E_I(j', K') = -U'_0 K' \int_{\xi_1}^{\xi_2} d\xi \Big/ L_x \int d^2k k_x c_x \sin(K'\xi) F_s(k, \xi) \tag{6.16}$$

where F_s is determined by (6.13) only. Evidently, depending upon the mode (j', K') either sign may be encountered in (6.16). The implication of this is that in the nonlinear regime, energy may be transferred among the IW modes through SW coupling.

7. Conclusions

We have described mechanisms for energy exchange between internal wave and surface wave fields. The important effect in the case of wind waves is the draining of energy from the IW field in the high frequency, long vertical wavelength domain. This would seem to be significant in assessing the factors which determine the total energy budget of the internal waves. In reviewing existing models which describe energy fluxes into and within the IW spectrum, we have tentatively identified mixed layer flows as a possible source of the required energy. Partial depletion of the IW spectrum in the region of high energy loss and at times of high energy loss might occur.

We have not explored here the dependence of the energy exchange rates on the Väisälä profile. To realistically assess the implications for internal wave energy balance, measured upper ocean profiles of N for selected locations and seasons should be used. Also, this should be related to historical records of wind speed for these locations.

As concluded by DD, a well collimated ocean swell may play a different role in that this can lead to rapid IW growth. Although this may be locally significant, it is not expected to be important for the IW total energy budget.

We have mentioned that external sources of SW modulation, such as the envelope of swell, wind variability, and Langmuir cells, may lead to IW generation. Nonlinear modulation, such as SW blocking, has been seen to introduce new aspects relating to SW–IW coupling.

Acknowledgments. I would like to thank Dr. Robert Pinkel for discussions of upper ocean internal wave activity and Dr. Joseph Reid for discussions of upper ocean stratification. This work was supported in part by ONR Contract N00014-87-K-0010.

APPENDIX

Derivation of Equation (3.5)

To derive (3.5) we first note that in the mixed layer the flow can be represented by a velocity potential Φ of the form

$$\Phi = \phi_g(\mathbf{x}, z, t) + \phi_l(\mathbf{x}, z, t). \qquad \text{(A1)}$$

Here $x = (x, y)$ is a vector in a plane of constant z. The term ϕ_g contains the high frequency, high wavenumber part of Φ associated with gravity waves, while ϕ_l contains the low frequency, low wavenumber part of Φ associated with internal waves. The vertical displacement of the ocean surface ζ, due to wave motion, can likewise be represented as a sum of a high frequency part ζ_g and a low frequency part ζ_l:

$$\zeta(x, t) = \zeta_g(x, t) + \zeta_l(x, t). \qquad \text{(A2)}$$

The SW–IW coupling was obtained in WWC from Bernoulli's equation at the surface (here ∇_s is the horizontal component of ∇):

$$\frac{\partial \zeta}{\partial t} + \nabla_s \cdot (\zeta \nabla_s \Phi) = w \quad \text{at} \quad z = \zeta, \qquad \text{(A3)}$$

where w is the vertical component of fluid velocity. On averaging (A3) over many realization of the SW field and on extracting the low frequency and low wavenumber part, WWC and DD obtained the relation [Eq. (2.12) of WWC or (6.3) of DD]

$$w_l = \frac{\partial \phi_l}{\partial z} = \langle \nabla_s \cdot (\zeta_s \nabla_s \phi_s) \rangle_{LF}$$

$$\equiv \Gamma(\mathbf{x}, t), \quad \text{at} \quad z = 0. \qquad \text{(A4)}$$

The symbol $\langle \quad \rangle_{LF}$ here implies both the ensemble average over SW field realization and the low pass filter in frequency and wavenumber. Also, in (A4) only the second order triad terms are kept.

We may use (2.14) to re-express (A4) in terms of the SW action density (as was done by DD):

$$\Gamma(\mathbf{x}, t) = \nabla_s \cdot \int d^2k \mathbf{k} F_s(\mathbf{x}, \mathbf{k}, t)/\rho_0. \qquad \text{(A5)}$$

This will be recognized as the gradient of the SW momentum per unit area. It represents the driver of internal wave excitation.

To satisfy the condition (3.6) WWC generalized (2.4):

$$w_l(\mathbf{x}, 0, t) = \sum_{j,\mathbf{K}} e^{i\mathbf{K}\cdot\mathbf{x}} A_{j,\mathbf{K}} W'_{j,\mathbf{K}}(0) + \Gamma(\mathbf{x}, t). \qquad \text{(A6)}$$

They then obtained a set of differential equations for the amplitudes Aj, k. On rewriting these in terms of the U of (2.7) we obtain (3.5).

REFERENCES

Apel, J. K., H. M. Byrne, J. R. Proni and R. L. Charnell, 1975: Observations of oceanic internal and surface waves from the Earth Resources Technology Satellite. *J. Geophys. Res.*, **80**, 865–881.

Ball, F. K., 1964: Energy transfer between external and internal gravity waves. *J. Fluid Mech.*, **19**, 465–478.

Bell, T. H., 1975: Topographically generated internal waves in the open ocean. *J. Geophys. Res.*, **80**, 320–327.

——, 1978: Radiation damping of inertial oscillations in the upper ocean. *J. Fluid Mech.*, **88**, 289–308.

Brekhovskikh, L. M., V. Goncharov, V. Kurtepov and K. Naugolnykh, 1972: Resonant excitation of internal waves by nonlinear interactions of surface waves. *Atmos. Oceanic Phys.*, **8**, 112–117.

Briscoe, M. G., 1983. Observations on the energy balance of internal waves during Jasin. *Phil. Trans. Roy. Soc. London*, **A308**, 427–444.

Curtin, T. B., and C. N. K. Mooers, 1975. Observation and interpretation of a high frequency internal wave packet and surface slick pattern. *J. Geophys. Res.*, **80**, 882–894.

Donelan, M. A., J. Hamilton and W. H. Hui, 1985: Directional spectra of wind-generated waves. *Phil. Trans. Roy. Soc. London*, **A315**, 509–562.

Dysthe, K. B., and K. P. Das, 1981: Coupling between a surface wave spectrum and an internal wave: modulational interaction. *J. Fluid Mech.*, **104**, 483–503.

Flatté, S. M., F. S. Henyey and J. A. Wright, 1985: Eikonal calculations of short-wavelength internal-wave spectra. *J. Geophys. Res.*, **90**, 7265–7272.

Fu, L. L., and B. Holt, 1984. Internal waves in the Gulf of California. Observations from a spaceborne radar. *J. Geophys. Res.*, **89**, 2053–2060.

Garget, A. E., P. J. Hendricks, T. B. Sanford, T. R. Osborn and A. J. Williams, 1981: A composite spectrum of vertical shear in the upper ocean. *J. Phys. Oceanogr.*, **11**, 1258–1271.

Garrett, C., and W. Munk, 1972a: Space-time scales of internal waves. *Geophys. Fluid Dyn.*, **2**, 225–264.

——, and ——, 1972b: Ocean mixing by breaking internal waves. *Deep-Sea Res.*, **19**, 823–832.

Gill, A. E., 1984: On the behavior of internal waves in the wake of storms. *J. Phys. Oceanogr.*, **14**, 1129–1151.

Gregg, M., 1987: Diapycnal mixing in the thermocline: A review. *J Geophys. Res.*, **92**, 5249–5286.

——, 1989: Scaling dissipation in the thermocline. *J Geophys. Res.*, **94**, 9686–9698.

——, E. D'Asarro, T Shay and N. Larson, 1986: Observations of persistent mixing and near-inertial waves. *J Phys Oceanogr.*, **16**, 856–885.

Hasselmann, K., 1967: Nonlinear interactions treated by the methods of theoretical physics. *Proc. Roy. Soc.*, **A299**, 77–99.

——, 1968: Weak-interaction theory of ocean waves. *Basic Developments in Fluid Mechanics*, Vol. 2, 117–182. M. Holt, Ed., Academic Press.

Hughes, B. A., 1978b: The effects of internal waves on surface wind waves. 2. Theoretical analysis. *J Geophys. Res.*, **83**, 455–465.

——, and H. L. Grant, 1978a: The effects of internal waves on surface wind waves 1. Experimental measurements. *J Geophys Res.*, **83**, 443–454.

Kanthu, L. H., 1979: On generation of internal waves by turbulence in the mixed layer. *Dyn Atmos Oceans*, **3**, 39–46.

Kenyon, K. E., 1968: Wave–wave interactions of surface and internal waves. *J. Mar. Res.*, **26**, 208–231.

Leaman, K. D., 1976: Observations on the vertical polarization and energy flux of near-inertial waves. *J Phys. Oceanogr.*, **6**, 894–908.

——, and T. B. Sanford, 1975: Vertical energy propagation of internal waves: a vector spectral analysis of velocity profiles. *J. Geophys. Res.*, **80**, 1975–1978.

Lueck, R. G., W. R. Crawford and T. R. Osborn, 1983: Turbulent dissipation over the continental slope off Vancouver Island. *J Phys Oceanogr.*, **13**, 1809–1818.

McComas, C. H., 1978: Equilibrium mechanisms within the oceanic internal wave field. *J Phys Oceanogr.*, **7**, 836–845.

——, and F. P. Bretherton, 1977: Resonant interactions of oceanic internal waves. *J Geophys. Res.*, **82**, 1397–1412.

——, and P. Muller, 1981: The dynamic balance of internal waves. *J Phys. Oceanogr.*, **11**, 970–986.

Munk, W. H., 1981: Internal waves and small scale processes. *Evolution of Physical Oceanography*, B. Warren and C. Wunsch, Eds., The MIT Press, 264–270.

Olbers, D. J., and K. Herterich, 1979: The spectral energy transfer from surface waves to internal waves. *J. Fluid Mech.*, **92**, 349–380.

Osborn, T., 1978: Measurements of energy dissipation adjacent to an island. *J Geophys. Res.*, **83**, 2939–2957.

Phillips, O. M., 1973: On the interactions between internal waves and surface waves. *Atmos. Oceanic Phys.*, **9**, 565–568.

——, 1977: *The Dynamics of the Upper Ocean* Cambridge University Press.

——, 1984: On the response of short ocean wave components at a fixed wavenumber to ocean current variations. *J. Phys Oceanogr.*, **14**, 1425–1433.

——, 1985: Spectral and statistical properties of the equilibrium range in wind-generated gravity waves. *J Fluid Mech.*, **156**, 505–531.

Pinkel, R., 1985: A wavenumber-frequency spectrum of upper ocean shear. *J Phys Oceanogr.*, **15**, 1453–1469.

Pomphrey, N., J. D. Meiss and K. M. Watson, 1980: Description of nonlinear wave interaction using Langevin methods. *J Geophys. Res.*, **85**, 1085–1094.

Snodgrass, F., G. Groves, K. Hasselmann, G. Miller, W. Munk and W. Powers, 1966: Propagation of ocean swell across the Pacific. *Phil Trans. Roy. Soc. London*, **259A**, 431–497.

Thorpe, S. A., 1966: On wave interactions in a stratified fluid. *J Fluid Mech.*, **24**, 737–751.

van Gastel, K., 1987: Imaging by *x*-band radar of subsurface features: a nonlinear problem. *J. Geophys. Res.*, **92**, 11857–11865.

Watson, K. M., 1985: Interaction between internal waves and mesoscale flows. *J Phys. Oceanogr.*, **15**, 1296–1311.

——, 1986: Persistence of a pattern of surface gravity waves. *J Geophys Res.*, **91**, 2607–2615.

——, B. J. West and B. I. Cohen, 1976: Coupling of surface and internal gravity waves: a mode coupling model. *J. Fluid Mech.*, **77**, 185–208.

Wigner, E. P., 1932: On the quantum correction for thermodynamic equilibrium. *Phys. Rev.*, **40**, 749–759.

Richardson Number Criterion for the Nonlinear Stability of Three-Dimensional Stratified Flow*

Henry D. I. Abarbanel, Darryl D. Holm,

Jerrold E. Marsden, and Tudor Ratiu

---

*. Reprinted from Physical Review Letters, Vol. 52, No. 26, pp. 2352-2355 (1984)

VOLUME 52, NUMBER 26 PHYSICAL REVIEW LETTERS 25 JUNE 1984

Richardson Number Criterion for the Nonlinear Stability of Three-Dimensional Stratified Flow

Henry D. I. Abarbanel
Scripps Institution of Oceanography and Project in Nonlinear Science,
University of California, San Diego, La Jolla, California 92093

and

Darryl D. Holm
Theoretical Division and Center for Nonlinear Studies, Los Alamos National Laboratory,
Los Alamos, New Mexico 87545

and

Jerrold E. Marsden
Department of Mathematics, University of California, Berkeley, California 94720

and

Tudor Ratiu
Department of Mathematics, University of Arizona, Tucson, Arizona 85721

(Received 15 March 1984)

With use of a method of Arnol'd, we derive the necessary and sufficient conditions for the formal stability of a parallel shear flow in a three-dimensional stratified fluid. When the local Richardson number defined with respect to density variations is everywhere greater than unity, the equilibrium is formally stable under nonlinear pertrubations. The essential physical content of the nonlinear stability result is that the total energy acts as a "potential well" for deformations of the fluid across constant density surfaces; this well is required to have definite curvature to assure stability under these deformations.

PACS numbers: 47.20.+m, 03.40.Gc, 92.10.Dh

With use of a method of Arnol'd[1] and others,[2,3] we have investigated the nonlinear stability of two- and three-dimensional incompressible flows of an inviscid stratified fluid treated as a Hamiltonian system. In this note, we report on the application of this technique to the important case of a shear flow with velocity profile $U(z)$, and density profile $\rho(z)$. We do not present the full set of conditions for nonlinear stability of this flow, but do exhibit the necessary and sufficient conditions for the formal stability of the flow. Formal stability means that a certain functional of the flow fields is definite in sign. Given formal stability, nonlinear stability requires additional convexity estimates to be satisfied. These do not alter the physical implications of the conditions derived here.[3]

The two-dimensional analysis[4] of the stratified fluid equations linearized about a planar shear flow $U(z)$, $\rho(z)$, shows that neutral stability (purely imaginary spectrum) occurs provided the Richardson number is everywhere greater than $\frac{1}{4}$. Here we derive the analogous criterion for formal stability for three-dimensional nonlinear deformations of the flow. Our criterion is that the local Richardson number defined with respect to variations across constant-density surfaces must be greater than 1. This focuses attention on the realm between $\frac{1}{4}$ and 1 for intensive theoretical and experimental investigation.

We treat stability in the Boussinesq approximation[4] for incompressible flow. See Ref. 2 for the treatment of nonlinear stability for compressible flows, and Ref. 3. for incompressible, stratified, non-Boussinesq flows. We address solutions of the momentum equation

$$\frac{\partial}{\partial t}\vec{u} + (\vec{u}\cdot\nabla)\vec{u} = -\nabla p - \rho g\hat{z}, \qquad (1)$$

along with

$$\frac{\partial}{\partial t}\rho + \vec{u}\cdot\nabla\rho = 0 \quad \text{and} \quad \nabla\cdot\vec{u} = 0, \qquad (2)$$

in a domain on whose boundary the normal component of the velocity $\vec{u}$ must vanish and the density ρ must be constant. In (1) and (2), p is the pres-

© 1984 The American Physical Society

sure and g is the constant gravitational acceleration in the $-\hat{z}$ direction. The constant-reference density multiplying the acceleration in (1) has been set equal to unity.

Solutions to these equations conserve the energy

$$\int d^3x\,\{\tfrac{1}{2}|\vec{u}|^2+\rho g z\}. \tag{3}$$

Both ρ and the potential vorticity

$$q=(\nabla\times\vec{u})\cdot\nabla\rho \tag{4}$$

are conserved along fluid particle trajectories. Thus, for an arbitrary function $G(q,\rho)$,

$$A(\vec{u},\rho)=\int d^3x\,\{\tfrac{1}{2}|\vec{u}|^2+\rho g z+G(q,\rho)+\lambda q\} \tag{5}$$

is conserved. The term λq in (5) is separated to cancel some boundary terms which arise below. The role of the function $G(q,\rho)$ is that of a familiar Lagrange multiplier expressing the constraints on the flow imposed by conservation of q and ρ.

We now examine the first variation of $A(\vec{u},\rho)$ and relate its critical points to stationary solutions $\vec{u}_e$. The first variation is

$$\delta A(\vec{u}_e,\rho_e)=\int d^3x\,\{\delta\vec{u}\cdot[\vec{u}_e-G_{qq}\nabla\rho_e\times\nabla q_e]+\delta\rho[gz+G_\rho(\nabla\times\vec{u}_e)\cdot\nabla G_q]\}$$
$$+(\lambda+G_q)|_s\int ds\hat{n}\cdot\{\delta\rho\,\nabla\times\vec{u}_e-\nabla\rho_e\times\nabla\vec{u}_e\}, \tag{6}$$

where $G_\rho=\partial G/\partial\rho$ evaluated at $q_e\rho_e$, etc., S is the boundary surface of the domain of the flow, and $\hat{n}$ is the outward unit normal vector on S.

δA in (6) vanishes at $\vec{u}_e$, ρ_e satisfying

$$\vec{u}_e=G_{qq}\nabla\rho_e\times\nabla q_e, \tag{7}$$

$$gz+G_\rho=(\nabla\times\vec{u}_e)\;\nabla G_q \tag{8}$$

in the interior, and

$$\lambda=-G_q \tag{9}$$

on the boundary. Flows satisfying (7) and (8) can be verified to be stationary solutions of (1) and (2). Expression (7) implies the requirements $\vec{u}_e\cdot\nabla\rho_e=\vec{u}_e\cdot\nabla q_e=0$ for stationary flows; (8) is the three-dimensional analog of Long's equation.[5]

We use (7) and (8) to determine $G(q_e,\rho_e)$ in terms of the Bernoulli function

$$K(q_e,\rho_e)=p_e+\rho_e gz+\tfrac{1}{2}|\vec{u}_e|^2, \tag{10}$$

via

$$G(q_e,\rho_e)=q_e\int^{q_e}\frac{dx}{x^2}K(x,\rho_e)+q_e\gamma(\rho_e), \tag{11}$$

where $\gamma(\rho_e)$ is an arbitrary function of ρ_e.

An equilibrium flow is said to be *formally stable* if the second variation of $A(\vec{u},\rho)$ at the critical point $\vec{u}_e,\rho_e$ is definite in sign. Formal stability implies[3] linearized stability since definiteness of δ^2A gives a preserved norm for the linearized solutions. As noted, nonlinear stability requires both formal stability and some convexity conditions on the function $G(q,\rho)$. For the present case, we find

$$\delta^2A(\vec{u}_e,\rho_e)=\int d^3x\left\{|\delta\vec{u}|^2+(\delta q,\delta\rho)\begin{bmatrix}G_{qq} & G_{q\rho}\\ G_{q\rho} & G_{\rho\rho}\end{bmatrix}\begin{bmatrix}\delta q\\ \delta\rho\end{bmatrix}\right\}. \tag{12}$$

From this we see that a *sufficient* condition for formal stability is that the eigenvalues of the two-by-two matrix in (12) are positive; namely,

$$G_{qq}>0, \tag{13}$$

and

$$G_{qq}G_{\rho\rho}-G_{q\rho}^{\;2}>0. \tag{14}$$

We can sharpen these sufficient conditions, however, by noting that $\operatorname{div}\nabla\cdot\delta\vec{u}=0$, so there are only two independent components of $\delta\vec{u}$, which along with $\delta\rho$ allow us to cast the definiteness of δ^2A into a linear three-by-three operator eigenvalue condition, whose eigenvalues must then be either all positive or all negative. This condition is made explicit in the example we now discuss.

Our example is the parallel equilibrium flow

$$\vec{u}_e(\vec{x})=(u(y,z),0,0), \tag{15}$$

$$\rho_e(\vec{x})=\rho(z). \tag{16}$$

This is a standard configuration and application of the Arnol'd method to it provides insight into the value of the technique. The validity of the linearized results on this flow have been examined in laboratory and geophysical situations. Our nonlinear result will thus provide impetus for further experimental study of these important flows. We separate the y and z dependences in $u(y,z)$ into a small, slowly varying y dependence plus a general z dependence $U(z)$. Thus, we write

$$u(y,z)=f(y)+U(z). \tag{17}$$

The role of $f(y)$ is to break the $q_e=0$ degeneracy of the two-dimensional $f=0$ flow, which is the conventional setup. The physical situation we wish to describe is a shear flow $U(z)$ with a smooth, small $f(y)$ imposed upon it to give the three-dimensionality needed for $q_e \neq 0$. We wish to parametrize $f(y)$ by a velocity scale, f_0, which is much less than $U(z)$, and by a length scale L which is large compared to any other lengths in the problem. We choose

$$f(y) = f_0 (y/L)^2; \quad f_0 << U(z); \tag{18}$$

and restrict the domain of y to be $|y| << L$. In what follows, we expand all quantities in L^{-1}, capturing the essence of the stability problem in the leading orders of L which are retained for L very large.

From the Bernoulli function, (10), we find (dropping the subscript e henceforth)

$$G(q,\rho)$$
$$= -[p + \rho g z + \tfrac{1}{2} U^2(z)] + \tfrac{1}{2} G_{qq} q^2 + O(q^4), \tag{19}$$

with

$$G_{qq} = \frac{u}{u_{yy}\rho_z^2} = \frac{L^2 U(z)}{f_0 \rho_z^2}\left(1 + \frac{f(y)}{U(z)}\right), \tag{20}$$

and we drop the last term commensurate with our assumptions on $f(y)$. G_{qq} is now a function of z (or ρ) alone. q in our flow is

$$q = (f_0/L)(y/L)(-\rho_z). \tag{21}$$

Since q is small for $|y| << L$, the neglect of higher-order terms in q, wherever they occur, is an excellent approximation.

Now we choose the two independent components of $\delta\vec{u}$ in (12) from the vertical velocity $v_3(\vec{x},t) = \delta\vec{u}\cdot\hat{z}$ and the vorticity $\omega_3(\vec{x},t) = (\nabla\times\delta\vec{u})\cdot\hat{z}$. This choice is motivated by the observation that the only essential dependence on the equilibrium flow is on the vertical coordinate z.[6] To leading order in L^{-1} a calculation shows that $\delta^2 A(\vec{u}_e,\rho_e)$ is given by

$$\delta^2 A(\vec{u}_e,\rho_e) = \int d^3x\,(v_3,\omega_3,\delta\rho)\begin{bmatrix} \nabla^2/\nabla_\perp^2 & 0 & 0 \\ 0 & -\dfrac{1}{\nabla_\perp^2} + \rho_z^2 G_{qq} & \rho_z U_z G_{qq}\partial_y \\ 0 & -\rho_z U_z G_{qq}\partial_y & G_{\rho\rho} - U_z^2 G_{qq}\partial_y^2 \end{bmatrix}\begin{bmatrix} v_3 \\ \omega_3 \\ \rho\delta_\rho \end{bmatrix}. \tag{22}$$

with $\nabla_\perp^2 = \partial_x^2 + \partial_y^2$ and $\nabla^2 = \nabla_\perp^2 + \partial z^2$. Precise meaning to $(\nabla_\perp^2)^{-1}$ is given by imposing periodic boundary conditions in x and y for each of v_3, ω_3, and $\delta\rho$. A term $f_y \partial_z \delta\rho$ has been neglected relative to $U_z \partial_y \delta\rho$, which is retained. This ordering means our choice of L must be large enough to overcome any very large vertical wave numbers in $\delta\rho$. The arbitrary function $\gamma(\rho_e)$ in (11) is set to zero.

For formal stability, we demand that $\delta^2 A$ be of definite sign for all independent variations in $(v_3,\omega_3,\delta\rho)$ space. That sign must be positive, as we see by looking in the direction $(v_3,0,0)$. Then by looking in the direction $(0,\omega_3,\delta\rho)$ we learn that the necessary and sufficient conditions for formal stability are that the two-by-two submatrix operator in (22) have only positive eigenvalues. This requirement is most easily expressed by Fourier transforming in x and y to wave numbers k_1 and k_2. The two-by-two submatrix becomes algebraic, and positivity of its eigenvalues occurs if and only if

$$1/k_\perp^2 + \rho_z^2 G_{qq} > 0, \tag{23}$$

and

$$G_{\rho\rho}[1 + k_\perp^2 \rho_z^2 G_{qq}] + k_2^2 U_z^2 G_{qq} > 0, \tag{24}$$

with $k_\perp^2 = k_1^2 + k_2^2$.

Since we allow arbitrary variations of v_3, ω_3, and $\delta\rho$, each of k_1 and k_2 can be as large as we like. This means that we must have

$$\rho_z^2 G_{qq} = u/u_{yy} > 0, \tag{25}$$

and

$$G_{\rho\rho} > \max_{(k_1,k_2)}\left[\frac{k_2^2 U_z^2 G_{qq}}{1 + k_\perp^2 \rho_z^2 G_{qq}}\right] = 0. \tag{26}$$

The first of these is the usual Rayleigh criterion for stability of shear flows in y. Its presence here is expected since we have no stratification in the horizontal direction. Condition (26) is the desired Richardson-number criterion. Note that

$$G_{\rho\rho} = -g\,\partial z/\partial\rho - \partial^2[\tfrac{1}{2}U^2(z)]/\partial\rho^2. \tag{27}$$

When $(U^2)_{\rho\rho}$ is positive, we may define the generalization of the usual Richardson number to be

$$N_{\mathrm{Ri}}(z) = N(z)^2/\{\rho_z^2 \partial^2[\tfrac{1}{2}U^2(z)]/\partial\rho^2\}, \tag{28}$$

with $N^2(z) = -g\,\partial\rho/\partial z$ the Brünt-Väisäla frequency in Boussinesq approximation. [N_{Ri} defined by (28) agrees locally with the standard gradient definition, if one uses the linearization of U and ρ (e.g., Ref. 3)]. The necessary and sufficient condition for formal stability then becomes

$$N_{\mathrm{Ri}}(z) > 1 \tag{29}$$

everwhere in the flow This is our central result.

In addition, there are situations where ρ_z positive (a statically unstable configuration) may be stabilized by the shear flow. To exhibit this stabilization, we assume $\rho_z \neq 0$ and define the "inverse Richardson number"

$$a(z) = \{\partial^2[\tfrac{1}{2}U^2(z)]/\partial\rho^2\}(-\rho z/g). \tag{30}$$

When $\rho_z < 0$, that is for statically stable stratification, all flows with $a(z) < 1$ are formally stable. When $\rho_z > 0$, that is for *statically unstable stratification*, all flows with $a(z) > 1$ are formally stable. The first case is usually understood by saying that the kinetic energy acquired by a parcel of fluid crossing density surfaces is not sufficient to overcome the potential energy required to move the parcel. The second case is less familiar and is only possible if second derivatives of U are relatively large. In this case, the potential energy that would be gained by a fluid parcel in crossing density surfaces is not sufficient to overcome kinetic energy lost in the same traverse.

The essence of our argument in this note is that the negative of the Bernoulli function (10) acts as a "potential well" for stratified flow. This is seen in (19) where G is, for this heuristic discussion, $-(p+\rho g z+\frac{1}{2}|\vec{u}|^2)$. Our requirement that $G_{\rho\rho} > 0$ tells us that this potential well has positive curvature for crossing density surfaces, when the flow is formally stable This note provides detailed demonstration of this notion, which itself was discussed as long ago as 1931 by Prandtl [7]

One of us (H.D.I.A.) would like to thank J. W Miles and W. H Munk for illuminating discussions on the physical content of this work. This work was supported in part by the U. S Department of Energy under Contracts No. W-7405-ENG-36 and No. AT-3-82ER12097, and by the Office of Basic Energy Sciences, Division of Applied Mathematical Sciences, and by the Office of Naval Research, Code 422PO One of us (T.R.) was a National Science Foundation postdoctoral fellow while at the University of California, Berkeley.

---

[1] V I. Arnol'd, Dokl. Nat. Nauk **162**, 773 (1965), and Am. Math. Soc. Transl. **79**, 267 (1969).

[2] D. D Holm, J. E. Marsden, T Ratiu, and A Weinstein, Phys. Lett **98A**, 15 (1983), and to be published

[3] H D I Abarbanel, D D Holm, J E Marsden, and T Ratiu, "Nonlinear Stability Analysis of Ideal Stratified, Incompressible Fluid Flow" (to be published)

[4] P G. Drazin and W H Reid, *Hydrodynamic Stability* (Cambridge Univ Press, Cambridge, England, 1981). Especially important for us is the work of Miles and Howard reported in Sect 44.

[5] R R. Long, Tellus 5, 42 (1953) See also the monograph by C. S. Yih, *Stratified Flows* (Academic, New York, 1980).

[6] See, for example, the discussion of thermal convection in S. Chandrasekhar, *Hydrodynamic and Hydromagnetic Stability* (Cambridge Univ Press, Cambridge, England, 1961).

[7] L Prandtl, *Führer durch die Strömungslehre* (Vieweg, Braunschweig, 1931), Sec. V, 12(d).

Vertical Directionality of Ambient Noise at 32°N as a Function of Longitude and Wind Speed*

W. S. Hodgkiss and F. H. Fisher

---

*. Reprinted from the Proceedings of the NATO Advanced Study Institute on Underwater Acoustic and Data Processing, pp. 99-104 (Y.T. Chan, Ed., Kluwar Scientific Publishers, 1989).

VERTICAL DIRECTIONALITY OF AMBIENT NOISE AT 32°N AS A FUNCTION OF LONGITUDE AND WIND SPEED

W.S. Hodgkiss and F.H. Fisher

Marine Physical Laboratory
Scripps Institution of Oceanography
San Diego, CA 92152

Abstract

Measurements have been made of the ambient noise field between 25 and 300 Hz with vertical arrays at 32°N (124°W, 136°W, and 150°W) Substantial differences in the vertical distribution of noise have been measured, especially at the higher frequencies which can be interpreted in the context of attenuation by seawater sound absorption of coastal shipping. Due to substantial differences in weather at the stations, these measurements also provide an opportunity to observe the effect of weather on the vertical distribution of ambient noise

1. Introduction

Ambient ocean noise in the low and mid-frequency regions has received a great deal of attention over the last 25 years. Downslope conversion of coastal shipping noise has been discussed as being a major contributor to the low-angle noise distribution in the vertical plane (angles close to the horizontal) [1-4]. If this is so, then sound absorption in seawater should produce changes in the distribution of low-angle noise in the vertical plane as a function of range from coastal shipping.

A decrease in the noise energy per unit angle in the vertical offers improved array performance as a function of distance from coastal shipping. In the Pacific for these latitudes (32°N), the attenuation is about 0.006 dB/km at 300 Hz and decreases to 0.0015 dB/km at 150 Hz. At a range of 1500 nmi (2778 km), the attenuation would be 16 7 dB at 300 Hz and only 4.2 dB at 150 Hz Therefore, if we had data on vertical noise distribution at short and long ranges from coastal shipping, we would expect to see substantial absolute differences at low angles between the 300 Hz data and much less for the 150 Hz data.

We have made such measurements - two at 32°N 124°W (approximately 350 nmi due west of San Diego), and one each at 32°N 136°W (approximately 1000 nmi west) and 32°N 150°W (approximately 1700 nmi west). Due to substantial differences in weather at the stations, these measurements also provide an opportunity to observe the effect of weather on the vertical distribution of ambient noise.

2. Experiment Description and Data Analysis

In October 1985 and again in April/May 1986, ambient noise experiments in the low-frequency and mid-frequency region (50-300 Hz) were conducted by MPL. The October 1985 data were obtained with the 48-element, uniformly spaced ($d = 2.4$ m, half-wavelength at 309 Hz), NORDA VEKA array. The April/May 1986 data were obtained with a 27 element, uniformly spaced ($d = 3.46$ m, half-wavelength at 217 Hz), MPL array. Both arrays were suspended in the vertical from FLIP and centered on the sound axis ($z = 750$ m). FLIP was in a tight, three-point moor at 32°N, 124°W for the October 1985 data and drifting slowly for the April/May 1986 data. Three separate stations at 32°N were established during the course of the April/May 1986 experiment (see Figure 1): (1) 124°W, (2) 136°W, and (3) 150°W. Note that the first station is identical with the location of the October 1985 experiment. Significantly different weather conditions were observed at the three stations during the two experiments.

The NORDA VEKA array data discussed here were taken with a sampling rate $f_s = 907.8$ Hz and the MPL digital array data were taken with a sampling rate of $f_s = 1176$ Hz. The results in the next

Y. T Chan (ed.), Underwater Acoustic Data Processing, 99–104.
© 1989 by Kluwer Academic Publishers.

section were produced with a FFT beamformer. The along-channel FFT's were 50% overlapped and 8192-points in length. A Kaiser-Bessel window ($\alpha = 2.5$) weighted the data prior to each FFT. The cross-channel FFT's were 512-points in length where the (complex) data first was windowed with a 48-point (NORDA VEKA array data) or a 27-point (MPL digital array data) Kaiser-Bessel window ($\alpha = 1.5$) and then zero-padded out to the FFT length. For this value of α, the first sidelobe is -35 dB.

3. Discussion

Analysis of this data indicates a strong relationship between wind speed and the characteristic vertical directionality of the ambient noise The following examples from the analysis are provided in the Figures 2-5 (see [5] for the complete analysis results):

(1) October 1985 (NORDA VEKA 48-element vertical array)
   (a) 32 ° N, 124 ° W (Tape #85010, wind speed 6 kts)
(2) April/May 1986 (MPL 27-element vertical array)
   (a) 32 ° N, 124 ° W (Tape #86060, wind speed 22 kts)
   (b) 32 ° N, 136 ° W (Tape #86247, wind speed 17 kts)
   (c) 32 ° N, 150 ° W (Tape #86180, wind speed 10 kts)

The figures display the time-evolving vertical directionality of ambient noise in a narrow band centered at 200 Hz (positive angles refer to downward looking beams). The plots have been calibrated to report ambient noise power spectral density per Hz per degree of vertical angle (dB re 1 μPa/$\sqrt{\text{HzDeg}}$)

A number of observations can be made by comparing the waterfall plots from the three stations Under calm weather conditions (Tapes #85010 and #86180), the vertical distribution of ambient noise clearly is concentrated within approximately ±15 ° of the horizontal Under poor weather conditions (Tape #86060), high wind speed has the effect of filling in the higher vertical angles while leaving the level within the low-angular region unchanged. Under intermediate weather conditions (Tape #86247), a transition between these two characteristics occurs which is frequency dependent (in the case of Tape #86247, the transition occurs in the the 125-150 Hz region). This frequency-dependent transition characteristic is consistent with single hydrophone measurements reported in the literature (e g see 6 where ambient noise levels above 100 Hz were very sensitive to wind speed while ambient noise levels below 100 Hz showed no wind speed dependence at all)

From 75 to 300 Hz, the change in the vertical distribution of noise with increasing range from coastal shipping (especially at higher frequencies) was in a manner consistent with the effect of chemical absorption on low-angle noise due to coastal shipping (see [5]) Whereas a shipping noise pedestal at low angles is observed at all frequencies at short range, at long range the absorption effect makes the vertical distribution of ambient noise more isotropic at higher frequencies than at low frequencies.

4. Summary

Downslope conversion of coastal shipping noise has been discussed as being a major contributor to the low-angle noise distribution in the vertical plane (angles close to the horizontal). The results reported here on the vertical directionality of ambient noise as a function of longitude are consistent with this hypothesis. Sound absorption in seawater appears to diminish the low-angle energy as a function of distance from the coast with the effect being more pronounced at higher frequencies than at lower frequencies.

Due to substantial differences in weather at the stations, these measurements also provided an opportunity to observe the effect of weather on the vertical distribution of ambient noise. Under calm weather conditions, the vertical distribution of ambient noise clearly is concentrated within approximately ±15 ° of the horizontal Under poor weather conditions, high wind speed has the effect c filling in the higher vertical angles while leaving the level within the low-angular region unchanged Under intermediate weather conditions, a frequency-dependent transition between these two characteristics occurs which is consistent with single hydrophone measurements of wind speed dependence

Acknowledgements

This work was supported by the Office of Naval Research under contract N00014-84-K-0097 and the Naval Air Systems Command and the Office of Naval Research under contract N00014-87-C-0127 Additional analysis of the data has been supported by the Office of Naval Research, Code 1125GA, under contract N00014-87-K-0010

References

1 R A Wagstaff, "Low-frequency ambient noise in the deep sound channel - The missing component," J Acoust Soc Am 69(4): 1009-1011 (1981)

2 W M Carey and R A Wagstaff, "Low-frequency noise fields," J Acoust Soc Am 80(5) 1523-1526 (1986)

3 W M Carey, "Measurement of down-slope sound propagation from a shallow source to a deep ocean receiver," J Acoust Soc Am 79(1) 49-59 (1986)

4 W M Carey I B Gereben and B A Brunson, "Measurement of sound propagation downslope to a bottom-limited sound channel" J Acoust Soc Am 81(2) 244-257 (1987)

5 W S Hodgkiss and F H Fisher "Vertical Directionality of Ambient Noise at 32°N as a Function of Longitude" TM-387, Marine Physical Laboratory, Scripps Institution of Oceanography (1987)

6 G B Morris, "Depth dependence of ambient noise in the northeast Pacific Ocean," J Acoust Soc. Am. 64 581-590 (1978)

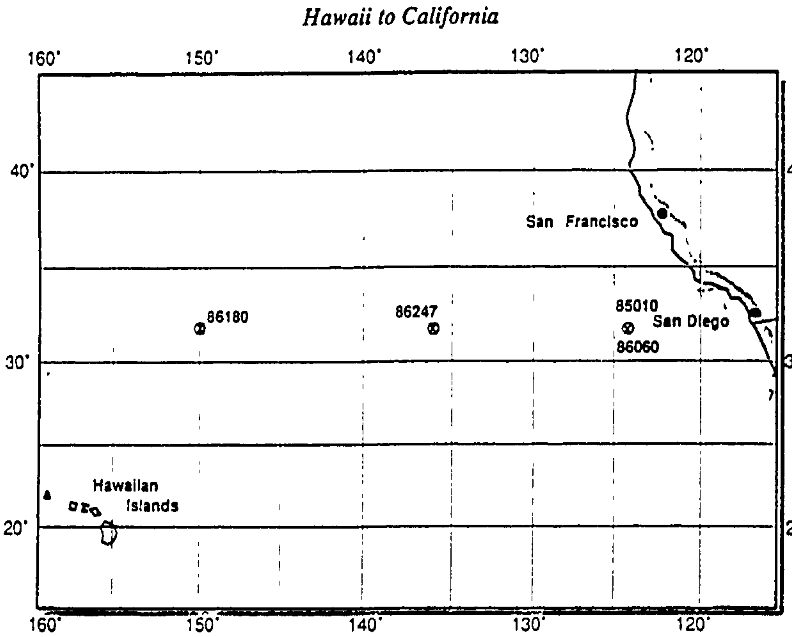

Figure 1. FLIP Stations for October 1985 and April/May 1986 Experiments.

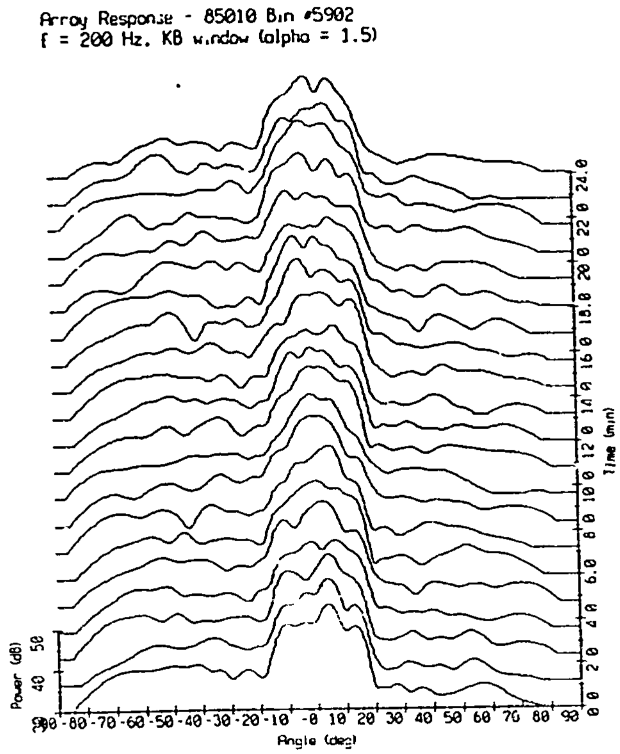

Figure 2. Ambient Noise Vertical Directionality: Tape #85010. 32°N 124°W. Wind speed 6 kts. 18 October 1985, 20:05 PDT.

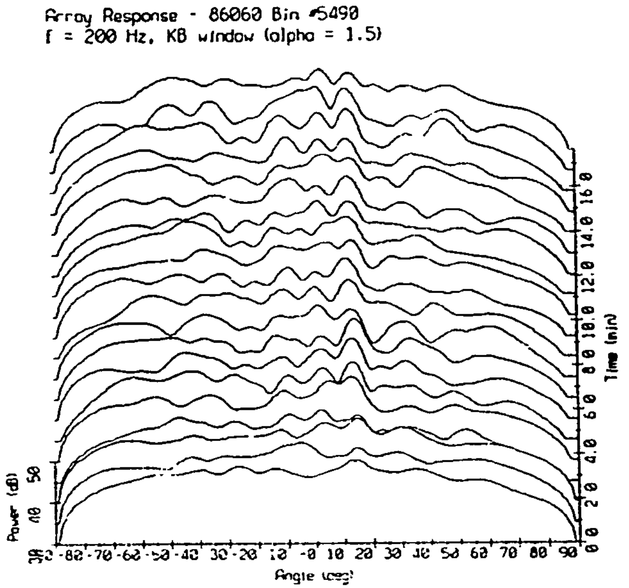

Figure 3. Ambient Noise Vertical Directionality· Tape #86060 32°N 124°W. Wind speed 22 kts 27 April 1986, 06:34 PDT.

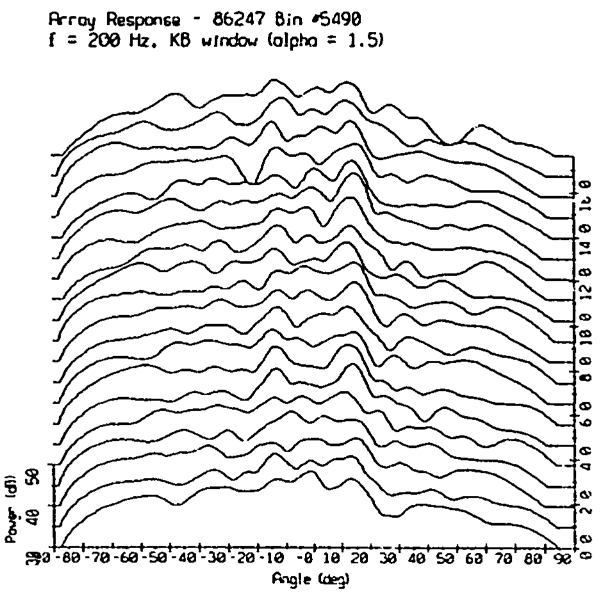

Figure 4. Ambient Noise Vertical Directionality. Tape #86247 32°N 136°W. Wind speed 17 kts 9 May 1986, 13:38 PDT.

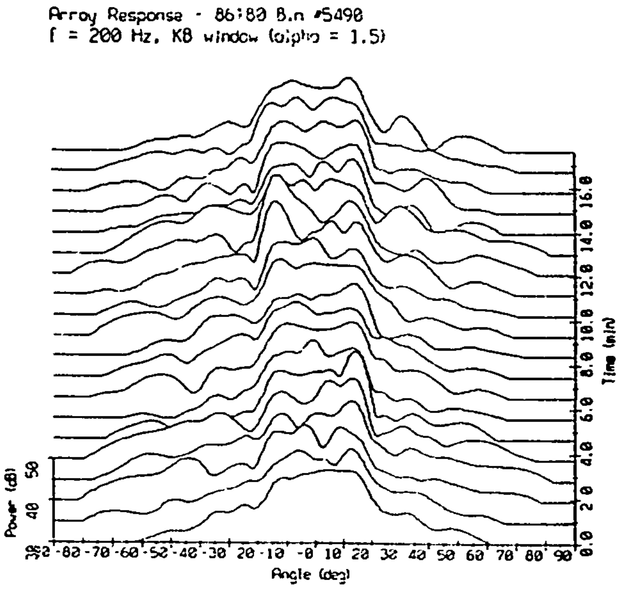

Figure 5. Ambient Noise Vertical Directionality: Tape #86180. 32°N 100°W. Wind speed 10 kts 5 May 1986, 10.09 PDT.

Coherence Lengths of Seafloor Noise:

Effect of Ocean Bottom Structure*

Anthony E. Schreiner and LeRoy M. Dorman

---

*. Reprinted from the Journal of the Acoustical Society of America, Vol. 88(3), pp. 1503-1514 (1990).

Coherence lengths of seafloor noise: Effect of ocean bottom structure

Anthony E. Schreiner and LeRoy M. Dorman
University of California, San Diego and Scripps Institution of Oceanography, Marine Physical Laboratory and Geological Research Division, La Jolla, California 92093-0215

(Received 11 July 1989; accepted for publication 3 May 1990)

Results are reported from an experiment, conducted in 1987, in which an ocean bottom seismograph array of 150-m aperture and minimally redundant design was used to record the ambient noise in deep water off the California coast. The minimum interelement spacing among the nine instruments was 8 m. The coherence lengths observed imply that the noise field in the 0.05- to 5-Hz band are fundamental and higher-mode Rayleigh/Stoneley/Scholte waves and the relative amplitudes of the modes imply that the excitation occurs within 20 km of the array. These observations imply that the noise energy is scattered into the seafloor waveguide at the boundaries of the sediment pond in which the array was sited. The implications for sub-bottom sensors are discussed.

PACS numbers: 43.30.Nb, 43.30.Ma

INTRODUCTION

Observations of ambient noise on the seafloor are being increasingly made at lower frequencies. Below 5 Hz, the oceanic microseism becomes the dominant source of noise. It is widely accepted that the microseism energy is the result of a highly efficient nonlinear interaction between ocean surface wave trains. However, the way in which this energy couples into ground motion is less well understood, due to a shortage of appropriate ocean floor measurements.

On land, important advances in the study of low-frequency ambient noise were made with the advent of large-scale seismometer arrays.[1,2] Sensor arrays enable the decomposition of the observed wave field into spatial frequencies, facilitating the identification of the mode of propagation. Until recently, there have not been any similar arrays of seismometers placed in the ocean. Ocean floor noise measurements have largely consisted of small numbers of instruments[3,4]

In April and May of 1987, an array of ocean bottom seismometers (OBS) was placed in a deep oceanic basin in a cooperative effort between the Scripps Institution of Oceanography (SIO) and the Naval Ocean Research and Development Activity (NORDA) [now the Naval Oceanic and Atmospheric Research Laboratory (NOARL)]. The purpose of this deployment was to measure the spatial characteristics of ambient noise on the ocean floor at small length scales.

This paper will be concerned primarily with the spatial coherence measurements made by the array. Wave-number spectra are another, very interesting observable from array data; but they are more sensitive to errors in sensor location and timing, and therefore will be discussed in a separate paper.

We conclude from the observed spatial coherence that Stoneley waves are an important component of ambient noise on the deep seafloor between 0.8 and 5 Hz. The depth of the ocean at this site is too great for direct excitation of these slowly propagating waves by the ocean surface wave field. Their presence requires that the ambient acoustic noise field be scattered at the ocean floor or within the sedimentary layer.

I. EXPERIMENT DETAILS

The OBS array, code named "CIRCUS," was deployed in the deep ocean, off the Patton Escarpment, which is the edge of the continental borderland off southern California (Fig. 1). The site was near DSDP hole 469 at a water depth of 3800 m. Reflection profiles and drill logs from this hole show sediments composed largely of clays and calcareous oozes, with compressional wave velocities ranging from 1500 to 1600 m s^{-1} (see Ref. 5).

This area was also the site of another seismic experiment where explosives were detonated on the ocean floor to gener-

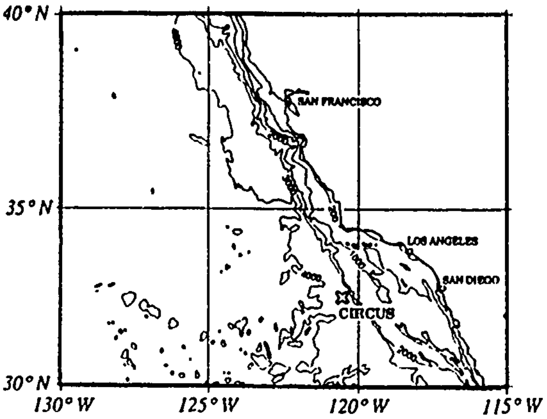

FIG 1 Location map for the CIRCUS array deployment. The site is at full ocean depth just to the west of the California borderland.

ate Stoneley/Scholte waves on the water–sediment boundary.[6] The energy of the interface waves was mostly confined to the range 1–5 Hz and the attenuation was very strong (Fig. 2). The dispersed wave from a 5-lb explosion became undetectable beyond a distance of 1.2 km. Dispersion analysis of the interface waves yielded shear wave velocities between 40 and 100 $\mathrm{m\,s^{-1}}$ in the upper 40 m below the ocean floor. The wavelength of the Stoneley waves was determined to be on the order of 100 m. Results from this experiment have a bearing on the array measurements in two ways. The CIRCUS array was an effort to observe naturally occurring Stoneley waves and therefore had to be designed with a very fine spatial sampling to avoid aliasing the measurements. Additionally, it will be shown that the phase velocity dispersion of the medium, as measured from the controlled sources, has a strong effect on the spatial coherence field.

A minimum redundancy array design[7] was used for the array to simultaneously maximize the array aperture while maintaining the necessary fine element spacing. The design is shown in Fig. 3, along with the actual sensor positions achieved by the deployment. The emplacement of a 100-m aperture array at a depth of nearly 4 km represented a significant technical challenge. The Deep-Tow system of acoustic transponder networks and wire-supported vehicles[8,9] made this task possible. The basic elements of the system are

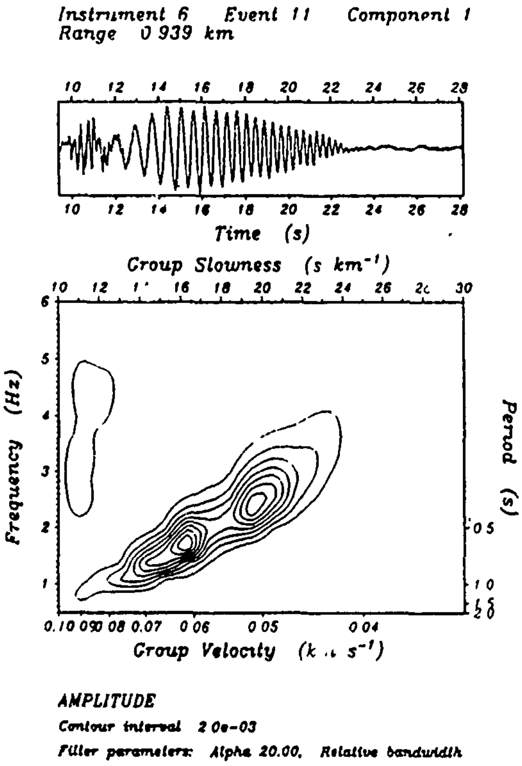

FIG 2 Dispersed wave train from an ocean bottom shot and multiple window dispersion analysis.

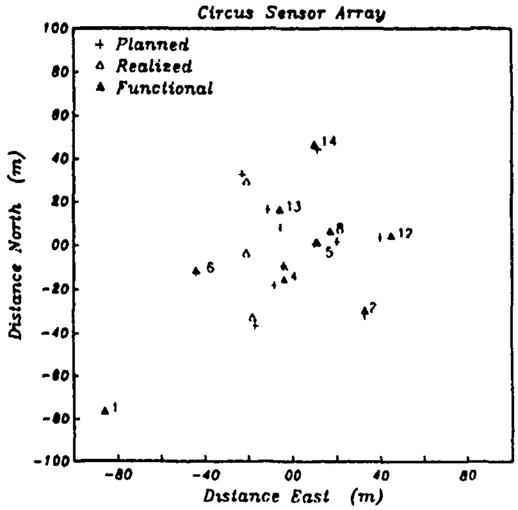

FIG. 3. Minimum redundancy design for the OBS array and realized sensor positions

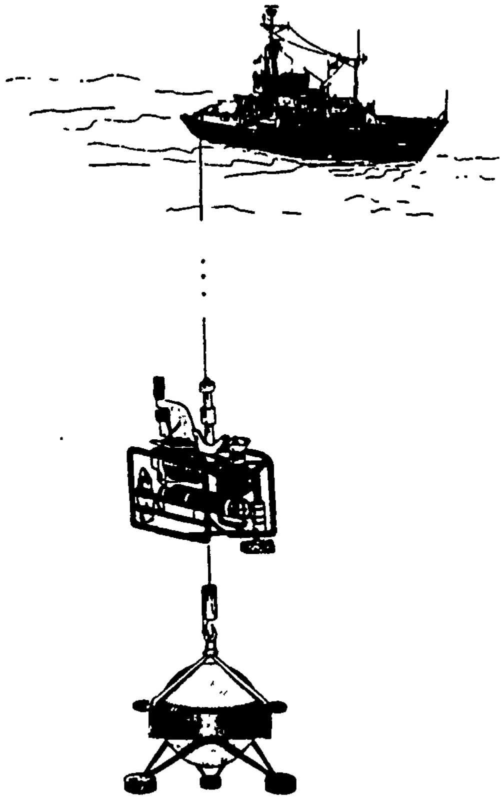

FIG 4 Essential components of the OBS deployment The OBS package hangs beneath the Thruster unit. The Thruster is connected by wire to the ship on the surface but has limited maneuverability of its own The position of the Thruster is monitored by exchanging acoustic pings with a net of transponders fixed to the ocean bottom.

shown in Fig. 4. Details of the deployment will be described in a later paper.

The OBSs were emplaced within 5 m of their target positions with two exceptions. In one case, the sensor packages was of a different configuration and did not fit on the tow vehicle's release hook. In the other case, an impending explosive shooting schedule would not permit the vehicle's 6-h round trip to the bottom. Both times, it was necessary to deploy the instruments in the conventional manner of releasing them at the ocean surface and letting them free-fall through the water. One of these OBSs is the one that is offset by 80 m from the array center (Fig. 3). Though unplanned, this large separation turned out to be of benefit to the interpretations.

The twelve SIO and NORDA seismographs were of the same design with only minor differences. The model has been in use at Scripps for nearly a decade.[10] The sensors are a triaxial configuration of seismometers and a pressure sensor. The seismometers are Mark Products model L-4C with a resonant frequency of 1 Hz. Two different types of pressure transducers were used: an Ocean and Atmospheric Systems model E-2DP crystal hydrophone, and a differential pressure sensor of a design by Cox *et al.*[11] In this paper we report only on data from the vertical seismometers.

The sensor output is fed through a variable gain preamp with a 54-dB range. The amplification level is determined independently for each channel by a long-term average of the ambient noise. The site was remarkably quiet, and the gain was usually at its maximum setting. The signal is further conditioned by a prewhitening filter and anti-aliasing filters with a cutoff frequency of 30 Hz. Figure 5 shows the transfer function for the seismometer channels.

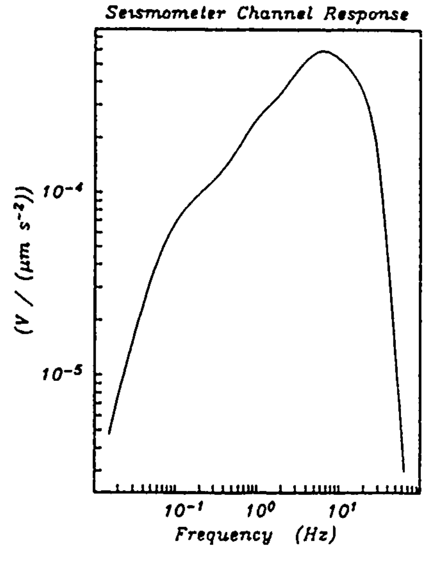

FIG. 5. Transfer function for the seismometer channel, including seismometer and filters.

A 12-bit digitizer operating at 128 samples per second converts the signal to digital form. The digitized data are stored in a 128-kbyte buffer and written to tape after the end of the recording window so that the mechanical movement of the tape does not affect the signal. The buffer memory has a capacity of 227 s of four-channel data at a rate of 128 Hz. The OBSs have since been extensively modified to reflect newer technology, with a new microprocessor and a large increase in recording capacity.

Nine of the thirteen instruments deployed returned usable data. In Fig. 3, these are marked by the filled triangles. Of the capsules that did not return data, one failed to resurface, two suffered malfunctions of an experimental data recorder, and one was not diagnosed.

II. SPECTRAL ANALYSIS

Spectral estimates were computed using the multiple prolate spheroidal taper method.[12] In this technique, the data are "windowed" by the N lowest-order prolate spheroidal wave functions, where N is dependent on the desired time–bandwidth product, and the spectrum (or cross-spectrum) estimator is a weighted average of the transforms of the windowed data. The frequency-dependent weights are adjusted to minimize a combination of variance and spectral leakage. The multiple taper method provides excellent protection against spectral leakage from adjacent frequency bands. An added benefit is that error estimates can be computed for the spectra, coherence, and phase. Since the spectral estimate is computed from a set of windowed transforms, it is possible to form a "jackknife" estimate of the variance by using all possible combinations of the windowed transforms.[13] A time–bandwidth product of 4 was used to compute the tapers, resulting in up to 16 degrees of freedom for the estimate. Generally 32- or 64-s segments of data were analyzed with an inherent resolution of 0.5 and 0.25 Hz, respectively.

Figure 6 shows an acceleration spectrum computed from a typical recording window. A noise spectrum from a quiet continental site is shown for comparison. The usual features of ambient noise spectra at infrasonic frequencies are evident. The microseism peak is the power maximum at 0.16 to 0.2 Hz. This feature has been studied extensively for many years and is due to acoustic energy created at the ocean surface by a nonlinear interaction of ocean swell sets and which propagates with little attenuation to the bottom to excite Rayleigh waves in the oceanic crust. The so-called "noise notch" is a quiet band at frequencies below the microseism and extending down to 0.02 Hz.[14–16] This represents a frequency regime between the ocean swell and very long period gravity waves. OBS system noise begins to dominate our results below 0.06 Hz. There is commonly a subsidiary peak near 1 Hz. The slope of the spectrum differs above and below the peak. The frequency of this peak varies markedly with time and appears to be controlled by wind state. At 5 Hz the slope of the spectrum changes drastically. Power above this frequency is affected by surface wind and ship traffic. At the quietest times, OBS system noise again becomes dominant.

Figure 7 is a measurement of mean squared coherence

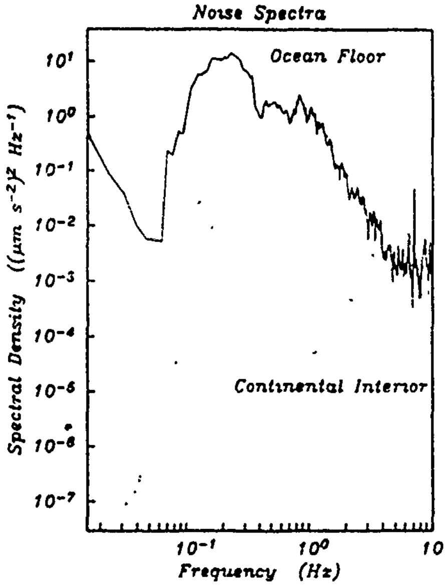

FIG. 6. Noise spectra from an OBS during CIRCUS (solid) and from a quiet continental site (dashed) at Queen Creek.[11,12]

between the vertical seismic components of a pair of instruments separated by 123 m. The heavy line is the estimate and the light lines are 95% confidence intervals on the estimate. Where the lower limit is positive, the coherence is reliably nonzero.

With a variety of offsets between sensors it is possible to make direct observations of the spatial coherence. The nine instruments give 36 different sensor separations. All the separations greater than 80 m are relative to OBS 1, which was separated from the rest of the array. The mean-squared coherence as a function of frequency and separation is shown in Fig. 8 for a particular window. The full two-dimensional coverage is created by a spline interpolation of the 36 sets of intersensor coherence estimates. The plot is typical of the observations at this site. There are two bands of high coherence, below 0.4 Hz and between 0.8 and 3 Hz. Between those two bands there is a notch of lower coherence that widens with increasing separation. This pattern is characteristic of the observations for the duration of the experiment. The depth of the notch may vary to some degree, but the notch edge frequencies did not vary.

III. COHERENCE MODEL

We explain the observed spatial coherence by the mode of propagation of noise energy in this environment. The coherence model will be developed from a combination of a distributed source function and the decomposition of horizontally propagating energy into seismic modes.

The ambient seismic noise field derives its characteristics from three processes: the source of energy, the coupling of energy into the seismic medium, and the propagation of energy in the elastic medium. The first is explained satisfactorily by the theory of Longuet-Higgins[17] and Hasselmann.[18] Under certain conditions, ocean surface swell can generate pressure fluctuations that reach the ocean floor unattenuated. For the second process, pressure fluctuations can couple into seismic wave propagation in the ocean floor when their wave number is equal to that of the resonant modes in the elastic medium. The wave number of the pressure fluctuations, because they propagate through the water, is limited to the range $|\mathbf{k}|<\omega/\alpha$, where α is the acoustic velocity of water. However, high wave-number (low-velocity) seismic waves are observed on the ocean floor, and their excitation requires a different interaction that is not well understood. The last process, the propagation of energy in the elastic medium, will be the focus of this section. The observed spatial coherence puts strong constraints on the nature of the seismic propagation between the coupling region and the receivers.

Motion of the ocean floor is forced by the pressure field induced by ocean surface waves in a limited region directly above. Seismic waves radiate out from each point on the ocean floor in all directions. On a purely flat bottom, the efficiency in which this motion is converted into propagating seismic waves depends on whether the wave number of the incident pressure field matches the wave number of a seismic mode in the ocean floor. However, because of topographic and subsurface effects, the efficiency of conversion may vary from point to point. The seismic field at any given point is therefore considered to be a harmonic wave field with energy that is a function of azimuth.

The spatial coherence can be determined from the directivity function.[19,20] This is accomplished by integrating the harmonic wave field over azimuth

$$K(f,r)=\left(\int_0^{2\pi}A(f,\theta)e^{ik(f)r\cos(\theta-\theta_r)}\,d\theta\right)\times\left(\int_0^{2\pi}A(f,\theta)\,d\theta\right)^{-1}, \tag{1}$$

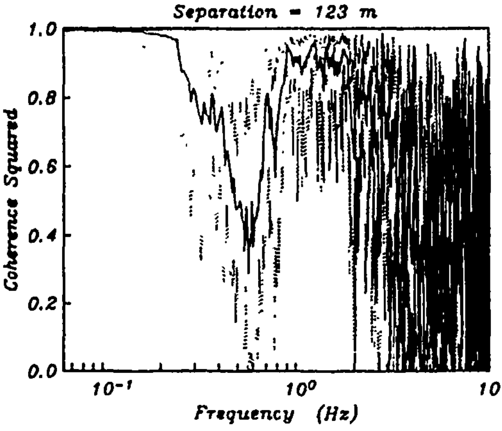

FIG. 7. Coherence between the vertical sensors for OBS 1 and OBS 13, separated by 123 m. The upper and lower traces are the 95% confidence limits.

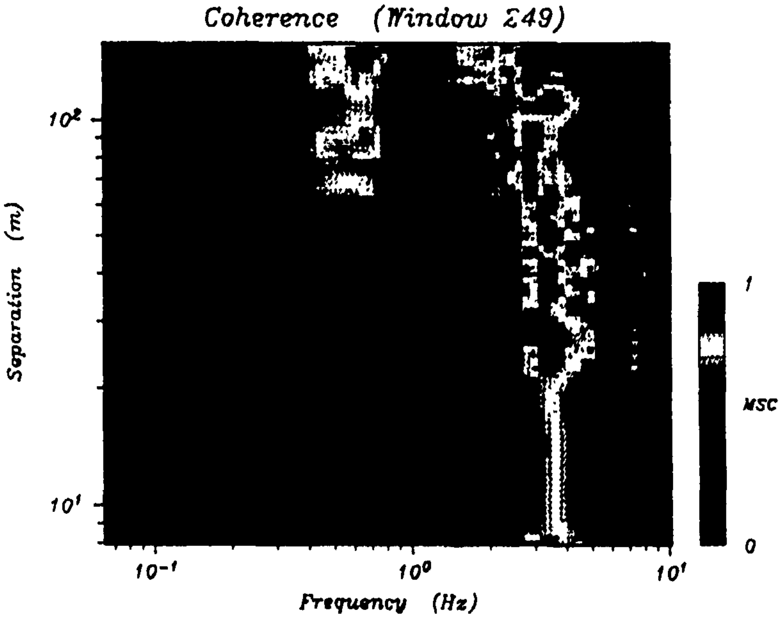

FIG 8 Coherence between the vertical seismometers for all active sensors for recording window 229 The ranges are discrete and the data were regridded

where $A(\theta)$ is the azimuthally dependent incident field strength. For an isotropic distribution, the directional spectrum is $A(\theta) = 1$, and the result

$$K(f,r) = J_0[k(f)r]. \tag{2}$$

where J_0 is the zero-order Bessel function, can easily be derived.

Measurements of the ocean surface wave directional spectrum have shown that the function $A(\theta) = \cos^{\mu}[\frac{1}{2}(\theta - \theta_0)]$ is an adequate model a for wave directivity.[21] In this representation, $\mu = 0$ corresponds to an isotropic distribution of energy, and $\mu = \infty$ corresponds to a plane wave propagating in the $\theta = \theta_0$ direction. The parameter μ may, in general, vary with frequency.

Webb[20] derived a general expression for the coherence between a sensor at the origin and a sensor at the point (r,θ) as a function of the beam parameter μ:

$$K(f,r,\mu) = \sum_{n=0}^{\infty} C_n i^n J_n[k(f)r] \cos[n(\theta - \theta_0)], \tag{3}$$

where

$$C_n = 2\left\{\Gamma\left(\frac{\mu}{2}+1\right)^2 \times\left[\Gamma\left(\frac{\mu}{2}+n+1\right)\Gamma\left(\frac{\mu}{2}-n+1\right)\right]^{-1}\right\},$$

where $\Gamma(s)$ is the gamma function. For even integer values of μ, the series truncates at $n = \mu/2$. Figure 9 shows squared spatial coherence for a variety of beam parameters. The features to note are: first, that as μ (the narrowness of the beam) increases, the spatial coherence length increases; and second, that the spatial coherence depends on the wavelength by way of the wave number in the argument of the Bessel function.

Since the coherence length depends on the wavelength of the propagating energy, we will incorporate realistic frequency-dependent wavelengths derived from synthetic dispersion curves. The dispersion was computed from a materi-

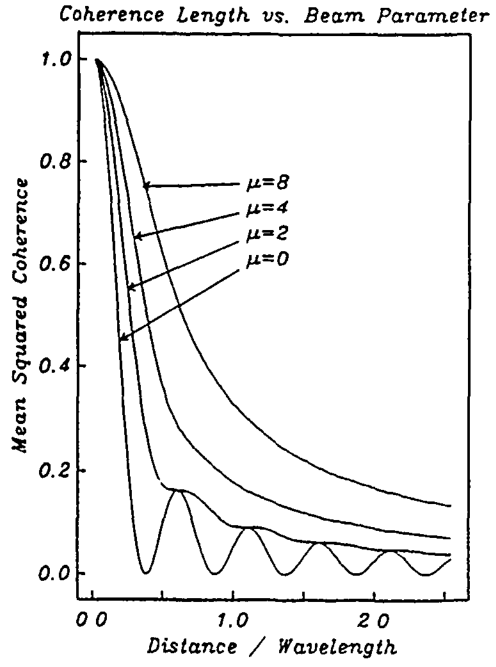

FIG. 9. Theoretical coherence as a function of distance for four different beam parameters.

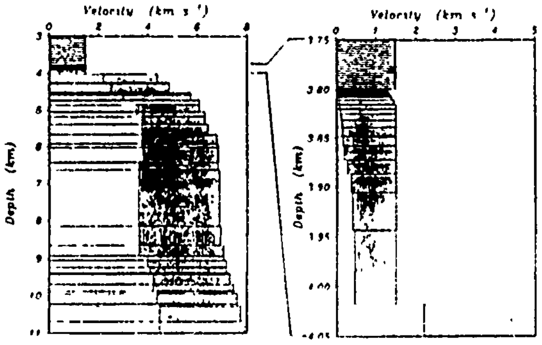

FIG 10 Velocity model derived from matching computed modes to observed dispersion of the ocean bottom shot data.

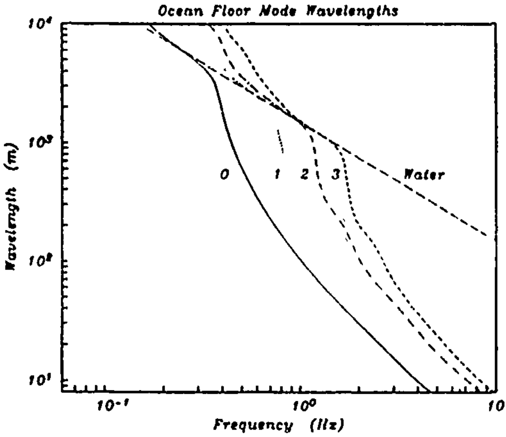

FIG 12 Wavelengths determined from the phase velocity dispersion function.

al property model inferred from past surveys. The model of Sauter *et al.*[6] achieved a good fit to the observed Stoneley waves in the frequency range of 0.5 to 3 Hz. We are interested in modeling the coherence to even lower frequencies, and since Sauter *et al.*'s[6] model only extended to a sub-bottom depth of 50 m, we have supplemented it with a crustal model from Spudich and Orcutt[22] (Fig. 10), which was inferred from seismic refraction observations in the Pacific Ocean off the coast of Mexico.

Dispersion curves were calculated using a normal mode formalism[23] as implemented by Gomberg and Masters.[24] This method is based on the Thompson–Haskell matrix but avoids much of the numerical instability that plagued earlier versions.

The phase velocity dispersion curves for the first four modes are shown in Fig. 11. For mode 0, the phase velocity undergoes a drastic change at 0.5 Hz as it makes the transition from the Rayleigh wave regime to the Stoneley wave regime. At the ocean floor, the Stoneley (or Scholte) waves are a continuation of Rayleigh waves to velocities lower than the acoustic velocity in water, 1.5 km s^{-1} (c.f.Tolstoy[25]). When the phase velocity is less than the propagation velocity in one of the adjacent layers, the wave becomes evanescent in that layer and becomes bound to the interface, in this case the ocean floor.

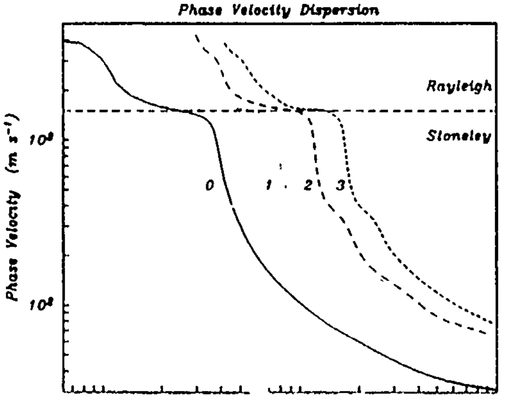

FIG 11 Dispersion curves computed from velocity model in Fig. 10. The velocity 1.5 km s^{-1} represents the compressional slowness of water. Propagation at lower velocity is evanescent into the water column and represents Stoneley waves.

To use these values in the coherence model, the phase velocities are converted to wavelength through $\lambda(f) = c(f)/f$. Wavelengths are shown for the first four modes in Fig. 12. The line labeled "water" corresponds to a wave propagating horizontally in the water. The $1/f$ dependence of the water wavelength shows up as a straight line on the log–log plot.

Spatial coherence is calculated from the wavelength with Eq. 3. Wavelength was shown up to 10 km in Fig. 12, but the CIRCUS observations of coherence were limited to a distance of 156 m; all subsequent figures will have an upper limit of 156 m. Figure 13 shows the spatial coherence calculation from mode 0 only and an isotropic energy distribution ($\mu = 0$).

Comparison of the model in Fig. 13 with the observations in Fig. 8 shows that the cutoff of the low-frequency, high-coherence band at 0.3 Hz is accounted for by mode 0. However, in the data, the coherence length increases again at 0.8 Hz. Higher modes have longer wavelengths and therefore longer coherence length, so the data suggest that higher-mode Stoneley waves predominate between 0.8 and 4 Hz. The present model can be generalized to account for this possibility.

For any given mode at a particular frequency, the coherence between two sensors will depend on the coherence length of the mode. If more than one mode is present, they will have different coherence lengths, and will make different contributions to the measured coherence. The squared coherence for a signal consisting of modes 0 through N can be shown through some straightforward but tedious algebra, and under some assumptions, to be

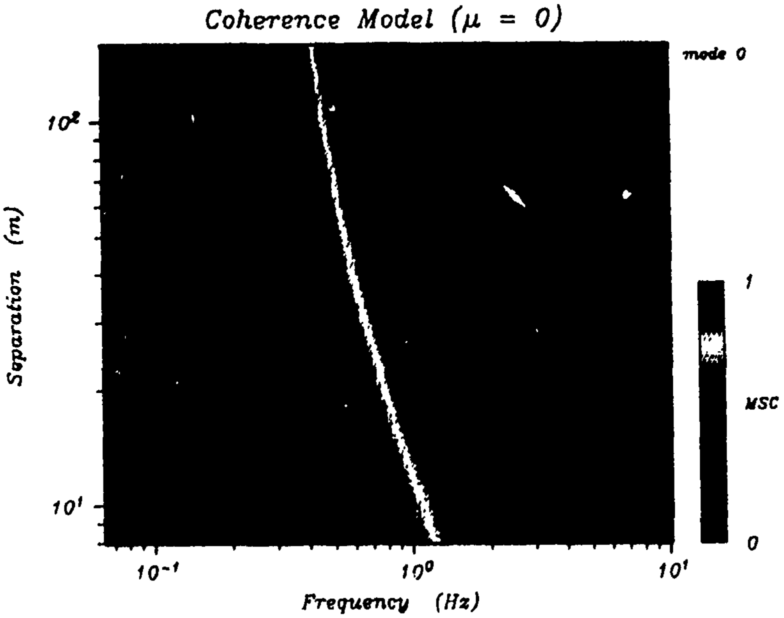

FIG. 15 Theoretical coherence for mode 0 derived from the computed wavelengths and an isotropic source distribution (beam parameter of 0)

$$K^2(f,r) = \sum_{i=0}^{N} \frac{S_i^2(f)}{S^2(f)} K_i^2(f,r) + 2 \sum_{i=0}^{N} \sum_{j=0}^{i-1} \frac{S_i(f) S_j(f)}{S^2(f)} \times \mathrm{Re}[K_i(f,r) K_j(f,r)], \quad (4)$$

where $K_i(f,r)$ and $S_i(f)$ are the coherence and power for the ith mode, and $K(f,r)$ and $S(f)$ are the coherence and power for the combined signal. The critical assumptions are: (1) that there is no coherence between the separate modes at the receiver, and (2) that the signal power is approximately equal at each receiver. The first assumption is justified by the fact that the different modes have large differences in phase velocity, and the noise source has a limited coherence time. The second assumption is acceptable when the distance between the sensors is much smaller than the distance to the source. The cross-power terms in Eq. (4) are limited by $2/N^2$ and are thus relatively small.

Mode spectra [Fig. 14(a)] can be computed at the same time that the dispersion curves are determined. The proportional power of each mode among the first four is shown in Fig. 14(b). The power in the higher modes becomes greater than the power in the fundamental mode at about 0.7 Hz. The frequency at which this occurs controls the location of the low-frequency edge of the intermediate frequency, high-coherence band. A coherence model using an isotropic noise energy distribution ($\mu = 0$) and these weights is shown in Fig. 15. A second calculation with the same weights and a beam parameter of $\mu = 4$ generated Figure 16. Comparison of these models with the observations (Fig. 8) reveals a good match to the gross behavior of the spatial coherence. The model explains the band of high coherence between 0.8 and 5 Hz, and the low-coherence notch between 0.4 and 0.8 Hz. The narrower beam model (Fig. 16) predicts to depth of the

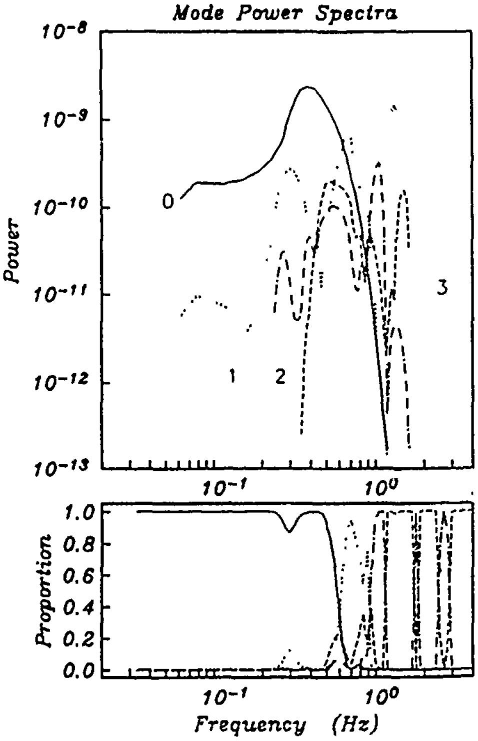

FIG. 14 (a) Power spectra for the first four modes, computed for a source distance of 20 km and a depth of 1 m below the ocean bottom (b) The proportion of variance in each mode to the total variance

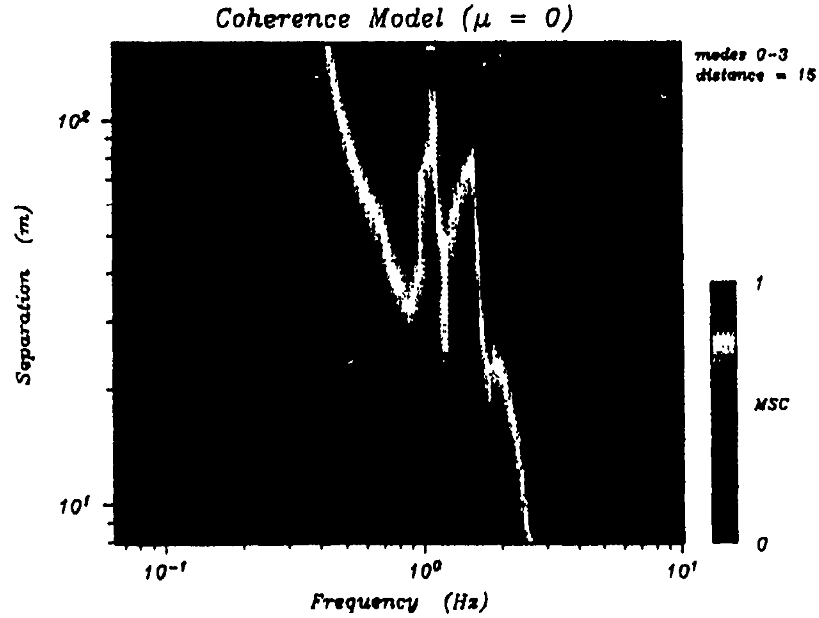

FIG 15 Coherence model using the mode variance partitioning of Fig. 14 and a beam parameter of 0

low-coherence notch more accurately. The coherence between sensors has a dependence on the angle of the separation relative to the azimuth of the main beam direction (for beam parameters greater than zero). The calculation in Fig. 16 assumes that the array is aligned along the beam direction. Inclusion of the angular dependence makes the model more ragged, increasing the similarity with the data in a qualitative way, but not bump for bump.

A plot of the mode Q (Fig. 17) helps to explain the energy partitioning. Mode Q is computed by a inner product integral over depth of the wave energy function and the material Q:

$$Q_R^{-1} = A \int_0^{z_{\max}} E_1(\lambda + 2\mu) Q_p^{-1} + E_2 \mu Q_s^{-1} dz, \qquad (5)$$

were Q_R is the Rayleigh mode Q, A is a normalizing factor,

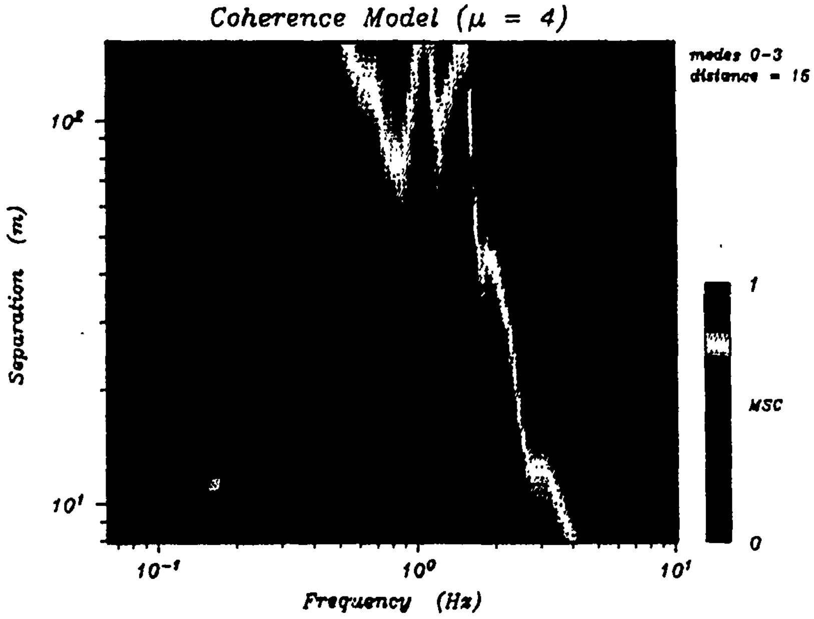

FIG. 16. Coherence model as in Fig 15 but with a beam parameter of 4

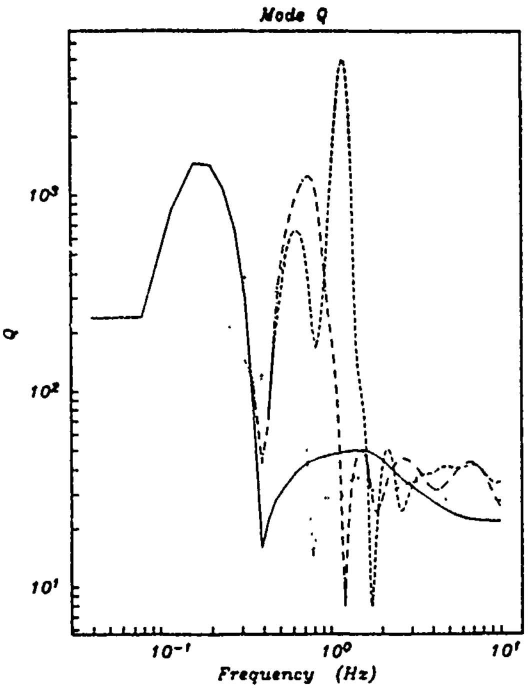

FIG. 17 Rayleigh mode Q computed for a source distance of 20 km.

and E_1 and E_2 are energy functions for compressional and shear waves, respectively, and Q_p and Q_s are material compressional and shear Q. This quantity is a spatial Q and therefore depends implicitly on the phase and group velocity of the mode (cf. Aki and Richards[26]). Very low values of Q occur at frequencies where the ratio of group velocity to phase velocity is lowest, because at those frequencies, the energy takes a long time to propagate to the receiver. The highest values of Q occur when the phase velocity is near 1.5 km s^{-1}; most of the mode energy is in the water column, which has a comparatively very high Q. The effective Q of the mode can thus be higher or lower than the material Q in any of the layers of the ocean floor.

The shape of the power spectra depends in a complicated way on the depth of the source and the source–receiver distance. The example in Fig. 14 was computed for a source depth of 1 m below the ocean floor and a distance of 15 km. The depth and distance are free parameters and they were chosen to make the closest fit between observation and model. The eigenfunction for the fundamental mode has its highest amplitude near the ocean floor. Mode 0 is thus excited strongly by a source near the ocean bottom interface, but since the Q of the uppermost sediments is low, it is more strongly attenuated with distance than are the higher modes. For a deeper source, the fundamental mode is not excited as strongly, so the power spectrum has less dependence on the distance. This is summarized by four examples in Fig 18. The frequency at which the higher modes exceed the fundamental mode is plotted as a function of distance and depth in

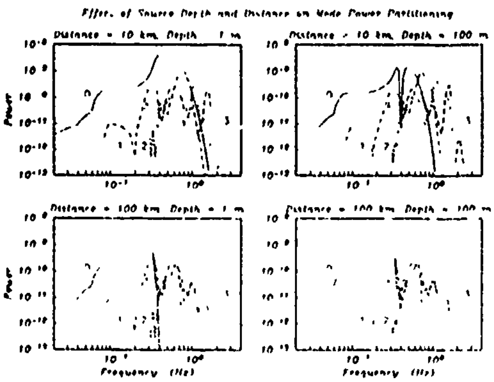

FIG. 18 Mode power spectra computed for a source at (a) 10-km distance and 1 m below the ocean floor, (b) 100-km distance and 1 m below the ocean floor, (c) 10-km distance and 100 m below the ocean floor, and (d) 100-km distance and 100 m below the ocean floor. The vertical dashed line marks the frequency where one of the higher modes becomes stronger than the fundamental.

Fig. 19. The source moment tensor can also affect the excitation of the modes. However, there was insufficient data to determine a realistic source moment tensor, so a diagonal tensor has been used in these calculations.

A physical interpretation can be associated with the 15-

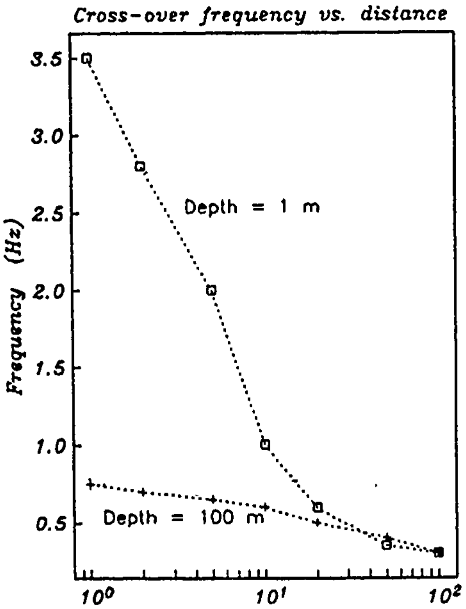

FIG. 19 Summary of the frequency at which the higher modes become dominant plotted as a function of source distance for source depth at 1 and 100 m. The hachure indicates the range of parameter values consistent with the data.

km distance value derived from the coherence model. Figure 20 shows a fine scale bathymetric map of the immediate vicinity of the experiment, with a 20-km scale showing the approximate source distance. Significant topographic features are located roughly at this distance, in particular the Patton escarpment to the east, and a seamount to the northwest. The improved fit of the model coherence for $\mu = 4$ over $\mu = 0$ is evidence that the incident noise field strength is asymmetric. This is reasonable in light of the fact that most of the departures from a flat ocean bottom occur on the northeast side of the array. It is likely that inhomogeneities in the ocean bottom boundary can scatter incident waves into the surficial layer. Levander and Hill[27] showed by numerical modeling how high-wave-number signals generated at depth (or analogously at the water surface) can be coupled into low-wave-number signals in the low velocity layer by scattering at the boundary. Dougherty and Stephen[28] demonstrated how volume heterogeneity could convert incident body waves into surface waves. While we cannot make a definitive distinction between these two possibilities, the reflection profiling data available to us most closely resemble the assumptions made by Levander and Hill.[27]

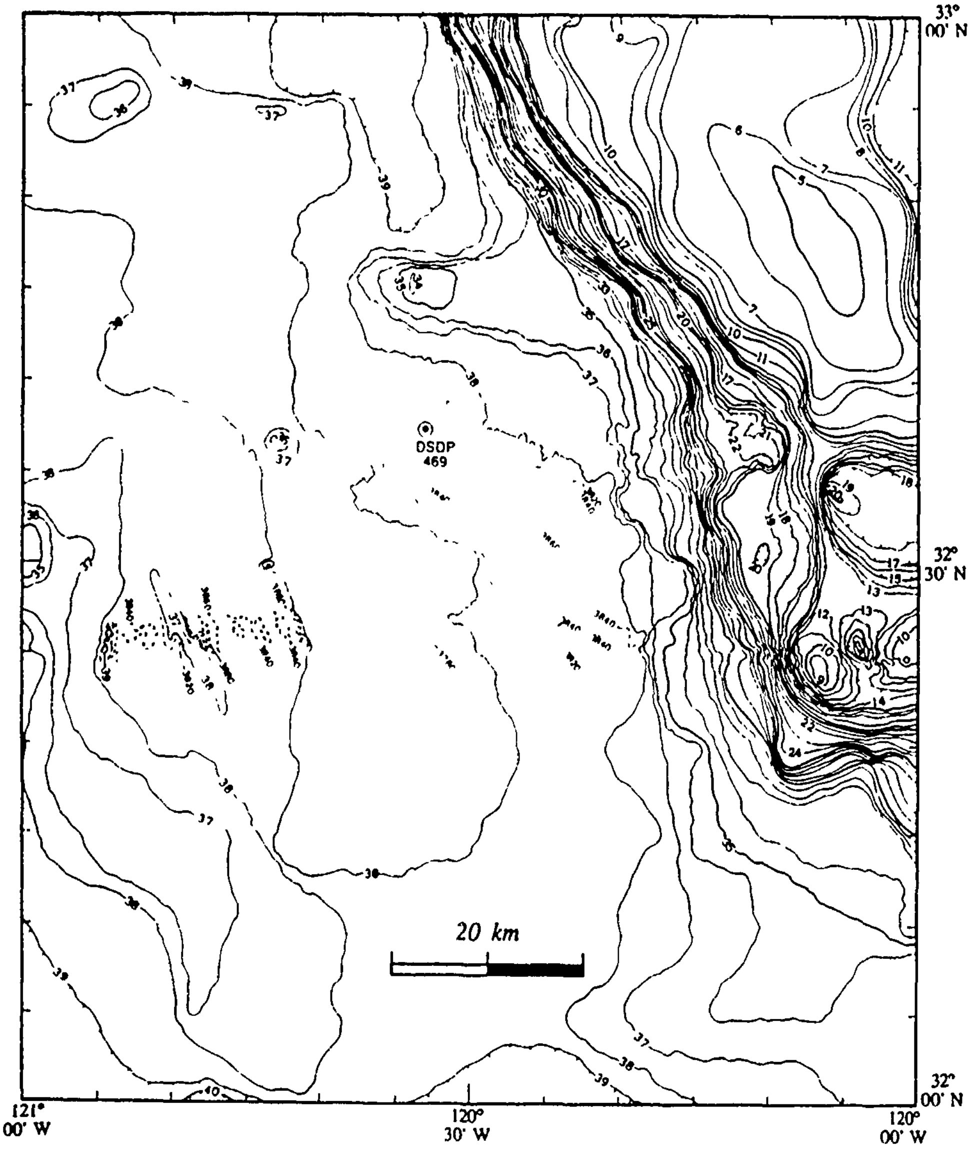

FIG 20. Bathymetry of the array vicinity. The closest boundaries of the sedimentary basin are 15- to 20 km distance away.

IV. DISCUSSION

Measurement with a 150-m aperture array has placed significant constraints on the coherence of ambient noise between 0.06 and 10 Hz. The variation of coherence length with frequency has suggested a physical model for the ambient noise on the ocean floor. The observed pattern of coherence is well modeled by a relatively broad beam distribution of low-order Rayleigh/Stoneley waves. The velocity and attenuation structure of the elastic waveguide affects the coherence structure by controlling the relative power of the different modes as a function of frequency and distance from the source. The coherence field at the CIRCUS site is thus profoundly affected by the low-velocity sediments that cover the basin. In the framework of this model, the band of high coherence length between 0.8 and 4 Hz suggests that seismic waves that comprise the noise are excited at a distance of 15 to 20 km from the array site, or alternatively at a depth greater than 100 m below the ocean floor. Either of these possibilities implies that the energy that is created at the ocean surface by the wave–wave interaction is scattered into the sedimentary layer at the boundaries of the basin.

The good fit of this model to the observed coherence indicates that, at this site at least, scattered energy is a more important source of seismic noise than is direct radiation from the sea surface above the sensors. This is in contrast to observations in shallow water where Kibblewhite and Ewans[20] have shown that direct radiation from the nonlinear wave–wave interaction produces the observed spectra and where Schmidt and Kuperman[21] have demonstrated that seafloor noise in shallow water is excited by direct coupling of sea-surface noise into the waveguide through the evanescent part of the wave function

The coherence length of ambient noise has important consequences for the design of arrays to be used for sensing known signals. The gain of the array only becomes substantial if the sensor separations are greater than the coherence length of the noise. Here the noise has short wavelengths and sensor groups that can be used as wave-number filters to suppress short-wavelength noise while leaving longer-wavelength signals (from ships, earthquakes, or explosions) unimpaired. This technique is widely used in sensor arrays used in reflection seismology both on land and in towed hydrophone arrays at sea.

At this site, the coherence length varies strongly with frequency. The array was too limited in extent to make spatial measurement below 0.1 Hz, but for higher frequencies, we can conclude that an observation array should have a group spacing of no less than 50 m, as long as the signal of interest has a substantially longer wavelength. If the signal and noise have roughly the same wavelength, more sophisticated data processing schemes will be required to separate them.

The decomposition of the noise field into seismic modes also has an important bearing on sub-bottom seismometer deployments. The justification for making the effort to deploy sensors in a borehole is that there is a potential for improving the signal-to-noise ratio of teleseismic signal. The degree to which this is true is a consequence of the depth dependence of the ambient noise compared to that of the desired signal. Body waves are often of interest, especially at frequencies above 0.1 Hz, and their amplitude does not depend directly on the distance from the seafloor. This study suggests that noise near the ocean floor consists predominantly of interface waves. The depth dependence of interface waves can be determined from the mode structure. At this site, the Rayleigh mode is the primary contributor to noise below 0.8 Hz. Above that, up to about 5 Hz, higher Rayleigh modes have higher amplitudes The higher modes decay less rapidly with depth than the fundamental mode so it is important to consider their effects when determining the depth of the sensor.

ACKNOWLEDGMENTS

We are grateful to L. D. Bibee, P.T C. Hammer, J A Hildebrand, A W. Sauter, and F N Spiess for their help with the field work. T G. Masters assisted us in the use of his mode program. A. Chave provided us his multiple-taper spectral estimation routines. We thank G Kirsch, J. A Hildebrand, G. H. Sutton, and the anonymous reviewers for their constructive suggestions for the manuscript This work was supported by the Office of Naval Research.

[1] R A Haubrich, and R. L. McCamy, "Microseisms: coastal and pelagic sources," Rev. Geophys 7, 539 572 (1969)

[2] R. T LaCoss, E. J Kelly, and M N. Toksoz,"Estimation of noise structure using arrays," Geophysics 34, 21–38 (1969)

[3] R. G. Adair, J A Orcutt, and T H Jordan,"Low-frequency noise observations in the deep ocean," J Acoust Soc Am 80, 633–645 (1986)

[4] S C Webb and C S Cox,"Observations and modeling of seafloor microseisms," J Geophys Res 91, 7343 7358 (1986)

[5] R S Yeats, B U Haq, J A Baron, D Bukry, J K Crouch, C Denham, A C Douglas, V I Grechin, M Leiner, A R Neim, S Pal, K A Pisciotto, R Z Poore, T. Shibata, and R Wolfart, "Site 469 Base of the Patton Escarpment," Vol 63, in *Init. Repts D S D P* (U S Govt. Printing Office, Washington, DC, 1981)

[6] A W. Sauter, L M. Dorman, and A. E Schreiner,"A study of sea floor structure using ocean bottom shots," Vol 16, in *Ocean Seismo-Acoustics, Low Frequency Underwater Acoustics*, edited by T Akal and J M Berkson (Plenum, New York, 1986).

[7] R. A. Haubrich, "Array design," Bull Seis Soc Am 58, 977–991 (1968)

[8] F. N. Spiess and P. Lonsdale,"Deep Tow rise crest exploration techniques," Mar Technol Soc J 16, 67–74 (1982)

[9] F N. Spiess, "Analysis of a possible sea-floor strain measurement system," Mar. Geodesy. 9, 385–398 (1985).

[10] R. D. Moore, L M Dorman, C -Y Huang, and D L Berliner,"An ocean bottom microprocessor-based seismometer," Mar Geophys Res 4, 451–477 (1981).

[11] C S Cox, T Deaton, and S C Webb,"A deep-sea differential pressure gauge," J. Atmos Ocean Tech. 2, 237–246 (1984)

[12] D. J Thomson, " Spectrum estimation and harmonic analysis," Proc IEEE 70, 1055-1096 (1982)

[13] B. Efron, *The Jackknife, the Bootstrap, and Other Resampling Plans* (SIAM, Philadelphia, PA, 1982)

[14] P W Pomeroy, G Hade, J Savino, and R Chander,"Preliminary results from high-gain, wide-band, long-period electromagnetic seismograph systems," J. Geophys Res 74, 3295–3298 (1969).

[15] J Savino, K McCamy, and G Hade,"Structure in earth noise beyond twenty second—A window for earthquakes," Bull Seismel Soc Am 62, 141–176 (1976)

[16] S. C. Webb and C S. Cox,"Pressure and electric fluctuations on the deep sea floor: Background noise for seismic detection," Geophys Res Lett 11, 967–970 (1984).

[17] M S Longuet-Higgins, M S,"A theory on the origin of microseisms," Philos. Trans Roy Soc., Ser A 243, 1–35 (1950)

[18] K A. Hasselmann, "A statistical analysis of the generation of microseisms," Rev Geophys Space Phys 1, 177–210 (1963)

[19] J Capon, "Signal processing and frequency-wavenumber spectrum anal-

ysis for a large aperture seismic array," in *Methods of Computational Physics*, edited by B. A. Bolt (Academic, New York, 1973), Vol. 13, pp 2-59

[20] S. C. Webb, "Coherent pressure fluctuations observed at two sites on the deep sea floor," Geophys. Res. Lett. **13**, 141-144(1986).

[21] G. L. Tyler, C. C. Teague, R. H. Stewart, A M. Peterson, W. H. Munk, and J W Joy, Deep Sea Res **21**, 989-1026 (1974).

[22] P. K Spudich and J A. Orcutt,"Petrology and porosity of an oceanic crustal site, results from wave modeling of seismic refraction data," J Geophys Res **85**, 1407-1413 (1980)

[23] J. H Woodhouse, "Efficient and stable methods for performing seismic calculations in stratified media," in *Proceedings of the International School of Physics Enrico Fermi Course* (North Holland, Amsterdam, The Netherlands, 1980), Vol 78, pp 127-151

[24] J S Gomberg and T G Masters,"Waveform modeling using locked-mode synthetic and differential seismograms application to determination of the structure of Mexico," Geophys J. **94**, 193-218 (1988).

[25] I Tolstoy, "Dispersive properties of a fluid layer overlying a semi-infinite elastic solid," Bull Seismol Soc Am **44**, 493-512 (1954).

[26] K. Aki and P. G. Richards, *Quantitative Seismology: Theory and Methods* (Freeman, San Francisco, 1980), p. 298.

[27] A. R. Levander and N. R. Hill, "*P-SV* resonances in irregular low-velocity surface layers," Bull. Seismol. Soc. Am **75**, 847-864 (1985).

[28] M E Dougherty and R. A. Stephen,"Seismic energy partitioning and scattering in laterally heterogeneous ocean crust," Pure Appl. Geophys **128**, 195-229 (1988)

[29] A C Kibblewhite and K C Ewans, "Wave-wave interactions, microseisms, and infrasonic ambient noise in the ocean," J Acoust Soc Am **78**, 981-994 (1986)

[30] H Schmidt and W A Kuperman, "Estimation of surface noise source level from low-frequency seismo-acoustic ambient noise measurements," J Acoust Soc Am **84**, 2153-2162 (1988)

Simultaneous Operation of the Sea Beam Multibeam Echo-Sounder and the SeaMARC II Bathymetric Sidescan Sonar System*

Christian de Moustier, Peter F. Lonsdale and

Alexander N. Shor

---

*. Reprinted from the IEEE Journal of Oceanic Engineering, Vol. 15, No. 2, pp. 84-94 (1990).

Simultaneous Operation of the Sea Beam Multibeam Echo-Sounder and the SeaMARC II Bathymetric Sidescan Sonar System

CHRISTIAN de MOUSTIER, MEMBER, IEEE, PETER F. LONSDALE, AND ALEXANDER N. SHOR

Abstract—A recent experiment aboard the Scripps Institution of Oceanography's (SIO) R.V. *Thomas Washington* demonstrated the seafloor mapping advantages to be derived from combining the high-resolution bathymetry of a multibeam echo-sounder with the sidescan acoustic imaging plus wide swath bathymetry of a shallow-towed bathymetric sidescan sonar. To avoid acoustic interferences between the ship's 12-kHz Sea Beam multibeam echo-sounder and the Hawaii Institute of Geophysics' 11-12-kHz SeaMARC II bathymetric sidescan sonar system during simultaneous operations, Sea Beam transmit cycles were scheduled around SeaMARC II timing events with a sound source synchronization unit originally developed at Scripps for concurrent single-channel seismic, Sea Beam, and 3.5-kHz profile operations. The scheduling algorithm implemented for Sea Beam plus SeaMARC II operations is discussed and the first results of their combined seafloor mapping capabilities are presented.

I. INTRODUCTION

IN THE LAST decade seafloor swath mapping systems using multi-narrow beam or bathymetric sidescan sonar technologies [1] have gained widespread use both in the research field to study seafloor geomorphology and in commercial applications such as reconnaissance seafloor surveys for submarine cable routes. Multi-narrow beam echo-sounders typically use hull-mounted sonars and an echo processor to give high-resolution bathymetry over a swath ranging from 75 to over 200% of the water depth. By comparison, bathymetric sidescan systems use a towed sonar and shipboard echo processing to produce both a high-resolution acoustic image of the seafloor and bathymetry over a swath often greater than three times the altitude of the tow body above the seafloor.

For deep-ocean survey work, two systems have been widely used by the oceanographic research community in the United States: The Sea Beam multibeam bathymetric survey system [2], [3], which uses hull-mounted transducer arrays, and the SeaMARC II bathymetric sidescan sonar system [4], [5], which uses a sonar package towed 400 to 500 m behind the ship and about 100-m below the sea surface. Advocates of each technology tend to focus on each system's advantages: High-resolution bathymetry, continuous operation, and "turn-key" convenience for hull-mounted multibeam systems versus wide coverage, acoustic imaging, and portability for towed sidescan systems. However, given that both the high-resolution bathymetry of the multibeam systems and the textural information derived from seafloor acoustic images produced by the sidescan systems are very useful for solving geomorphologic and tectonic research problems, it would be advantageous to operate these systems simultaneously (Fig. 1). But because the Sea Beam and SeaMARC II systems operate at almost the same acoustic frequencies (12.158 kHz for Sea Beam, 11 kHz (port) and 12 kHz (stbd) for SeaMARC II), they cannot be used concurrently without interfering with each other unless the transmit sequences of both systems are controlled. The simplest control algorithm which would allow the simultaneous operation of the two systems with minimum mutual acoustic interference merely permits each system to transmit on alternate pings at the end of the receive window of the other one. Although simple, this method is very inefficient.

A more elaborate algorithm has been developed and was implemented in May 1989, during Leg 18 of the Roundabout expedition of the Scripps Institution of Oceanography's (SIO) R.V. *Thomas Washington*. This algorithm takes into account the timing requirements of both systems and schedules the Sea Beam transmit sequences for optimum data density in a dual operation. Timing events were controlled by a sound-source synchronization unit originally developed by SIO's Shipboard Computer Group to schedule the firing rates of a single-channel seismic system, the Sea Beam system, and a 3.5-kHz subbottom profiler [6]. In the following we describe the timing requirements of the Sea Beam and SeaMARC II systems and the algorithm developed to synchronize them for simultaneous operation. We then present the first results of this joint operation.

II. SEA BEAM TIMING

The Sea Beam system derives its depths measurements from a set of 16 preformed acoustic beams spaced roughly 2-2/3° apart, with beam widths of about 2-2/3° at the half-power points. Together, these beams delimit an angular sector of about ±22° on either side of the ship's vertical axis. These beam directions are fixed within the ship's reference frame. Roll and refraction corrections are performed by the Sea Beam echo processor before the depths and horizontal distances are computed for each transmission cycle.

Manuscript received October 2, 1989; revised January 8, 1990. Institutional funds from the Scripps Institution of Oceanography and the Hawaii Institute of Geophysics made it possible to carry out this experiment as an ancillary project to a Sea Beam survey funded by the Office of Naval Research.

C. de Moustier and P. F. Lonsdale are with the Marine Physical Laboratory, Scripps Institution of Oceanography, La Jolla CA 92093.

A. N Shor is with the Hawaii Institute of Geophysics, University of Hawaii at Manoa, 2525 Correa Road, Honolulu, HI, 96822.

IEEE Log Number 9034670.

0364-9059/90/0400-0084$01.00 © 1990 IEEE

side W (horizontal range):

$$R_{ss} = t_{bd}/\cos(a\tan(2W/ct_{bd})) \tag{2}$$

where c is the nominal sound speed in seawater expressed in meters per second, and R_{ss} represents the minimum repetition rate for a given depth below the tow vehicle.

In contrast to the sidescan subsystem, the bathymetry subsystem acquires data to a limiting angle rather than a horizontal range as in (2). Bathymetry is derived from measurements of the phase difference of echoes received at two transducer rows separated by about half a wavelength in a plane parallel to the face of the corresponding acoustic array. These phase angles are sampled at 4 kHz and binned into a two-dimensional histogram of phase angles versus time after bottom detection. These data are subjected to modal picking (selecting the time bin with the largest number of samples in each angle row) and filtering to extract a table of arrival times as a function of the phase angle for each transmit cycle. A simple theoretical relationship ties differential phase angles ϕ to acoustic arrival angles θ_a, formed by the direction of the incoming sound energy and the normal to the face of the array:

$$\theta_a = \arcsin\left(\frac{\lambda\phi}{2\pi D}\right) \tag{3}$$

where λ is the acoustic wavelength, and D is the distance between the acoustic centers of the two rows. However, as described by Blackinton [5], because (3) assumes ideal array beam patterns and does not take into account sound refraction effects through the water column, it is not sufficient to obtain accurate bathymetry with the SeaMARC II system. Instead, phase angles are converted directly to depths and horizontal distances through a table lookup process. The lookup table is determined empirically by running the sonar system over a "known" portion of the seafloor in the vicinity of the survey area.

In the bathymetry subsystem, the reception window over which useful phase angle measurements are obtainable is limited by (i) the near-nadir insonification effects, (ii) interferences from bottom multiples, and (iii) decreasing signal-to-noise ratio for signals arriving at the two rows from far ranges, yielding large variances in the phase-angle measurements and estimates of depth that are unreliable.

Differential phase measurements are unreliable for echoes received near nadir because the outgoing acoustic pulse insonifies instantaneously a large area of the seafloor, resulting in a low spatial coherence between the bottom echoes received at each transducer row. In the SeaMARC II bathymetric subsystem this results in a blind zone spanning roughly ± 10° on either side of the vertical incidence. By analogy, a multibeam echo-sounder is beam-limited in the near-nadir region as the pulse insonifies an area larger than the beam footprint. Moving away from the nadir, the pulse begins to "propagate horizontally" and the backscatter process is pulse limited, allowing discrete phase measurements.

The first bottom multiple is the acoustic energy that traveled from the tow vehicle to the bottom, to the sea surface, back to the bottom, and then back to the tow vehicle. This signal arrives at the tow vehicle at the same time as a bottom echo at incidence angle θ_m such that:

$$\theta_m = \arccos\left(\frac{F_a}{2F_a + F_d}\right) \tag{4}$$

where F_a is the altitude of the tow vehicle above the bottom, and F_d is the depth of the tow vehicle below the surface. Because in most cases the SeaMARC II tow depth is small (typically about 100 m) compared to the total water depth, θ_m is usually a few tenths of a degree greater than 60°. In addition, the time-picking algorithm used during real-time processing does not give reliable results beyond the first bottom multiple. Therefore, to avoid acquisition of differential phase data from bottom multiples and multiple target reflections that would potentially contaminate true bottom returns, the bathymetry reception window is forced to close at (or before, as in (7), below) twice the bottom detection time, which corresponds to the arrival at 60° incidence. With this limiting angle and the roughly half-wavelength spacing between the transducer rows, the measured phase angles do not overlap (wrap around 2π) within the reception window except over extremely steep topography where duplicate phase angles can be received. Thus for the bathymetry subsystem the minimum repetition rate R_{smb} is:

$$R_{smb} = 2t_{bd}. \tag{5}$$

The 60° bathymetry swath width and the one-sided sidescan swath width coincide for F_a, such that:

$$F_a = W/\sqrt{3}. \tag{6}$$

For a one-sided swath width W of 5120 m, this corresponds to a tow vehicle altitude F_a of 2956 m or a bottom detection time of 3.94 s. Therefore, the sidescan mode determines SeaMARC II timing for bottom detect times below 3.94 s, and the bathymetry mode controls the timing above 3.94 s.

For bottom detection times greater than 4 s, a further timing limitation is imposed by the SeaMARC II hardware in the bathymetric subsystem. Binary counters determine the time window over which phase data are sampled by using a linear function of the bottom detection time. Starting at 4 s, the window closes at

$$R_{smb} = 0.75t_{bd} + 5. \tag{7}$$

With the existing SeaMARC II sidescan swath limit of 10.24 km, even this narrowing imposed on the bathymetric swath will yield swath widths greater than 10 km for vehicle altitudes where bottom detection times exceed 4 s. In such cases, bathymetry acquisition continues beyond the sidescan acquisition.

Subsequent to the joint operation on the *Thomas Washington*, an option was added to the SeaMARC II bathymetry subsystem to allow acquisition of 4 s of data after bottom detection, resulting in an alternative to (7):

$$R_{smb} = t_{bd} + 4. \tag{8}$$

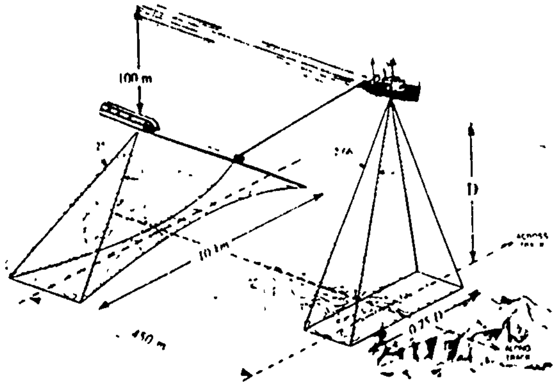

Fig. 1 Geometry of a dual Sea Beam-SeaMARC II operation

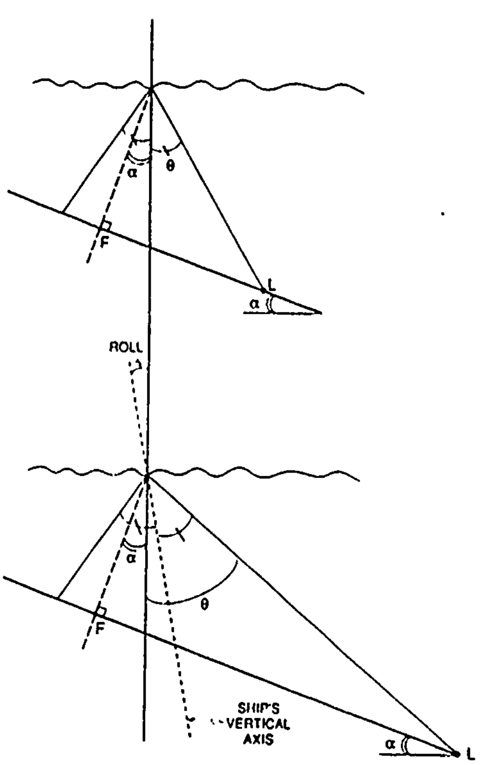

Fig. 2 Athwartships geometry. α is the bottom slope; θ is the 1/2 width of the overall receiving angular sector; F is the point corresponding to the first echo arrival; and L is that of the last echo arrival.

With this acoustic geometry, the minimum time interval between transmissions R_{sb} is a function of the time of first echo arrival after transmit t_{fa}, and of the width of the echo reception window delimited by an angular sector $\theta + \alpha$ encompassing the first and last echo arrivals (Fig. 2):

$$R_{sb} = t_{fa} / \cos(\alpha + \theta) \qquad (1)$$

where α is the absolute value of the bottom slope in the cross-track direction, and θ is half the width of the reception angular sector plus the ship's roll angle. For the Sea Beam system, $\theta = 22° + \text{roll}$. For practical purposes the bottom slope α can be given an upper limit of 20°, which is representative of average apparent slope angles measurable in steep topography with the Sea Beam system.

TABLE I
SEAMARC II SIDESCAN OPTIONS

Pixel Size (m)	0.5	1	2.5	5	5
Swath Width (m)	1,024	2,048	5,120	10,240	10,240
Altitude setting	Low	Low	Low	Low	High
Transmit Rep. Rate (s)	1	2	4	8	8 16
Min Vehicle Altitude (m)	25	50	100	250	1,022
Max Vehicle Altitude (m)	250	500	1,250	2,500	10,220

Aboard the R. V. *Thomas Washington* the Sea Beam system is keyed by the edge trigger of a linescan recorder whose sweep rate is a multiple of 1 s. As a result, effective Sea Beam ping rates are set to the nearest integral second after the Sea Beam echo processor has enabled the system's transmit function.

For the generation of multibeam echo-sounders developed in the 1980's (e.g., ECHOS XD, EM-12/24, Hydrosweep, Sea Beam 2000) with an angular coverage of ±45° or more, the ship's roll correction takes place during the beamforming operation. For these systems, θ in (1) is only the half-width of the reception angular sector with respect to the true vertical.

III. SEAMARC II TIMING

To operate as a sidescan sonar and a bathymetric mapping system, SeaMARC II uses two subsystems that acquire data independently. Both subsystems begin data acquisition upon receipt of the first seafloor return, defined as the first echo whose amplitude exceeds a preset threshold in the bottom detection circuitry common to both subsystems. Depending on water depth and swath width, different timing schedules are used. The digitized sidescan swath contains 1024 samples per side, and the swath width is determined by the pixel size selected by the operator according to the vehicle's altitude above the seafloor. In addition, because the system cannot resolve pixels in the near-nadir region, it blanks out the first 40 pixels on each side of the track. Pixel size and vehicle altitude options, the corresponding swath widths, and transmit repetition rates are listed in Table I.

In water depths in excess of 1000 m the system is usually operated at a total swath width of 10 240 m with either the low-altitude option, whose transmit repetition rate is fixed at 8 s, or the high-altitude option, whose transmit repetition rate is selectable in increments of 1 s, starting at 8 s.

Different timing schedules apply to the sidescan or bathymetry functions depending upon the vehicle's altitude above the seafloor and the pixel size—hence swath width—selected. For sidescan operation alone the minimum repetition rate is a function of the time of the first echo arrival or bottom detection time t_{bd} and the swath width to one

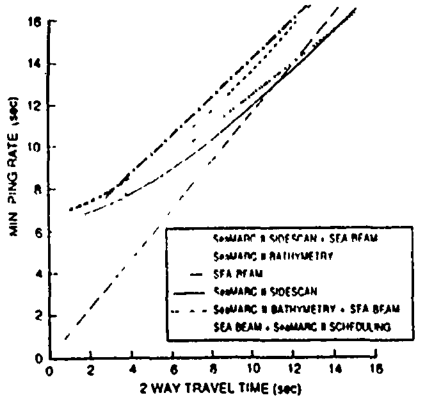

Fig. 3 Ping rates for Sea Beam and SeaMARC II operating individually or jointly (equations (1), (2), and (7) in text).

Selection of either option depends upon whether the maximum SeaMARC II bathymetric swath width (8) or an increased transmit cycle frequency (7) is desired.

For bottom detection times less than 4 s, (5) determines the timing of the bathymetry subsystem. However, for the overall SeaMARC II timing, when the bottom detection time is less than 3.94 s, the sidescan timing (2) dominates. Thus (5) applies only to the interval 3.94 s to 4 s and is ignored in the combined SeaMARC II-Sea Beam operation described below.

IV. ALGORITHM FOR COMBINED SEAMARC II-SEA BEAM OPERATION

Equations (1), (2), and (7) form the bases of the scheduling algorithm which allows the joint operation of the Sea Beam and SeaMARC II systems. These functions are represented graphically in Fig. 3, where the ordinate corresponds to the minimum repetition rates required for each operation, whether individually or jointly scheduled. Because of its relatively narrow swath, the Sea Beam system would normally operate at ping repetition rates more than twice those of the SeaMARC II system for bottom detection times of 4 s or less. In such situations, interferences of the type illustrated in Fig. 4, where each system runs independently, would be difficult to avoid unless the ping rate of the Sea Beam system were slowed down by running its graphic recorder on a sweep rate of 6 s or longer.

Because the SeaMARC II system requires longer repetition rates, it is more practical to schedule the Sea Beam system based on the SeaMARC II ping rate rather than vice versa. This is also true for operational reasons because SeaMARC II, as presently configured, cannot accept an external trigger, so it was operated with a fixed transmission repetition rate. With SeaMARC II set for a 10 240-m total swath width, SeaMARC II sidescan timing (2) is used to determine the joint ping rate for bottom detection times below 4 s; above 4 s, SeaMARC II bathymetry timing (7) (alternatively, (8)) is used, yielding the following algorithm, where

Initialization

$W = 5120$ m SeaMARC II one-sided swath width,
$c = 1500$ m/s nominal sound speed,
$\alpha + \theta = 45°$ Sea Beam "angle of incidence,"
$F_d = 100$ m nominal SeaMARC II tow depth,
$d = 450$ m nominal SeaMARC II tow distance,
R Sea Beam ping rate (s),
S ship's speed (m/s),
$A = 1/\cos(\alpha + \theta)$ constant in (1), (9a)
$B = 2W/c$ constant in (2). (9b)

For each ping

$$index = \text{integer}(d/(SR)). \tag{9c}$$

Index is the approximate number of pings required to account for the horizontal separation between the ship and the tow vehicle (Fig. 1). The time of first arrival t_i is estimated from the shallowest depth measured by the Sea Beam system during the previous transmission cycle. A different time must be used for the SeaMARC II bottom detection time as the vehicle is usually towed 400 to 450 m behind the ship. With a ship's speed of 8 kn (4 m/s) and a 12-s transmission cycle, the SeaMARC II bottom detection time t_{bd} therefore corresponds to the shallowest depth measured by the Sea Beam system 10 pings prior, minus the depth of the tow vehicle below the surface. The SeaMARC II bottom detection time is then:

$$t_{bd_i} = t_{i-\text{index}} - 2F_d/c_i. \tag{9d}$$

Hence the repetition rates for Sea Beam:

$$T_{SB_i} = At_i + \Delta t - t_{bd_i}(1 - 1/\cos(\text{atan}(B/t_{bd_i}))),$$

$$0 < t_{bd_i} \leq 4 \tag{9e}$$

$$T_{SB_i} = At_i + \Delta t + 5 - t_{bd_i}/4, \qquad t_{bd_i} \geq 4. \tag{9f}$$

With (8), (9f) would be:

$$T_{SB_i} = At_i + \Delta t + 4, \qquad t_{bd_i} \geq 4. \tag{9g}$$

This algorithm is illustrated in the timing diagram shown in Fig. 5, and the results of the corresponding scheduling appear on a sample of a SeaMARC II real-time raw sidescan record shown in Fig. 6. To accommodate the longer reception time required by the SeaMARC II system, Sea Beam is forced to transmit before SeaMARC II transmits so that it has completed receiving by the time the SeaMARC II receive window opens (the time of previous bottom detect − 0.067 s). The time interval between transmit pulses (T_i in Fig. 5) from both systems corresponds to the Sea Beam reception time window plus an adjustment factor Δt which allows the scheduling algorithm to track the bottom upslope or downslope along the ship's track. During this experiment Δt was set conservatively to 1 s.

The foregoing algorithm is coded as a FORTRAN 77 program which runs on the shipboard VAX 11/730 computer used for the real-time acquisition and processing of underway geophysical data and navigation on the *Thomas Washington* [7]. Whereas inputs such as depths measured by the Sea Beam system and the ship's speed are obtained directly from data

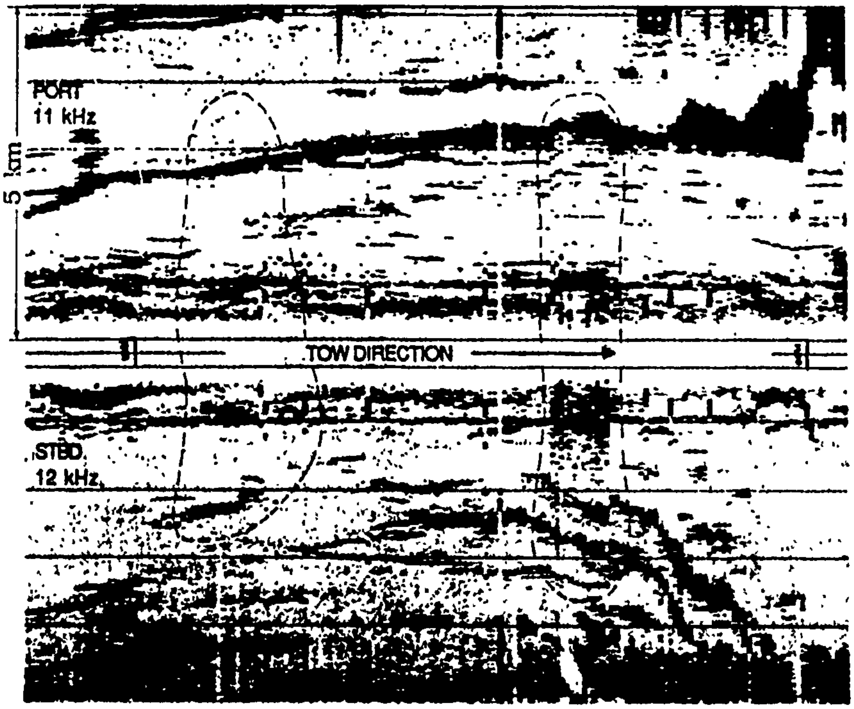

Fig 4 SeaMARC II sidescan record showing Sea Beam interferences occurring when both systems are run simultaneously without synchronization Interferences (within dashed areas) are strongest near the center of the swath and on the starboard side where the receivers are tuned to 12 kHz

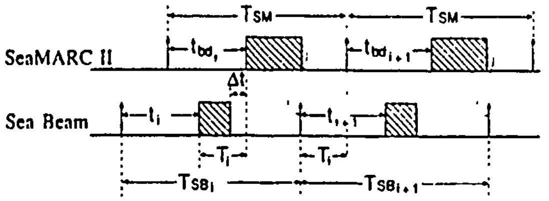

Fig 5. Timing diagram for a joint Sea Beam-SeaMARC II operation T_{SM} is the SeaMARC II ping rate, held fixed in this application. T_{SB_i} is the ping rate of the Sea Beam system as determined by the scheduling algorithm and updated at every ping. t_i is the time of the first echo arrival received by Sea Beam, and t_{bd_i} is the bottom detect time for SeaMARC II, estimated from the corresponding Sea Beam time a number of pings before Stripped blocks represent the receiving windows of each system. For SeaMARC II, the window length is the largest of the bathymetry of sidescan receive windows

files on the VAX, timing information is obtained through a sound source synchronization unit (Sync Box) interfaced with the VAX [6]. To tie the sound sources to a common time base, the Sync Box synchronizes its internal clock with the trigger pulse of the device given highest priority, and this clock serves as a reference for scheduling the other sound sources. Timing events for each source are transmitted by the Sync Box to the VAX, where a FORTRAN program determines the optimum firing schedule for the next cycle and transmits the corresponding parameters back to the Sync Box.

A similar scheme was used to schedule transmissions of the SeaMARC II and Sea Beam systems. Because it was not practical to control remotely the SeaMARC II timing with the hardware configuration available during the experiment, the SeaMARC II transmission rate was held constant and its trigger pulse was used as the reference. The Sync Box synchronized its internal clock to this pulse and passed the information to the VAX, where scheduling parameters were determined according to (9) and sent back to the Sync Box.

V. First Results

The algorithm described above was implemented successfully for several SeaMARC II lowerings along a transect between Honolulu, Hawaii, and San Diego, California (Fig. 7) Examples of the data gathered at depths of 5000 m in the vicinity of the Murray Fracture Zone and at depths as shallow as 500 m on the continental slope off Point Arguello, California, are shown in Figs. 8 and 9, which are used here to illustrate the benefits and disadvantages of the dual operation.

At the 5000-m depth the SeaMARC II transmitted at a fixed

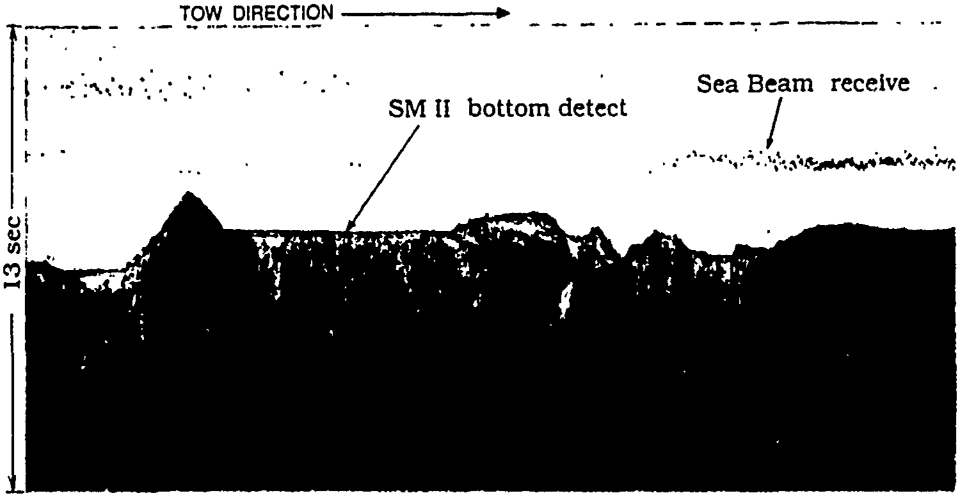

Fig. 6. Real-time SeaMARC II raw sidescan display for the starboard side (12 kHz) showing the timing events due to the scheduling algorithm. The width of the display is 13 s, as set by the sweep rate of the recorder. The Sea Beam reception window seen in this figure falls well outside the SeaMARC II reception window, which begins at $t_{bd} = 0.067$ s, and does not interfere with the SeaMARC II bottom detect function.

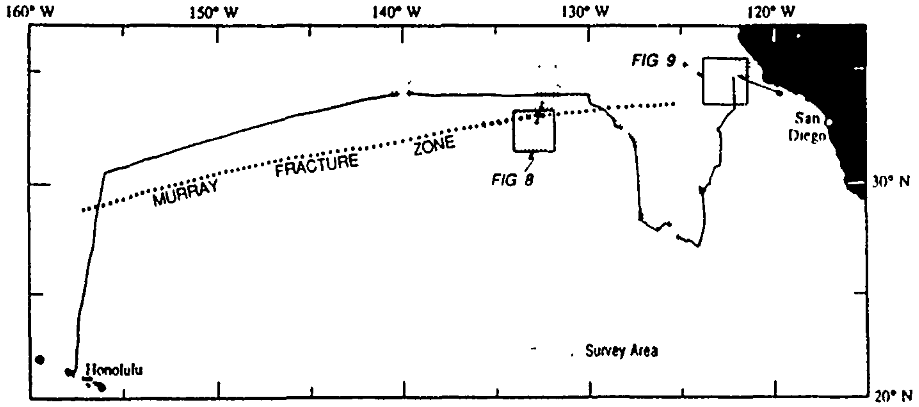

Fig. 7. R V *Thomas Washington*'s track chart for Leg 18 of the Roundabout expedition, showing the locations of Figs. 8 and 9 in geographic coordinates. Stippled areas indicate surveys carried out with the dual operation.

transmit repetition rate of 13 s, and the Sea Beam was scheduled accordingly. As illustrated in Fig. 3, at 5000 m (6.6 s) Sea Beam usually transmits every 8 s, so that the depth samples are spaced about 46-m-apart along-track for the ship's speeds of 11-12 kn (5.5-6 m/s). However, while towing SeaMARC II, the ship's speed had to be reduced to 9 kn or less; thus in spite of the 13-s repetition rate, the along-track spacing of Sea Beam depth samples only increased by roughly 27%, with sampling ratios along-track versus across-track of 4 to 1.

Because the lowest repetition rate available for the 10 240-m SeaMARC II swath is 8 s, in waters shallower than 2000 m the resulting along-track depth sampling of the Sea Beam system can be reduced by more than half, compared to its stand-alone operation. However, the limit at which the spacing of depth samples in the along-track direction becomes lower than that of cross-track samples is not reached, and full coverage at the cross-track resolution of the echo-sounder is still maintained. Therefore, compared to their respective standard operations, the dual Sea Beam-SeaMARC II operation entails lower survey speeds and lower data densities for the Sea Beam system and, in some cases, a slight decrease (usually less than 8%) in the data density for SeaMARC II, none of which degrades the coverage past the 100% mark. However, this reduction in data density during dual operation is compensated by several benefits discussed below.

A SeaMARC II survey is enhanced by simultaneously operating Sea Beam from the towing vessel in at least three ways:

1) Multibeam bathymetry data fill the data gap directly beneath the SeaMARC II vehicle, a central swath from which no useful sidescan or bathymetry data are collected but where multibeam performance is optimal. As shown in Fig. 8, this gap may be as wide as 750 m at full ocean depths; SeaMARC

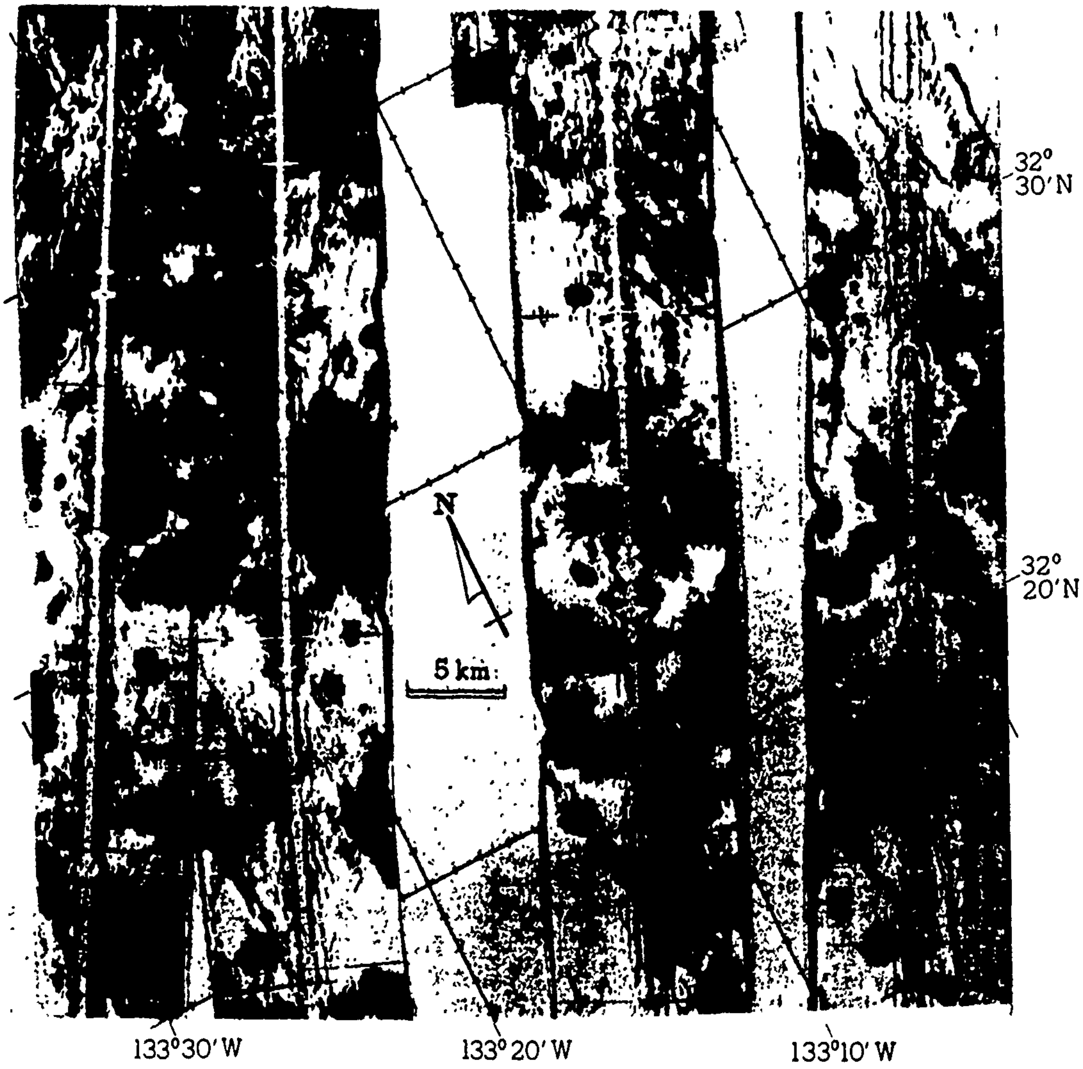
32°
30'N
32°
20'N
N
5 km
133°30'W
133°20'W
133°10'W

Fig. 8(a). 5000-m-depth survey example SeaMARC II sidescan in the vicinity of the Murray Fracture Zone (Fig. 7).

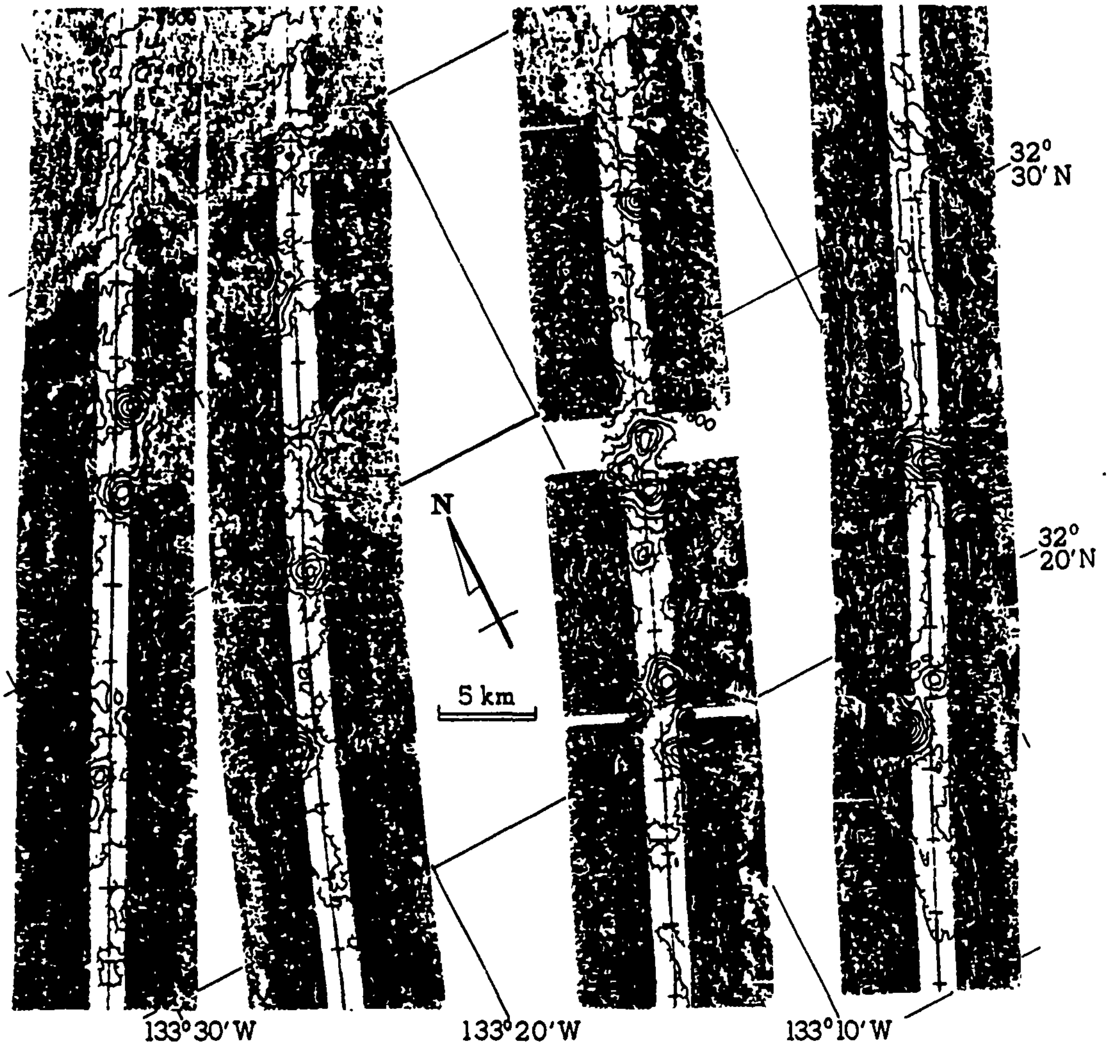
32°
30′ N
32°
20′N
N
5 km
133°30′W
133°20′W
133°10′W

Fig. 8(b). 5000-m-depth survey example. SeaMARC II plus Sea Beam bathymetry in the vicinity of the Murray Fracture Zone (Fig 7). Contours at 100-m intervals from Sea Beam data (black lines) are overlaid on SeaMARC II bathymetry (color filled).

II bathymetry data have a central blank zone extending about 10° on either side of the nadir line (i.e., 1 8-km wide at a 5-km water depth). The benefit extends beyond merely infilling gaps in the SeaMARC II mapping: It provides an accurate bathymetric profile for use in interpreting other ancillary observations (e.g., seismic reflection, gravity, and magnetic measurements) that may also be made along the ship's track. Indeed, the along-track depth profile beneath the ship measured by the Sea Beam system provides a valuable quality assurance for the bottom detection times recorded by the SeaMARC II system and can be used to convert slant ranges into horizontal ranges assuming a flat bottom, although a conventional echo-sounder is also adequate for this purpose.

2) At all water depths, the multibeam echo-sounder measures water depth more precisely and accurately than can be achieved by the phase difference measurement of SeaMARC II The signal used for the latter measurement is extremely noisy when returned by sediment-covered (usually low backscatter) seafloors deeper than 4000 m, to the extent that the bathymetric data are not amenable to machine contouring, and is best presented as layer-colored displays (e g., Fig. 8). Over a more reflective, shallower seafloor it proved possible to process and machine-contour SeaMARC II bathymetry using SIO's Sea Beam processing software [8], and good matches with overlapping Sea Beam contours were achieved with a 50-m vertical interval. (Before making these matches, corrections must be made for the vertical and horizontal separation of the ship and the SeaMARC II tow vehicle.) Sea Beam contours, by comparison, are generally valid at a 10-20-m interval. Although the concurrent acquisition of bathymetric data from both systems allows more quantitative comparisons to be made, such analyses are beyond the topic of this paper and will be presented in a forthcoming paper.

3) Matching high-resolution bathymetry at track crossings allows for the rectification of a survey's navigation (e.g., [8], [9]). This technique, an essential element of Sea Beam surveying except where very precise positioning systems are available, facilitates the production of accurate SeaMARC II mosaics

Conversely, Sea Beam surveys benefit from simultaneously collecting SeaMARC II data because:

1) The broader swath of the sidescan system allows a wider spacing of survey tracks to achieve complete coverage or the percentage of coverage judged necessary to solve the particular problem being addressed by the survey, hence making more efficient use of ship-time. As now configured, the SeaMARC II system yields a sidescan swath 10.24-km wide and a bathymetric swath (where signal strength is adequate) equal to roughly 3.4 times the water depth. The swath width of the Sea Beam system on the *Thomas Washington* is equal to only 0.7 times water depth (although second-generation multibeams with swaths twice the water depth or more are now in scientific use). The disparity in width of coverage is most marked at shallow depths, e.g., at the continental slope site shown in Fig. 9, where the Sea Beam swath is only a few hundred meters wide. In this situation, the matching of targets on SeaMARC II sidescan images may be the most effective method of rectifying navigation. Note also that in Fig. 8(a), deep-water tracks 8-10-km apart have an overlap of SeaMARC II data (allowing mutual adjustment of their navigation), but not of Sea Beam data.

2) The sidescan data enhance the geologic interpretation of the bathymetry by providing an acoustic characterization of the seafloor from which geologic composition (rock, sand, or mud) can be inferred. For example, the high backscatter of the circular targets in Fig. 8 allows them to be interpreted as small rocky volcanoes rising above a sedimented plain, while the low backscatter of the channel axes in Fig 9 suggests sandy fills. Some characterization of acoustic backscatter can be achieved with multibeam systems by recording the amplitudes and phases of the echoes received by each beam (e g., [10], [11]), but with a 16-beam system the results are much inferior to SeaMARC II sidescan in both resolution (the acoustic pulse length used in Sea Beam is seven times longer than that in SeaMARC II at the 10 24-km swath) and swath width

3) The SeaMARC II sidescan system can resolve targets with or without bathymetric expression that have much smaller horizontal dimensions than the relief features resolved by Sea Beam. The cross-track resolution of SeaMARC II, when operated with a 10.24-km swath, is 5 m (pixel size), compared to a cross-track resolution, over a 5-km-deep seafloor, of about 240 m for Sea Beam Small-scale features may be of great significance for many geologic problems; for example, mapping narrow lines of rock outcrops may be crucial for establishing the structural lineation of a mainly sedimented seafloor, although if the sediment cover is complete, we have found that the higher resolution multibeam bathymetry may delineate underlying structural trends more accurately than any sidescan system can.

There are three disadvantages of a dual Sea Beam-SeaMARC II operation: The one most obvious to our sponsors is the high cost of operating both systems simultaneously. This cost could be reduced by the cross training of the two sets of technicians and engineers to make them more versatile. As already noted, we also incurred some degradation of Sea Beam performance and survey speed. A less obvious problem is that, in general, the goal of acquiring a sidescan mosaic severely constrains the survey pattern to mainly parallel tracks that are at low oblique angles to the grain of the relief. Other patterns may be effective for particular geologic targets (e.g., we surveyed a large guyot with a nested pentagon variant of concentric circular tracks), but a pattern optimized for sidescan coverage frequently results in a suboptimal magnetic or seismic reflection survey. Multibeam surveys are much less sensitive to track orientation, although the best data are obtained with tracks at high angles to the relief. Furthermore, once a sidescan survey is underway, there is a limited flexibility to adaptively change the pattern in response to bathymetric discoveries; this makes SeaMARC II a much better tool for describing the morphology of features whose extent and orientation is known, rather than for exploring regions of unknown relief (a common objective with multibeam echo-sounders).

VI. CONCLUSIONS

We have demonstrated the feasibility of running concurrent Sea Beam and SeaMARC II surveys from a single ship

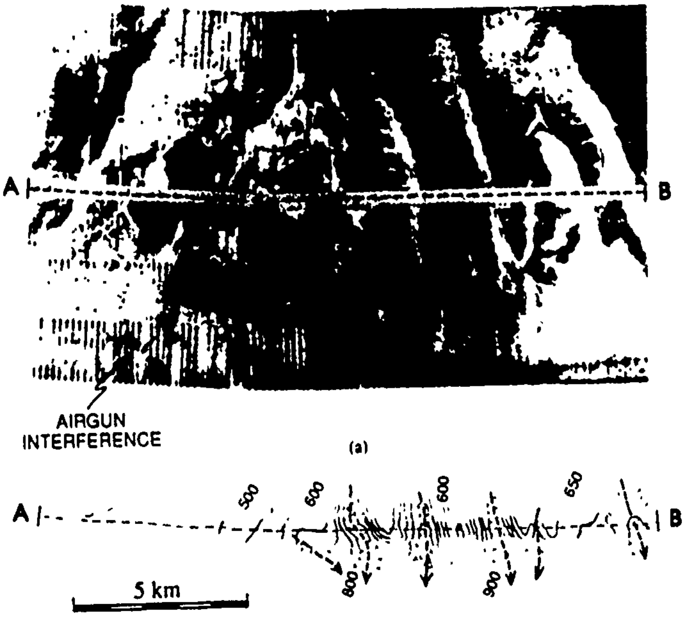

Fig. 9 500-m-depth survey example (a) SeaMARC II sidescan, and (b) SeaMARC II plus Sea Beam bathymetry off Point Arguello, CA (Fig 7). Arrows indicate the flow channels clearly seen in the sidescan image. The contour interval is 50 m, the heavy lines are Sea Beam data, and the dotted lines are SeaMARC II bathymetry. No attempt was made to avoid the airgun interference seen in the sidescan record, as it occurred only in shallow water

and of avoiding mutual acoustic interferences between the two systems using a sound source synchronization scheme. Joint operation of these systems without synchronization resulted in marked interferences in the SeaMARC II sidescan image. During most of the survey a single-channel seismic system was deployed along with the SeaMARC II system, and although no attempt was made to avoid interferences from airgun sources, the sidescan records were only affected in shallow water (~500 m).

Towing the SeaMARC II vehicle requires a 2-3-kn reduction in the ship's speed from the usual 11-12 kn attained during standard Sea Beam bathymetric surveys on the *Thomas Washington*. However, the slower ship's speed compensates somewhat for the decreased transmission cycle (hence the data density along-track) imposed on the Sea Beam system during joint operations. Second generation commercial multibeam echo-sounders, with swath widths of twice the water depth or more, will not be affected as much by this decrease in the data density along-track because their timing will be closer to that of the SeaMARC II system. Also, where a 5-m pixel resolution in the sidescan image is adequate for the goals of the survey, being able to tow at up to 9 kn offers a significant advantage (by more than a factor of four) in track coverage per unit time over previous dual Sea Beam-sidescan deployments with instruments towed near the bottom at less than 2 kn (e.g., Sea Beam+Deep Tow, Sea Beam+SeaMARC I, Sea Beam + SAR).

The co-registered, high-resolution bathymetry provided by the multibeam echo-sounder in the center of the wider sidescan image and bathymetry swaths output by the SeaMARC II system yields more information for geomorphology than either data set taken individually. It also helps resolve navigation uncertainties in each data set and permits wide track spacings (up to 10 km in our case) while retaining 100% quantitative coverage of the seafloor. Second generation SeaMARC II systems currently under development promise an increase in the swath width to 30 km. If these systems were operated in conjunction with second generation multibeam echo-sounders according to the scheme described here, seafloor gravity surveys for which track spacings often exceed 30 km could be supplemented with almost complete bathymetric coverage.

ACKNOWLEDGMENT

The authors wish to thank J. S. Charters for implementing the Sea Beam-SeaMARC II algorithm in the Sync Box, J. Griffith for the art work, and M. Rognstad and two anonymous reviewers for constructive comments. They are indebted to the captain, crew, and scientific party of the *Thomas Washington* during Leg 18 of the Roundabout expedition.

REFERENCES

[1] C de Moustier, "State of the art in swath bathymetry survey systems," *Int. Hyd Rev* , vol 65, no 2, pp. 25-54, 1988

[2] V Renard and J. P Allenou, "Sea Beam multibeam echo-sounding in 'Jean Charcot': Description, evaluation and first results," *Int Hyd. Rev.*, vol 56, no 1, pp. 35-67, 1979

[3] H. K. Farr, "Multibeam bathymetric sonar: Sea Beam and Hydrochart," *Marine Geodesy*, vol. 4, no 2, pp. 77-93, 1980.

[4] J. G. Blackinton, D M. Hussong, and J. G Kosalos, "First results from a combination side-scan sonar and seafloor mapping system (SeaMARC II)," in *Proc Offshore Tech. Conf* (Houston, TX), 1983, pp 307-314

[5] J. G Blackinton, "Bathymetric mapping with SeaMARC II: An ele-

vation angle measuring side-scan sonar system,' Ph D. dissertation, Hawaii Inst of Geophys., Univ. of Hawaii, Manoa, 1986

[6] J C. Phillips, J L. Abbott, and C. de Moustier, "A sound source synchronizer for seafloor surveying," in *Proc Offshore Tech. Conf.* (Houston, TX), 1988, vol 4, pp. 497-504.

[7] J M Moore, J S Charters, and C de Moustier, "Multi-sensor real-time data acquisition and preprocessing at sea," in *Proc IEEE MTS Oceans'88 Conf* (Baltimore, MD), 1988, vol 2, pp 509-517

[8] J S Charters, "SIO Sea Beam software documentation,' Scripps Inst Oceanogr , La Jolla, CA, unpublished report, 1987

[9] C E Nishimura and D W Forsyth, "Improvements in navigation using Sea Beam crossing errors," *Marine Geophys Res* , vol 9, pp 333 352, 1988

[10] C de Moustier, "Approaches to acoustic backscattering measurements from the deep seafloor," in *Current Practices and New Technology in Ocean Engineering* New York: ASME, 1986, OED vol 11, pp 137-143

Also reprinted in *Trans ASME, J Energy Res Tech* , vol 110, pp 77-84, 1988

[11] C de Moustier and F V Pavlicek, "On line Sea Beam acoustic imaging,' in *Proc IEEE-MTS Oceans'87 Conf* (Halifax, NS, Can), 1987 pp 1197-1201

★

Christian de Moustier (M'86) received the Diploma of Engineer from the Ecole Superieure d'Ingénieurs de Marseille, Marseille, France, in 1979, and the Ph D degree in oceanography (applied ocean sciences) from the University of California, San Diego, in 1985

He is currently an Assistant Research Oceanographer at the Marine Physical Laboratory of the Scripps Institution of Oceanography, La Jolla, CA, and has been serving as a Scientific Advisor to the Shipboard Computer Group at Scripps for the past two years His present research interests are in underwater acoustics, with emphasis on the physics of bottom interacting sound and sound reverberation in the ocean, seafloor acoustic imaging and contour mapping, and digital image processing applied to sonar data.

★

Peter F. Lonsdale was born in Sandown, Isle of Wight (England) on April 1, 1948 He graduated with the B A degree from the University of Cambridge in 1969, and the Ph D degree from the Scripps Institution of Oceanography, La Jolla, CA, in 1974

Since then he has been at the Scripps Institution, where at present he is a Professor of Oceanography and Research Geologist His principal research interest is in the geomorphology of the abyssal seafloor, especially in regions of active tectonic, volcanic, or bottom current activity

★

Alexander N. Shor is an Associate Geophysicist on the research staff of the Hawaii Institute of Geophysics (HIG) of the University of Hawaii at Manoa He has directed the SeaMARC II program at HIG since 1986 His research interests include, in addition to seafloor mapping, the study of submarine fans and deep ocean currents as agents of sediment transport in the deep sea. Prior to 1986 he was on the staff of the Lamont-Doherty Geological Observatory of Columbia University, where he conducted marine geologic studies using multibeam echosounders and deeply towed side-scan sonar systems His research and mapping projects with SeaMARC II include parts of all major oceans, from the sub Antarctic to the Norwegian Sea

A Seafloor and Sea Surface Gravity Survey of Axial Volcano*

John A. Hildebrand, J. Mark Stevenson, Philip T. C. Hammer, Mark A. Zumberge, and Robert L. Parker

---

*. Reprinted from the Journal of the Geophysical Research, Vol. 95, No. B8, pp. 12,751 (1990).

JOURNAL OF GEOPHYSICAL RESEARCH, VOL. 95, NO. B8, PAGES 12,751-12,763, AUGUST 10, 1990

A Seafloor and Sea Surface Gravity Survey of Axial Volcano

JOHN A. HILDEBRAND, J. MARK STEVENSON, PHILIP T. C. HAMMER,
MARK A. ZUMBERGE, AND ROBERT L. PARKER

Scripps Institution of Oceanography, University of California, San Diego, La Jolla

CHRISTOPHER G. FOX AND PHILIP J. MEIS

Marine Resources Research Division, Pacific Marine Environmental Laboratory, NOAA
Hatfield Marine Science Center, Newport, Oregon

Seafloor and sea surface gravity measurements are used to model the internal density structure of Axial Volcano. Seafloor measurements made at 53 sites within and adjacent to the Axial Volcano summit caldera provide constraints on the fine-scale density structure. Shipboard gravity measurements made along 540 km of track line above Axial Volcano and adjacent portions of the Juan de Fuca ridge provide constraints on the density over a broader region and on the isostatic compensation. The seafloor gravity anomalies give an average density of 2.7 g cm^{-3} for the uppermost portion of Axial Volcano. The sea surface gravity anomalies yield a local compensation parameter of 23%, significantly less than expected for a volcanic edifice built on zero age lithosphere. Three-dimensional ideal body models of the seafloor gravity measurements suggest that low-density material, with a density contrast of at least 0.15 g cm^{-3}, may be located underneath the summit caldera. The data are consistent with low-density material at shallow depths near the southern portion of the caldera, dipping downward to the north. The correlation of shallow low-density material and surface expressions of recent volcanic activity (fresh lavas and high-temperature hydrothermal venting) suggests a zone of highly porous crust. Seminorm minimization modeling of the surface gravity measurements also suggest a low-density region under the central portion of Axial Volcano. The presence of low-density material beneath Axial caldera suggests a partially molten magma chamber at depth.

Copyright 1990 by the American Geophysical Union.

Paper number 90JB00781.
0148-0227/90/90JB-00781$5.00

Very Low Frequency Coherency Studies

Spahr C. Webb

Introduction.

This was a very small proposal to construct one instrument and to use this instrument in conjunction with an existing instrument to study the coherence of pressure fluctuations measured at the deep seafloor as a function of frequency and the distance separating the instruments.

Background

A series of measurements at several sites on the Pacific sea floor of the spectrum of pressure fluctuations has revealed some universality in the shape of the spectrum at frequencies below 1 Hz. The prominent microseism peak near .2 Hz is now known to be associated with seismo-acoustic waves created by an interaction of surface gravity waves through the nonlinearity of the surface gravity wave governing equations. Energy at very low frequency is associated with infragravity waves and an absence of sources in an intermediate band leads to very low signal levels in the "noise notch" between 0.03 and 0.1 Hz in deep water.

Measurements of the spectrum provide little information about the wavenumber content of the pressure field associated with microseisms. There may be energy both on the dispersion curves of the modes of the oceanic waveguide and off the dispersion curves associated with local forcing. The energy distribution as a function of angle on the dispersion curves indentifies source regions and can provide constraints of the effect of scattering on the propagation of low frequency modes within the oceanic waveguide. A simple two instrument experiment can not hope to delineate the complicated wavenumber field expected at deep sea sites, but can provide a ground work for experiments involving larger arrays of instruments.

Work Accomplished

An instrument was constructed with this funding and has been used on perhaps nine cruises since its construction. The project, as intended, laid the groundwork for much larger experiments using arrays of instruments (BASIC, NACHOS, PEGASUS, VENTS and SAMSON) which have begun to delineate the wavenumber structure of low frequency pressure fluctuations in the deep sea. Two papers which discuss recent results are listed in the Bibliography..

The instruments that were developed and tested during this project carried a 8088 microcomputer on the C-44 bus and recorded data on a SCSI device. This architecture has now been adapted for a fleet of 36 "ONR ocean bottom seismometers" developed to study the low frequency noise problem. The original instruments carried a small 40 Mbyte tape recorder and measured pressure fluctuations using a differential pressure gauge. During more recent experiments, the instruments were equipped with 400 Mbyte optical disk drives, and recorded ground displacement detected using seismometers deployed within an package external to the recording system. The instruments have been deployed in the Pacific, the Atlantic and now in the Arctic beneath the polar ice cap.

Bibliography

Webb, S.C. and W. Crawford, and X. Zhang, "Infragravity waves in the deep ocean", J. Geophys. Res, in press, 1990.

Webb, S. C., "Very low frequency sound studied using multielement seafloor arrays", Proc. of the conference on "Natural physical sources of sound in the ocean", Cambridge, England, 1990.

Open Ocean Surface Wave Measurement Using Doppler Sonar*

R. Pinkel and J. A. Smith

---

*. Reprinted from the Journal of Geophysical Research, Vol. 92, No. C12, pp. 12,967-12,973 (1987).

JOURNAL OF GEOPHYSICAL RESEARCH, VOL. 92, NO. C12, PAGES 12,967–12,973, NOVEMBER 15, 1987

Open Ocean Surface Wave Measurement Using Doppler Sonar

R. PINKEL AND J. A. SMITH

Marine Physical Laboratory, Scripps Institution of Oceanography, University of California, San Diego, La Jolla

In October–November 1983, Doppler sonars mounted on the research platform *Flip* were used to scatter 75-kHz sound from the underside of the sea surface at low angle, as well as from the interior of the mixed layer. Surface gravity waves were seen in velocity estimates from the surface scattering sonar, even though the wave conditions were unusually calm. Valid measurements of sea surface motion were obtained over the range interval 600 to 1400 m from *Flip*. A second sonar which transmitted horizontally and scattered from the interior of the mixed layer also sensed surface waves, although with amplitude reduced in proportion to the decay of the motions with depth. Wave number-frequency spectra of the observed motions are consistent with linear theory. The existence (emergence) of this technology enables the synthesis of kilometer-long surface wave arrays in the open sea, without the cost and logistical support usually associated with large-aperture arrays. In addition, the Doppler acoustic approach can provide information on lower-frequency surface currents and on the spatial variations in these low-frequency currents, such as Langmuir cells, which might affect wave propagation.

1. INTRODUCTION

In October and November 1983, a series of mixed layer and upper ocean observations were made from the research platform *Flip*, in conjunction with the Mixed Layer Dynamics Experiment (MILDEX). The experiment was centered at 34°N, 127°W, approximately 500 km west of Point Conception, California, in water 4 km deep. Six Doppler sonars were mounted on *Flip*'s hull, with the objective of remotely profiling the velocity field in the mixed layer and upper thermocline. One of the sonars, mounted at a depth of 35 m, had a beam directed slightly up from horizontal. This beam traveled upward through the mixed layer for 600 m and then grazed the underside of the sea surface for a subsequent 900 m. A second sonar, mounted at a right angle in azimuth to the first, had a horizontal beam. The surface scattering was predominantly from subsurface bubbles, while zooplankton were the predominant scatterers in the mixed layer interior. From the Doppler shift of the return echo, the component of velocity parallel to each sonar beam was determined. Averages of the velocity over several minutes are useful for seeing the current patterns associated with Langmuir cells and other low-frequency mixed layer flows [*Smith et al.*, 1987]. Here we show that "single-ping" profiles, produced every 2 s, are useful for observing surface gravity waves.

Surface-scanning sonars have previously been used to trace wave breaking and bubble cloud evolution through scattering intensity variations [*Thorpe*, 1986, and references therein]. For winds greater than about 2 m/s, the 75-kHz acoustic returns described here are also dominated by scattering from near-surface bubbles, rather than scattering from Bragg resonant gravity-capillary waves [*McDaniel and Gorman*, 1982; *Thorpe*, 1986]. As a consequence, it should be possible to use the sonar intensity to trace the density of bubbles in the near-surface layer of water, as was done in the previous works of *Thorpe* [1986] and *Vagle and Farmer* [1986]. In these works it was found that intense bubble injection "events" accompany the passing crests of breaking waves, with stronger breaking resulting in greater numbers of bubbles injected to greater depth.

While bubbles constitute the dominant scattering source in this experiment, Bragg scattering (from surface gravity-capillary waves) may contribute as well. A component of the fluctuations in scattering strength in these data is seen to propagate at the phase speed of the waves. Whether this is related to the modulation of short surface waves by the swell or is a geometric consequence of tilting of the surface layer by the waves is not yet clear. New in this work is the ability to correlate the observed intensity fluctuations with the flow field, as estimated from the Doppler shift of the same sonar returns.

Doppler radar techniques have also been used to observe the ocean surface over periods of time [e.g., *Plant et al.*, 1983]. Surface-scattering radars and sonars differ in a way which may make them complementary. For moderate to grazing incident angles, radars scatter primarily through Bragg resonance with short surface waves [e.g., *Valenzuela*, 1978; *McDaniel and Gorman*, 1982]. In contrast, as has been mentioned, the 75-kHz sonars described here scatter primarily from near-surface bubbles [*McDaniel and Gorman*, 1982; *Thorpe*, 1986]. Thus radars can provide information about the short, modulated waves [e.g., *Plant et al.*, 1983], while the sonars provide information about bubble density and thus about whitecaps or breaking events [*Thorpe*, 1986; *Vagle and Farmer*, 1986]. Since the short waves are strongly coupled to the wind, and since bubbles are linked to breaking events, simultaneous radar and sonar measurements could provide information about the energy input to and output from the surface wave field.

To our knowledge, Doppler analysis of surface-scattering acoustic returns has not previously been done. In the following sections the 1983 experiment is more fully described. Examples of two- and three-dimensional wave number–frequency spectral estimates are presented. A brief discussion of the results concludes the work.

2. DATA COLLECTION

A schematic and plan view of *Flip*, as configured for MILDEX, is shown in Figure 1. Four downward looking sonars, as well as the two quasi-horizontal devices considered here, were operated continuously over an 18-day period. In operating the six sonars, it is necessary to record and process

Copyright 1987 by the American Geophysical Union.

Paper number 7C0671.
0148-0227/87/007C-0671$05.00

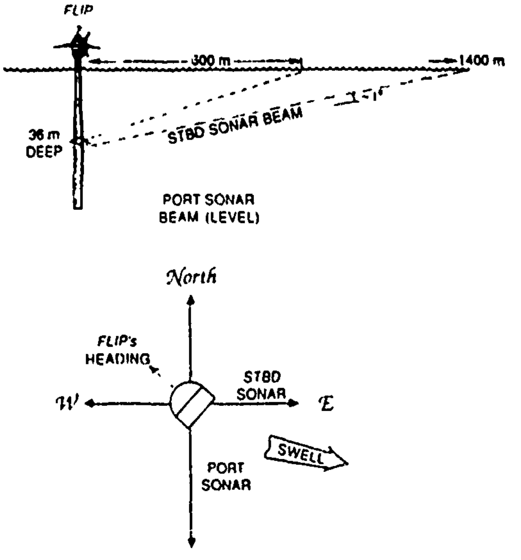

Fig. 1 (top) Schematic and (bottom) plan view of *Flip* during the data collection The east sonar beam grazed the surface; the south beam remained about 35 m below.

25,000 numbers per second. To permit continuous operation of the system, a Map 300 array processor is used to compute statistics of the raw echo data and to average these statistics over 30-s intervals On the night of October 26, 1983, 1 hour of unaveraged data from all six sonars was recorded on tape, filling one 1200-foot (366 m) tape roughly every 7 min. This was the only segment of data recorded during MILDEX which was capable of resolving surface gravity waves. During this "raw data" run, *Flip* was oriented with the starboard sonar pointing due east (90°) and the port sonar pointing due south (180°). A servo-controlled thruster, linked to the ship's gyrocompass, maintained this orientation to within ± 5°. Henceforth these sonars will be referred to as the east and south systems. The east sonar is the one which grazed the surface. The wind was steady at about 4 to 5 m/s from 30°T, and a 12-s swell of about 0.5 amplitude (1-m crest to trough) was incident from the WNW.

In operation, each sonar transmitted a sequence of four tones every 2.0 s. Velocity estimates were formed using the complex covariance technique [*Rummler*, 1968], with the covariance evaluated at a lag of 2.0 ms. The velocities shown here in Figures 2 and 3 and in Plates 1 and 2 are from covariance averages formed over the four tones and nine consecutive samples in range, corresponding to a net offset in range of 13.5 m per estimate. (Plates 1 and 2 can be found in the separate color section in this issue.) The duration of each tone (30 ms) corresponds to range averaging over 22.5 m for each sample. With nine-sample averages, the half-power points remain 22.5 m apart in range.

The "Cramer-Rao" lower bound for the rms error in the velocity estimate, $\Delta V_{\rm rms}$, is given by

$$\Delta V_{\rm rms} \Delta R \, N^{1/2} \geq c^2/8\pi f_0$$

where ΔR is the range resolution, c is the speed of sound, f_0 is the sonar carrier frequency, and N is the number of pulses incoherently averaged in forming the velocity estimate [*Theriault*, 1986]. Here it is assumed that the signal to noise ratio is very large and that the echo autocovariance is averaged in time for a duration equal to the transmitted pulse length.

For the present system, this theoretical bound is 2.7 cm/s. However, the autocovariance values used in this work have been averaged over only one half pulse length This should increase the noise bound somewhat

An empirical estimate of measurement precision can be obtained from inspection of the power spectrum of the measured velocities. Using spectral values at the highest frequencies to estimate a "white noise" level, a 9-cm/s rms error is suggested. This estimate includes any real velocity variance within the range bins. For the 12-s waves of 0.5-m amplitude seen here, the steepness is about 1/70. Averaging over phase, the rms velocity gradient is then about 1/200 s^{-1}. Within an individual range cell the actual velocity variability is of the order of 5 cm/s. This geophysical variability can plausibly account for the difference between the lower bound and empirical error estimates.

The horizontal width of the acoustic beams is about 2.2°, to the half-power points. At a typical range of 1 km, the surface footprint of each velocity estimate on the east sonar is 22.5 m (range) by 40 m (across beam). For the south beam, the vertical spread of 0.44° also enters, yielding a sample volume at 500-m range of about 22.5 × 20 m horizontally by 4 m vertically, centered somewhere between 25- and 45-m depth depending on the instantaneous tilt of *Flip*.

In general, surface scattering may arise from either gravity-capillary waves at the surface or bubbles just below. The 75-kHz sound used here scatters resonantly from bubbles of about 40-μm radius near the surface. This is near the observed peak in bubble size spectra [*Johnson and Cooke*, 1979]. In typical conditions, the subsurface bubble cloud is the dominant scatterer [*McDaniels and Gorman*, 1982; *Thorpe*, 1986]. The bubble cloud has been observed to decrease roughly exponentially with depth [*Thorpe*, 1986]. The depth scale of the decay increases slightly with wind strength, from about 0.4 m for 4-m/s winds (at 10 m) to about 0.7 m for 10-m/s winds. For given wind conditions, this depth scale remains quite constant, although the absolute intensity at a specific depth can vary by 2 orders of magnitude [*Thorpe*, 1986]. The depth scale of the "surface measurements" shown here is taken to be about 0.4 m below the instantaneous surface. In this experiment, the surface-backscattered (east) intensity is observed to be about 35 to 40 dB greater than the nonsurface (south) intensity at the greatest ranges. Thus although the farthest south ranges are lost to noise, the east sonar signal remains quite strong over the full 1400 m.

Sheltering of distant wave crests by the nearer troughs can occur for the surface-grazing beam. However, it is probably not a significant factor in these calm weather measurements. At the farthest range, 1400 m, the upward angle to the surface from 35-m depth is about 1/40. Again, the maximum slope of the dominant 12-s swell observed is about 1/70. Thus the rms slope is just slightly over half the minimum slope of the beam. Sheltering must be infrequent.

The passage of the wave crests causes *Flip* to oscillate. The horizontal motion of the attached sonars appears as a range independent velocity fluctuation. This range independent signal has been removed in the subsequent analysis to facili-

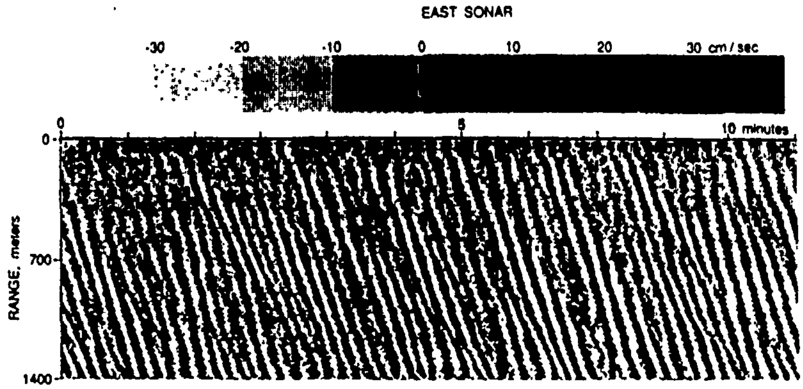

Fig. 2 An 11-min record of velocity data from the east sonar. Surface return dominates from about 600 m to 1400 m Note the wavelike disturbances propagating away from *Flip* The individual "stripes" correspond to peaks (white) and troughs (black) of the waves as they propagate away from *Flip*. The broader "bands" of higher-intensity fluctuations correspond to groups of waves The group velocity (represented by the slope of these bands) is about half the phase velocity (the slope of individual stripes) See Plate 1

tate observation of the waves. The range independent response is roughly equal in the two beams

Surface gravity wave propagation is evident in the data from both sonars (Figures 2 and 3; Plates 1 and 2) The dominant wave frequency is 12 s The observed crest to trough fluctuation in orbital velocity is of the order of 60 cm/s, corresponding to a wave of 0.5-m amplitude

Swell propagation also appears in the surface backscattering intensity signal of the east sonar, to a small extent. To bring this out, a time average of intensity at each range can be removed. This reduces the effects of beam spreading and attenuation with range. Additional variations of intensity with range due to tilting of *Flip* are then reduced by subtracting a least squares-fitted quadratic curve from the intensity versus range of each ping. A sample of the resulting intensity anomaly field is shown in Figure 4 and Plate 3. (Plate 3 can be found in the separate color section in this issue.) Clear signs of fluctuations in scattering strength which propagate at the wave phase speed are seen. To further investigate, the cross spectrum $\langle V(k)I^*(k)\rangle$ between the east sonar velocity and intensity anomaly has been calculated for various wave numbers, averaging over the entire data set. The associated coherence and phase estimates are presented in Table 1. To provide a rough estimate of the effective degrees of freedom, the total averaging time (~ 56.1 min) is divided by the maximum period corresponding to each wave number k (i.e., assuming the waves to be going due east) The corresponding standard deviations from zero (68% confidence levels) are shown in the last column of Table 1. The most significant correlations, for wave numbers 3 ($\lambda = 285$ m) and 5 ($\lambda = 170$ m), correspond to the strongest scattering located about 65° to 70° toward *Flip* from the trough, on the rising face of the waves (the face tilted toward *Flip*, when viewed from below). This might be an indication that the scatterers (e g., Bragg-resonant short surface waves) are preferentially enhanced on the forward faces of the swell. Alternatively, the effect might be explained by simple geometric deformation of the surface layer by the passing swell.

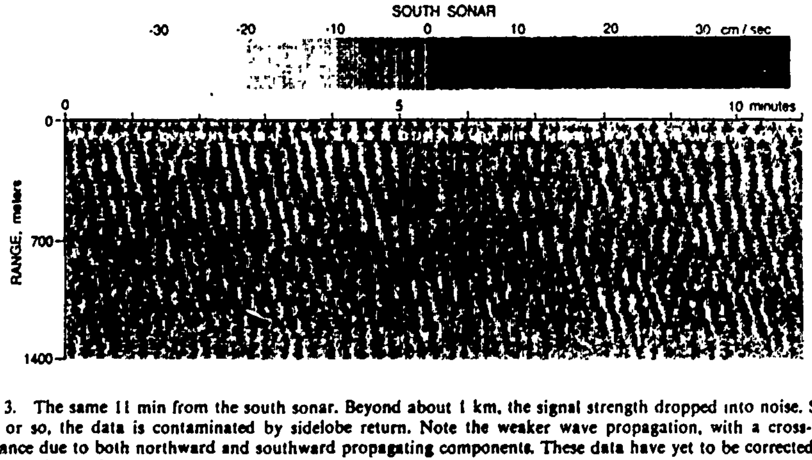

Fig. 3. The same 11 min from the south sonar. Beyond about 1 km, the signal strength dropped into noise. Short of 120 m or so, the data is contaminated by sidelobe return. Note the weaker wave propagation, with a cross-hatched appearance due to both northward and southward propagating components. These data have yet to be corrected for the exponential decay of wave velocity with depth. See Plate 2.

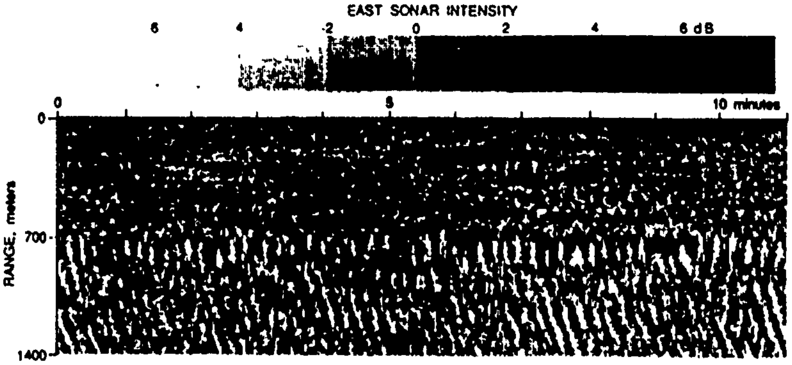

Fig. 4. Intensity anomaly versus range and time, from the east sonar, as for velocity in Figure 2 and Plate 1. Note the suggestion of fluctuations moving away from *Flip*, especially at the far ranges. Surface returns dominate from roughly 600 m to 1400 m. See Plate 3.

3. ONE-COMPONENT WAVE NUMBER-FREQUENCY SPECTRA

Wave number frequency spectra are presented here for each beam separately. The spectral estimates are of velocity variance, $\langle U^2 \rangle$ and $\langle V^2 \rangle$, as a function of both frequency and the along-beam component of wave number. These are formed from 26 sequential data samples, each consisting of 64 ranges by 64 pings (864 m by 128 s). The total averaging time is about 55 min.

At any given frequency, waves incident on a single beam at some angle θ will produce a signal with an along-beam wave number component $k \cos \theta \leq k$. In addition, the sonar detects only the component of orbital velocity parallel to the beam, $\hat{u} = u_{orb} \cos \theta$. Thus for free waves at a frequency ω with an isotropic directional distribution, the one-beam wave number spectrum would have sharp high-wave number cutoffs at $k = \pm \omega^2/g$ (at the dispersive values). Within these cutoffs, the fraction of power detected is proportional to $\cos^2 \theta$.

3.1. *East Sonar*

The east sonar grazes the surface from about 600 m to 1400 m. The wave number-frequency spectrum (Figure 5) was calculated from these far ranges, after removing the range-independent velocity (the mean). Thus, Figure 5 is derived from a double Fourier transform of Figure 2/Plate 1. As shown, almost all of the detected energy is on the $+k$ half, corresponding to eastward propagation. In addition, the energy is very strongly concentrated near the maximum (dispersion) wave number, indicating that the swell is oriented so that propagation is very nearly straight down the beam (i.e., from the west).

The highest frequency wave activity evident in Figure 5 is near 0.15 c/s (or 6.7-s period), at the upper right-hand corner. The corresponding wavelength is about 70 m (14 c/km). Higher-frequency activity is suppressed owing to the 22.5-m range averaging acting on the shorter associated wavelengths.

3.2. *South Sonar*

To produce data from the south sonar comparable to those from the east, additional processing is required. As *Flip* tilts in response to the waves, the sonar beam moves vertically through the existing shear. This introduces a spatially varying trend as well as a mean in the velocity data. This trend also must be removed from each 2-s profile. A nonuniform shear (e.g., a thin shear layer at the thermocline) could introduce higher spatial harmonics, correlated with the wave frequencies, as well. For now, we neglect this potential problem. In future experiments, when properly designed "side scan" type transdu-

TABLE 1. Coherence and Phase of Velocity and Intensity From the East Sonar

Cycles per 864 m	Wavelength, m	Phase, deg	Coherence	68% Estimate
1	864	12.8345	0.0166	0.0840
2	432	111.3184	0.0141	0.0707
3	288	65.1740	0.2351	0.0639
4	216	50.9758	0.0848	0.0594
5	173	71.6068	0.1646	0.0562
6	144	73.2922	0.0910	0.0537
7	123	79.7480	0.0900	0.0517
8	108	74.8335	0.0777	0.0500
9	96	83.3032	0.0685	0.0485
10	86	77.7762	0.0680	0.0473
11	79	69.6089	0.0339	0.0462
12	72	84.0478	0.0226	0.0452

Phase angle increases toward *Flip* from the wave trough (at 0°). The coherence at the 68% significance level is estimated in the right-hand column. The 68% level is exceeded for wavelengths between 86 and 288 m.

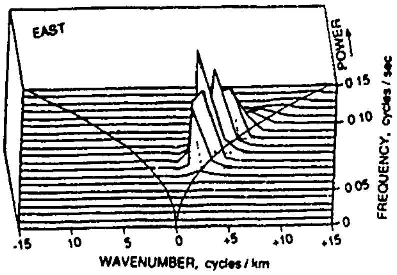

Fig. 5. The frequency-wave number spectrum from the east sonar. Each transverse line represents energy variations with wave number at a set frequency. The two curves crossing the frequency lines give the theoretical dispersion relation $\omega^2 = gk$. Positive k (right) corresponds to eastward propagation (away from *Flip*).

cers are used, the effect of platform motion will be much less significant.

Wave orbital velocity decays exponentially with depth. To correct for this decay, the wave number magnitude is estimated from the measured frequency using the linear dispersion relation. A single correction factor is then applied at each frequency. The adjusted frequency-wavenumber spectrum for the South sonar is shown in Figure 6.

From examining the single-beam spectra shown in Figures 2 and 3 and in Plates 1 and 2, it appears that the swell was propagating more from the west than from the northwest. The "eastward" side (positive wave numbers) of Figure 2/Plate 1 is much more energetic than the "westward," with a sharp cutoff at the wave number matching dispersion. In contrast, the "southward" energy levels (positive wave numbers) of Figure 3/Plate 2 exceed the "northward" only slightly. The power in the south beam spectrum tends to peak at wave numbers smaller than the maximal value given by linear dispersion.

4. A DIRECTIONAL-FREQUENCY SPECTRUM

To demonstrate the potential of this observational system, the three-dimensional wave number-frequency power spectrum $S_{kl\omega}$ is estimated (Figure 7). No attempt is made to "optimize" the estimate using advanced signal processing techniques. Rather, an extremely simple Mills cross processing scheme is used [*Pinkel*, 1981], with the objective of illustrating the inherent strengths and weaknesses of the approach. As with the single-beam spectra, these are spectra of surface velocity, not elevation. Recall that a surface wave elevation spectrum with an ω^{-5} frequency dependence corresponds to a velocity spectrum with an ω^{-3} dependence. For reference, the peak spectral value (in Figure 7*e*) times the $\Delta\omega\Delta k\Delta l$ cube surrounding it, $(2\pi/64\ \mathrm{s})(2\pi/864\ \mathrm{m})^2$, corresponds to a velocity amplitude of 5.24 cm/s, or an elevation amplitude of 12 cm, rms.

The "Mills cross technique", as applied to data from a pair of orthogonal sonar beams, can be summarized as follows. The east and south velocity measurements are written as

$$U(x, 0, t) = \mathrm{Re} \sum_k \sum_l \sum_\omega \cos\theta\ \omega A_{kl\omega} e^{i(kx-\omega t)}$$

$$V(0, y, t) = \mathrm{Re} \sum_k \sum_l \sum_\omega \sin\theta\ \omega A_{kl\omega} e^{i(ly-\omega t)}$$

Here x is the eastward coordinate and U the eastward velocity component, y and V are northward, the angle θ is reckoned from east (x), and $A_{kl\omega}$ is the amplitude of a surface wave spectral component. Note the $\cos\theta$ (or $\sin\theta$) response of the sonars: only the radial component of velocity is detected by Doppler shift.

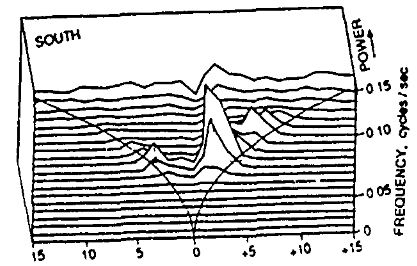

Fig. 6. The frequency-wave number spectrum from the south sonar. Positive k (to the right) corresponds to southward propagation (away from *Flip*).

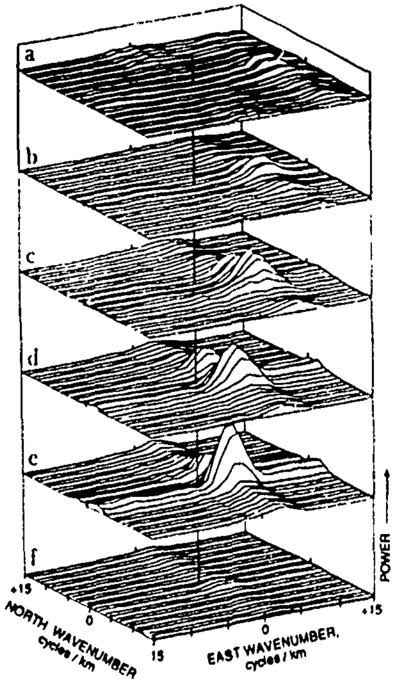

Fig. 7. The three-dimensional power spectrum, $S_{kl\omega}$, estimated from the sonar velocity data. Each surface represents the velocity variance (energy) as vertical displacements at each location on the (k, l) plane, in the frequency band corresponding to periods of (*a*) 7.1 to 8.0 s, (*b*) 8.0 to 9.1 s, (*c*) 9.1 to 10.7 s, (*d*) 10.7 to 12.8 s, (*e*) 12.8 to 16 s, and (*f*) 16 to 21 s. The vertical displacement between frequency planes corresponds to a spectral density of 885 m^4/s (units of velocity squared per $\Delta\omega\ \Delta k\ \Delta l$, using radians, meters, and seconds). The peak value (in Figure 7*e*) is about 520 m^4/s.

Several processing steps are required to produce the spectral estimate. First, the frequency transforms u, v, of the time series U, V, at each selected range along each beam are taken. Here, 64 "range bins" have been selected along each beam: from 135 m to 999 m along the south (subsurface) sonar, and from 540 m to 1404 m along the east (surface scattering) sonar. Time series of 1024 points (34 min) are transformed at each range bin. A 64 × 64 element cross-covariance matrix, $C_\omega(x, y) \equiv \langle u(x, 0, \omega)v^*(0, y, \omega)\rangle$, is then formed for six analysis frequencies, ω. Statistical stability is achieved through averaging products from 32 Fourier frequency bands into the covariance matrix at each analysis frequency. Note that

$$C_\omega(x, y) = \sum_k \sum_l \sin\theta \cos\theta\ \omega^2 \langle AA^* \rangle e^{i(kx-ly)}$$

Fourier transformation of this cross-covariance matrix leads directly to an estimate of $\omega^2\langle AA^*\rangle$ and hence of the spectrum. However, this estimate of the spectrum will be real only if $C_\omega(x, y) = C_\omega^*(-x, -y)$. Such a covariance matrix occurs when a true Mills cross array is used, with the origin of the coordinate system centered at the intersection of the legs of the array. In the present system, the two legs of the array never meet, and Fourier transformation of the spatial data results in an estimate of the wave number-frequency spectrum which is complex. The complex nature of this spectral estimate is an artifact of little importance, as can be seen from the following considerations. Suppose the east spatial array is centered at point $x = X$ rather than $x = 0$. The y data are similarly centered at $y = Y$. We now change variables, writing $\hat{x} = x - X$, $\hat{y} = y - Y$, which yields

$$C_{ij}(\hat{x}, \hat{y}) = \sum_{k} \sum_{l} \sin\theta \cos\theta \, \omega^2 \langle AA^* \rangle e^{ik\hat{x} - il\hat{y}} e^{ikX - ilY}$$

The digital Fourier transform of this is

$$F_{k,l,\omega} = \frac{1}{2L_x} \frac{1}{2L_y} \int_{-L_x}^{L_x} \int_{-L_y}^{L_y} C_{ij}(\hat{x}, \hat{y}) e^{-ik_n\hat{x} + il_n\hat{y}} \, d\hat{x} \, d\hat{y}$$

$$= \sin\theta \cos\theta \, \omega^2 \langle AA^* \rangle e^{ik_nX - il_nY}$$

Finally, the power spectral estimate of wave orbital velocity is

$$S_{(k_n,l_n,\omega)} = \omega^2 \langle AA^* \rangle / \Delta k \Delta l \Delta \omega = \frac{F_{k,l,\omega}}{\sin\theta \cos\theta} \frac{e^{-ik_nX + il_nY}}{\Delta k \Delta l \Delta \omega}$$

The effect of the spatial offset in the legs of the array can be corrected either by multiplying by $e^{i(k_nX - l_nY)}$ or by noting simply that the absolute value of the output of the two-dimensional Fourier transform provides the desired spectral estimate.

Several aspects of this "simplest method" should be noted. First, the $\sin\theta \cos\theta$ response function implies that no estimate is available along either axis (north or east). This is because only cross products between beams are used. Additional information is contained in correlations along each beam separately but is neglected here. (In Figure 7 the spectral estimates along each axis were set to zero, and then 3 × 3 smoothing in the (k, l) planes was applied. This effectively interpolated the on-axis spectral estimates from adjacent values.) Second, estimates adjacent to each axis are contaminated by noise, due to amplification by the $1/\sin\theta \cos\theta$ factor. This effect is noticeable in Figure 7*a* (the highest-frequency plane): ridges appear near the axes at higher wave numbers (though spread out slightly by the 3 × 3 smoothing). Third, statistical sampling errors lead to artificially large correlation magnitudes along crosses centered on any large "true" power estimate (see, for example, Figure 7*e*). For a band average over 32 frequencies, the magnitude of this effect is about 0.18 times the product of the two amplitudes, which is further magnified by the $\sin\theta \cos\theta$ response correction. This results in ridges leading away from the large amplitude peaks in Figure 7, which flare up both near the axes and at high wave numbers as either $\sin\theta$ or $\cos\theta$ approaches zero.

The directional-frequency spectrum shown in Figure 7 is consistent with the visual observations. The swell is highly directional, from the WNW. While the peak amplitude in Figure 7 appears in the 13- to 16-s band, the mean period is closer to 12 s, owing to the sharp low-frequency cutoff and broader high-frequency decay. As frequency increases, the peaks in Figure 7 move toward higher wave numbers and also move closer to the east axis. This last effect is perhaps an artifact of the analysis. Recall that the south sonar data is amplified to compensate for exponential decay with depth. The higher the frequency, the noiser the resulting south sonar data is. With finite statistical precision, there is a finite contribution to the correlation estimates near the east axis from the product of amplified noise and the (genuine) east component velocities. These are further amplified by the $\sin\theta \cos\theta$ correction. Thus the true peaks may be further from the east axis than is shown in Figure 7.

These trial estimates demonstrate the potential of surface-grazing Doppler sonar for detecting directional-frequency spectra of open ocean surface waves. Many of the difficulties discussed above could be avoided by implementing two (or more) surface-grazing beams. With more sophisticated analysis techniques [c.f. *Long and Hasselmann*, 1979; *Lygre and Krogstad*, 1986], greatly enchanced estimates should be possible.

5. SUMMARY AND DISCUSSION

During a period of fairly gentle 12-s swell, a surface-grazing Doppler sonar was used to observe surface wave propagation along a nearly 1 km path. The sonar sampled the motions every 2 s, with 22.5-m range resolution. Propagating surface waves were seen in the Doppler velocity estimates and also, to a lesser extent, in the backscattering intensity. The weak maxima in scattering intensity appeared to occur on the forward faces of the waves.

Three-dimensional wave number-frequency spectra were estimated using the Doppler data. Wave motions were resolved to periods as short as 7 s (70-m wavelength) in these spectra. The influence of linear dispersion was clearly seen. The noisiness of the south sonar, due to the exponential decay with depth of the waves, introduced some uncertainty in interpreting the rather simple estimates produced here. Considerable improvement can presumably result by using two (or more) surface-scattering beams and more sophisticated analysis techniques. Our intent here is to point out the existence and the potential of this surface-scanning acoustic Doppler technique for measurement of directional spectra and breaking events.

An ideal sonar for this type of work would transmit a fan-shaped beam, broad in the vertical plane but narrow in azimuth. This would illuminate (ensonify) the sea surface more evenly than the vertically narrow beams used here. With fan-shaped beams the return intensity would be more easily related to bubble density. Also, platform motion would become a less significant problem. Pitch and roll of the transducer would affect the output very little. Only yaw, variation in azimuth, would need to be suppressed. Thus surface wave measurement from subsurface moorings or from slowly moving ships becomes a possibility. Intensity variations can also be used to observe breaking events and the subsequent decay of the resulting bubble cloud [*Thorpe*, 1986; *Vagle and Farmer*, 1986], providing a useful supplement to the surface wave directional information. The prospect of being able to measure surface wave propagation continuously for distances greater than a kilometer, to sense the surface currents which interact with the wave field, and to get a measure of breaking activity (bubble formation) using a single instrument encourages further study and development.

Acknowledgments. This work was supported under Office of Naval Research contract N00014-79-C-0472. We would like to thank Lloyd Green, Steve Beck, Eric Slater, Mike Goldin, and the crew of the research platform *Flip* for assistance in collection of the data.

REFERENCES

Johnson, B. D., and R. C. Cooke, Bubble populations and spectra in coastal waters, *J. Geophys. Res.*, *84*, 3761–3766, 1979.

Long, R. B., and K. Hasselmann, A variational technique for extracting directional spectra from multi-component wave data, *J. Phys. Oceangr.*, *9*(2), 373–381, 1979.

Lygre, A., and H. E. Krogstad, Maximum entropy estimation of the directional distribution in ocean wave spectra, *J. Phys. Oceanogr.*, *16*(12), 2052–2060, 1986.

McDaniel, S. T., and A. D. Gorman, Acoustic and radar sea surface backscatter, *J. Geophys. Res.*, *87*, 4127–4136, 1982.

Pinkel, R., On the use of Doppler sonar for internal wave measurements, *Deep Sea Res., Part A*, *28*, 269–289, 1981.

Plant, W. J., W. C. Keller, and A. Cross, Parametric dependent of ocean wave-radar modulation transfer functions, *J. Geophys. Res.*, *88*, 9747–9756, 1983.

Rummler, W. D., Introduction of a new estimator for velocity spectral parameters, *Rep. MM-68-4141-5*, Bell Telephone Lab., Murray Hill, N. J., 1968.

Smith, J. A., R. Pinkel, and R. A. Weller, Velocity structure in the mixed layer during MILDEX, *J. Phys. Oceanogr.*, *17*(4), 425–439, 1987.

Theriault, K. B., Incoherent multibeam Doppler current profiler performance, I, Estimate variance, *IEEE J. Oceanic Eng.*, *OE-11*, 7-15, 1986.

Thorpe, S. A., Bubble clouds: A review of their detection by sonar, of related models, and of how K_r may be determined, in *Oceanic Whitecaps and Their Role in Air-Sea Exchange*, 294 pp., D. Reidel, Hingham, Mass., 1986.

Urick, R. J., *Principles of Underwater Sound*, 2nd ed., McGraw-Hill, New York, 1975.

Vagle, S., and D. Farmer, Sea surface studies using underwater sound FASINEX, Preliminary Results (abstract), *Eos Trans. AGU*, *67*, 1034, 1986.

Valenzuela, G. R., Theories for the interaction of electromagnetic and oceanic waves—A review, *Boundary Layer Meteorol.*, *13*, 61–85, 1978.

R. Pinkel and J. A. Smith, Marine Physical Laboratory, Scripps Institution of Oceanography, University of California, San Diego, La Jolla, CA 92093

(Received October 2, 1986;
accepted July 30, 1987.)

Long-Period Acoustic and Seismic Measurements and Ocean Floor Currents*

Spahr C. Webb

---

*. Reprinted from the IEEE Journal of Oceanic Engineering, Vol. 13 (4), pp. 263-270 (1988).

IEEE JOURNAL OF OCEANIC ENGINEERING, VOL. 13, NO. 4 OCTOBER 1988

Long-Period Acoustic and Seismic Measurements and Ocean Floor Currents

SPAHR C. WEBB

(Invited Paper)

Abstract—Pressure fluctuations caused by a strong ocean floor current are evident during most of an eighty-day-long record of very low-frequency acoustic ambient noise measured by an instrument on the seafloor in the western Atlantic. The differential pressure gauges on the instrument produce useful measurements over a wide frequency band extending from 0.0005 to 16 Hz. The spectrum of current-induced pressure fluctuations is red with a power law dependence on frequency with an exponent of 1.5. Turbulence in the ocean floor boundary layer is the source of these pressure fluctuations rather than the effects of flow around the transducers. This record of boundary-layer pressure fluctuations is used to predict the effect of seafloor currents on long-period seismograph measurements from the seafloor and from under the seafloor in boreholes.

I. INTRODUCTION

THE FOCUS of this paper is the problem of measuring very low-frequency seismic and acoustic signals on the deep seafloor in the presence of deep ocean currents. A recent resurgence of interest in measurements at frequencies below 1 Hz has lead to the first deployments on the seafloor of coherent arrays of seismometers and pressure transducers [1]-[3], and we may soon see the first new deployments of long-period seismometers on the deep seafloor after nearly 20 years [4]. Ocean floor currents must be considered in the site selection for these experiments.

In this paper, only measurements from instruments deployed directly on the seafloor or deployed into boreholes below the seafloor are considered. Acoustic wavelengths at frequencies below 1 Hz are too long for efficient trapping of acoustic waves within the sound channel, so mid-water column measurements are not required. While interface waves may interfere with seafloor acoustic measurements, these deployments are logistically much simpler than mid-water measurements which may require a freely drifting instrument to avoid the problem of cable strum [5].

Pressure fluctuations in the band from about 0.0005 to 32 Hz can now be measured using differential pressure gauges [6]. These gauges were developed during several experiments sited in the eastern Pacific [7], [8]. Those measurements demonstrated that most data collected previously with conventional hydrophones had been badly contaminated by noise of electronic origin at all frequencies below about 0.3 Hz [9]. Estimates of the pressure spectrum from several deep sites in the eastern Pacific are remarkably similar in appearance (Fig. 1). The spectrum rises toward lower frequency into the well-known microseism peak between 0.1 and 0.5 Hz. The spectrum then falls abruptly 40 to 60 dB at slightly lower frequencies into what has been termed the "noise notch." Below the noise notch the spectrum of pressure fluctuations rises sharply again, as the direct pressure signal associated with long waves on the surface of the ocean reaches the deep seafloor. At still lower frequencies, the spectrum continues to rise slowly except for sharp peaks associated with the tides [10].

The spectrum of the displacement of the seafloor is quite

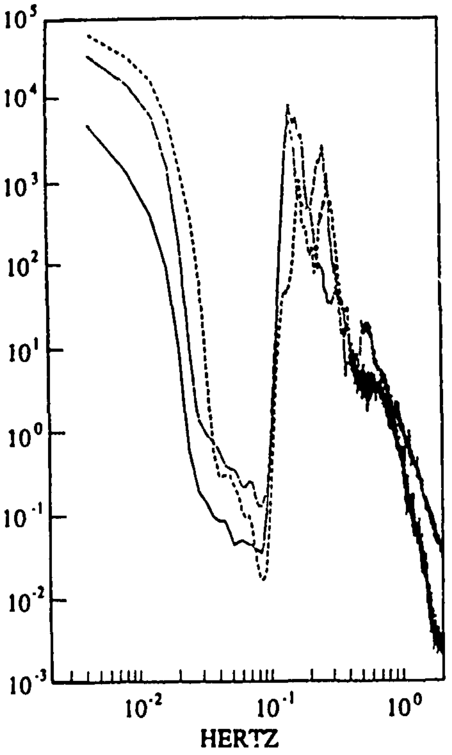

Fig. 1. The spectrum of pressure fluctuations in the band from 0.002 to 2 Hz, measured at three sites in the eastern Pacific.

Manuscript received January 27, 1988; revised July 25, 1988. This work was supported in part by ONR under Contract no N00014-85-C-0001 and by a WHOI postdoctoral fellowship.

The author is with the Marine Physical Laboratory of the Scripps Institution of Oceanography, University of California, San Diego, La Jolla, CA 92093.

IEEE Log Number 8823798

0364-9059/88/1000-0263$01.00 © 1988 IEEE

similar across this entire band although the noise notch is probably not as deep [11]. Both long-period pressure and seismometer spectra can look very different in shallow (continental shelf) regions [12], but not always [13]; however, I will not discuss that very different regime here.

An eighty-day time series of pressure fluctuations in a frequency band from 0.005 to 8 Hz was obtained during the Fall of 1985 from the deep seafloor in the western Atlantic. The site of this experiment was chosen to address a single problem: Do deep ocean currents limit seafloor acoustic measurements at very low frequencies? Of particular interest was whether the noise level in the "noise notch" was set by flow noise or by some other process. Strasberg [14], [15] provides an excellent theoretical discussion of how ocean currents may influence seafloor acoustic measurements. I have found no relevant published measurements. Flow noise problems at frequencies above 1 Hz are mostly caused by the strumming of cables and other noise associated with the flow around the transducers. At lower frequencies the mechanism of current-related noise is different. The flow velocity is reduced near the seafloor where the measurements are made, so the disturbances around the transducers are small. The pressure fluctuations associated with turbulent eddies in the ocean floor boundary layer do not diminish toward the seafloor, and so are larger than the disturbances associated with the flow around the transducers when the transducers are mounted close to the seafloor. This paper ends with a discussion of the problems associated with seismometers exposed to these bottom currents and the advantages of deploying a seismometer in a borehole.

II. HEBBLE AND THE SEAFLOOR MEASUREMENTS

Photographs from large regions of the deep seafloor show furrows and ripples in the sediments clearly associated with strong currents. A compilation of these photographs suggests that strong seafloor currents may frequently occur along the western edges of all the ocean basins and under the Antarctic circumpolar current [16]. Broad regions of the shelves also experience strong currents.

A small patch of the Nova Scotia Rise has been the site of a multiyear, multidisciplinary experiment designed to study the effects of bottom currents on the geology and biology of the area. The experiment was given the acronym HEBBLE for High Energy Benthic Boundary Layer Experiment. This experiment is described in a special volume of *Marine Geology* [17].

A long-term deployment of several bottom lander tripods during the Fall and Winter of 1985/86 provided an opportunity to obtain measurements of the effect of currents on pressure measurements. A differential pressure gauge was placed on each of the three corners of a HEBBLE tripod. The tripod stands 6 m high and is 3 m along a side at the base. The transducers are 30 cm long and 20 cm in diameter and were mounted 0.9 m off the seafloor inside of fiber-filled cylindrical plastic cases of slightly larger dimensions (25 cm diameter × 40 cm height). These cases served to reduce the direct effect of flow on the sensors and to slow temperature fluctuations near the sensors (Fig. 2).

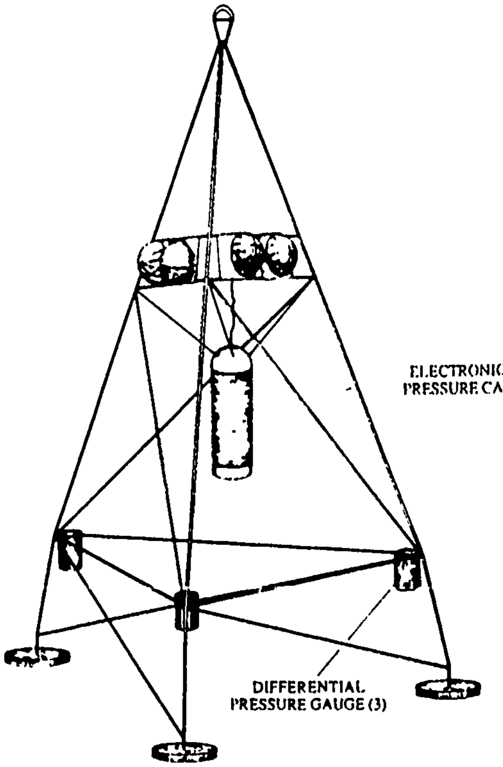

Fig. 2. The differential pressure gauges deployed in the three corners of a HEBBLE tripod. The base below the transducers detaches for recovery. Two acoustic releases and a small camera were mounted near the top of the tripod. The recorder and analog electronics are housed in the 12" O.D. pressure case hung from the upper platform of the tripod.

This tripod was deployed in 4817 m of water at the HEBBLE site on the Nova Scotia Rise (40°21.57′ N, 62° 21.57′ W) on September 21, 1985, and was recovered in April, 1986. A small cartridge tape drive was used to record eighty-three days of data starting on September 22, 1985, and ending December 14, 1985. The battery and tape capacity limited the length of the record. The recording schedule was set so that six contiguous, one-hour-long records sampled at 1 Hz and one, 225-second-long record sampled at 16 Hz were collected each day. No data was saved during the remainder of the day.

Dr. A. J. Williams of the Woods Hole Oceanographic Institution (WHOI) deployed several other tripods within 100 m of the site. Three components of current velocity were measured by BASS (Benthic Acoustic Stress Sensor) sensors mounted on a nearby tripod at six heights from 1 to 5 m. These sensors are small baseline acoustic time-of-flight flow sensors, well suited for measurements of turbulence. A record of the mean current was derived from 15 min averages of the data from the sensor at 5 m. The current varies on time scales from weeks to months (Fig. 3), characteristic of ocean eddies [18]. There is also evidence of an inertial or tidal cycle with a peak-to-peak amplitude of about 5 cm/s.

Estimates of the pressure spectrum derived from the pressure record show clearly the effect of strong bottom

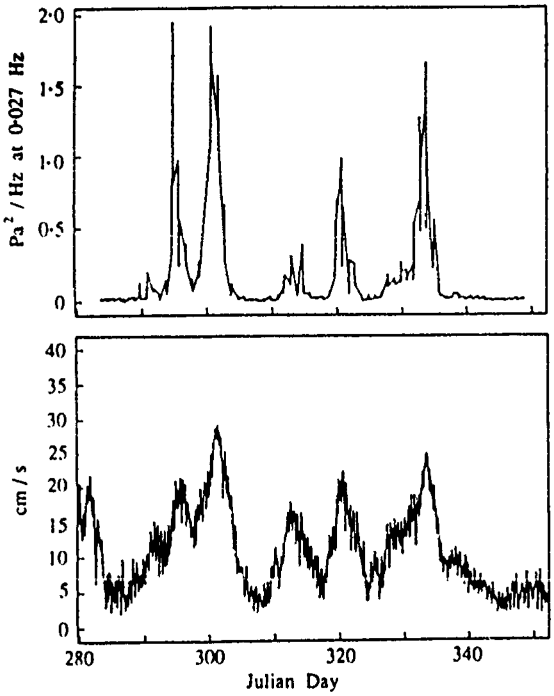

Fig. 3 The spectral density in a band near 0.027 Hz versus time in days (top graph) The mean current at 5 m (15 min averages, from an adjacent tripod) versus time in days (bottom graph)

currents on the pressure fluctuations measured at the seafloor Fig. 4 displays two spectra, one obtained on a day when the mean current velocity (at 5 m) was less than 5 cm/s, and another on a day with currents greater than 30 cm/s. The spectrum of pressure fluctuations associated with the current is red, with a power law dependence of $f^{-1.5}$.

There is an obvious relationship between the power in the pressure spectrum in a fixed frequency band (near 0.027 Hz) and the current record (Fig. 3). The record of pressure fluctuations in this diagram is incomplete since the data were only recorded for 6 hours per day The pressure signal is much larger during the intervals of strong bottom current. The relationship between the pressure fluctuations and the current is demonstrated in a scatter plot of the spectral density in the band near 0.027 Hz versus the current velocity (Fig. 5) The scatter plot suggests the seafloor pressure spectrum varies as the current to the fourth power. The scatter in the plot is an indication of the variance associated with an estimate of the mean flow over the finite averaging time, and other measures of the turbulence display similar variance. In the next section, a model of the turbulent pressure fluctuations under a boundary layer shall be considered and this theory compared against these measurements.

III. Boundary Layer Turbulence

A hydrophone, pressure transducer, or seismometer when placed in a current will measure two fluctuating components, one associated with turbulent fluctuations existing in the ocean current which are advected past the sensor, and the other component associated with turbulence generated by current flow around the sensor Perhaps surprisingly, the flow noise associated with the flow around the sensors will be shown to be of secondary importance when the sensors are deployed close to the seafloor.

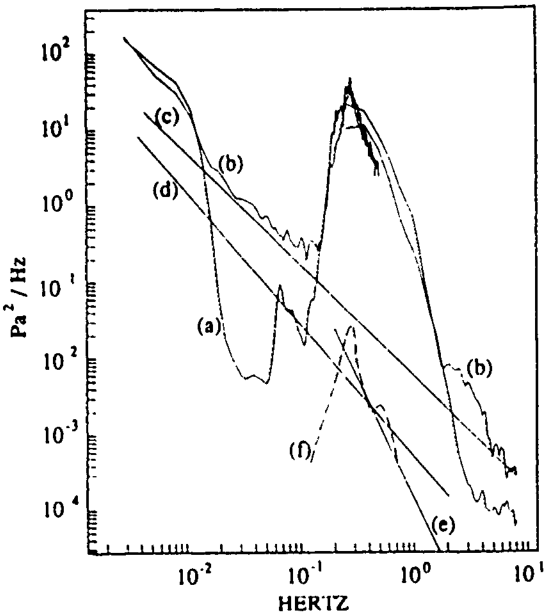

Fig 4 Pressure spectra derived from two sets of measurements under different current conditions (a) less than 5 cm/s, and (b) 30 cm/s Four models of flow noise sources are also plotted (c) the model derived in this paper for boundary-layer pressure fluctuations (the line has a slope of −1.5), (d) Strasberg's model for boundary-layer turbulence, (e) an estimate of the noise caused by flow around the transducer, and (f) a second spectrum derived from measurements of pressure upstream of a cylinder (the amplitude is scaled arbitrarily)

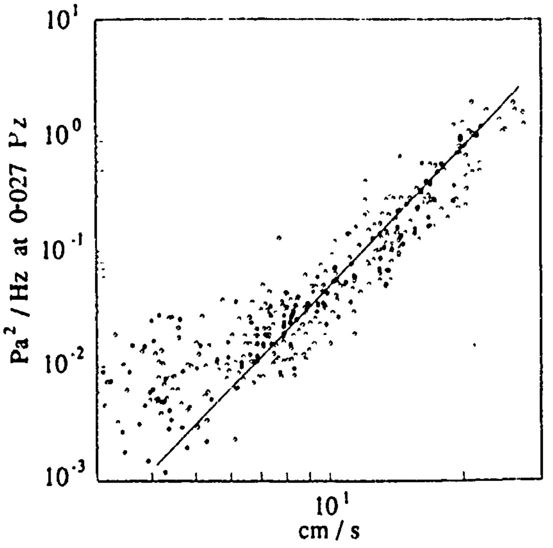

Fig 5 Scatter plot of the spectral density in a band near 0.027 Hz versus the mean current at a 5 m height A line with a slope of four is plotted on the figure

A drag coefficient of about 0.001 leads to a value of the corner frequency of $\omega_0 \approx 80F \approx 0.008$ rad/s at the latitude of the HEBBLE site. If the drag coefficient formulation is valid, the corner frequency is independent of the velocity in the boundary layer. A single drag coefficient is probably only valid over a narrow range of velocities, but this result is a useful first approximation.

Under these assumptions this model for the pressure fluctuations at the seafloor from the turbulence in the bottom boundary layer becomes

$$S_P(f) \approx 14\,200(U_5)^4 \left(1+\left(\frac{f}{.00127}\right)^{1/2}\right)^{-3}.$$

Here $C_D = 0.001$, $\rho = 1000$ kg/m^3, U_5 is velocity at 5 m in m/s, and f is frequency in Hz. The units of the spectrum S_p are Pa^2/Hz. The limiting form at high frequencies becomes

$$S_P(f) \approx .6(U_5)^4 f^{-1.5}.$$

Strasberg [14] also used Elliot's data to predict the pressure spectrum of turbulence in the ocean floor boundary layer. He suggests

$$S_P(f) \approx .5(U_\infty)^{5.7} f^{-1.7}$$

which differs slightly from the expression derived above, probably because of a slightly different treatment of the scaling problem for the boundary-layer thickness.

These two models of the pressure spectrum are plotted on Fig. 4 along with two measurements of the pressure spectrum on different days. The mean current at 5 m during the more energetic day was about 30 cm/s and the two models were evaluated assuming this current. The free-stream velocity (U_∞) was probably a little greater than this estimate from 5 m (perhaps 40 cm/s), so perhaps the Strasberg model estimate should be shifted upward by a factor of about five. The two models fit the observed spectrum well, and there is more than enough room in the uncertainties of the physics to explain the differences observed. The relationship of the spectrum to the velocity observed in Fig. 5 is clearly very close to the power of four suggested by the theory presented here and conflicts with the power of 5.7 suggested by Strasberg.

The flow noise spectrum is obscured at frequencies below 0.03 Hz and in the band between 0.1 and 3 Hz by other natural sources of (acoustic) noise. We are unable to observe the spectrum near the corner frequency, and so are unable to test the model to any great extent. A spectrum of current velocity near the seafloor measured previously [19] showed some indication of a flattening of the spectrum near the appropriate frequency. The only constraint here on the corner frequency results from the constraint on the total power in the spectrum. A fit of the model to the data seems to fix the corner frequency to within about a factor of ten, assuming the model is valid. Any effect of rotation on the pressure spectrum, beyond the constraint on the boundary-layer thickness, has also been ignored in this formulation.

Both models underestimate the spectrum at frequencies above 1 Hz, but it is likely that the measurements are disturbed at these frequencies by the strumming of various parts of the tripod and similar problems. Some authors have suggested that high-phase velocity components are associated with turbulence [25], [26]; if this were true, it would be necessary to include propagation effects in these calculations, however theory [27], [28] suggests negligible sound production by turbulence at a low Mach number.

IV FLOW NOISE

The HEBBLE tripod deployment was a compromise between resources and experimental design; it would have been preferable to deploy the sensors much closer to the bottom. Strasberg provides an estimate of the direct effect on pressure measurements of turbulence generated by the flow around the transducer (flow noise). This model was derived from measurements of noise on microphones surrounded by cylindrical and spherical wind screens:

$$S_N(f) \approx 3 \times 10^{-8}(U/fD)^{2.5}\rho^2 U^4 f^{-1}$$

where U is the mean current, D is the diameter of the wind screen, ρ is the water density, and f is the frequency. The spectrum varies faster than velocity to the sixth power, so small variations in flow velocity lead to enormous variations in the noise. The diameter of the transducer cases is about 25 cm; a flow velocity of 24 cm/s is assumed at the transducer height of less than 1 m ($U_5 \approx 30$ cm/s). Inserting these values and the density of seawater into the previous expression, the model becomes

$$S_N(f) \approx 2 \times 10^{-4} f^{-3.5} \quad (\text{Pa}^2/\text{Hz}).$$

This model is also plotted on Fig. 4. The model very much underestimates the observed pressures at high frequencies and suggests very large values if extrapolated toward lower frequencies. The predicted dependence on velocity (power of 6.5) is not observed in the ocean floor measurements.

The range of validity of this model (based on the original measurements) only extends down to about 0.16 Hz. A cylinder in a steady flow sheds periodic vortices at a frequency given by

$$f = St\,\frac{U}{D}$$

where $St \approx 0.2$ is the Strouhal number. The previous expression is only valid at frequencies well above this Strouhal frequency. Pressure and velocity signals measured near a cylinder in a flow will typically be very nearly harmonic with a frequency equal to the Strouhal frequency. The spectra of these variables are usually very narrow band, although the second harmonic may also be present [29].

Measurements of the spectrum of the acoustic radiation upstream from a stationary, rigid cylinder in a flow closely resemble Strasberg's model spectrum at frequencies above the Strouhal frequency [30]. This spectrum also varies with velocity to roughly the sixth power, and with the frequency as $f^{-3.5}$. However, there is a narrow peak in the spectrum near the Strouhal frequency and the spectrum falls precipitiously at lower frequencies. To illustrate this point, this spectrum is sketched on Fig. 3. The amplitude of the spectrum is arbitrarily scaled so that it "patches" into the Strasberg spectrum (S_N) at frequencies well above the Strouhal number. This curve falls well below the spectrum of current related noise detected in the seafloor measurements. Different parts of the tripod will shed eddies of many scales, but the pressure fluctuations associated with these eddies will mostly be limited to frequencies above the various Strouhal frequencies. The Strouhal frequency of the transducer cases is probably the lowest associated with any structure in the bottom part of the tripod.

These measurements and this theory strongly suggest that the low-frequency pressure fluctuations are caused by turbulence in the ocean floor boundary layer rather than to flow noise as defined here. The model spectrum based on boundary-layer turbulence is a good fit to the pressure spectrum observed at the deep seafloor under a strong current. Some reservations must remain because the problem of predicting the flow noise around the transducers and tripod is obviously very difficult. Although the tripod structure was designed to minimize flow interference, a complicated effect must be present.

V. Flow Noise and Seismometry

It is appropriate to conclude this discussion of seafloor noise with a discussion of the effects of ocean currents on long-period seismometer measurements. Most long-period, terrestrial seismic instruments are now installed in boreholes to avoid the noise associated with atmospheric pressure variations. This noise component is a result of quasi-static deformations of the earth in response to the surface pressure fluctuations. The noise is most severe on the horizontal component seismometers because of tilting caused by the short wavelength components. The tilts change the level on these components so that the force of gravity disturbs the centering of the mass (a component of the acceleration of gravity is rotated into each component). The apparent horizontal accelerations due to this tilting are calculated separately from the true horizontal accelerations associated with deformation of the earth. Fluctuating forces on the seismometer associated with the flow also induce motion of the seismometer. The horizontal component of this noise source also includes a separate tilt component.

The pressure fluctuations at the base of the atmospheric boundary layer on a moderately windy day (7 m/s) are of similar amplitude ($\approx$ 1 Pa) to those observed on the deep seafloor under a 30 cm/s current. The frequencies associated with the pressure fluctuations on the seafloor are also similar, perhaps slightly lower because of a lower mean velocity compared to the boundary-layer depth. We should expect boundary-layer pressure fluctuations to be as much a problem on the seafloor in regions with energetic currents as at typical continental sites. The solution is the same on the seafloor as for a terrestrial site; the seismometer should be installed in a borehole. Fortunately, the typical scale lengths associated with ocean floor pressure fluctuations are substantially shorter than for the atmospheric boundary layer because of the much slower mean-flow velocities. The depth of burial required to avoid the noise is therefore much less, but the tilts are larger.

Fortunately, much of the seafloor has weak bottom currents. The currents at the deep seafloor of the eastern Pacific are typically less than 1 cm/s and so a site in this region might be expected to be quiet. Distinct "noise notches" were observed in the measurements of the spectrum from all three components of a long-period seismometer that was installed on the seafloor off of the northern California coast; this suggests the absence of significant currents, although a small tidal cycle was detected in the noise on the horizontal components [4], [11].

Sorrells [31], [32] has looked at the problem of seismometer noise generated by atmospheric pressure fluctuations. The large eddies in the boundary layer are advected by the mean flow at a speed slightly less than the free-stream velocity, so the wavenumber k associated with a pressure disturbance of frequency ω (in rad/s) will be assumed to be approximately ($k = \omega/U_\infty$). Sorrells' results for the vertical (w) and horizontal (u) accelerations as a function of depth associated with a propagating pressure disturbance of amplitude P at the surface of a half space are

$$u \approx \frac{iPU_\infty \omega}{2\rho\beta^2}\left(\frac{\beta^2}{\alpha^2-\beta^2} - kz\right) \exp(-kz) \exp(i(\omega t - kx))$$

$$w \approx \frac{PU_\infty \omega}{2\rho\beta^2}\left(\frac{\alpha^2}{\alpha^2-\beta^2} + kz\right) \exp(-kz) \exp(i(\omega t - kx)).$$

The tilting of the seismometer adds more noise to the horizontal components than the directly generated horizontal accelerations. The apparent acceleration is the tilt times the acceleration of gravity

$$u' \approx \Theta g \approx \frac{iPg}{2\rho\beta^2}\left(\frac{\alpha^2}{\alpha^2-\beta^2} + kz\right) \cdot \exp(-kz) \exp(i(\omega t - kx)).$$

The induced accelerations can be large because the shear velocity (β) of surficial deep seafloor sediments can be very low (as low as 25 m/s). In the results discussed below, the compressional (α) and shear velocities are assumed to be 1500 and 25 m/s, and the density of the sediment (ρ) is set to 2000 kg/m^3. The free-stream velocity is assumed to be 30 cm/s.

In Fig. 6, these estimates of the accelerations caused by the pressure fluctuations in the boundary layer are compared with several estimates of the spectrum of seismic noise at continental and oceanic sites [33], [34]. Only the effect of tilt on the horizontal components (u') and the estimate of the vertical accelerations (w) are plotted here. The horizontal accelerations associated with elastic deformation (u) are very small and plot well-off the bottom of the graph. The pressure spectrum was derived from the model developed earlier in this paper. Again, the spectra are plotted only at frequencies well above the corner frequency, so the slope of the lines is essentially constant.

The flow generated accelerations are large, but a seismometer does not need to be buried very deeply to escape the boundary-layer noise, since the noise decays with depth as e^{-kz}. At a 1 s period the wavenumber is about 2 m^{-1}; at 100 s,

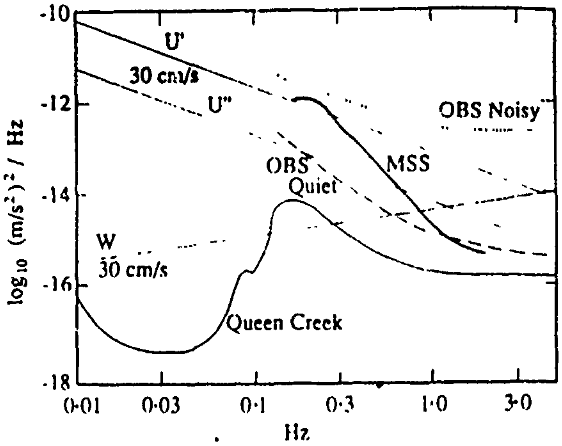

Fig. 6 Seismic noise detected on vertical component seismometers from a quiet continental site (Queen Creek, [29]), an ocean floor borehole seismometer (MSS), and measurements from a noisy and a quiet seafloor site [30]. Three model curves are also plotted for noise induced by the current near the seafloor. Lines labeled *W* and *U'* correspond to the vertical accelerations and apparent horizontal accelerations (from tilting) due to the elastic deformation of the seafloor caused by boundary-layer pressure fluctuations. The spectrum labeled *U"* corresponds to the apparent horizontal accelerations from tilting of the seismometer caused by the action of fluctuating currents

the wavenumber is 1/50 m^{-1}. The seismometers must be buried 1 or 2 m to avoid flow-induced noise at 1 s, and perhaps 100 m to avoid noise at 100 s. Again, it is assumed in these calculations that there is negligible energy associated with the turbulence in high-phase velocity components (which might couple into elastic waves).

Other authors who have discussed the problem of flow noise on seafloor seismic measurements have focused on the strumming of various elements of the seismometer packages, such as the radio antennas, because the high-frequency flow noise seemed to be narrow band in frequency [35], [36]. Removing or reducing the size of antennas provided for quick improvement of performance in regions with strong currents. Redesign of the typical OBS from a tall, thin (but easily deployable) object into a short, squat, low-profile instrument was also advocated. Some present-day ocean bottom instruments have the seismometer packages deployed externally to the main body of the instrument for these same reasons.

One can make a simple estimate of how a low-profile instrument will perform in a strong current under ideal conditions to compare against these other calculations. I will assume a spherical OBS of radius a mounted on a base of radius b resting on the seafloor. The largest term is again associated with the tilting of the instrument. If the force on the sphere is (F_s), the torque on a moment arm of length a must balance the torque applied by the force on the footpads (F_b) times the moment arm b. The displacement (Δz) of each of the two footpads is

$$\Delta z = \frac{F_b(1-\upsilon^2)}{4Er}$$

where r is the radius of a footpad, and E and υ are the Young's modulus and Poisson's ratio of the underlying half-space [33]. I will assume the force on the sphere is given by a drag law

$$F_s \approx 1/2 C\rho U^2 A$$

where C is a drag coefficient for a sphere of about 0.4, A is the area of the cross section of the sphere, ρ is the density of the seawater, and U is the velocity of the flow. The tilt of the sphere is simply $\Omega = \Delta z/b$, which in this model becomes

$$\Omega \approx \frac{\pi C\rho U^2 a^3}{8b^2 r}\,\frac{(1-\upsilon^2)}{E}.$$

Evaluating this expression for $a = 0.125$, $b = 0.3$, $r = 0.2$, $E = 3 \times 10^6$, and $\upsilon = 0.499$, we get

$$\frac{\Omega}{U^2} \approx 8.5 \quad \mu\text{rad/m}^2/\text{s}^2.$$

For a current of 0.18 m/s we expect a tilt of about 0.27 μrad.

The mean tilt may not be important; it is the spectrum of fluctuations about this mean which determines the noise on the horizontal components of the seismometer. The force on the sphere fluctuates both because of changes in the flow velocity impinging on the sphere and because of eddies spun off the backside. The first problem is treated here, since there are good measurements of the fluctuating component of the velocity in the ocean floor boundary layer. If the fluctuations are small compared to the mean flow, then the spectrum of the tilt S_ω is related to the spectrum of the flow fluctuations S_u by

$$S_\omega \approx \frac{4\Omega^2}{U^2} S_u$$

where here Ω refers to the mean tilt and U, the mean velocity.

Using the measurements of Gross *et al.* [19] of the spectrum of velocity fluctuations 1 m above the bottom in the HEBBLE area

$$\frac{S_U}{U^2} \approx 9 \times 10^{-4} f^{-1.5}$$

the apparent horizontal acceleration spectrum is just g^2 times the tilt spectrum. The acceleration spectrum under a 0.18 m/s current (at 0.2 m) is then

$$S_{u''} \approx 7 \times 10^{-15} f^{-1.5} \quad (\text{m/s}^2)^2/\text{Hz}$$

where f is in Hz. This estimate is also plotted on Fig. 6. This source of noise is comparable to the noise generated directly through elastic deformations induced by the pressure fluctuations. These results suggest that a shallow emplacement of a seismometer to avoid the direct effect of flow around the transducer will yield only moderate improvement in signal to noise beyond that gained by careful streamlining of the instrument package to avoid strumming, etc. Shallow-to-deep emplacement (meters to 10's of meters) is required to escape the flow-induced deformations of the earth.

VI. CONCLUSIONS

The purpose of this paper was to provide some measurements of flow noise useful for planning future experiments with long-period instruments. These calculations provide some warning that the simple view of flow noise as solely related to the flow around the transducer is incorrect when applied to low-frequency seafloor measurements. The pressure fluctuations detected by sensors at the seafloor under a strong bottom current are instead well fit by a model based solely on turbulence in the ocean floor boundary layer.

There are two comparable components to current-induced noise for seafloor seismometer installations. The seismometer is moved and tilted by fluctuating forces on the exterior of the seismometer. This source of noise can be avoided by shallow emplacement of the seismometer. The second component is the result of deformations of the seafloor caused by large-scale eddies in the benthic boundary layer. Deep burial is required to avoid this noise at low frequencies, but this source is negligible at shallow depths at frequencies above a few Hz.

ACKNOWLEDGMENT

The project would never have gotten off the ground without the help of Drs. G. M. Purdy, C. Hollister, and N. McCave. I would like to especially thank Dr. A. J. Williams and Prof. C. S. Cox for the loan of valuable equipment and of their time. An anonomous reviewer and T. F. Duda provided many helpful comments on the original manuscript.

REFERENCES

[1] S. C. Webb and S. C. Constable, "Microseism propagation between two sites on the deep sea floor," *Bull. Soc. Seismo. Amer.*, vol. 76, no. 5, pp. 1433-1445, 1986.

[2] A. E. Schreiner *et al.*, "Wavelength and correlation length of deep ocean and ambient noise," *EOS*, vol. 68, no. 45, p. 1373, 1987.

[3] D. Lahav, J. A. Orcutt, C. S. Cox, and P. M. Shearer, "Low frequency noise from OBS hydrophone data," *EOS*, vol. 67, no. 44, 1986.

[4] G. H. Sutton, "Ocean bottom seismic observatories," *Proc. IEEE*, vol. 53, no. 12, pp. 1909-1921, 1965.

[5] W. S. Hodgkiss and V. C. Anderson, "Acoustic positioning for an array of freely drifting sensors," *IEEE J. Oceanic Eng.*, vol. 8, pp. 1267-1294, 1983.

[6] C. S. Cox, T. K. Deaton, and S. C. Webb, "A deep sea differential pressure gauge," *J. Atm. Oceanic Tech.*, vol. 1, no. 3, pp. 237-246, 1984.

[7] S. C. Webb and C. S. Cox, "Observations and modeling of sea floor microseisms," *J. Geophys. Res.*, vol. 91, pp. 7343-7358, 1986.

[8] S. C. Webb, "Observations of seafloor pressure and electric field fluctuations," Ph.D. dissertation, Scripps Institution of Oceanography, 1984.

[9] R. H. Nichols, "Infrasonic ocean noise measurements: Eleuthera," *J. Acoust. Soc. Amer.*, vol. 69, pp. 974-981, 1981.

[10] J. H. Filloux, "Pressure fluctuations on the open ocean floor over a broad frequency range: New program and early results," *J. Phys. Oceanogr.*, vol. 10, pp. 1959-1971, 1980.

[11] G. H. Sutton, private communication, 1987.

[12] A. Turgut *et al.*, "High resolution bottom shear modulus profiler: A shallow water real time OBS array," Rosentiel School of Marine and Atmospheric Science, Rep. TR87-007, 1987.

[13] A. C. Kibblewhite and K. C. Ewans, "Wave-wave interactions, microseisms and infrasonic ambient noise in the ocean," *J. Acoust. Soc. Amer.*, vol. 78, no. 3, pp. 981-994, 1985.

[14] M. Strasberg, "Hydrodynamic flow noise in hydrophones" in *Adaptive Methods in Underwater Acoustics*, H. Urban, Ed. Boston: Reidel, 1985.

[15] M. Strasberg, "Nonacoustic noise interference in measurements of infrasonic ambient noise," *J. Acoust. Soc. Amer.*, vol. 66, pp. 1487-1493, 1979.

[16] C. D. Hollister, A. R. M. Nowell, and P. A. Jumars, "The dynamic abyss," *Sci. Amer.*, vol. 250, pp. 42-53, 1985.

[17] *Marine Geology*, vol. 66, 1985.

[18] G. L. Weatherly and E. A. Kelley, Jr., "Storms and flow reversals at the HEBBLE site," *Marine Geology*, vol. 66, pp. 205-218, 1985.

[19] T. F. Gross, A. J. Williams, and W. D. Grant, "Long term *in situ* calculations of kinetic energy and Reynolds stress in a deep sea boundary layer," *J. Geophys. Res.*, vol. 91, pp. 8461-8469, 1986.

[20] W. D. Grant, A. J. Williams, and T. F. Gross, "A description of the bottom boundary layer in the HEBBLE site: Low frequency forcing, bottom stress and temperature structure," *Marine Geology*, vol. 66, pp. 219-241, 1985.

[21] W. W. Willmarth, "Pressure fluctuations beneath turbulent boundary layers," *Annu. Rev. Fluid Mech.*, vol. 7, pp. 13-38, 1975.

[22] J. A. Elliot, "Microscale pressure fluctuations measured within the lower atmospheric boundary layer," *J. Fluid Mech.*, vol. 53, pp. 351-383, 1972.

[23] H. Tennkes, "The logarithmic wind profile," *J. Atmos. Sci.*, vol. 30, pp. 234-238, 1973.

[24] E. D'Asaro, "Velocity structure of the benthic ocean," *J. Phys. Oceanogr.*, vol. 12, pp. 313-322, 1982.

[25] M. A. Isakovich and B. F. Kuv'yanov, "Theory of low frequency noise in the ocean," *Sov. Phys.—Acoust.*, vol. 16, pp. 49-58, 1970.

[26] J. H. Wilson, "Very low frequency (VLF) wind generated noise produced by turbulent pressure fluctuations in the atmosphere near the ocean surface," *J. Acoust. Soc. Amer.*, vol. 66, pp. 1499-1507, 1979.

[27] M. J. Lighthill, "On sound generated aerodynamically, I: General theory," *Proc. Roy. Soc., Ser. A*, vol. 221, pp. 564-587, 1952.

[28] G. P. Haddle and E. J. Skudrzyk, "The physics of flow noise," *J. Acoust. Soc. Amer.*, vol. 46, pp. 130-157, 1969.

[29] P. W. Bearman, "On vortex shedding from a circular cylinder in the critical Reynolds number regime," *J. Fluid Mech.*, vol. 37, pp. 577-585, 1969.

[30] B. Etkin, G. R. Korbacher, and R. T. Keefe, "Acoustic radiation from a stationary cylinder in a fluid stream (Aeolian tones)," *J. Acoust. Soc. Amer.*, vol. 28, 1957.

[31] G. G. Sorrells and T. T. Goforth, "Low frequency earth motion generated by slowly propagating partially organized pressure fields," *Bull. Soc. Seismo. Amer.*, vol. 63, pp. 1583-1601, 1973.

[32] G. G. Sorrells and E. J. Douze, "A preliminary report on infrasonic waves as a source of long period seismic noise," *J. Geophys. Res.*, vol. 79, pp. 4908-4917, 1974.

[33] B. S. Melton, "The sensitivity and dynamic range of inertial seismographs," *Rev. Geophys.*, vol. 14, pp. 93-116, 1976.

[34] R. G. Adair, "Microseisms in the deep ocean: Observations and theory," Ph.D. dissertation, Univ. of California, San Diego, p. 165, 1985.

[35] A. Trehu, "A note on the effect of bottom currents on an ocean bottom seismometer," *Bull. Soc. Seismo. Amer.*, vol. 75, pp. 1195-1204, 1985.

[36] F. K. Duennebier, G. Blackington, and G. H. Sutton, "Current generated noise recorded on ocean bottom seismometers," *Marine Geophys. Res.*, vol. 5, pp. 109-115, 1981.

★

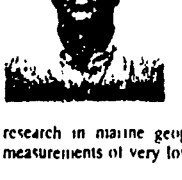

Spahr C. Webb received the B.S. degree in physics from the Massachusetts Institute of Technology, Cambridge, in 1978, and the doctoral degree in oceanography from the Scripps Institution of Oceanography, University of California, San Diego, in 1984.

He worked at the Woods Hole Oceanographic Institution, Woods Hole, MA, from 1984 to 1986 before returning to the Scripps Institution to join the Marine Physical Laboratory. His primary focus is the development of new tools and techniques for research in marine geophysics and oceanography, with an emphasis on measurements of very low-frequency sound in the ocean.

Evaluation and Verification of Bottom Acoustic Reverberation Statistics Predicted by the Point Scattering Model

D. Alexandrou and C. de Moustier

The point scattering model offers a parameterization of the reverberation probability density function (p.d.f.) in terms of the average number of scatterers contributing to the return and the presence of a coherent component in the received process. Computer simulations were used to verify model predictions and to evaluate their usefulness in the context of seafloor classification. As part of the verification study, the scatterer density was determined from the kurtosis of the reverberation quadrature p.d.f. The influence of a coherent component on the reverberation statistics was examined, yielding a better understanding of problems associated with its experimental measurement. To evaluate the potential of this parameterization as an acoustic signature for seafloor classification purposes, tests were conducted with alternative simulated scatterer distributions exhibiting a degree of clustering and regularity. Further tests were conducted with real reverberation data collected by the Sea Beam sonar system in two different seafloor areas.

On-Line Sea Beam Acoustic Imaging[*]

C. de Moustier and F. V. Pavlicek

---

*. Reprinted from Proceedings of MTS/IEEE Oceans '87, CH2498, pp. 1197-1201 (1987)

ON-LINE SEA BEAM ACOUSTIC IMAGING

C de Moustier and F V Pavlicek

Marine Physical Laboratory
Scripps Institution of Oceanography
La Jolla, CA 92093, U S A

ABSTRACT

This paper describes a system designed and built at the Marine Physical Laboratory of the Scripps Institution of Oceanography to produce acoustic images of the seafloor on-line with a Sea Beam multibeam echo-sounder This system uses a stand alone interface between the Sea Beam system and a grey-scale line-scan recorder The interface is built around a Motorola 68000 microprocessor and has digitizing capabilities It digitizes the detected echo signals from each of the 16 preformed beams inside the Sea Beam echo processor as well as the roll information given by the ship's vertical reference The acoustic data are then roll compensated and combined into a port and a starboard time series These time series are eventually output in digital format to a line-scan recorder which produces the grey scale acoustic image Results are discussed for Sea Beam acoustic images of the seafloor and of the Deep Scattering layers

1 INTRODUCTION

As part of a program to investigate seafloor acoustic backscatter measured with a Sea Beam multibeam echo sounder the Marine Physical Laboratory (MPL) of the Scripps Institution of Oceanography built a parallel acoustic data acquisition system using a DEC LSI 11/73 minicomputer (1,2) to preserve the echo signals received by the Sea Beam system which has no internal provisions to do so The Sea Beam system is primarily a high-resolution bathymetric survey tool which transmits a 7ms pulse of 12 158 kHz over a fan-shaped beam (2 2/3° fore-aft by 54° athwartships) stabilized in pitch, and which receives bottom echoes on 16 adjacent preformed beams (each 20° fore aft by 2 2/3° athwartships) It processes the echoes and outputs a contour chart of a swath of seafloor with a width roughly equal to 3/4 of the water depth below the ship For detailed descriptions of the Sea Beam system the reader is referred to the works by Renard and Allenou (3), Farr (4) and de Moustier and Kleinrock (5)

While analyzing bottom echo signals received by the Sea Beam system and recorded with this parallel data acquistion system we found that in spite of the multibeam geometry, the equivalent of a side-scan sonar image of the seafloor could be obtained by combining beams on either side of vertical (6) Such an acoustic image of the seafloor yields qualitative information about the texture of the bottom and complements the high-resolution bathymetry normally derived from the Sea Beam system Because this textural information is a potentially important clue for geomorphological interpretations, it would be very valuable to the investigator in real time during the course of a survey For this reason, we decided to build an on line acoustic imaging system which would give immediate access to the data as opposed to recording them on tape and producing grey-scale displays in a post-processing operation

In the following, we describe this on-line Sea Beam acoustic imaging system which consists of a "smart" interface, built around a Motorola 68000 microprocessor, between the Sea Beam system and a line scan recorder We first give an overview of the general system configuration with the various peripherals involved, we then describe the microprocessor controlled unit that orchestrates the acoustic imaging scheme, and we presents some data samples

2 GENERAL SYSTEM ARCHITECTURE

In this section, we briefly describe the general configuration of the acoustic imaging system and its links to the Sea Beam echo-sounder

As seen in Figure 1, the major components of the system consist of a microprocessor-controlled unit (stippled area) interfaced to a Sea Beam system, a set of peripherals including a CRT console for operator interactions and a line scan recorder for data output, and a link to a host processor for software down-loading We use the DEC LSI-11/73 minicomputer of our acoustic data acquisition system mentioned above as the host processor The line scan recorder is a 4 bit grey scale Raytheon LSR-1807M dry paper recorder with digital input and 4 kbytes of memory

Three types of signals are taken from the Sea Beam system clock signals for time reference and synchronization, roll signals for vertical reference and acoustic signals from the 16 beams To minimize interferences with the Sea Beam system the acoustic signals and the clock signals are tapped by high-impedance buffer amplifiers inside the Sea Beam system, and are transferred differentially to the interface The roll signals are transformer coupled

The microprocessor-controlled unit consists of 3 boards linked by a 16-bit data bus The heart of the unit is the processor board which includes a 68000 processor, 16 kbytes of EPROM holding monitor software and 20 kbytes of RAM for monitor management functions This board also has serial ports that are used for RS-232 links to the operator's console and to the host processor The second board is a memory expansion board configured to hold up to 256 kbytes of memory In its current configuration, 192 kbytes of RAM are installed on this board Provision has been made to install up to 64 kbytes of EPROM's in order to make a completely stand alone system The third board is the interface board which services inputs from the Sea Beam system and from the unit's front panel, and outputs to the line-scan recorder The unit's front panel features a set of 8 switches for operator interaction (setting of initial values or modifying program constants) and a two-digit LED display for performance monitoring

CH2498-4/87/0000-1197 $1.00 ©1987 IEEE

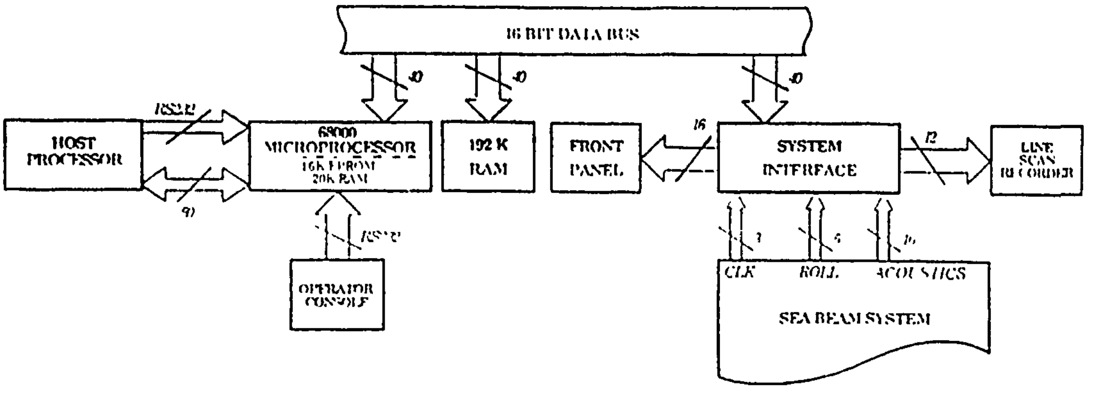

Figure 1 General system block diagram, the stippled area delimits the microprocessor system

The processor board and the memory expansion board are off-the-shelf units and we will not discuss them further in this paper On the other hand, we have configured the interface board specifically for this system and we shall describe it in more details in the following section

3 INPUT OUPUT INTERFACE

As indicated in the previous section the main function of the input output interface board is to service inputs from the Sea Beam system and the unit's front panel as well as outputs to the recorder

Figure 2 illustrates the signal paths from the Sea Beam system to the microprocessor through the interface At the center of this interface is a data control and timing unit which gets its inputs from the sonar key pulse and the Sea Beam system's 12 158 kHz reference frequency The sonar key pulse indicates the onset of a transmission cycle in the Sea Beam system and it serves here as the time zero reference The 12 158 kHz reference frequency produced by the Sea Beam system s transmit signal generator is fed into a phase lock loop whose output is divided down and used as the digitizing clock on the interface board The roll signals come in synchro format (3 phases 120° apart and 400 Hz reference) from the ship's vertical reference and are fed to a synchro-to-digital (S/D) converter The outputs of the S/D converter are held in D-type registers which interface directly with the system bus so that the processor can access the roll data directly at a dedicated memory address The 16 acoustic channels corresponding to the 16 Sea Beam preformed beams are input differentially into a 16-channel analog multiplexer whose common output is held in a sample and hold amplifier interfaced to a 12-bit analog to-digital (A/D) converter As mentioned above the A/D converter is clocked by a timing signal which is an integer sub multiple of the 12 158 kHz reference frequency The multiplexer is also synchronously controlled to change channels between each A/D digitizing cycles In the present configuration, the sampling rate is approximately 500 Hz per channel The digitized data is stored in a 512-word First-in First-out (FIFO) memory which is directly accessible to the processor through the system bus

Inputs from the switches on the unit s front panel are directed to the system bus by way of bus drivers whenever the microprocessor reads data from the memory address assigned to the front panel Likewise, bus access to the LED display on the front panel is done directly through D-type registers when the microprocessor writes to the front panel's memory address

Outputs to the line scan recorder are interrupt driven The recorder issues a time zero interrupt to the processor when the stylus reaches the left hand edge of the paper When the processor is ready to service this interrupt, it writes four bits of data (a nibble) to a D-type register at the address of the recorder parallel port The microprocessor sends 4096 such nibbles to this address and a separate circuit strobes the data into the recorder buffer Note that this sequence of events is specific to a Raytheon LSR-1807M recorder, provisions have been made on the interface board to accomodate EPC type recoders which interrupt the processor for each transmission of a 4-bit pixel in addition to the aforementioned time zero interrupt

Timing Sequence for Data Acqusition

The various input and output operations outlined above are managed by the data control and timing unit according to a prescribed sequence for data acqusition The timing diagram shown in Figure 3 illustrates the sequence of events taking place between two sonar key pulses (time zero) during data acquisition The sonar key pulse triggers a decrementing counter previously loaded with a time delay proportional to the time necessary for sound to reach the seafloor and return to the ship When a program is first started this depth dependent time delay must be set from the front panel switches according to the current water depth below the ship From then on, the program tracks the bottom and updates the delay timer automatically

When the timer reaches zero, it starts the A/D and the S/D conversions As indicated above the output of the A/D converter is held in a 512-word FIFO memory The FIFO sends an interrupt to the processor on the half-full flag (256 words) and the processor must read data off the FIFO into memory in order to clear the interrupt A/D conversions and FIFO interrupts continue until the specified number of samples has been digitized for each channel and stored into memory For the S/D data, the processor need only read the data off the bus and interleave the roll samples into memory with every 256-word interrupt sequence

The next set of operations includes data processing and displays The data processing is mainly concerned with automatic bottom tracking, roll compensation and formatting of the digitized acoustic data for display on the grey-scale recorder We shall discuss this processing in more detail in section 4 As seen in the timing diagram (Figure 3) data processing must be completed before the next A/D conversion sequence begins The amount of time avail

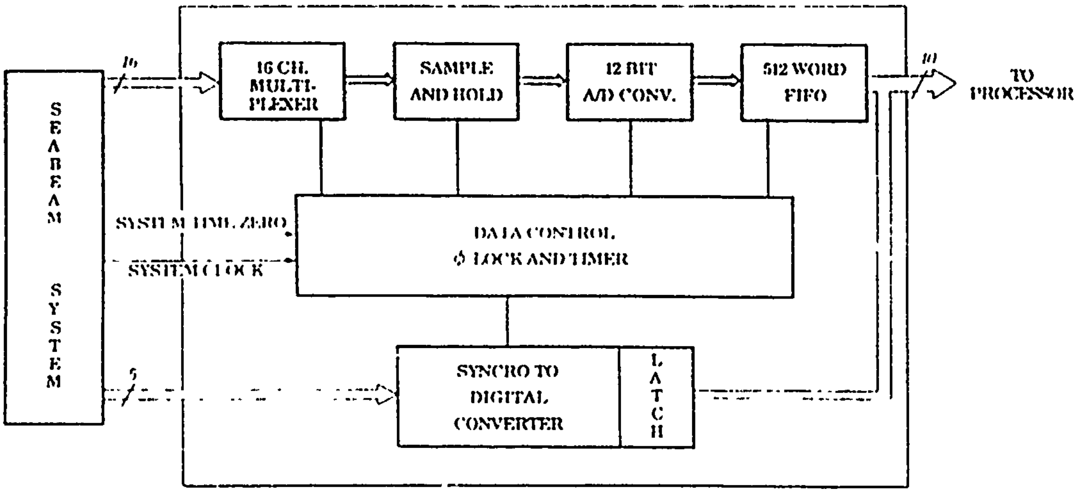
16
16 CH. MULTI-PLEXER
SAMPLE AND HOLD
12 BIT A/D CONV.
512 WORD FIFO
16
TO PROCESSOR
SEABEAM SYSTEM
SYSTEM TIME ZERO
SYSTEM CLOCK
DATA CONTROL, φ LOCK AND TIMER
5
SYNCRO TO DIGITAL CONVERTER
LATCH

Figure 2 Interface architecture

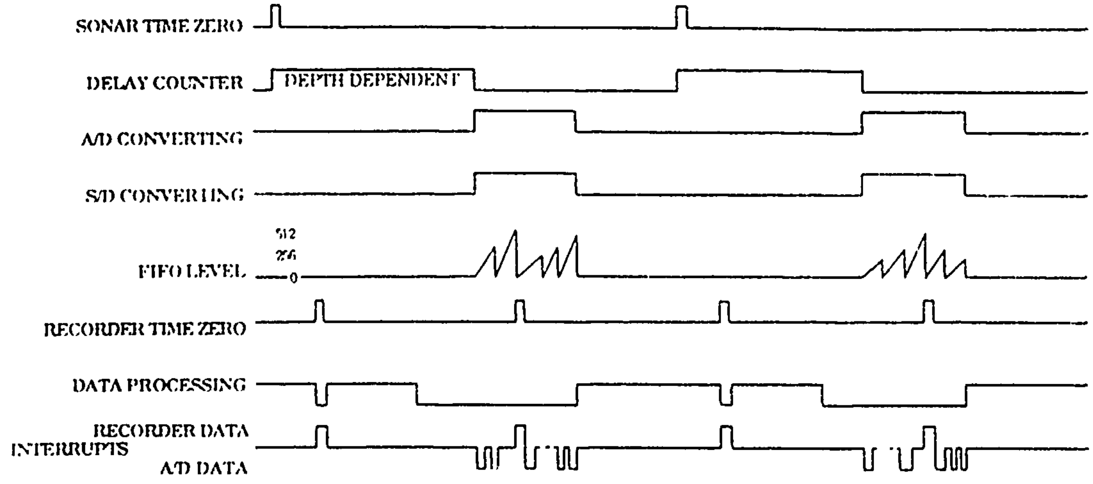
SONAR TIME ZERO
DELAY COUNTER
DEPTH DEPENDENT
A/D CONVERTING
S/D CONVERTING
512
256
0
FIFO LEVEL
RECORDER TIME ZERO
DATA PROCESSING
RECORDER DATA
INTERRUPTS
A/D DATA

Figure 3 Timing diagram showing the sequence of events happening between two sonar transmission cycles

able for processing is therefore dependent on the water depth which determines the sonar key pulse interval (e g 6 s in 3000 m of water depth) and on the number of samples required for each channel (e g 500 samples in 3000 m of water depth)

During all the above operations, the recorder sends interrupts to the processor at a rate determined by the scan rate selected by the operator (typically 1-4 s) However these recorder interrupts are given a lower priority level than the A/D interrupts so that the processor does not service them while A/D interrupts are pending

4 DATA PROCESSING

When the required number of samples of echo amplitudes and roll information have been digitized and stored in a data buffer in memory, the microprocessor stops all digitization and begins processing the data. In the current configuration, three main processing tasks are performed bottom traking roll correction and data formatting

Bottom tracking consists in finding the first amplitude exceeding a given threshold in any one of the 16 preformed beams The position of this data point with respect to the beginning of the data buffer gives the time elapsed since the onset of the digitization sequence to receive the first bottom echo. The bottom tracking routine strives to optimize this time interval and to constrain it within a 200 ms window by adjusting the time delay between the sonar key pulse and the onset of digitization (Figure 3). Because noise spikes and interferences from other sound sources operating simultaneously with the Sea Beam system occasionally cause false bottom detection, bottom tracking history from previous transmission cycles is also included in the computation of this time delay adjustment.

The first arrival found by the bottom tracking routine is then used as a time reference to compute a port and a starboard time series of echo amplitudes. However, in order to determine which beams belong to either port or starboard a roll correction must be applied. The preformed beams are nominally spaced 2 2/3° apart and centered in the ship's reference frame as shown in Figure 4. This figure is an example of bottom echo amplitudes received and detected on the 16 preformed beams for one sonar transmission cycle. The x-axis is time in seconds after transmission and amplitudes are displayed in volts and have been corrected for acoustic transmission loss through the water column by a time varying gain in the Sea Beam echo processor hardware. The digitized roll angles correspond to the angle between the ship's vertical axis and true vertical during echo reception. As beams are equally spaced, these roll angles can be used to enter a table of beam offsets with respect to vertical and the roll correction is performed through a table look-up. Note that this roll correction scheme is only a first approximation which is sufficient to produce a useable time series of amplitudes as a function of slant range. For a display of amplitudes as a function of horizontal range, the roll correction needs to take ray bending effects into account.

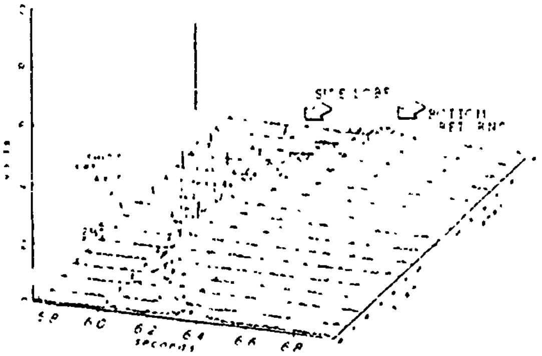

Figure 4. Envelopes of bottom echoes received by the 16 preformed beams

In the present configuration the time series on both port and starboard are formed through a peak detection process at incremental slant ranges from the first arrival. These data are then converted from the 12-bit format given by the A/D conversion to a 4 bit format by table look-up. This yields 16 levels of grey to be displayed on the recorder. The grey-level conversion table can be modified to accomodate overall differences in signal amplitude levels from one Sea Beam system to another. Although not currently implemented, provisions have also been made to include a table look-up correction for angular dependence of seafloor acoustic backscatter.

5 RESULTS

A Seafloor Acoustic Images

An example of the acoustic image resulting from the above processing is shown in Figure 5. This image (Figure 5a) was actually replayed from Sea Beam acoustic data recorded aboard the R V *Thomas Washington* on the East Pacific Rise and processed as described in section 4. The cross-track dimension in seconds corresponds to differential slant range (seconds from first arrival). The along-track dimension of this image is in kilometers and matches that of the corresponding swath contour plot produced by the Sea Beam system (Figure 5b). The contour intervals are 10 m in the upper portion of the swath (1) and 20 m in the lower portion (2). The acoustic image and the contoured swath complement each other as the qualitative textural information seen in the image would be missed if one only had the contours. Likewise, the quantitative bathymetry given by the contours could not be inferred reliably from the acoustic image. The fact that the lineation pattern seen in the acoustic image is not obvious in the contours at the 10 m or 20 m contour intervals indicates that the corresponding relief is lower than 10 m. Although bathymetry data from the Sea Beam

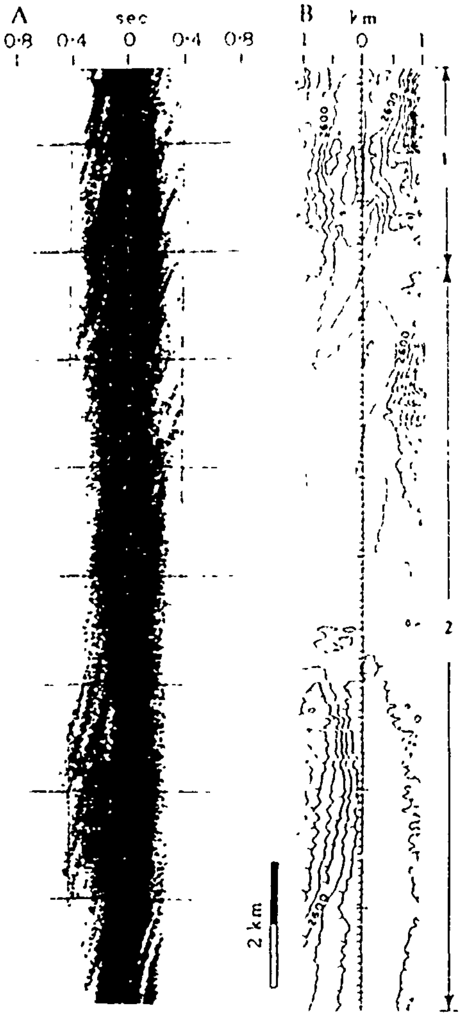

Figure 5. Sea Beam acoustic image of the seafloor (A) and corresponding contoured bathymetry (B)

system can be contoured at intervals lower than 10 m, such contours are typically noisy and are therefore difficult to interpret Note also that the trend of the lineations seen in the acoustic image is distorted by the slant range representation, the actual trend would appear at a greater angle to the ship's track

B Images of the Deep Scattering Layers

A relatively simpler form of on-line Sea Beam acoustic display consists in outputting the echo amplitude as a function of time for individual beams This type of display is useful as a quick check of the performance of the echo-sounder part of the Sea Beam system It is also most useful when tracking Deep Scattering Layers (DSL) in the ocean Figure 6 is an example of such an on line acoustic image of the DSL recorded at dusk in the tropical Northern Pacific aboard the R V *Atlantis II* Three individual beams are represented in this picture (port 8, port 1 and starboard 7) corresponding to incidence angles of roughly 20°, 2° and -18° respectively The horizontal axis spans approximately 60 nmi and the vertical lines are spaced 30 min apart with the ship progressing at 12 knots from left to right In this on-line display, spacing between the 30 min time marks varies as a function of the transmission repetition rate which is determined by the water depth Closer time marks indicate a deeper bottom The vertical axis is slant range in uncorrected meters (1500 m/s) This slant range is equivalent to depth for the center beam (port 1) The pattern seen in all three beams of Figure 6 is the well known migration pattern of midwater nekton towards the sea surface at night-fall (7,8) On the left side of the image, discrete layers converge upward to the 2 h time mark and some of the scatterers seem to reassemble into discrete layers in the first 150 m towards the right of the image while layers are still visible between 400 m and 600 m

Compared with similar images of the DSL obtained in the past with conventional wide-beam 12 kHz echo sounders these images offer greater spatial resolution both along and across the ship's track The 16 2 2/3° beams of the Sea Beam system yield 16 simultaneous discrete measurements where the conventional echo-sounder integrates over the same volume of ocean to give one measurement This higher spatial resolution makes it possible to investigate the patchiness of the distribution of the 12 kHz biological scatterers in the DSL's and to provide real-time clues on the lateral extent of a given patch during trawling operations

6 CONCLUSIONS

The on-line Sea Beam acoustic imaging system we have described in this paper allows investigators to extract more information out of the echo signals received by the Sea Beam system than is available in the standard swath bathymetry output We have shown that acoustic images of the bottom or of the DSL's can be derived from the echoes received on the 16 preformed beams with a small amount of hardware and without interfering with the normal bathymetric function of the Sea Beam system The additional information provided by this imaging system is a real-time complement to the contoured bottom data and it allows the investigator to make better decisions about survey patterns and data quality while at sea

Future improvements to this imaging system should include a capability to incorporate the bathymetric information produced by the Sea Beam echo processor into the data processing software in order to perform slant-range correction on seafloor acoustic images The depths and cross-track distances computed for each transmission cycle could be input on the microprocessor bus through a parallel port Such a data transmission scheme as already been implemented on the microprocessor as we use it as a spooling interface between our LSI-11/73 minicomputer and the linescan recorder for post-processing operations and for play backs from digitally tape-recorded data

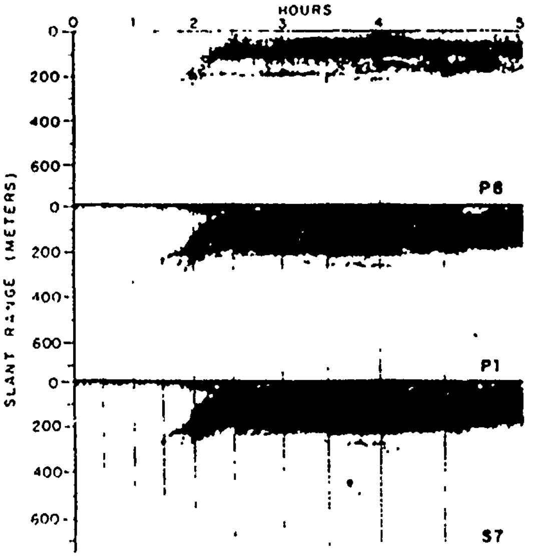

Figure 6 Tracking the DSL on individual beams

7 ACKNOWLEDGMENTS

The work reported here has been supported by the Office of Naval Research (contract No N00014-79-C-0472) whose funding is gratefully acknowledged

8 REFERENCES

1 de Moustier, C, 1985, Sea Beam acoustic data acquisition system Marine Physical Laboratory, Scripps Institution of Oceanography, San Diego CA

2 de Moustier, C and F V Pavlicek, 1987, A fully transportable Sea Beam complex acoustic data acquistion system, OTC 5514, Proc 19th Offshore Tech Conf, Vol 3, pp 269-274

3 Renard V and J P Allenou, 1979, Sea Beam Multibeam echo-sounding in *Jean Charcot* Description, evaluation and first results, Int Hydrog Rev, Vol 56(1), pp 35-67

4 Farr, H K, 1980, Multibeam bathymetric sonar Sea Beam and Hydrochart, Mar Geol, Vol 4, pp 77-93

5 de Moustier, C and M C Kleinrock, 1986, Bathymetric artifacts in Sea Beam data how to recognize them and what causes them, J G R, Vol 91, No B3, pp 3407-3424

6 de Moustier, C, 1986, Approaches to acoustic backscattering measurements from the deep seafloor, in Current Practices and New Technology in Ocean Engineering, OED-Vol 11, A S M E, T McGuinness and H H Shih eds, pp 137-143

7 Farquhar, G B, 1977, Biological sound scattering in the oceans a review, in Oceanic sound scattering prediction, Plenum Press, N R Andersen and B J Zahuranec eds, pp 493-527

8 Raitt, R W., 1948, Sound scatterers in the sea J Marine Res, Vol VII, No 3, pp 393-409

Modulation of Short Wind Waves by Long Waves*

Jerome A. Smith

---

*. Reprinted from Surface Waves and Fluxes (G. L. Geernaert and W. J. Plant, Eds.), Vol. 1, Chapt 8, pp. 247-251 (1990).

Chapter 8

MODULATION OF SHORT WIND WAVES BY LONG WAVES

JEROME A. SMITH
The Marine Physical Laboratory of
The Scripps Institution of Oceanography
University of California, San Diego A-013
La Jolla, CA 92093

1. Introduction

The behavior of short surface waves (wavelength less than a meter or so) riding on longer wind waves or swell has sparked interest for several decades now. In the problem as posed here, the energetic waves near the peak of a wind-wave or swell spectrum are treated as a large-scale, slowly varying "medium" in which short gravity-capillary waves evolve. This "WKB approximation" should be well founded, since the time and space scales of the long and short waves are widely separated, and no reflections of the short waves occur. Short wave "packets" or "components" are examined independently as they evolve under the influence of slowly varying winds and currents, and later reassembled into a larger picture. Resonant non-linear exchanges are not explicitly included, although (for example) a "packet" might be regarded as a set of tightly coupled wavenumbers rather than as a pure sine-wave component.

This should be considered as a kind of "thought experiment." Beware of any who claim to have solved this problem: There remain too many ill-known or even unknown aspects of the total interaction of long and short surface and surface shear layers to hope for a final solution. However, by combining physics and physically motivated hypotheses with as many observations as can be brought to bear on the problem, the possibilities can be greatly reduced. Some qualitative conclusions can be reached, and directions for further work indicated (on both the theoretical and observational sides).

An eclectic review of the history of the long-wave/short-wave problem is given next, with apologies to the many whose contributions are neglected. A good starting point is with observations made by Cox (1958): His surface slope and elevation measurements showed a mean square surface slope which was highest near and just ahead of the peaks of the longer waves generated mechanically in the tank. Later, M.S. Longuet-Higgins (1963) showed that "parasitic" capillary waves are generated by sharp crests, with group velocities equal to the long wave phase speed. Also, in a now famous series of papers, Longuet-Higgins and Stewart (1960, 1961, 1962, 1964) defined a surface wave "radiation stress," describing changes in momentum flux due to the interaction of surface waves with larger scale (in the WKB sense) flows. These analyses showed that long-wave orbital velocities alternately compress and expand the shorter waves, leading (in the absence of growth and dissipation) to

G. L. Geernaert and W. J. Plant (eds.), Surface Waves and Fluxes, Volume I, 247–284.
© 1990 *Kluwer Academic Publishers. Printed in the Netherlands.*

maximal amplitudes at the crests of the longer waves, but with no net exchange of energy over a full long-wave period. Phillips (1963) then noted that, being of larger amplitude yet shorter wavelength at the crests, these short waves were likely to dissipate preferentially there. Since the "excess energy" of the short waves came from the long waves, he concluded that this results in damping of the long waves. But, Longuet-Higgins (1969a) pointed out, these short waves also carry momentum, so their dissipation must also result in a transfer of momentum, acting like a variable stress along the long wave surface. This variable stress acts on the long-wave orbital velocity, resulting in an energy transfer much greater than Phillips' damping term, and which favors growth when the waves go in the same direction, and damping when opposed (e.g., swell propagating into the wind). Since the observed growth rates of the longer wind waves are larger than those calculated by, e.g., Miles (1962), and since swell are known to be damped effectively by an opposing wind, this "maser mechanism" fit rather well into a perceived gap in the theory of surface wave generation. The reign of this "maser mechanism" was brief, however. Hasselmann (1971) pointed out that, in addition to momentum, the short waves induce mass-flux. When the short waves dissipate, they create a mass divergence (or convergence) at the long wave surface. Since the long-waves' surface elevation corresponds to gravitational potential, Hasselmann (1971) showed that a transfer of potential energy also occurs, exactly canceling the "maser" term, and leaving just Phillips' damping once more. A few years later, two groups (Valenzuela and Wright 1976, Garrett and Smith 1976) independently noted that Hasselmann had assumed no correlation between short wave growth and long wave phase, and that this term can result in net transfer to the longer waves. A simple physical interpretation is easily devised: Consider a surface layer (thin compared to long-wave scales) which contains both the short waves and the surface wind-drift. Then, when the short waves dissipate, both the momentum and corresponding mass flux are merely transferred to the "drift component" of this layer. In terms of the underlying long wave, it makes little difference which component of the surface layer carries the momentum or mass-flux, as long as it's still within this surface layer. On the other hand, variations in short wave generation represent momentum gained from the wind, and so change the total surface layer budget and can therefore affect the long waves as well.

At about the same time, work by Gent and Taylor (1976) suggested that variations in short waves amplitude would also affect the long wave growth indirectly, by acting as variable-sized "roughness elements" and changing the air-flow over the long waves. Put very simply, for potential flow of air over the waves, the Bernoulli effect gives rise to a large pressure variation which is in quadrature with the vertical velocity, and so does no work. Any slight change in the phase of this pressure field, induced (for example) by variations in the turbulent shear stresses, could therefore greatly alter the long-wave growth rate. The short waves can act as "roughness elements" for the airflow over the long waves. Therefore, it's not too surprising that the modulation of short waves can bring about enormous variations in the phase of this induced pressure field. Thus, in addition to the "direct" effect alluded to above, variations in short wave generation can also alter long wave growth indirectly, by altering the airflow. The results of Gent and Taylor's (1976) aerodynamic model indicate that this effect may be quite large for under-developed seas (with long wave phase speeds less than the wind), but may be less important for waves (swell) moving with or faster than the wind. A major conclusion of the present study is that more work along these lines is sorely needed.

Keller and Wright (1975) approached the problem from a different perspective. They and their associates at the Naval Research Laboratory had been making pioneering measurements and downwind-directed "looks," they could effectively remove variations due to tilting of the surface from the intensity of the returns, leaving mainly those due to modulations of the short Bragg-resonant scatterers. What they found was surprising: the measured modulations of short wave energy are as much as 15 to 20 times the long waves steepness, not the measly 2 times or so derived from the conservative interaction. Also, the maximum amplitudes appear just ahead of the crests, rather than at them, in agreement with the earlier observations by Cox (1958). It is important to realize that, with tilting effects removed, the radar scatters are from an essentially fixed wavenumber, rather than a "fixed wavetrain," as considered in the theoretical treatments. Straining by longer waves changes the wavelength as well as amplitude of the short waves. Viewing a fixed wavenumber, energy is effectively transported from adjacent spectral bands. For a typical "equilibrium spectrum" of gravity waves, the energy (amplitude squared) goes about as k^{-4}, so this spectral transport can be significant; in fact, it would raise the "conservative" modulation to about 6 times the long wave slope (2 from amplitude modulation plus 4 from spectral transport). For the observed short waves (near the gravity-capillary transition, and near the viscous cut-off as well), actual spectral slopes can be greater than k^{-4}. By introducing relaxation towards an "equilibrium spectrum," Keller and Wright could reproduce a maximum slightly forward of the crests, as indicated by the measurements. However, even with measured spectral slopes, the predicted amplitude of the modulation falls short of the observed levels. A higher-order model (Valenzuela and Wright 1979) does not improve this. Thus, Wright et al. suggested that the "equilibrium level" is itself modulated by the long wave environment.

With the work of Keller and Wright (etc.), and with the development of remote sensors such as SAR, scatterometry, etc., which depend on the behavior of such short waves, the focus of the problem shifted from the effect on long wave growth to accurate modelling of the short waves themselves. Some work had already been done on coupled shear-flow and short wave development (e.g. Valenzuela 1976), and on triad interactions which operate effectively near the gravity-capillary transition (e.g. Valenzuela and Laing 1972). But, to improve on models of the short waves requires observations as well as theory. Thus, there followed an inspiring series of studies on growth rates (Larson and Wright 1975, Plant and Wright 1977) advection by wind drift (Plant 1982 and 1987), and the short wave modulation under various wind speeds, swell steepness, directions, etc. (Wright, Plant, and Keller, 1090; Plant, Keller, and Cross, 1983; Keller, Plant, and Weissman 1985; etc.).

Some of the salient features of observed short-wave modulations are summarized by the results shown in Figs. 1 and 2 (from Plant *et al.* 1983). These show measured 'modulation transfer functions' (MTFs) for two wavelengths: 2.1 cm (Fig. 1) and 12 cm (Fig. 2), from a variety of cases where the wind, waves, and radar "look directions" are all parallel. Although the MTFs (defined as backscattered intensity modulations divided by the long-wave steepness, U^L/C^L) include other effects, the major features reflect the modulation of the short-waves themselves, at a fixed wavelength. There is a consistent decrease in the magnitude of the modulation with long-wave (driving) frequency, and the phase of the modulation is stable, with maximum amplitudes occurring around 0 to 30° ahead of the long-wave crests. Finally, the X-band (2.1 cm) modulations decrease with increasing winds (over the range 5 to 14 m/s), while the L-band (12 cm) modulations are relatively insensitive to windspeed (in the range 7 to 15 m/s),

Here, a model for short wave behavior including growth and dissipation is developed. The dissipation is based on a wave-steepness criterion which depends also on the wind-drift profile. Perturbations about a mean balance between growth and dissipation of the short waves are considered. The model is first "tuned" by comparing the "predictions" of this mean balance with observations of backscatter vs wind (at X and L bands), and with observed high-frequency/wavenumber spectra. To first order in the long-wave slope, there is a damped harmonic response, as in the relaxation model of Keller and Wright (1976). As noted, the total "conservative" forcing is too small to explain the observations. Of the mechanisms investigated here, only large variations in the wind stress can account for the large observed modulations. Considering variations in both the direct generation and dissipation of the waves due to the forcing of the surface drift, estimates can be made of what wind stress variations are required to explain the measured observations.

The organization of this chapter is as follows: First, general equations for the interaction of surface waves with large-scale flows are reviewed, and phrased in terms of the mean and wave-induced momentum (Section 2). Section 3 focuses on the long-wave/short-wave problem within this formulation. The short-wave growth rate is prescribed as an arbitrary function of long-wave phase, and an expansion in long-wave harmonics is introduced. Section 4 proceeds with a hypothetical model for short wave dissipation which depends on details of the near-surface wind drift. In Section 5, a drift model is developed to describe the effects of modulation of the wind drift by the "long-wave environment," including variations in wind-stress as well as direct straining. Finally, results are combined to estimate the net modulation of the short waves. By comparing results with observations, some ill-known parameters in the model (such as the magnitude and phase of wind stress variations with the long wave) are examined for self-consistency and plausibility. At the same time, sensitivities of the model results help to indicate which of the many "unknowns" are most in need of investigation.

The Newtonian Gravitational Constant*

John A. Hildebrand, Alan D. Chave, Fred N. Spiess,

Robert L. Parker, Mark E. Ander, and Mark A. Zumberge

---

*. Reprinted from EOS, Vol. 69, No. 32, pp. 779-780 (1988).

Eos, Vol. 69, No. 32, August 9, 1988, Pages 769, 779–780

The Newtonian Gravitational Constant

On the Feasibility of an Oceanic Measurement

John A. Hildebrand[1]*, Alan D. Chave*[2]*,*
Fred N. Speiss[1]*, Robert L. Parker*[1]*,*
Mark E. Ander[3]*, and Mark A. Zumberge*[1]

Introduction

The Newtonian gravitational constant G is a fundamental parameter of physics relating the gravitational force to the product of body masses by an inverse square of the separation G has been measured with an accuracy of about 7 parts in 10^5 in individual laboratory experiments [e.g., *Luther and Towler*, 1982], but the consistency of all modern laboratory measurements is only about 7 parts in 10^4 (Figure 1), making it one of the most poorly determined physical constants of nature [cf. *Cohen and Taylor*, 1986; *Gillies*, 1987]. For the past century, virtually all experiments to measure G have been conducted on a scale (i.e., separation between test masses) of 50 cm or less, using a modification of the Cavendish balance. In recent years there has been increasing interest in determinations of G over larger scales than can be achieved in the laboratory. Some theoretical attempts to combine gravity with the other forces of nature predict the existence of a fifth force in addition to the classical gravitational, electromagnetic, weak, and strong forces. The fifth force would produce departures from Newtonian or inverse square law gravity at mass separations of tens of meters to tens of kilometers. Geophysical experiments are uniquely suited to measure the gravitational constant at these scales, and in this paper we outline the advantages of conducting such an experiment in the ocean.

It is expected on theoretical grounds that departures from Newtonian gravity will be manifest by the addition of one or more exchange interaction terms to the classical gravitational potential [e.g., *O'Hanlon*, 1972]. *Gibbons and Whiting* [1981] give the potential energy V of two masses m and m' at a separation r and affected by an exchange interaction with wavelength λ and coupling coefficient α as

$$V = -G_\infty(mm'/r)(1+\alpha e^{-r/\lambda}) \qquad (1)$$

where the force between the masses is

$$F = G_\infty[(mm'/r^2)[1+\alpha(1+r/\lambda)e^{-r/\lambda}] \qquad (2)$$

and the effective (range-dependent) gravitational constant is

$$G(r) = G_\infty[1+\alpha(1+r/\lambda)e^{-r/\lambda}] \qquad (3)$$

Positive values of α correspond to attractive exchange interactions, while negative values give repulsive ones. The exchange term vanishes for large distances $r \blacktriangleright \lambda$, and Newtonian gravity is observed with gravitational constant G_∞. *For small distances* $r \blacktriangleright \lambda$, (2) is equivalent to Newtonian gravity with

$$G_0 = G_\infty(1 + \alpha) \qquad (4)$$

This is the value measured in laboratory experiments and is the same as the large distance value G_∞ only in the absence of exchange interactions. Astronomical observations cannot yield estimates of G_∞ independent of the mass of Earth or some other body, and precise observations are required over distances of order λ to detect possible non-Newtonian effects.

The ratio of two measurements of G at different ranges constrain α and λ to an allowed region in α–λ, commensurate with the measurement errors *Stacey et al.* [1987] reviewed the available laboratory, global, geophysical, and astronomical data restricting α–λ (see Figure 2). While the data effectively preclude values of λ under a few meters or over a few kilometers unless α is smaller than can reasonably be measured, the constraints for λ in the range of 10–1000 m are weak.

Interest in assessing the gravitational constant over hundred-meter scales has led to a renewed interest in geophysical G experiments. Measurements of the acceleration of gravity g, the medium density ρ, and the location r in a geological body can be used to back-calculate $G(r)$ and bound α and λ. Stacey and coworkers have presented extensive data sets from two Australian mines [e.g., *Holding et al.*, 1986]. Their results systematically give a value for G that is larger than the accepted laboratory value, and the discrepancy exceeds the stated error bounds. *Holding et al.* [1986] use the most complete mine data set to obtain $\alpha \sim -0.007$, $\lambda \sim 200$ m, although the constraints on λ are not especially good. This suggests a repulsive term in (2) and a maximum deviation from Newtonian gravity of about 0.7%. For a thorough review of these experiments, as well as many other geophysical determinations of G, see *Stacey et al.* [1987]. More recently, *Hsui* [1987] and *Eckhardt et al.* [1988] (*Eos*, January 12, 1988) have also reported anomalous values for G from geophysical experiments.

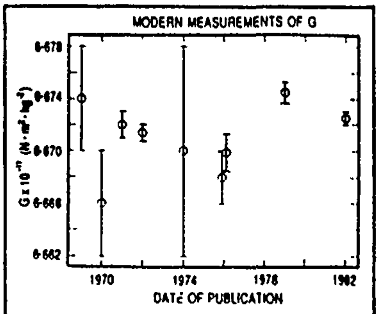

Fig 1. Composite of all measurements of G from Cavendish-type experiments made since 1969 plotted as a function of the date of publication. The quoted precision of each measurement is given as error bars. The scatter between the values is a measure of the overall accuracy of laboratory measurements of G and is about 7 parts in 10^4. The sources of the data are *Rose et al.* [1969], *Facy and Pontikis*, [1970, 1971], *Pontikis* [1972], *Renner* [1974], *Karagioz et al.* [1976], *Luther et al* [1976], *Sagitov et al* [1979], and *Luther and Towler* [1982].

The results of these experiments are not conclusive (although they are certainly suggestive) despite the care with which they were performed The mine estimates of rock density are based on coring and hand samples or gamma ray logs and may not represent the in situ density. Current rock mechanical models are not adequate to estimate in situ density with high precision from removed samples, principally because unloading effects are not reversible A 1% discrepancy in G would be produced by a 1% error in estimating in situ density, and errors in the estimated density for a considerable distance about the measurement point must be considered. Furthermore, the region surrounding a mine is certainly inhomogeneous (or else the mine would not be there). There is also a possible problem (recognized by Stacey) from deep-seated density anomalies within the Earth's deep crust and mantle that can produce anomalous regional gravity gradients and

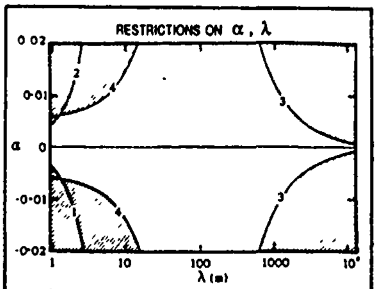

Fig. 2. Restrictions on the parameters α–λ imposed by torsion balance experiments and the hydroelectric lake beam-balance experiment described by *Stacey et al* [1987] (left side) and surface to satellite gravity comparisons (right side). The shaded areas are disallowed. Notice that constraints on α for 10 m<λ<1000 m are very weak.

---

[1] Scripps Institution of Oceanography, La Jolla, Calif.

[2] AT&T Bell Laboratories, Murray Hill, N. J.

[3] Los Alamos National Laboratory, Los Alamos, N. M.

Copyright 1988 by the American Geophysical Union.
0096-3941/88/6932/769$01.00

yield systematically different values for G at a given site. It is not known whether deep anomalous bodies are present at the above measurement sites

An interest in performing geophysical-scale G experiments led the authors to plan two efforts. The first of these is based on measurements of g through a profile in the polar ice cap in Greenland [*Ander et al.*, 1986; *Chave et al.*, 1987] and uses standard land geophysical technology It was conducted in the late summer of 1987 (*Eos*, July 14, 1987), and analysis of the data is currently underway A more accurate experiment conducted in the deep ocean is feasible and is described here

An Ocean Experiment

An oceanic measurement of G was first suggested by *Stacey* [1978]. There are several advantages to an oceanic measurement of G over one made on land or ice The most important of these are the high accuracy with which water density can be measured in three dimensions in the ocean, the ability to make gravity measurements at diverse locations; the availability of long, continuous gravity profiles at the sea surface, allowing detection of deep mass anomalies, the relative simplicity of suboceanic structure compared to land sites; and the relatively smooth seafloor topography in many parts of the oceans The ocean slab is a thick and homogeneous entity; no other geological body approaches it in either size or uniformity of structure. The major potential problems for an oceanic G experiment are technical difficulties in the measurement of the Earth's gravitational acceleration. The ocean is in motion on a variety of temporal and spatial scales, and the precise measurement of accelerations in such a medium poses a challenge However, most of the developments needed to deal with these problems have already been made, and careful integration of these will yield the required sensitivity Overall, an accuracy of 2–3 parts in 10^4 for G should be possible in the ocean; this is a substantial improvement over any ice experiment and even approaches the accuracy with which Cavendish experiments can be performed (see Figure 1).

A scenario for an ocean G experiment consists of five components:

- measurements of the Earth's gravitational acceleration g along a 5000-m profile in the water column
- measurements of the depth and horizontal position at which the gravity measurements are made, also yielding the east-west velocity and accelerations of the gravimeter at the time of measurement
- determination of the seawater density as a function of depth and horizontal position relative to the gravity measurement site
- correction for the gravity field due to sources other than the slab of water, especially seafloor topography and sediment
- integration of all of these to yield G and, by comparison with laboratory values, its variation with mass separation

Geophysical Considerations

Consider a flat slab of water having uniform density and overlying the Earth. Two effects determine the difference in gravitational accelerations g between points on either side of the slab The first is the Earth's free air gravity gradient, and the second is the attraction of the slab itself These terms combine to yield a gravity difference

$$g_{top} - g_{bottom} = 4\pi G\rho\Delta z - \gamma\Delta z \qquad (5)$$

where γ is the Earth's free air gravity gradient (~3.09 µGal/cm; 1 Gal is 1 cm s^{2} or about 10^{3} times the Earth's surface gravity field) and ρ is the water density (which is close to 1.030 gm/cm^3 throughout the water column). It is feasible to acquire a gravity profile over an interval Δz of 5000 m in many parts of the oceans. Using these approximate values gives

$$\begin{aligned} g_{top} - g_{bottom} &\approx 432 \text{ mGal} - 1545 \text{ mGal} \\ &\approx -1113 \text{ mGal} \end{aligned} \qquad (6)$$

Most of the total gravity increase with depth in the ocean is due to the Earth The signal containing G is only that portion of the gravity change that is due to the water (432 mGal) To obtain a fractional uncertainty of $\epsilon = 1 \times 10^{4}$ in the value of G, it is necessary to measure Δg with an accuracy of $\epsilon \times 432$ mGal = 43 µGal Because the in situ gravity gradient is ~2 2 µGal/cm, the depth of the gravity meter must be known to 43 µGal/ 2 2 µGal cm^{1} or 20 cm. The signal containing G depends directly on the water density, so it will need to be known to $\epsilon \times \rho$ or roughly 0 0001 gm/cm^3. Finally, the gravity gradient from ocean bottom topography will need to be calculated to an accuracy of 43 µGal/ 5000 m ~ 9 µGal/km This will require a map of the bottom structure having a resolution of ~5 m in depth. The flat slab discussed above is a simplified model of the Earth A more complex, ellipsoidal layered Earth has been considered and can be used to predict the gravity difference with an accuracy of 1 part in 10^5 [*Stacey et al.*, 1981; *Dahlen*, 1982]

Oceanic Considerations

The oceanic water mass moves under the influence of a variety of forces There are two different types of phenomena that must be considered: density fluctuations that can alter the local apparent gravity, and vertical accelerations and east-west velocities that may affect the gravity measurements The first of these is only significant if the density fluctuations are local (i.e., in proximity to the gravimeter) or if their length scale is large compared to the measurement depth. In particular, density perturbations from small-scale phenomena like surface gravity waves are not important at abyssal depths. The second phenomenon consists of instrumental accelerations that are only a source of error at the level at which they cannot be detected and corrected. Since the characteristic time scale for deep ocean motions is several hours, this can be handled by careful acoustic tracking

Considerable difficulty can be avoided if a relatively benign part of the oceans is chosen for the experiment Regions of intense currents should certainly be avoided. This precludes operation in the western half of northern hemisphere ocean basins, where boundary currents and mesoscale eddies are dominant; coastal regions, where intense mixing can occur; equatorial regions, where strong current shear is observed; and mid-latitude convergence zones like that near 42°N, where density and current fluctuations are comparatively large. By contrast, the mid-gyre region of the North Pacific is ideal; it is one of the most quiescent parts of the world oceans, with weak mesoscale variability and weak mean currents below the main thermocline.

Further complications can be avoided if the relatively energetic surface mixed layer above the main thermocline and the benthic boundary layer near the seafloor are avoided. Density and velocity fluctuations in the upper few hundred meters of the mid-gyre Pacific are substantially larger than those at depth due to wind-induced mixing. Similarly, the bottommost few hundred meters should be avoided, both to minimize boundary layer and topographic effects

Spectra of water velocities in mid-gyre regions are dominated by the barotropic (depth-independent) tides and internal waves at periods shorter than about a day A good estimate of the effect of the ocean can be achieved by studying only these two types of phenomena Oceanic variability is weak at periods of 1–5 days, and longer period disturbances are effectively static on a 1-week experimental time scale. Thus the density field at depth can be considered as a combination of two parts: a mean component which changes on a time scale of days to months, and a fluctuating component, which changes on a scale of hours The mean component may be regarded as stationary for a G experiment, and is easily measured to an accuracy of a part in 10^5 using standard oceanographic techniques.

A prominent feature of the deep ocean is the barotropic tides, which typically exhibit surface displacements of 1 m or less, horizontal water velocities of 1–2 cm/s, and horizontal length scales of 1000 km or more A great deal of effort has gone into global ocean tide modeling in recent years, and it is now possible to predict the principal barotropic tides with accuracies of 10% or better in the open ocean [*Schwiderski*, 1980]. A simple estimate of the gravitational effect of displaced water associated with the tides may be made using an infinite slab Bouguer model, yielding Δg ~ 40 µGal. This number is reduced when consideration of the solid earth deflection is included In any case, correction to 10% reduces the tidal effect to below 10 µGal. Similarly, the vertical acceleration imparted by the tide may be obtained using a simple harmonic model $a = \omega^2 H$, where ω is the angular frequency and H is the tidal displacement This acceleration is about 2 µGal for a semidiurnal tide, and about 4 times smaller for diurnal ones. The horizontal accelerations are comparable. Therefore tidal accelerations are completely negligible, and correction for the shifted mass associated with the tides, while not neglectable, is easily accomplished.

Internal waves occur due to water density gradients and they are a ubiquitous feature of the deep ocean Motions due to internal waves range from the local inertial frequency (~1 cpd at mid-latitudes) to the buoyancy or Brunt-Väisälä frequency (1 cph or less) The horizontal length scales of internal waves range from meters to kilometers, with the larger waves occurring at lower frequencies. Below the thermocline, the density fluctuations due to internal waves are a negligible contribution to the observed gravity. Density fluctuations above the thermocline may be larger, but their effects will be small in the ocean's interior because of their small length scales

Internal waves are the dominant source of acceleration noise for an ocean G experiment. The power spectral density of vertical accelerations from internal waves may be computed from the Garrett-Munk displacement spectrum [Munk, 1981], scaled by ω^4. The mean-squared vertical acceleration is found by integrating over frequency and summing over all possible modes. This gives an rms acceleration of about 1.3 mGal at the base of the mixed layer and about 20 μGal at the seafloor. These accelerations can be corrected by monitoring the instrument position acoustically, since the time scales on which they occur are an hour or more. Similarly, it can be shown using the Garrett-Munk spectrum that the rms horizontal accelerations are at most 2.4 mGal and that they are reduced substantially at depth.

In conclusion, density fluctuations associated with the most common high-frequency oceanic motions, except the barotropic tides, are not significant. Correction for the tides is accomplished using standard models. Ocean-induced accelerations may be significant when compared to the measurement accuracy but may be corrected since they occur on a long time scale.

Site Specific Considerations

Site selection. Minimizing the gravity signatures from local geophysical structures and from oceanic conditions are the principal criteria for site selection. One desirable site characteristic is a minimum of ocean bottom topography; large scale topographic features such as seamounts, ridges, or trenches should be avoided. In addition, regions of contact between oceanic and continental crust should be shunned due to the gravity gradient created by differences in deep crustal and lithospheric structure. The oceanic problems mentioned in the last section also require consideration.

The minimum topographic relief that can be expected in nonsedimented areas on the seafloor is due to abyssal hills. These are lineated features due to normal faulting and have an average wavelength of 5 km and an amplitude of 100–200 m. The ocean bottom will acquire increasing amounts of sediment with age which will smooth the apparent seafloor topography. However, sedimented regions may be undesirable because the density contrast between the sediment and the basement will introduce gravity gradients. Heavily sedimented sites may require extensive (and expensive) seismic reflection surveys to map the regional depth to the basement topography, and it is uncertain if such a survey would have sufficient spatial resolution. It is preferable to work in a lightly sedimented area where multibeam sonar can be used to map the basement directly and precisely.

A site survey should be conducted to obtain a detailed map of the regional bathymetry. The Sea Beam multibeam sonar system provides elevation of the ocean bottom with a precision of better than 10 m over a 200 m by 200 m footprint. A shipboard gravity survey (~1 mGal accuracy) should also be conducted during the site survey. The intent of the shipboard gravity survey is to provide information on density contrasts within the ocean basement rock, to delineate the effects of the topography on the gradient of gravity as discussed above, and to ensure that local gravity gradients are small. In addition, strong constraints can be placed on the rock-water density contrast by conducting a seafloor gravity survey immediately about the measurement site using an ocean bottom gravimeter from a surface ship. Comparison of the ocean bottom gravity field and the ocean surface gravity field alone can yield an estimate of G (and its scale dependence) that is accurate to about 1 part in 10^3. An expedition to obtain these measurements is being supported by the Office of Naval Research and will be conducted by the authors during the summer of 1988.

Regional effects. Large-scale regional effects or unrecognized density variations at depth within the Earth could cause an anomalous local gravity gradient. This can be dealt with in several ways. First, long-wavelength (low degree) terms in satellite geoid data can be used to estimate the size of large-scale gravity anomalies; as the wavelength gets larger, the associated gravity gradient decreases. The lateral undulations of the geoid can be related to the vertical gradient in gravity through Laplace's equation. Second, more localized effects can be addressed by analyses of shipboard gravity data archived at major oceanographic institutions. Finally, modeling of large-scale bathymetric features, such as fracture zones, can be conducted. These corrections must be considered in any geophysical experiment to determine G and are not unique to an ocean experiment. However, the availability of the satellite-derived oceanic geoid makes correction for large-scale effects relatively simple for an ocean experiment.

Components of the Experiment

Measuring Gravity in an Ocean Slab

Gravity measurements can be made within the ocean slab using a LaCoste-Romberg underwater gravimeter. This is a version of the standard LaCoste-Romberg land gravity meter adapted for remote operation at the end of a wire and in a pressure case. These instruments have a repeatability of better than 20 μGal with reading times on the order of a few minutes.

A possible scenario for water-column gravity measurements consists of two separate packages, one for telemetry and another for gravity measurements. A soft tether would connect the two packages and decouple motion of the telemetry package from the gravity sensor. The gravimeter package would contain the LaCoste-Romberg instrument, a precision pressure gauge, a transponder pinger, and a buoyancy compensation chamber. At each gravity station the buoyancy compensation chamber trims the gravimeter package for neutral buoyancy. This can be accomplished with a compressible fluid for bulk compensation and a small pumpable chamber for fine compensation control.

To minimize the motions induced on the gravimeter package from the surface, it is beneficial to use the research floating instrument platform (FLIP) as the support vessel for the measurements. FLIP is a 100 m long spar-buoy surface platform that can be anchored with a three-point mooring at full ocean depths. She is designed to reduce the effect of 10- to 20-s ocean swell by at least a factor of 10, so that her vertical displacement in a 1-m sea is only a few cm [*Rudnick*, 1964]. No conventional ship can approach this level of performance. The motion experienced by the package can be reduced by another factor of ~3 through use of an accumulator on the topside winch.

Measuring the Position

Two independent methods can be used for precisely locating the gravity meter's position in the water column. One method involves use of acoustic transponders to measure the range between the gravimeter and a set of known, fixed locations on the seafloor. Combining three or more transponder ranges allows calculation of the gravimeter position in both the horizontal and the vertical. A favorable geometry would include one transponder placed on the seafloor beneath the gravimeter package and three transponders placed in an equilateral triangle around it. The transponder directly beneath the package provides its depth, whereas the triangle of transponders provides information on the lateral position. A new type of transponder, designed for centimeter positioning accuracy in geodetic work [*Spiess*, 1985] is especially suitable for this application. To obtain centimeter accuracy, a survey of sound speed must be conducted along the transponder sound paths.

An additional method for determining the package depth involves measurement of the ambient pressure. Under the hydrostatic approximation, the depth is given if the density is known, the latter can be computed from a conductivity, temperature, and depth (CTD) profiler on the telemetry package. Problems with long-term drift of the pressure gauge will occur and can be addressed by recording its reading at marked positions of the wire on each profile through the water column. However, pressure measurements are limited in accuracy by hysteresis and effects from nonhydrostatic water motions. They cannot be relied upon alone to provide the instrument depth with adequate precision, nor can they give necessary information on horizontal velocities and accelerations. A careful approach would utilize both of these techniques at the same time to produce some redundancy.

Additional information is needed on the north-south position of the gravimeter for accurate latitude correction and the east-west velocity for accurate Eötvös correction. At mid-latitudes, north-south lateral positioning of ~50 m is required for 1 part in 10^4 determination of G, and this is easily accomplished with a properly surveyed acoustic transponder network. East-west velocity of the gravimeter will change the centrifugal acceleration that it experiences and is corrected by the Eotvös term. At mid-latitudes and for a velocity of 2 cm/s the Eötvos correction is ~206 μGal. Velocities of this order may be encountered due to internal waves and the barotropic tides, but correction for their effects can be accomplished due to the long time scales on which they occur.

Measuring Density

The large-scale, nearly stationary part of the oceanic density field can be measured using conventional CTD instrumentation and an empirical equation of state for seawater [*Millero et al.*, 1980]. With careful precruise and postcruise calibration and the use of salinity check samples (which are measured on board-ship using a salinometer), a standard CTD profiler can measure temperature to a millidegree and salinity to 2 parts per thousand, yielding the density with an accuracy of a few parts per million. Depth is measured using a quartz pressure gauge, and the accuracy of the measurement is limited by hysteresis effects to about 1–2 m. This is more than adequate to characterize the large-scale density field.

A detailed CTD survey must be made at the location of the gravity measurements, and for a distance of ~25 km about the measurement site. The errors associated with terminating the survey at 25 km are at the 1 part in 10^5 level in *g* for any reasonable estimate of oceanic density fluctuations. Lateral density changes associated with baroclinic mesoscale eddies may be the largest source of local density contrasts in the experimental region. An eddy of 100-km size may produce a fractional density change of 4 parts in 10^5. Furthermore, other density contrasts, especially those associated with poorly understood fronts, may be present in the experimental area. A CTD survey provides the best way to be certain that the density field is adequately known.

Terrain and Sediment Correction

The density contrast due to basement rock topography and sediment will affect the local gravity gradient. To quantify these effects, the bathymetry can be modeled as a one-dimensional stationary random process, exploiting the strong lineation seen in most seafloor bathymetry. Figure 3 shows a power spectrum of the seafloor topography at a site in the eastern North Pacific (36°N, 137°W). Neglecting nonlinear terms, the gravity gradient caused by the topography can be expressed as a convolution of the topography with a filter function [*Parker*, 1973].

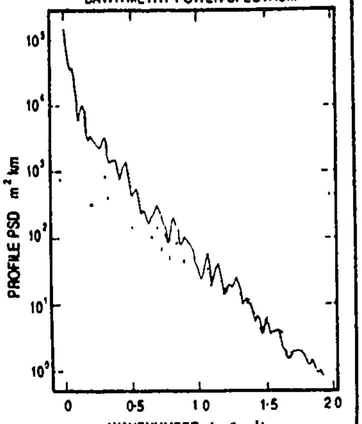

Fig. 3. Power spectrum of a 300-km-long section of Sea Beam bathymetry collected near 36°N, 137°W by P. Lonsdale of Scripps Institution of Oceanography. The solid line gives the spectrum of the basement terrain, and the dashed line gives the result for a sediment layer described in the text.

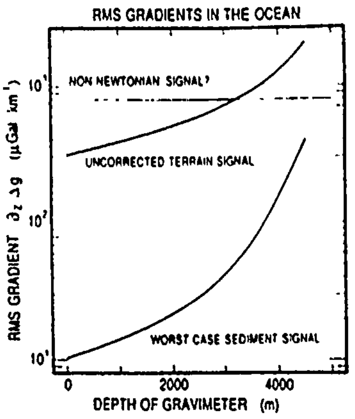

Fig. 4. The root-mean-square gravity gradient as a function of depth in the water column produced by a 1% non-Newtonian signal (800 µGal/km) compared to the uncorrected basement terrain signal using the bathymetry from Figure 3 and the uncorrected sediment signal using the model described in the text. For 1 part in 10^4 accuracy the terrain and sediment signals must be corrected to about 8 µGal/km.

Figure 4 shows the rms gravity gradient computed from the topography spectrum of Figure 3. The gradient produced by the density contrast at the water-rock interface is small compared to the predicted non-Newtonian gradient for measurements made in the water column above 3000 m. The gradients computed here may be overestimates because isostatic compensation has been neglected, a factor significant at the longest wavelengths where most of the topographic power is concentrated. For the lower section of the water column the topographic signal can be corrected using the site bathymetry and an estimate of the rock density. Uncertainties in rock density will cause the largest error, but it is unlikely to be wrong by more than a few percent, and much less if a seafloor gravity survey is performed. By terrain correction, the bathymetric signal can be reduced by at least a factor of 30, making it small in comparison to the predicted non-Newtonian field. The rms gradient produced from half filling the valleys with sediment is shown in Figure 4. The gradient due to sediment fill is small for almost all depths in the column. However, seismic reflection profiles can be used to determine sediment cover thickness for inclusion in the terrain correction.

Total Uncertainty in G

To summarize and compare the contributions of the experimental errors described above, a root-sum-square (rss) total uncertainty can be computed. This is a worst case estimate of the uncertainty. For example, the actual analysis of field data will consist of a least squares fit to a number of observations spaced along a profile and will account for systematic errors separately from random ones. Also, the gravity uncertainty is correlated with the depth uncertainty because of the vertical gravity gradient. Nevertheless, it is instructive to list the sources of uncertainty in an error budget shown in Table 1. The predicted ocean experimental error $\Delta G/G$ of 2.7 × 10^{-4} is within a factor of 4 of the best laboratory precision of 0.7 × 10^{-4} and is comparable to the overall accuracy with which *G* is known.

TABLE 1 Rss Uncertainty in *G*

Source of Uncertainty	Absolute Error	Effect on $\Delta G/G$ $\times 10^{-4}$
gravity record	50 µGal	1.2
package depth	20 cm	1.0
seawater density	1×10^{-5} gm/cm³	0.1
basement density	0.1 gm/cm³	2.0
basement topography	5 m	1.0
total uncertainty	$\Delta G/G = [\Sigma\, \mathrm{error}_i^2]^{1/2} = 2.7\times10^{-4}$	

An experiment such as the one described in this paper is multidisciplinary, requiring geophysics, physical oceanography, and ocean engineering. The goal of this experiment is to use the ocean as a natural laboratory for measurement of the Newtonian gravitational constant at a kilometer scale length. This is a unique opportunity for geophysical techniques to contribute to fundamental physics by testing the existence of intermediate-range gravitational forces.

Acknowledgments

This study was supported by the Institute of Geophysics and Planetary Physics at the Los Alamos National Laboratory and by the Office of Naval Research. We thank George Backus for helpful discussions regarding this work.

References

Ander, M. E., M. A. Zumberge, G. E. Backus, A. D. Chave, J. A. Hildebrand, and F. N. Spiess, Toward a geophysical determination of the Newtonian gravity constant, *Eos Trans. AGU*, *67*, 909, 1986.

Chave, A. D., M. A. Zumberge, M. E. Ander, J. A. Hildebrand, and F. N. Spiess, Polar ice test of the scale dependence of G, *Nature*, *326*, 250, 1987.

Cohen, E. R., and B. N. Taylor, The 1986 adjustment of the fundamental physical constants, *CODATA Bull.*, *63*, 1–36, 1986.

Dahlen, F. A., Variation of gravity with depth in the Earth, *Phys. Rev. D*, *25*, 1735, 1982.

Eckhardt, D. H., C. Jekeli, A. R. Lazarewicz, A. J. Romaides, and R. W. Sands, Tower gravity experiment: Evidence for non-Newtonian gravity, *Phys. Rev. Lett.*, *60*, 2567, 1988.

Facy, L., and C. Pontikis, Determination de la constante de gravitation par une methode de resonance, *C. R. Acad. Sci.*, *Ser. B*, *270*, 1970.

Facy, L., and C. Pontikis, Determination de la constante de gravitation par la methode de resonance, *C. R. Acad. Sci.*, *Ser. B*, *272*, 1397, 1971.

Gibbons, G. W., and B. F. Whiting, Newtonian gravity measurements impose constraints on unification theories, *Nature, 291*, 636, 1981.

Gillies, G. T., The Newtonian gravitational constant: An index of measurements, *Metrologia, 24 (Suppl.)*, 1–56, 1987.

Holding, S. C., F. D. Stacey, and G. J. Tuck, Gravity in mines—An investigation of Newton's law, *Phys. Rev. D, 33*, 3487, 1986.

Hsui, A. T., Borehole measurement of the Newtonian gravitational constant, *Science, 237*, 881, 1987.

Karagioz, O. V., V. P. Izmaylov, N. I. Agafonov, E. G. Kocheryan, and Yu. A. Tarakanov, The determination of the gravitational constant with an evacuated torsion balance, *Izv. Acad. Sci. USSR Phys. Solid Earth, Engl. Transl., 12*, 351, 1976.

Luther, G. G., W. R. Towler, R. D. Deslattes, R. Lowry, and J. Beams, *International Conference on Atomic Masses and Fundamental Constants*, vol. 5, edited by J. H. Sanders and A. H. Wapstra, Plenum, New York, 1976.

Luther, G. G., and W. R. Towler, Redetermination of the Newtonian gravitational constant *G*, *Phys. Rev. Lett., 48*, 121, 1982.

Millero, F. J., C. Chen, A. Bradshaw, and K. Schleicher, A new high pressure equation of state for seawater, *Deep Sea Res., 27*, 255, 1980.

Munk, W. H., Internal waves and small-scale processes, in *Evolution of Physical Oceanography*, edited by B. Warren and C. Wunsch, pp. 264–291, MIT Press, Cambridge, Mass., 1981.

O'Hanlon, J., Intermediate-range gravity: A generally covariant model, *Phys. Rev. Lett., 29*, 137, 1972.

Parker, R. L., The rapid calculation of potential anomalies, *Geophys. J. R. Astron. Soc., 31*, 447, 1973.

Pontikis, C., Determination de la constante de gravitation par la methode de resonance, *C. R. Acad. Sci., Ser. B, 274*, 437, 1972.

Renner, Y., Determination of gravitational constant in Budapest, in *Determination of Gravity Constant and Measurement of Certain Fine Gravity Effects, NASA Tech. Transl. F-15,722, Accession Code N74-30831*, edited by Y. D. Boulanger and M. U. Sagitov, pp. 26–31, U. S. Government Printing Office, Washington, D. C., 1974.

Rose, R. D., H. M. Parker, R. A. Lowry, A. R. Kuhlthau, and J. W. Beams, Determination of the gravitational constant G, *Phys. Rev. Lett., 23*, 655, 1969.

Rudnick, P., FLIP—An oceanographic buoy, *Science, 146*, 1268, 1964.

Sagitov, M. U., V. K. Milyukov, Ye. A. Monakhov, V. S. Nazarenko, and Kh. G. Tadzhidinov, A new determination of the Cavendish gravitational constant, *Dokl. Akad. Nauk SSSR, 245*, 567, 1979. (*Dokl. Akad. Nauk SSSR Earth Sci., 245*, 20, 1981.)

Schwiderski, E. W., On charting global ocean tides, *Rev. Geophys., 18*, 243, 1980.

Spiess, F. N., Suboceanic geodetic measurements, *IEEE Trans. Geosci. Remote Sens., GE-23*, 502, 1985.

Stacey, F. D., Possibility of a geophysical determination of the Newtonian gravitational constant, *Geophys. Res. Lett., 5*, 377, 1978.

Stacey, F. D., G. J. Tuck, S. C. Holding, A. R. Maher, and D. Morris, Constraint on the planetary scale value of the Newtonian gravitational constant from the gravity profile within a mine, *Phys. Rev. D, 23*, 1683, 1981.

Stacey, F. D., G. J. Tuck, G. I. Moore, S. C. Holding, B. D. Goodwin, and R. Zhou, Geophysics and the law of gravity, *Rev. Mod. Phys., 59*, 157, 1987.

The Performance of Two Classes of Active Sonar Detectors in a Shallow Water Environment[*]

D. Almagor and W. S. Hodgkiss

---

[*]. Reprinted from Proceedings of the ICASSP 90, Vol. CH2847, pp. 2723-2726 (1990)

Reprinted from PROCEEDINGS OF THE ICASSP 90 — 1990 INTERNATIONAL
CONFERENCE ON ACOUSTICS, SPEECH, AND SIGNAL PROCESSING,
Albuquerque, New Mexico, April 3-6, 1990

U1.1

THE PERFORMANCE OF TWO CLASSES OF ACTIVE SONAR DETECTORS IN A SHALLOW WATER ENVIRONMENT

D. Almagor and W.S. Hodgkiss

Marine Physical Laboratory
Scripps Institution of Oceanography
San Diego, Ca 92152

ABSTRACT

Boundary acoustic reverberation can leak through the receive beamformer sidelobe structure of an active sonar system and mask the presence of target echoes. Two classes of active sonar detectors designed to combat boundary reverberation are developed in this paper and a two-beam active sonar scenario is set up. Based on a special reverberation generator (REVSIM), the Monte-Carlo derived performance of the two systems is then evaluated and compared through their ROC curves.

I. INTRODUCTION

Acoustic reverberation is a phenomenon which active sonar systems have to combat. Boundary reverberation (surface or bottom), can leak through the receive beamformer sidelobe structure and mask the presence of target echoes. One intuitive approach to the detection problem suggests the use of an adaptive beamforming structure which dynamically steers spatial nulls in the direction of the boundary patch (surface or bottom) responsible for the reverberation, followed by a matched filter. The adaptive structure is known as a noise canceler [1]. It is not at all clear that this noise canceler structure yields an optimal detector (under any optimization criterion). Implementations of such adaptive beamforming structures which take advantage of the spatial separation between desired signals and boundary reverberation contaminants are presented in [2]. Additional relevant references are [3,4].

Another approach suggests treating the problem as a whole right from the beginning without imposing intuitive components on the processor structure, and using all a-priori knowledge available. Detection theory provides us with a mathematical framework out of which optimum processors can be designed. The processor will evolve out of the mathematical solution of the problem, and will not be restricted to using familiar structures. Here, any uncertain parameters are treated as random variables and all knowledge about them is summarized in a-priori probability density functions.

Although Bayes optimal processors have been derived for the case of volume reverberation [5], little work has been done which takes advantage of a-priori knowledge of the time-evolving spatial characteristics of boundary reverberation. Related Bayes optimal work concerning interference sources of certain and uncertain (but not time varying) location is contained in [6] and [7-9] respectively.

This paper considers an active sonar scenario in which the sonar array is placed at a relatively shallow depth and is prone to surface interference. The array depth is either known or unknown, with known probability density function. The paper then examines the performance of two detectors representative of the detection approaches discussed above using a reverberation simulation generator (REVSIM) [10] presented at ICASSP88. The performance comparison is made in terms of detector ROC curves.

II. OCEAN ACOUSTIC REVERBERATION

In general, the performance of underwater systems is limited by external noise sources and not internal (thermal) noise. In the absence of hostile jammers, this external noise usually is divided into two main categories, namely ambient ocean noise and reverberation. The systems considered in this paper are assumed to operate in conditions which dictate that performance is reverberation limited.

Reverberation is the result of scattering of energy originating from the propagating pulse, by inhomogeneities in the ocean and its boundaries. In some respects, this problem is akin to the radar "clutter" problem. Reverberation is usually divided into three classes, namely, surface, volume and bottom reverberation. Irregularities in the ocean surface and the acoustic impedance contrast of the air/sea interface, gives rise to surface reverberation. This type of reverberation varies with wind speed and transmission frequency [11-13]. In the ocean body, air bubbles, suspended sediment, thermal inhomogeneities, fish, plankton, and other biological sources are the main contributors to what is classified as volume reverberation [14]. Bottom reverberation is caused by energy scattered from the sea floor, and is highly dependent on the sea floor type. Both particle size and bottom relief are important factors [15,16].

In general, ocean acoustic reverberation has a very complex nature and a highly variable power spectrum. In some situations, where the sonar is fairly close to the ocean boundaries, or when its sidelobes are pointing towards those boundaries the energy reflected off of the boundaries makes a significant contribution to the range-Doppler map. This contribution usually has a sudden onset, may appear at nonzero Doppler frequencies, and therefore may mask legitimate sonar echoes.

A typical range-Doppler map of a reverberation return is shown in Figure 1. It was generated using a reverberation simulation package (REVSIM) developed for this research and presented at ICASSP88 [10]. Here, the vehicle purposefully was given a relatively high speed (30 m/s) so as to well separate boundary reverberation from volume reverberation in the frequency domain and make each of them well defined. The range-Doppler map also has been left

CH2847-2/90/0000-2723 $1.00 © 1990 IEEE

shifted to compensate for the vehicle's own speed The sonar array is placed at a depth of 100 m, where the ocean depth is 400m. The transmit beam illuminates a sector ±75° in elevation, and the receive beam spans ±60°. Early in the ping, around 0.1 sec, the onset of the surface reverberation is easyly seen. It slowly creeps towards 0 Doppler joining the volume reverberation Around 0.5 sec, the onset of bottom reverberation appears. It, too, then slowly joins the volume reverberation until around 1 sec the two spectral peaks become very close.

III. SIGNAL DETECTION IN BOUNDARY REVERBERATION

Traditionally, sonar systems have discriminated against boundary reverberation by forming fixed receiving beams which have low sidelobe characteristics in the direction of the ocean boundaries. However, the energy leaking through the low sidelobes may still be a major contributor to the overall noise background level. Furthermore, since the sonar system can be moving and varying its depth in the water column, the direction of boundary reverberation is not fixed.

The above reasoning led many researchers to propose using an adaptive structure in order to track the interference direction and place spatial beamformer nulls in that direction. Such a beamformer may learn continuously the boundary interference direction and adjust itself to cancel it out, thereby enhancing signal to noise ratio and improving the detection performance. Implementation of such an ad-hoc structure follows the lines of the well known adaptive noise canceler. In addition to a main beam which receives well in the desired look direction, one or more reference beams are formed. The reference beams receive well in the direction of the boundary interference, and have spatial nulls in the main look direction The output of the main beam contains both the desired signal, and a contaminant which is the contribution of the boundary interference leaking through side lobes or the edges of the main lobe Ideally, the reference beams contain only a replica of the interference The output of the reference beam, or beams, is processed by an adaptive filter and then subtracted from the main beam The adaptive filter tries to provide a good estimate of the interference portion of the main beam output, and the final error output ideally contains only the desired signal Implementation of such adaptive reverberation cancellation schemes is reported in [2]. The boundary reverberation canceled output of the adaptive structure can now be treated as containing a known signal in noise (the volume reverberation), a classical, solved problem.

Another approach suggests treating the problem as a whole right from the beginning without imposing intuitive components on the processor structure, and using all a-priori knowledge available. Detection theory provides us with a mathematical framework out of which optimum processors can be designed. The processor will evolve out of the mathematical solution of the problem, and will not be restricted to using familiar structures.

Although Bayes optimal processors have been derived for the case of volume reverberation, little work has been done which takes advantage of a priori knowledge of the time-evolving spatial characteristics of boundary reverberation. Related Bayes optimal work concerning interference sources of certain and uncertain (but not time varying) location is contained in [6] and [7-9] respectively.

Here, a classical detection theoretic approach is applied to the processing of a vector time series That vector may be composed of the single array element outputs, or of some preformed beams. An optimality criterion is chosen, and then the processor structure is allowed to evolve freely out of the mathematical solution of the problem. Any uncertain parameters are treated as random variables and all knowledge about them is summarized in a-priori probability density functions.

IV. TWO SONAR PROBLEMS AND THEIR CORRESPONDING DETECTORS

The problem setting is as follows an active sonar system is mounted on an underwater platform which is submerged in shallow water The ocean depth is chosen such that there is a significant no overlap zone between the two boundary (surface and bottom) interferences, and therefore only one of them is considered, meaning the detection decision is performed in the no overlap zone. The platform's depth in the water column is either known or has a known probability density function. Sound speed profiles are assumed isovelocity, i.e. acoustic energy propagates through the medium in straight lines. The platform is completely stationary in the water column, i.e. the effective own Doppler speed is zero. The sonar's front end is a four row sensor array whose preformed beam outputs are available to the processor in the form of a sampled vector time series The preformed beam ensemble contains a sum beam which is formed by summing all row outputs, and a difference beam formed by subtracting two adjacent row outputs. It is further assumed that the transmission pulse is narrowband, that the incoming signal characteristics are completely known, and that the target is stationary. The sonar is assumed to be limited in performance by acoustic reverberation and not by ambient ocean noise

Depicted in Figure 2, The two sub scenarios, are as follows

1. Platform is at a fixed, precisely known depth
2. Platform is at an unknown depth, but the depth probability density function
   is known precisely.

As discussed above, one system developed here uses an ad hoc engineering approach, and is implemented using an adaptive noise canceler followed by a matched filter. The second system is developed following classical detection theoretic principles, and implements a likelihood ratio detector. Figure 3 depicts the structure of the two detectors.

Since the transmitted energy is propagating through the water, the boundary interference direction is changing constantly In the case where platform depth is known exactly, the interference direction is also known exactly. When there is uncertainty in platform depth, it translates to uncertainty in the direction of the incoming boundary interference.

Studies show that the complex envelope magnitude of acoustic reverberation is Rayleigh distributed, and that the real and imaginary components of this envelope are jointly Gaussian distributed. This property of reverberation justifies using Gaussian probability density functions in all the derivations of the Bayes optimum detectors in this paper

A general expression for the likelihood function in the case of a known signal in spatially correlated Gaussian noise is :

$$\Lambda(Z) = \frac{p(Z/H_1)}{p(Z/H_0)} = \exp[-(Z-m)^* Q^{-1}(Z-m) + Z^* Q^{-1} Z] \quad (1)$$

where Z is the observed vector, m and Q are the observed vector mean and covariance matrix, and H_0 and H_1 are the signal absent and present hypotheses respectively. Equation (1) serves as the basis for computing the Bayes optimum detectors in the two sub scenarios addressed in this paper. In the second sub scenario, when there is depth uncertainty represented in the form of a probability density, the likelihood ratio is developed through integrating over the uncertain parameter

V. DETECTOR EVALUATION AND COMPARISON

The array used in the comparison is a four row array, where the main beam was composed of summing all four row outputs, and the reference beam was generated by subtracting two adjacent row outputs.

Each comparison between the two detection approaches is based on a Monte-Carlo simulation of 500 runs. Each run has been synthesized using a unique multi-channel reverberation time series generator [10]. In the first comparison made, the sonar array was placed at a known depth, and the Bayes optimum detector was given that depth. Signal to surface interference ratio was set to 2.8. The comparison is made in terms of Receiver Operating Characteristic (ROC) curves, which present the probability of detection as a function of the probability of false alarm, and summarize completely the detector performance. Figure 4 shows the ROC curves of both detectors. Obviously, the Bayes Optimum detector (BOD) performs better than the ad-hoc Adaptive Noise Canceler (ANC).

In the next comparison, array depth is not a known quantity. What is known is its probability density function, which is assumed uniform between 3 m and 57 m. This way, the average depth is kept the same as the previous comparison's depth (30 m) The comparison is based again on 500 Monte-Carlo simulation runs, where the array was placed physically at various depths, commensurate with a uniform distribution. Figure 5 shows the ROC curves for this comparison.

The BOD's performance has degraded, but with this level of uncertainty, it is still performing better than the ANC.

VI. SUMMARY

This paper has developed two active sonar detectors for a specific boundary reverberation problem and has compared their performance As expected, the performance of the optimum detector was shown to be better than that of the ad-hoc detector.

Acknowledgements

This work was supported by the Office of Naval Research, Contract N00014-87-K-0010.

References

1. Widrow, B., J. R. Glover, J. M. McCool , J. Kaunitz , C. S Williams , R. H. Hearn , J. R. Zeidler , E. Dong, Jr. , and R. C. Goodlin, "Adaptive noise cancelling principles and applications," *Proc. IEEE*, vol. 63, pp. 1692-1716, 1975.
2. Hodgkiss, W. S. and D. Alexandrou, "Sea surface reverberation rejection," *ICASSP*, vol. 33, pp 7.1-7.4, 1984.
3. Trees, H. L. Van, *Estimation and Linear Modulation Theory.*, Wiley, New York, 1971.
4. Whalen, A. D , *Detection, Estimation of Signals in Noise*, Academic Press, New York, 1971.
5. Trees, H. L. Van, *Radar Sonar Signal Processing and Gaussian Signals in Noise*, Wiley, New York, 1971
6. Adams, S. L. and L. W. Nolte, "Bayes optimum array detection of targets of known location," *J. Acoust Soc. Am.*, vol. 58 No. 3, 1975.
7. Hodgkiss, W. S and L. W Nolte, "Optimal array processor performance trade-offs under directional uncertainty," *IEEE Trans. Aerosp. Electron. Sys*, vol AES-12, pp. 605-615, 1976.
8. Hodgkiss, W. S. and L. W. Nolte, "Adaptive optimum array processing," *J. Acoust. Soc. Am.*, vol. 61, pp 763-775, 1976.
9. Hodgkiss, W. S. and L. W. Nolte, "Array processor performance under directional uncertainty," *IEEE Trans. Aerosp. Electron. Sys.*, vol. AES-14, pp 827 832, 1978.
10. Hodgkiss, W.S. and D. Almagor, "Element level reverberation time series synthesis," *Proceedings of ICASSP*, vol. 5, pp. 2701 2704, New York, 1988.
11. Urick, R J and R M Hoover, "Backscattering of sound from the sea surface, its measurement, causes and application to the prediction of reverberation levels," *Jour Acoust. Soc. Am*, vol. 28, pp. 1038-1042, 1956.
12. Chapman, R.P and J.H Harris, "Surface backscattering strengths measured with explosive sound sources," *Jour. Acoust. Soc. Am.*, vol. 34, pp. 1592-1597, 1962.
13. Garrison, G.R, S.R Murphy, and D S Potter, "Measurement of the backscattering of underwater sound from the sea surface," *Jour Acoust Soc. Am*, vol. 32, pp. 104-111, 1960
14. Clay, C.S and H. Medwin, *Acoustical Oceanography*, Wiley, New York, N.Y , 1977.
15. Mckinney, C.M and C D Anderson, "Measurement of backscattering of sound from the ocean bottom," *Jour. Acoust. Soc. Am.*, vol. 36 No 1, pp 158-163, 1964
16. Buckley, J P and R J Urick, "Backscattering from the deep sea bed at small grazing angles," *Jour Acoust Soc. Am*, vol. 44 No. 2, pp. 237-252, 1968

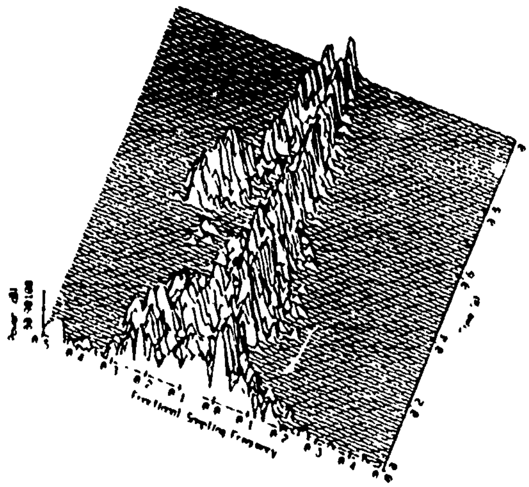

Figure 1. Typical reverberation range-Doppler map

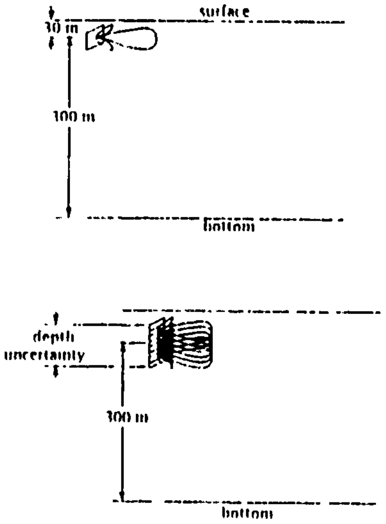
surface
30 m
100 m
bottom
depth
uncertainty
100 m
bottom

Figure 2. The two sub-scenarios

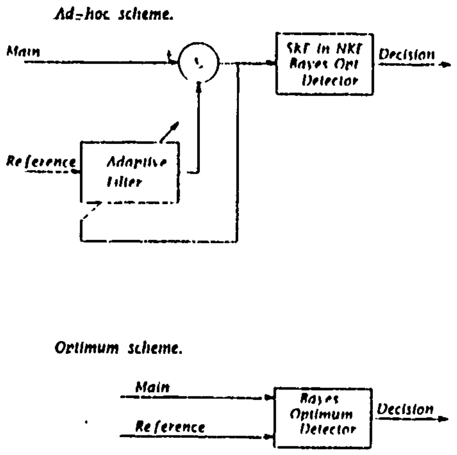
Ad-hoc scheme.
Main
Reference
Adaptive
Filter
SKF in NKF
Bayes Opt
Detector
Decision
Optimum scheme.
Main
Reference
Bayes
Optimum
Detector
Decision

Figure 3. The two detector structures

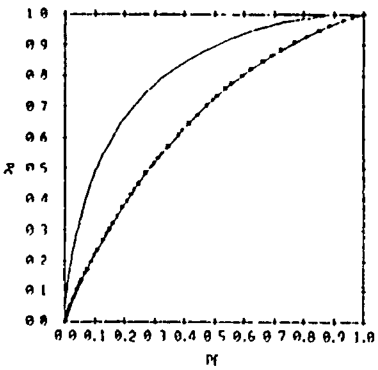

Figure 4. Known depth ROC curves. Bayes Optimum Detector vs. Adaptive Noise Canceler (ANC is *****).

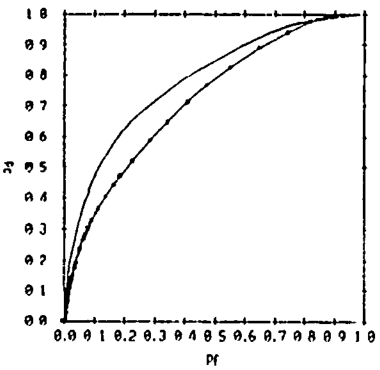

Figure 5. 54 m depth uncertainty ROC curves. Bayes Optimum Detector vs. Adaptive Noise Canceler (ANC is *****).

III. BIBLIOGRAPHY

Abstracts

1. J. A. Hildebrand and R. L. Parker, "Analysis of seamount magnetic anomalies," EOS, Trans. Am. Geohys. Union **65**, 1079 (1984).

2. J. Hildebrand and R. L. Parker, "Pacific palaeomagnetic poles derived using non-uniform modeling of seamount magnetic anomalies," EOS, Trans. Am. Geohys. Union **66**, 864 (1985).

3. P. T. C. Hammer and J. A. Hildebrand, "Modeling non-uniform seamount internal density from gravitational field inversion," EOS, Trans. Am. Geohys. Union **67**, 1001 (1986).

4. Mark E. Ander, Mark A. Zumberge, George E. Backus, Alan D. Chave, John Hildebrand, and Fred N. Spiess, "Toward a geophysical determination of the Newtonian gravity constant," EOS, Trans. Am. Geohys. Union **67**, 909 (1986).

5. C. de Moustier and D. Alexandrou, "Characterization of seafloor type and roughness from 12 kHz acoustic backscattering measurements," J. Acoust. Soc. **82**, S123 (1987).

6. P. T. C. Hammer, J. A. Hildebrand, and R. L. Parker, "Modelling non-uniform internal density using semi-norm gravity inversion - Jasper Seamount," EOS, Trans. Am. Geohys. Union **68**, 1248 (1987).

7. F. N. Spiess, J. A. Hildebrand, and D. E. Boegeman, "New systems for seafloor studies," EOS, Trans. Am. Geohys. Union **68**, 1335 (1987).

8. A. E. Schreiner, L. M. Dorman, J. A. Hildebrand, D. Lahav, and F. N. Spiess, "Wavelength and correlation length of deep ocean ambient seismic noise," EOS, Trans. Am. Geohys. Union **68**, 1373 (1987).

9. J. Gee, L. Tauxe, J. Hildebrand, and H. Staudigel, "Magnetics of Jasper Seamount: Implications for seamount paleopole determination," EOS, Trans. Am. Geohys. Union **68**, 1255 (1987).

10. J. M. Stevenson, P. T. C. Hammer, J. A. Hildebrand, and C. G. Fox, "The sea-surface and seafloor gravity field of Axial Volcano, Juan de Fuca Ridge," EOS, Trans. Am. Geohys. Union **69**, 1467 (1988).

11. S. C. Webb and J. A. Hildebrand, "Constraints on crustal structure beneath axial volcano derived from long period acceleration and pressure measurements," EOS, Trans. Am. Geohys. Union **69**, 1484 (1988).

12. D. Lahav, J.A. Orcutt, C.S. Cox, S.C. Webb, and S.C. Constable, "Low frequency ocean bottom noise measurements," EOS, Trans. Am. Geohys. Union **69**, 1319 (1988).

13. C. de Moustier and D. Alexandrou, "Investigation of 12 kHz deep scattering layers observed with the multibeam echo-sounder Sea Beam," J. Acoust. Soc. Am. **83**, 548 (1988).

14. J. A. Hildebrand, A. D. Chave, F. N. Spiess, R. L. Parker, M. A. Zumberge, J. M. Stevenson, P. T. C. Hammer, and M. E. Ander, "An oceanic determination of the scale dependence of *G*," EOS, Trans. Am. Geohys. Union **69**, 1046 (1988).

15. G. E. Updegraff and V. C. Anderson, "*In situ* acoustic signature of low sea state microbreaking," J. Acoust. Soc. Am. **85**, S146 (1989).

16. C. de Moustier, "High-frequency acoustic imaging of the seafloor," J. Acoust. Soc. Am. **86**, S32 (1989). [Invited Presentation].

17. C. de Moustier and B. J. Sotirin, "Performance limitations of hull-mounted sonar arrays in the presence of air bubbles," J. Acoust. Soc. Am. **88**, 131 (1990).

18. J-M. Q.D. Tran and W. S. Hodgkiss, "Matched-field processing of 200 Hz CW signals," J. Acoust. Soc. Am. **87(1)**, S153 (1990).

Research Articles, Books and Conference Proceedings

1. R. L. Culver and W. S. Hodgkiss, "Comparison of Kalman and least squares filters for locating autonomous very low frequency acoustic sensors," IEEE J. Oceanic Engineering **13**, 282-290 (1988).

2. C. de Moustier, T. Hylas, and J. C. Phillips, "Modifications and improvements to the Sea Beam system on board R/V Thomas Washington," Proc. MTS/IEEE Oceans '88, 372-378 (1988).

3. C. de Moustier, "State of the art in swath bathymetry survey systems," Vol. OED-13, in *Current Practices and Technology in Ocean Engineering*, edited by G. K. Wolfe and P. Y. Chang (American Society of Mechanical Engineers, New York, N.Y., 1988), pp. 29-38. Also appears with revisions in International Hydrographic Review, MONACO, Vol. LXV(2), pp. 25-54 (1988)..

4. C. de Moustier, "State of the art in swath bathymetry survey systems," International Hydrographic Review, Monaco **LXV(2)**, 25-54 (1988). English-to-French translation by C. de Moustier..

5. J.S. Jaffe, "Underwater optical imaging: The design of optimal systems," Oceanography Society Journal **1**, 40-41 (1988).

6. J. A. Hildebrand, A. D. Chave, F. N. Spiess, R. L. Parker, M. E. Ander, G. E. Backus, and M. A. Zumberge, "The Newtonian gravitational constant: On the feasiility of an oceanic measurement ," EOS, Trans. Am. Geohys. Union **69**, 769,779-780 (1988).

7. Spahr C. Webb, "Long period acoustic and seismic measurements and ocean floor currents," IEEE J. Oceanic Eng. **13**, 263-270 (1988).

8. M. E. Ander, M. A. Zumberge, T. Lautzenhiser, R. L. Parker, C. L. V. Aiken, M. R. Gorman, M. M. Nieto, A. P. R. Cooper, J. Cooper, J. Ferguson, E. Fisher, G. A.

McMechan, A G. Sasagawa, J. M. Stevenson, G. Backus, J. Greer, P. Hammer, A L. Hansen, J. A. Hildebrand, A R. Kelty, A C. Sidles, A F. N. Spiess , and J. Wirtz, "A test of Newton's inverse-square law in the Greenland ice cap," Phys. Rev. Lett. **62**, 1 (1989).

9. W. S. Hodgkiss and F. H. Fisher, "Vertical directionality of ambient noise at 32°N as a function of longitude and wind speed," in *Underwater Acoustic Data Processing*, edited by Y. T. Chan (Kluwer Publishers, Kingston, Canada (1988), 1989), pp. 99-104. Proceedings of the NATO Advanced Study Institute on Underwater Acoustic and Data Processing.

10. K. L. Smith, W. C. Schwab, M. and Nobel, and C. de Moustier, "Physical, geological and biological studies on four Pacific seamounts: Introduction in the Central-Pacific," Deep Sea Research **36**, 1785-1790 (1989).

11. J. A. Hildebrand, "The paleomagnetism of eastern Nazca plate seamounts ," Tectonophysics **170**, 279-287 (1989).

12. J. A. Smith, "Doppler sonar and surface waves: range and resolution," J. Atmos. and Oceanic Tech. **6**, 680-696 (1989).

13. W. S. Hodgkiss and F. H. Fisher, "Vertical directionality of ambient noise at 32°N as a function of longitude and wind speed," IEEE J. Oceanic Eng. **15**, 335-339 (1990).

14. J. A. Hildebrand, J. M. Stevenson, P. T. C. Hammer, M. A. Zumberge, and R. L. Parker, "A seafloor and sea-surface gravity survey of axial volcano," J. Geophys. Res. **95**, 12,751-12,763 (1990).

15. K. M. Watson, "The coupling of surface and internal gravity waves: Revisited," J. Phys. Oceanogr. **20**, 1238-1248 (1990).

16. C. de Moustier, P. F. Lonsdale, and A. N. Shor, "Simultaneous operation of the Sea Beam multibeam echo-sounder and the SeaMARC II bathymetric sidescan sonar system," IEEE J. of Oceanic Engr. **15**, 84-94 (1990).

17. D. Almagor and W. S. Hodgkiss, "The performance of two classes of active sonar detectors in a shallow water environment," IEEE Int'l Conf. Acoustics, Speech, & Signal Processing **CH2847-2**, 2723-2726 (1990).

18. S. C. Webb , X. Zhang, and W. Crawford, "Infragravity waves in the deep ocean," J. Geophys. Res. **96**, 2723-2736 (1991).

19. J-M. Q.D. Tran and W. S. Hodgkiss, "Matched-field processing of 200 Hz CW signals," J. Acoust. Soc. Am. **89**, 745-755 (1991).

20. W. C. Schwab, K. L. Smith, C. de Moustier, and M. and Nobel, "General overview of the geologic and biologic of seamounts in the Central-Pacific," Deep Sea Research (in prep).

21. C. de Moustier, K. L. Smith, and D. Alexandrou, "12 kHz acoustic measurements of the DSL over two Central-Pacific seamounts with the multibeam echo-sounder Sea Beam," Deep Sea Research (in prep).

22. C. de Moustier and D. Alexandrou, "Angular dependence of 12 kHz seafloor acoustic backscatter," J. Acoust. Soc. Am. (in press).

23. W. S. Hodgkiss and D. Almagor, "Oceanic reverberation time series synthesis," IEEE J. Oceanic Eng. (in press).

24. G. E. Updegraff and V. C. Anderson, "Bubble noise and wavelet spills recorded one meter below the ocean surface," J. Acoust. Soc. Am. (in press).

25. J-M. Q.D. Tran and W. S. Hodgkiss, "Experimental observation of temporal fluctuations at the output of the conventional matched-field processor," J. Acoust. Soc. Am. (in press).

26. G. E. Updegraff and V. C. Anderson, "An instrument for the *in situ* measurement of sea surface noise from a depth of one meter under low wind conditions," J. Acoust. Soc. Am. (in press).

27. S.C. Webb and J.A. Hildebrand, "Seafloor compliance observed by long pressure and displacement measurements," J. Geophys. Res. (in press).

28. J.S. Jaffe, "Performance characterization of underwater imaging systems," IEEE J. Oceanic Eng. (Previously submitted to Appl. Optics) (in press).

29. J-M. Q.D. Tran and W. S. Hodgkiss, "Subaperture beamforming of large aperture vertical line arrays," IEEE J. Oceanic Engineering (submitted).

30. J.S. Jaffe and C. Dunn, "A model-based comparison of underwater imaging systems," Ocean Optics IX (submitted).

31. P. T. C. Hammer, J. A. Hildebrand, and R. L. Parker, "Gravity inversion using seminorm minimization: Density modeling of Jasper Seamount," Geophysics (submitted).

Scripps Institution of Oceanography Reference Series

1. Richard L. Culver, "Localizing and beamforming freely-drifting VLF acoustic sensors," SIO Reference 88-16, Scripps Institution of Oceanography, San Diego, CA (1988). Ph.D. Dissertation.

2. G. E. Updegraff, "In Situ investigation of sea surface noise from a depth of one meter," SIO Reference 89-21, Scripps Institution of Oceanography, Marine Physical Laboratory, San Diego, CA (1989). Ph.D. Dissertation.

3. Anthony E. Schreiner, "Observations of seafloor ambient noise with an ocean bottom seismometer array," SIO Reference 89-27, Scripps Institution of Oceanography, Marine Physical Laboratory, San Diego, Calif. (1989). Ph.D. Dissertation.

4. Jeffrey Thomas Sherman, "Observations of fine-scale vertical shear and strain in the upper ocean," SIO Reference 89-11, Scripps Institution of Oceanography, San Diego, CA (1989). Ph.D. Dissertation.

5. David Almagor, "Least squares adaptive and Bayes optimal array processors for the active sonar problem," SIO Reference 89-16, Scripps Institution of Oceanography,, San Diego, California (1989). Ph.D. Dissertation.

6. J-M Q. D. Tran, "Approaches to the processing of data from large aperture acoustic vertical line arrays," SIO Reference 90-21, Scripps Institution of Oceanography, Marine Physical Laboratory, San Diego, CA (1990). Ph.D. Dissertation.

Technical Memorandums

1. G. L. D'Spain, R. L. Culver, W. S. Hodgkiss, and G. L. Edmonds, "Freely drifting Swallow float array: April 1987 trip report," MPL TM-397, Marine Physical Laboratory, Scripps Institution of Oceanography, San Diego, CA (1987).

2. R. L. Culver, W. S. Hodgkiss, G. L. Edmonds, and V. C. Anderson, "Removing resonant oscillation from Swallow float data," MPL TM-395, Marine Physical Laboratory, Scripps Institution of Oceanography, San Diego, CA (1987).

3. G. L. D'Spain, R. L. Culver, W. S. Hodgkiss, and G. L. Edmonds, "Freely drifting Swallow float array: May 1987 trip report," MPL TM-402, Marine Physical Laboratory, Scripps Institution of Oceanography, San Diego, CA (1988).

4. R. K. Brienzo, "Iterative method for the estimation of shot and sea floor depths using hydrophone streamer data," MPL TM-398, Marine Physical Laboratory, Scripps Institution of Oceanography, San Diego, California (1988).

5. R. L. Culver, W. S. Hodgkiss, G. L. Edmonds, and V. C. Anderson, "Low frequency oscillation in 1986 Swallow float data," MPL TM-394, Marine Physical Laboratory, Scripps Institution of Oceanography, San Diego, CA (1988).

6. G. D'Spain and W. S. Hodgkiss, "Comparison of Swallow float ocean bottom seismometers and sonobuoy data in the VLF band," MPL TM-404, Marine Physical Laboratory, Scripps Institution of Oceanography, San Diego, CA (1988).

7. C. de Moustier, R. M. Lawhead, and J. Pinpin, "Post processing software tools for Sea Beam complex acoustic data," MPL TM-406, Marine Physical Laboratory, Scripps Institution of Oceanography, San Diego, CA (in prep).

ONR/MPL GENERAL DISTRIBUTION LIST

Chief of Naval Research
Department of the Navy
Arlington, Virginia 22217-5000
Code 12, 122(2), 125
1121, 112, 1122,
1123, 1125, 1125 OA,
1125 GG, 23

ONRDET
Stennis Space Center
Bay St. Louis, Mississippi 39529-5004
Code 125

Commander
Naval Sea Systems Command
Washington, D. C. 20362
Code 63DB, 933A

Commanding Officer
Naval Ocean Research and
Development Activity
Stennis Space Center
Bay. St. Louis, Mississippi 39529-5004
Code 100, 110, 300, 330,
200, 220, 240, 250, 270,
320, 360, 350

Commander
U.S. Naval Oceanographic Office
NSTL Station
Bay St. Louis, Mississippi 39522-5004
Atten: Bill Jobst

Assistant Secretary of the Navy
(Research Engineering & Systems)
Department of the Navy
Washington, D. C. 20350

Defense Advanced Res. Proj. Agency
TTO - Tactical Technology Office
1400 Wilson Boulevard
Arlington, Virginia 22209-2308
Atten: John N. Entzminger

National Oceanic & Atmospheric
Administration
Ocean Engineering Office
6001 Executive Boulevard
Rockville, Maryland 20852

Commander
Space and Naval Warfare
Systems Command
Washington, D. C. 20360-5100
Code PMW-180T, PMW-180-5

Commander
Naval Ship Res. & Dev. Center
Bethesda, Maryland 20084

Executive Secretary
Naval Studies Board
National Academy of Sciences
2101 Constitution Avenue, N.W.
Washington, D.C. 20418

Director
Strategic Systems Proj Ofc.
Department of the Navy
Washington, D. C. 20361
Code NSP-20

Commander
Naval Ocean Systems Center
San Diego, California 92152
Code 00, 01, 16, 94,
54, 541, 605, 71, 72, 701

Commander
Submarine Development Group ONE
139 Sylvester Road
San Diego, California 92106

Commanding Officer
Civil Engineering Laboratory
Naval Construction Battalion Center
Port Hueneme, California 93043
Code L40, L42

Commanding Officer
Naval Underwater Systems Center
Newport, Rhode Island 20844
Atten: E.L. Sullivan

Officer in Charge
Naval Underwater Systems Center
New London Laboratory
New London, Connecticut 06320
Code 900, 905, 910, 930, 960

Director of Research
U.S. Naval Research Laboratory
Washington, D. C. 20375
Code 2620, 2627, 5000, 5100, 5800

Officer in Charge
Naval Surface Warfare Center
10901 New Hampshire Avenue
White Oak Laboratory Detachment
Silver Spring, Maryland 20903-5000
Attn: E232 Tech Library

Commanding Officer
Naval Coastal Systems Laboratory
Panama City, Florida 32401

STOIAC
Battelle Columbus Laboratories
505 King Avenue
Columbus, Ohio 43201

Commander
Naval Air Systems Command
Washington, D. C. 20361
Code 370

Commanding Officer
U.S. Naval Air Development Center
Attention: Bruce Steinberg
Warminister, Pennsylvania 18974

Director
Defense Documentation Center
(TIMA), Cameron Station
5010 Duke Street
Alexandria, Virginia 22314

Institute for Defense Analyses
1801 North Beaugard Street
Arlington, Virginia 22311

Superintendent
U.S. Naval Postgraduate School
Monterey, California 93940

Chief Scientist
Navy Underwater Sound Reference Div.
U.S. Naval Research Laboratory
P.O. Box 8337
Orlando, Florida 32806

Supreme Allied Commander
U.S. Atlantic Fleet
ASW Research Center, APO
New York, New York 09019
Via: ONR 100 M, CNO OP092D1,
Secretariat of Military,
Information Control, Committee

Director
Institute of Marine Science
University of Alaska
Fairbanks, Alaska 99701

Director
Applied Physics Laboratory
Johns Hopkins University
Johns Hopkins Road
Laurel, Maryland 20810
Atten: J. R. Austin

Director
College of Engineering
Department of Ocean Engineering
Florida Atlantic University
Boca Raton, Florida 33431

Director
Marine Research Laboratories
c/o Marine Studies Center
University of Wisconsin
Madison, Wisconsin 53706

Director
Applied Research Laboratory
Pennsylvania State University
P.O. Box 30
State College, Pennsylvania 16802

Director
Applied Physics Laboratory
University of Washington
1013 NE 40th Street
Seattle, Washington 98195

Director
The Univ. of Texas at Austin
Applied Research Laboratory
P.O. Box 8029
Austin, Texas 78712

Director
Lamont-Doherty Geological Observatory
Torrey Cliff
Palisades, New York 10964

Director
Woods Hole Oceanographic Institution
Woods Hole, Massachusetts 02543

Director
Inst. of Ocean Science Engineering
Catholic University of America
Washington, D.C. 20017

National Science Foundation
Ocean Sciences Division
Washington, D. C. 20550

Office of Naval Research
Resident Representative
c/o Univ. of California, San Diego
Mail Code Q023
La Jolla, California 92093

University of California, San Diego
Marine Physical Laboratory
Branch Office
La Jolla, California 92093

August 1989